UNIVERSITÀ
DEGLI STUDI
DI PADOVA

Università degli Studi di Padova

Dipartimento di Fisica e Astronomia Galileo Galilei

Ph.D. course in Physics

Ciclo XXXIV

Investigating the ^{46}Ar proton wave function with the ^{46}Ar(^{3}He,d)^{47}K direct reaction

Coordinator: Prof. Franco Simonetto

Supervisor: Prof. Daniele Mengoni

Co-Supervisor: Dr. Andrea Gottardo
Co-Supervisor: Dr. Jose Javier Valiente-Dobón

PhD Student: Daniele Brugnara

Dissertation submitted to the
Facoltà di Fisica e Astronomia, University of Padova

A mamma e papà

Abstract

The evolution of the nuclear shell closure at $N = 28$ has gathered much interest due to the observed discrepancies between the well-established shell model with SDPF-U interaction and measurements of the semi-magic ^{46}Ar isotope.

In particular, while a remarkable agreement was observed between theoretical and experimental neutron separation energies, transition probabilities measured with intermediate Coulomb excitation diverge by more than a factor of two from their predicted values. The reason behind this mismatch has been pinned down to the proton transition matrix elements and hints at an incorrect description of the *sd* proton space below $Z = 20$.

The experiment analyzed and discussed in the present thesis addressed this problem by directly probing the proton component of the wave function via a proton-pickup direct reaction in inverse kinematics: ^{46}Ar(^{3}He, d)^{47}K at an energy of 9 MeV/u.

The measurement, performed at the Spiral 1 facility in GANIL with a post-accelerated radioactive ^{46}Ar beam impinging on a high-density cryogenic ^{3}He target, aimed at quantifying the transfer cross section to the $3/2^+$ level relative to the $1/2^+$ ground state in ^{47}K, relying on a state-of-the-art experimental setup for a precise reconstruction of the kinematics of the reaction. The heavy reaction fragment was identified by the high acceptance magnetic spectrometer, VAMOS, while the high-granularity silicon DSSD detector, MUGAST, allowed the measurement of the angular distribution of the light ejectile while also performing particle identification. The AGATA gamma-ray tracking germanium array measured the photons produced by the decay of the ^{47}K excited states.

The experimental evidence indicates a substantially suppressed $L = 2$ transfer to the first excited state of ^{47}K, at odds with shell-model calculations that predict the $s_{1/2}$ and $d_{3/2}$ orbitals as almost degenerate and not entirely occupied. The results will also be discussed in the framework of ab initio and mean-field calculations. In these theoretical results, the low occupancy of the $s_{1/2}$ orbital, in agreement with the high relative spectroscopic factor measured, implies a central depletion of the proton wavefunction: a so-called bubble structure.

Daniele Brugnara
Padova, February 2022

Contents

List of Figures

List of Tables

Chapter 1

Introduction

The advances in the study of the atomic nucleus are based on the comparison between experimental observables and theoretical models that aim at understanding the quantum many-body problem that describes the atomic nucleus and its fundamental constituents.

While this objective has sparked the interest of many physicists since the discovery of radioactivity in 1896, the intent is far from achieved. A coherent picture of the whole landscape would imply understanding all observables of some 3600 known isotopes, combined with a similar amount of predicted and yet unknown nuclei. Each atomic charge Z and mass A combination constitutes an entirely different quantum-mechanical many-body system. Nevertheless, some patterns and similarities emerge between different nuclei based on the underlying physical laws. These patterns are fundamentally tied to physical phenomenons and laws, and their study is essential for the progress in a modelization of the nucleus based on its physics.

In the current interpretation, the existence of a single unified model that possesses the ability to describe and predict every isotope of the Segrè chart with satisfactory precision does not exist. The unification and coherence of all nuclear models is a very desirable goal, yet the current capabilities in terms of computational powers and advancements in nuclear structure theory need to resort to approximations that can be more or less effective based on the system and observables of interest. While great effort is being fruitfully spent towards deriving theoretical tools such as interaction potentials from fundamental physical principles, the nuclear theory structure mainly relies on two models: the shell model and the mean-field methods. Both models aim at the simplification of a strongly-interacting many-body system by extracting the effect of the interaction of multiple particles as an average interaction, which generates various configurations of bound states. The mean-field picture consists of an iterative approximation of the solution to the many-body problem by generating an average field where each particle is independent. The common field is generated by the nucleons and computed at every iteration. On the other hand, the shell model is based on the experimental evidence that some configurations of protons and neutrons are characterized by intrinsic stability and related to the so-called magic numbers. The first attempt was a description of the system as non-interacting particles in a common containing field. While this description proved successful in deriving the magic numbers, different observables were hardly reproduced. The more refined evolution of the model required the addition of an interaction term in the Hamiltonian that previously only contained the common field. The quantum states of interest are expressed in terms of those of the non-interacting model, translating the problem to the diagonalization of the

interacting Hamiltonian matrix in the new basis. In a vast simplification of the matter, the shell-model picture best describes the nuclear properties of isotopes close to these particular configurations. In contrast, the mean-field picture generally shows a complementary ability of best describing configurations far from the magic numbers. The root of this duality can be found in the capability of the mean-field framework to describe strongly correlated systems which feature coherent (collective) behaviors. In order to obtain an accurate description in the shell model picture of a strongly correlated system, the dimension of single-particle basis states required for the diagonalization of the Hamiltonian matrix can quickly reach a prohibitive computational cost.

Recent developments in the field of nuclear structure are quickly emerging thanks to technological advances in the production and acceleration of radioactive (unstable) isotopes. The new state-of-the-art facilities for the production of exotic beams opened the possibility for the study of nuclei that are not present in nature but are always of great interest for their physical or astrophysical properties.

The current work aims to add insight on the current knowledge nuclear structure of the ground state of a particular isotope, ^{46}Ar. This isotope is composed of 28 neutrons and 16 protons. As a consequence, it lies in a region of semi magicity: along the $N = 28$ shell closure. In the shell model picture, it can be obtained by removing a pair of protons from the doubly magic ^{48}Ca. As it turns out, ^{46}Ar is located in a region where state-of-the-art shell-model calculations are able to reproduce observables with remarkable precision. These observables consist, for instance, in energy spectra, neutron separation energies, or transition probabilities among different states. Moreover, recent developments have shown the failure of these calculations in reproducing the quadrupole transition probability between the ground state and first excited state in ^{46}Ar. This inconsistency is even more surprising if one considers how the same calculations are able to reproduce precisely the neutron separation energy of this isotope as well as the nearby ones. Recent developments and considerations have pointed out that the problem might lie in the proton component of the wave function. In particular, the proton contribution to the matrix elements that describe the quadrupole transition probability between the two states appears overestimated in the model.

The intent of this work is to probe the proton component of the wave functions of ^{46}Ar directly. The means of the study will focus on a direct proton-transfer reaction on this radioactive isotope: ^{46}Ar(^{3}He,d)^{47}K at an energy of 10 MeV/u. Theoretical considerations on the nuclear structure properties of ^{46}Ar will be presented and discussed in relation to the experiment.

The experiment exploits the capabilities and latest developments in terms of radioactive beams produced with the Isotope mass Separation Online (ISOL) in GANIL, France. This technique relies on the post acceleration of the extracted ions, which, in turn, guarantees precise optical characteristics of the beam, essential for the study of direct reactions in inverse kinematics.

The detection and reconstruction of the nuclear reaction rely on a state-of-the-art array that combines the latest technology in the nuclear field in terms of heavy and light charge particle detection and γ-ray spectroscopy. The light

charged particle detection and discrimination is performed by position-sensitive double-sided silicon strip detector, MUGAST. The heavy-ion, ^{47}K, is tagged and measured by the large acceptance magnetic spectrometer VAMOS while γ rays emitted from the recoiling isotope are measured with a high-purity position-sensitive tracking germanium array, AGATA.

The high granularity of the setup allows for a precise measurement of the dynamics of the reaction as well as the consistency check on the acquired data.

This work is organized in the following Chapters:

- Chapter 2 focuses on a brief introduction of the theoretical background concerning direct reactions and their implication on the nuclear structure, in particular in the framework of the shell model.
- Chapter 3 introduces part of the current studies performed on ^{46}Ar and, more in general on the $N = 28$ shell closure. The problem of transition probabilities and the current understanding of these aspects are also be discussed in more detail
- Chapter 4 describes the experimental setup, the calibrations, and its performance.
- Chapter 5 presents the Monte Carlo Geant4 simulations performed to characterize the experimental setup
- Chapter 6 documents the DWBA direct reaction calculations performed with the Fresco code for the system of interest and other related cases
- Chapter 7 delineates the analysis procedure and the experimental outcome
- Chapter 8 discusses the results in the framework of current theoretical models such as *ab initio*, mean-field and shell-model calculations.

Chapter 2

Background on the Theory of Nuclear Structure and Reactions

2.1 The Nuclear Shell Model

The hydrogen atom and, more generally, the atomic shell model represents one of the main milestones in the development and the study of quantum mechanics. In particular, in the atomic case, the model is developed as a central potential generated in the nucleus of the atom that allows for the creation of quantized bound states for the orbiting electrons. A spin-orbit coupling and other considerations are also necessary for an accurate description of the system. While the case of a single electron orbiting the central potential features an analytical solution, the same cannot be said in the case of multiple interacting electrons, where the problem needs to be solved with practical approximations that often resort to quantum mechanical perturbation theory.

In the case of the nuclear shell model, the physical system in itself is similar, in a way, to the atomic case, where nucleons can be thought of as orbiting a common potential with one key difference: the overall potential is not external but is generated by nucleons themselves. The overall common potential is the sum of all interactions, and the spin-orbit component of the final potential determines the energy levels generated by this common field.

Specific configurations of the quantum mechanical system, or in other words, some numbers of protons and neutrons, can feature remarkable stability. These unique configurations are one of the strongest pieces of evidence that the nuclear shell model is a powerful tool in the description of the nuclear quantum many-body system.

2.1.1 The Independent Particle Model

It is possible to imagine that a single nucleon orbiting in this central potential will perturb the overall common field only slightly, so low-lying states can be described as non-interacting particles in different quantum states. The single-particle Schrodinger equation will have the following form [6]:

$$H_{0,i}\phi_i(\mathbf{r}) = \left(-\frac{\hbar^2}{2m}\nabla^2 + V_0(\mathbf{r})\right)\phi_i(\mathbf{r}) = \epsilon_i\phi_i(\mathbf{r})$$

In this expression, m represents the mass of the nucleon, V_0 a central potential, ϵ_i the single-particle energy and ϕ_i the wave function. The total Hamiltonian of the system will be the sum of all single-particle Hamiltonians: $\sum_i H_{0,i}$.

In this case, the many-body system is described by the single-particle Hamiltonian, where the complex many-body system is reduced to the more

straightforward case of non-interacting nucleons orbiting in a common potential $V(\mathbf{r})$. On the other hand, the wave function will consist of the Slater determinant containing the single-particle wave functions of the single nucleons.

Unfortunately, this approximation is too coarse. Nevertheless, it serves as a *starting point* for one of the most successful techniques in the description of this many-body quantum.

The shape of the mean potential $V(\mathbf{r})$ will have a radial contribution which can be chosen as a simple harmonic-oscillator potential (which has the advantage of a closed-form solution) or another function tailored to the mean nuclear potential such as the Woods-Saxon well. This choice, while important under some aspects, is not crucial as the single-particle states ϕ_i will be used as the *basis* to span the real solutions of the interacting-particle shell model, which accounts for the nucleon-nucleon interactions.

Historically another term has been added to the central potential, which in itself was not able to correctly predict the occurrence of the magic numbers, the configurations with inherent stability. The inclusion of a spin-orbit component was proven to be successful in describing the presence of the following magic numbers: 2, 8, 20, 28, 50, 82, 126. The potential, in a simplified form, can be expressed by a central well and a spin-orbit interaction:

$$V_0(\mathbf{r}, \mathbf{l}\cdot\mathbf{s}, \mathbf{l}^2) = -V_0 + \frac{1}{2}m\omega^2\mathbf{r}^2 - V_{so}\,\mathbf{l}\cdot\mathbf{s} - V_B\,\mathbf{l}^2 \tag{2.1}$$

where V_0 represents the depth of the well, V_{so} (V_B) the strength of the spin-orbit (total angular momentum) term, and ω the harmonic oscillator frequency. It is a common choice for the spin-orbit coefficient to include a dependence on the position coordinate $\mathbf{r}$, often as proportionality with the derivative of the radial potential (mainly in the case of the Woods-Saxon). Nevertheless, in equation 2.1, no radial dependence is be expressed so that the solution to this simplified single-particle Hamiltonian will reduce to that of a simple harmonic oscillator with all the considerations due to the angular momentum and spin couplings. The coupling of the spin and orbit term renders the angular momentum states no longer eigenstates of the system. As a consequence, the total angular momentum quantum number $\mathbf{J} = \mathbf{l} + \mathbf{s}$ needs to be used. The quantum numbers of the system, which can be divided in spherical harmonics and a radial component due to the symmetry of the potential, are the common radial quantum number n, the orbital angular momentum l, the total angular momentum j and its projection on the quantization axis m_j. The single-particle energy has the following expression [6]:

$$\begin{aligned}\epsilon_{n,l,j} = &- V_0 + \hbar\omega\left(2n + l + \frac{3}{2}\right) \\ &- V_{so}\frac{\hbar^2}{2}\left(j\,(j+1) - l\,(l+1) - \frac{3}{4}\right) - V_B\hbar^2 l\,(l+1)\end{aligned}$$

The principal quantum number $\mathcal{N} = 2n + l$ is often introduced due to the presence of the degeneracy. A state relative to a given principal quantum number contains all possible combinations of the sum of n and l [6]:

$$\begin{aligned} \mathcal{N} &= 0, 1, 2, \dots \\ l &= \mathcal{N}, \mathcal{N} - 2, \dots, 1 \text{ or } 0 \\ n &= \frac{\mathcal{N} - l}{2} \end{aligned}$$

The single particle wave function will consist of the product of the radial part $u_{n,l}^{H.O.}$ with the coupling of the spherical harmonic functions Y_{l,m_j} with the spin component X_{s,m_s} to the good quantum number j:

$$\phi_i = \phi_{nljm} = \frac{u_{n,l}^{H.O.}(r)}{r} \left[Y_{l,m_j}(\theta, \phi) \otimes X_{s,m_s} \right]_{m_j}^{j}$$

The radial component will consist in the solution of the differential equation:

$$-\frac{\hbar^2}{2m} \frac{d^2 u(r)}{dr^2} + \left[\frac{l(l+1)\hbar^2}{2m\, r^2} + V_0(r) \right] = \epsilon u(r)$$

The radial component of the wave function is shown in Figure 2.1 where the dependence of the probability density is shown as a function of the principal quantum number (top) and a combination of different angular momenta.

The Slater determinant is created by progressively filling the lowest energy states generated by the potential. Figure 2.2 shows the energy levels when the orbit and spin-orbit perturbations are added to a simple harmonic oscillator potential. The produced states are degenerate as no dependence on the total angular momentum m_j is produced so that the degeneracy of each *orbit* is $2(j + 1)$.

An evident phenomenon arises: the presence of significant energy gaps between some of the states. Given the *ansatz* of the non-independent particle model, in some nuclei which correspond to filling the low lying states progressively, remarkable stability properties should be observed. While the independent particle model clearly fails on accounting for nucleon-nucleon interactions (nucleons in a strongly interacting system such as the nucleus cannot be expected not to interact), other aspects are also not considered. Protons are affected by an additional Coulomb interaction, and the symmetry energy which favors $N = Z$ nuclei is also not present. These aspects can be dealt with by considering a different potential for protons and neutrons and other considerations beyond the scope of this introduction.

Moreover, the physical justification behind the strong spin-orbit coupling in the nucleus is not clear since its introduction [8]. More recent developments associate the importance of the three-body forces for the occurrence of the so-called spin-orbit shell closures [12].

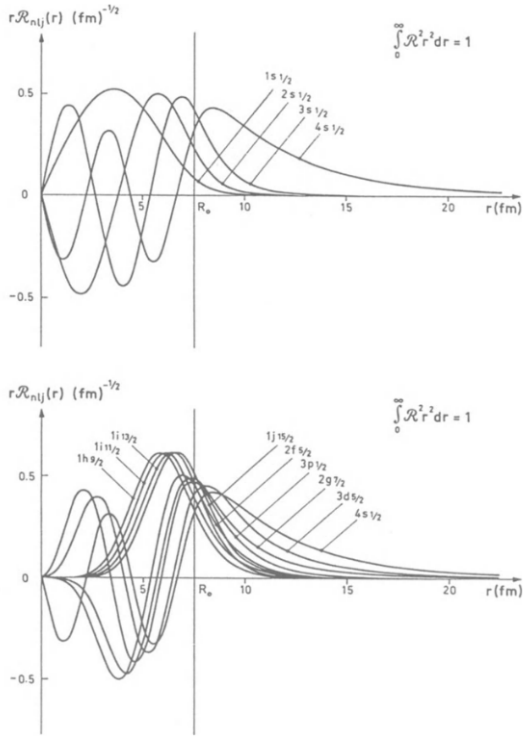

Figure 2.1: Neutron radial wave functions of different orbits for $A = 208$ and $Z = 82$ with a Wood-Saxon potential. More central orbits are associated to low values of the angular quantum number l. Figure adapted from reference [6].

2.1.2 The Interacting Shell Model

While the non-interacting model is able to describe well some experimental evidence, such as the occurrence of magic numbers, the assumption of the absence of interaction between particles is too broad for the description of many characteristics of the nucleus. This interaction cannot be treated perturbatively and can be strong enough to modify dramatically the orbits generated by the mean-field. In particular, a model of non-interacting particles will not be able to describe the transition between different nuclear states, which requires non-diagonal terms in the Hamiltonian matrix. As a consequence, it is necessary to introduce some interaction between the particles and to observe its effect on the structure properties of the nucleus.

It is clear that the potential assumed in equation 2.1 represents an approximation of the complex many-body potential:

$$V(\mathbf{r}_1, \ldots, \mathbf{r}_A) = \sum_{i,j}^{A} V_{2b}(\mathbf{r}_i, \mathbf{r}_j) + \sum_{i,j,k}^{A} V_{3b}(\mathbf{r}_i, \mathbf{r}_j, \mathbf{r}_k)$$

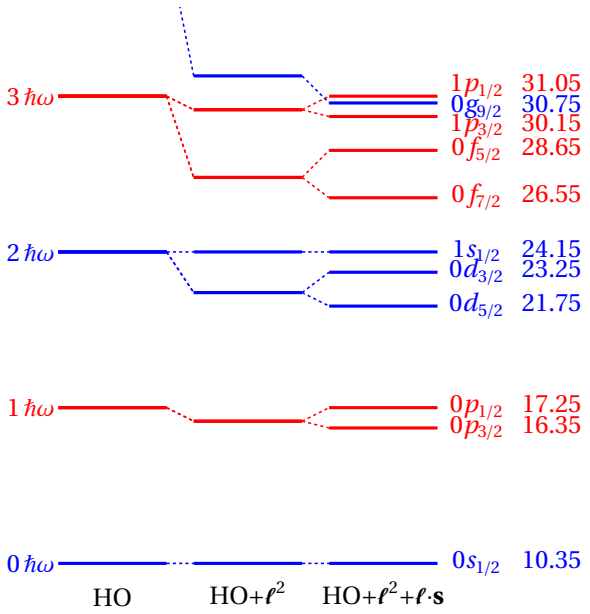

Figure 2.2: Example of effective single particle energies from an harmonic oscillator potential. The addition of the spin orbit coupling term $l \cdot s$ to the harmonic oscillator well generates energy gaps which are associated to nuclear shells.

In this expression, the three-body potential V_{3b} can be thought of as necessary due to the fact that nucleons are not elementary particles and have their own structure due to their additional degrees of freedom. Nevertheless the idea of a common potential remains powerful and it is possible to express the general potential in equation 2.1.2 as the common potential V_0 in equation 2.1 plus a residual interaction potential U:

$$V(\mathbf{r}_1, \ldots, \mathbf{r}_A) = V_0(\mathbf{r}, \mathbf{l} \cdot \mathbf{s}, \mathbf{l}^2) + U(\mathbf{r}_1, \ldots, \mathbf{r}_A)$$
$$\text{where} \quad U(\mathbf{r}_1, \ldots, \mathbf{r}_A) = V(\mathbf{r}_1, \ldots, \mathbf{r}_A) - V_0(\mathbf{r}, \mathbf{l} \cdot \mathbf{s}, \mathbf{l}^2)$$

Building upon the results of the previous section, one can express the Hamiltonian as the sum of the single-particle components plus the residual (effective) interaction U. At the same time, the solution $|\Psi\rangle$ of the full Hamiltonian can be expressed as a linear combination of the states $|\phi\rangle$ that are the solution to the non-interacting shell model:

$$H|\Psi\rangle = (H_0 + U)|\Psi\rangle = E|\Psi\rangle \quad \text{where} \quad |\Psi\rangle = \sum_{k=1}^{N} a_k |\phi_k\rangle$$

It is possible to express the Hamiltonian in terms of the matrix elements in the single-particle basis $|\phi_i\rangle$. The matrix will contain diagonal terms consisting in the single-particle energies and non-diagonal terms introduced by U:

$$H_{l,k} = \langle\phi_l| H |\phi_k\rangle \Longrightarrow H_{l,k} = \epsilon_k \delta_{l,k} + \langle\phi_l| U |\phi_k\rangle$$

In practice, the diagonalization of this matrix will return new levels and new states, which will be the solution of the interacting shell model. Considering a simple two level system, the Hamiltonian matrix will be a 2×2 matrix with terms $H_{1,1}, H_{2,2}$, and $H_{2,1} = H_{1,2}$ [6]. Solving the eigenvalue problem, the two energies of the mixed configuration will be separated by:

$$\Delta E_{1,2} = \sqrt{(H_{1,1} - H_{2,2})^2 + 4H_{1,2}^2}$$

In this case, the off-diagonal term has the effect of increasing the separation in energy of the two levels. The term $a_{1,2}^2$ expresses the amount of mixing between the two original configurations or, more precisely, the overlap between the solution of the single particle Hamiltonian and that of the interacting one:

$$a_{1,2} = \left(1 + \frac{H_{1,2}}{H_{1,1} - E_1}\right)^{-\frac{1}{2}}$$

The effect of the $H_{1,2}$ term is to increase the amount of the $|\phi_2\rangle$ state in $|\Psi_1\rangle$, thus increasing the mixing between the two configurations.

In practice, considering a system of n particles and many orbitals leads to more involved calculations that need the introduction of angular momentum algebra and other concepts for the derivation of one and two-body matrix elements. Nevertheless, it is sufficient to know that, even in this more complex case, it is always possible to express n-particle matrix elements in terms of their one and two-body counterparts [6].

2.1.3 Effective Interactions

The derivation of a two-particle residual interaction, here defined with U, is not a straightforward procedure. One of the reasons is that the interaction is strongly dependent on the model space, opening the possibility of different procedures for the definition of this quantity.

In particular, one type of approach consists in the so-called *realistic interactions*. The intent is to derive U from the free nucleon-nucleon interaction based on experimental evidence. They are often obtained by fitting data of *pp* and *pn* scattering experiments such as phase shifts or polarization data. The general shapes of these potentials are chosen to respect all symmetries such as translation, time-reversal, or rotation.

While this procedure attributes the most physical significance to the interaction, a number of problematic aspects emerge to hinder the overall results. In particular, protons and neutrons interact within the nuclear medium and not in the vacuum. This difference requires the introduction of a process called

renormalization of the force. Additional aspects are introduced by the truncation scheme, which reduces the dimension of the basis of shell-model calculations and thus limits the number of correlations that can be introduced by nucleons outside the valence space. The evidence of a non-inert core is called core polarization and accounts for the excitation of nucleons not considered in the valence space.

Effective (*phenomenological*) *interactions* change the approach to the problem by neglecting to pin down the physical significance. Two body matrix elements and single-particle energies are treated as free parameters and fitted to reproduce experimental data such as excitation energies. An example is the SDPF-U interaction [10] developed by F. Nowacki and A. Poves to describe nuclei in the $sd-pf$ valence space.

It is often convenient to separate the contributions to the Hamiltonian into two components: the monopole and multipole Hamiltonians [4]. The former describes the spherical mean-field and is thus responsible for the global saturation properties and for the evolution of the spherical single-particle energies. The latter contains the terms which are suited to describe the pairing and other types of correlation, such as quadrupole interaction.

The combination of effective interactions with large-scale shell-model calculations has accompanied the experimental efforts in the nuclear structure community [3].

2.2 Direct Reactions as a Probe of the Nuclear Structure of a Nucleus

This section will focus on addressing the interplay between the physics of nuclear structure and that of reaction dynamics. Colliding nuclei can undergo a multitude of possible reactions and their physical modeling can vary significantly. In the course of this work, only a few reactions which mainly occur at low energies will be considered:

- **Elastic reaction**: The scattered fragment is deflected but retains the same center of mass-energy. The final state of the colliding nuclei remains unchanged after the collision. The study of this process is crucial for the definition of the optical potential of the system.
- **Inelastic reaction**: The scattered fragment has a different center of mass-energy. The collision causes the excitation to nuclear states in the colliding nuclei. It is studied because it gives information on the nuclear structure of the colliding nuclei, such as the spin and parity of the excited states.
- **Pickup/Stripping**: In a direct transfer reaction, a nucleon is added or removed from an orbital of the colliding nuclei. The reaction can be considered direct if the other nucleons can be considered spectators in the process. They can be considered a probe of the nuclear structure of the nuclei, as will be discussed in this section.

- **Fusion evaporation**: In this case, all nucleons contribute to the reaction. This collision is central, and the two systems merge in a compound nucleus populating high excitation energy states. Often the excitation energy of the compound nucleus is high enough to permit the evaporation of particles which is then followed by an internal decay via γ-ray emission.

In particular, this work will focus on the use of direct transfer reaction for the study of the nuclear structure of ^{46}Ar. The choice of this reaction is justified by the possibility of extracting information on the nature of particular states by measuring the cross-section for the population of energy levels of interest. To first approximation, the transfer of one proton to the ground state of ^{46}Ar will leave all other nucleons inert to the reaction, and the probability of populating different states of ^{47}K will give information on the overlap between the ground state of ^{46}Ar and the excited states of ^{47}K.

The interplay between reaction dynamics and the nuclear structure leads to the concept of spectroscopic factors.

2.2.1 A Hint on Scattering Theory

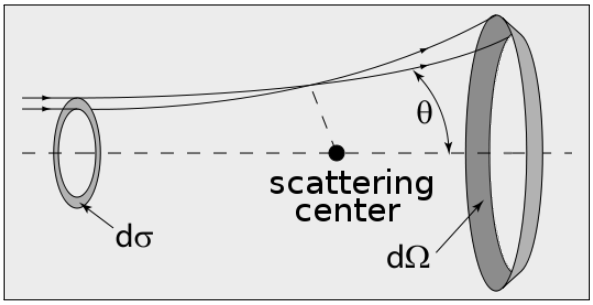

Figure 2.3: Diagram of the geometry involved in the differential cross section.

The differential cross-section $d\sigma/d\Omega$ is defined experimentally as the probability density function (PDF) related to the flux of scattered particles by a scattering center (cf. Figure 2.3). The PDF is a function of the spherical coordinates θ and ϕ. The differential cross-section integrated over a finite solid angle $\Delta\Omega$ can be experimentally thought as the ratio between the scattered and incoming fluxes of particles where the former is measured by instruments detecting particles over a finite solid angle $\Delta\Omega$ [5, 9]:

$$\int_{\Delta\Omega} d\Omega' \frac{d\sigma}{d\Omega'} = \frac{\textit{Detected scattered flux in } \Delta\Omega}{\textit{Incoming Flux}}$$

In reality, multiple scattering centers ($n_t \times A$) are present in the area A hit by the incoming flux; as a consequence, the number of detected scattered events I is proportional to the incoming flux, as well as the density of scattering centers n_t:

$$I = I_0\, n_t \int_{\Delta\Omega} d\Omega' \frac{d\sigma}{d\Omega'} \tag{2.2}$$

In order to treat the differential cross-section from the perspective of quantum mechanics, it is necessary to identify this observable starting from Schrodinger's equation. In relative coordinates, it is possible to work in the center of mass frame of reference, neglecting the total kinetic energy part of the equation. The Hamiltonian will include the relative kinetic energy $\hat{T}$ and m will represent the reduced mass ($m = \frac{m_1+m_2}{m_1 m_2}$)[1]:

$$\hat{H}\Psi = E\Psi \quad \text{where} \quad \hat{H} = \hat{T} + \hat{H}_p + \hat{H}_t + V \tag{2.3}$$

where $\hat{T}$ is the kinetic energy operator of the system, $\hat{H}_p$ and $\hat{H}_t$ the Hamiltonians accounting for the internal degrees of freedom (ξ) of respectively the projectile and the target and V the interaction potential between the two nuclei.

In the most general case, all interaction potentials need to be computed as the sum of all nucleon-nucleon interactions. However, the system is best described by considering the colliding nuclei as separate entities in the Hamiltonians $\hat{H}_p, \hat{H}_t$ which contain part of this interaction potential: U_t, U_p. In the case of the shell-model framework, these two potentials will be described by the effective potential used in the model.

The residual part of the interaction will describe the effective projectile-target interaction potential V:

$$V_{tot} = \sum_{\{i_j\}_{i_j \in p,t}} V(\mathbf{r}_i, \mathbf{r}_j) = U_t + U_p + V \tag{2.4}$$

For the purpose of this section, it is assumed that the solution $\phi_i, i \in \{p, t\}$ to the nuclear Hamiltonian that describes the internal structure of projectile and target is known:

$$(\hat{H}_i - \epsilon_i)\phi_i = 0 \quad \text{where} \quad i \in \{p, t\}$$

The information contained in the equation represents the spectroscopic properties of the nucleus, stripping all other components in the dynamic equation 2.3 that describes the nuclear reaction.

It is convenient to combine in a single Hamiltonian $\hat{H}_p + \hat{H}_t = \hat{H}_\alpha$ and wave function $\phi_t\phi_p = \phi_\alpha$ the projectile and target components. Since target and projectile consist of two independent systems, ϕ_α is a direct product so that also the total energy will be the sum $\epsilon_{\alpha_p} + \epsilon_{\alpha_t} = \epsilon_\alpha$. Conversely, β will represent the direct sum (product) of the final-nuclei Hamiltonians (wave functions).

Let $\Psi^0_\alpha(\xi, \mathbf{k}, \mathbf{r})$ be the solution to the homogeneous equation of the dynamic system of non-interacting nuclei, function of the relative coordinate $\mathbf{r}$ and wave vector $\mathbf{k}$:

[1] Due to the translational symmetry of the system, the center of mass coordinates will only generate an additional phase in the wave function

$$(\hat{T} + \hat{H}_\alpha - E)\Psi^0_\alpha(\xi, \mathbf{k}, \mathbf{r}) = 0$$

Since only the kinetic term $\hat{T}$ is present, the solution takes the form of a product of a plane wave between the relative motion component and the nuclear wave function:

$$\Psi^0_\alpha(\xi, \mathbf{k}, \mathbf{r}) = \phi_\alpha(\xi) e^{i\mathbf{k}_\alpha \cdot \mathbf{r}} \quad \text{and} \quad E = E_{k_\alpha} + \epsilon_\alpha = \frac{\hbar^2 k_\alpha^2}{2m_\alpha} + \epsilon_\alpha$$

where $\mathbf{r}$ represents the relative coordinate $\mathbf{r}_1 - \mathbf{r}_2$ and is contained in the plane wave solution ($e^{i\mathbf{k}\cdot\mathbf{r}}$).

Since the interest behind this modelization of a nuclear reaction lies on a specific reaction channel β described by two specific reaction fragments with the wave function ϕ_β, it is necessary to multiply both sides of equation 2.3 by ϕ^*_β and integrate over all the internal coordinates ξ. Rearranging the equation, the result does not have a trivial solution:

$$(E - \epsilon_\alpha - \hat{T}_\alpha)\, \psi_\beta(\mathbf{r}_\alpha) = \int d\xi\, \phi^*_\beta\, V\, \Psi_\alpha \quad \text{where} \quad \psi_\beta(\mathbf{r}_\alpha) = \int d\xi\, \phi^*_\beta \Psi_\alpha \tag{2.5}$$

The label β indicates the reaction channel and is equal to α in the case of the elastic reaction channel.

It is often useful to formulate the equation in terms of Green's functions G^0, which are defined as the solution to the *modified* version of equation 2.5:

$$(E - \epsilon_\alpha - \hat{T}_\alpha)\, G^0_\beta(k_\beta, \mathbf{r}, \mathbf{r}') = \delta(\mathbf{r} - \mathbf{r}')$$

The final solution will have the form of the sum of the homogeneous wave plus the Green's integral [5]:

$$\psi_\beta(\mathbf{r}_\alpha) = e^{i\mathbf{k}_\beta \cdot \mathbf{r}}\, \delta_{\alpha\beta} + \int d\mathbf{r}'\, G^0_\beta(k_\beta, \mathbf{r}, \mathbf{r}') \left(\int d\xi\, \phi^*_\beta(\xi)\, V\, \Psi_\alpha(\mathbf{r}', \xi) \right) \tag{2.6}$$

It is possible to show, using the Fourier transform [5], that the Green's function takes the form of equation 2.7.

$$G^0_{\beta,\pm} = -\frac{m}{2\pi\hbar^2} \frac{e^{\pm i k_\beta |\mathbf{r} - \mathbf{r}'|}}{|\mathbf{r} - \mathbf{r}'|} \tag{2.7}$$

So that, explicitly, equation 2.6 can be expressed in terms of the *outgoing* Green's function:

$$\psi_\beta(\mathbf{r}_\alpha) = e^{i\mathbf{k}_\beta \cdot \mathbf{r}}\, \delta_{\alpha\beta} + \frac{m}{2\pi\hbar^2} \int d\mathbf{r}'\, \frac{e^{i k_\beta |\mathbf{r} - \mathbf{r}'|}}{|\mathbf{r} - \mathbf{r}'|} \left(\int d\xi\, \phi^*_\beta(\xi)\, V\, \Psi_\alpha(\mathbf{r}', \xi) \right) \tag{2.8}$$

In the case of short range interactions, an asymptotic expression of the Green's function in equation 2.9 can be derived, keeping in mind that: $|\mathbf{r}-\mathbf{r}'| \xrightarrow[r\to\infty]{} r - r'\cos\theta$ and $1/|r-r'| \xrightarrow[r\to\infty]{} 1/r$:

$$G^0_{\beta,\pm} \xrightarrow[r\to\infty]{} -\frac{m}{2\pi\hbar^2}\,\frac{e^{ik_\beta r}}{r}\,e^{i\mathbf{k}'_\beta\cdot\mathbf{r}'} \tag{2.9}$$

where $\mathbf{k}'_\beta$ indicates a vector of the same magnitude of $\mathbf{k}_\beta$ but with direction parallel to $\mathbf{r}$. Equation 2.8 in a region far from the potential, takes the following asymptotic form [5]:

$$\psi_\beta(\mathbf{r}_\alpha) = e^{i\mathbf{k}_\beta\cdot\mathbf{r}}\,\delta_{\alpha\beta} + \frac{m}{2\pi\hbar^2}\,\frac{e^{ik_\beta r}}{r}\int d\mathbf{r}'\,e^{-i\mathbf{k}'_\beta\cdot\mathbf{r}'}\left(\int d\xi\,\phi^*_\beta(\xi)\,V\,\Psi_\alpha(\mathbf{r}',\xi)\right) \tag{2.10}$$

It is now possible to define the well known *scattering amplitude* as the integral part of equation 2.10:

$$f_{\alpha\beta}(\theta) = -\frac{m}{2\pi\hbar^2}\int d\mathbf{r}'\,e^{i\mathbf{k}'_\beta\cdot\mathbf{r}'}\left(\int d\xi\,\phi^*_\beta(\xi)\,V\,\Psi_\alpha(\mathbf{r}',\xi)\right) \tag{2.11}$$

Up to this point, only projections of the solution Φ_α on the possible final states have been considered. The final wave function is the combination of all these overlaps that should generate, thanks to their completeness, the full solution. In the asymptotic form, the wave function should take the following form:

$$\Psi_\alpha = \begin{cases} \phi_\alpha e^{i\mathbf{k}_\alpha\cdot\mathbf{r}_\alpha} + \phi_\alpha f_{\alpha,\alpha}(\theta)\frac{e^{i\mathbf{k}_\alpha\cdot\mathbf{r}_\alpha}}{r_\alpha} & \text{elastic} \\ \sum_{\alpha'\neq\alpha}\phi_{\alpha'} f_{\alpha',\alpha}(\theta)\frac{e^{i\mathbf{k}_{\alpha'}\cdot\mathbf{r}_\alpha}}{r_\alpha} & \text{inelastic} \\ \sum_\beta \phi_\beta f_{\beta,\alpha}(\theta)\frac{e^{i\mathbf{k}_\beta\cdot\mathbf{r}_\beta}}{r_\beta} & \text{transfer} \end{cases} \tag{2.12}$$

The overlaps relate to different possible reaction channels.

These results show that the *outgoing* wave function is a superposition of the plane wave, with multiple spherical waves, each with its own proportionality factor f that represents the scattering process and a reaction channel each.

2.2.2 The Differential Cross Section

Equation 2.2 represents the experimental cross-section; the connection with the theoretical modelling is related to the wave functions through fluxes of probability currents $\mathbf{J}$:

$$\frac{d\sigma}{d\Omega} = \frac{d\Phi(\mathbf{J}_{out})}{|\mathbf{J}_{inc}|d\Omega} \quad \text{where} \quad \mathbf{J} = \frac{\hbar}{2mi}(\Psi^*\nabla\Psi - \Psi\nabla\Psi^*) \tag{2.13}$$

With a substitution of the incident plane wave solution and the outgoing spherical solution, it is possible to obtain:

$$\mathbf{J}_{inc} = \frac{\hbar\mathbf{k}}{m} \quad \mathbf{J}_{out} = \frac{\hbar\mathbf{k}}{m} + \frac{\hbar k}{m}|f(k,k',\theta)|^2\hat{\mathbf{e}}_{\mathbf{r}} + \mathcal{O}\left(\frac{1}{r^3}\right)$$

So that far away from the scattering center, the outgoing flux of probability in the solid angle $d\Omega$ is asympthotically:

$$d\sigma(\mathbf{J}_{out}) = |f(k,k',\theta)|^2\frac{\hbar k}{m}d\Omega + \mathcal{O}\left(\frac{1}{r}\right)$$

The first order of the expansion, according to equation 2.13 returns an elegant expression of the cross section in terms of the function f.

$$\frac{d\sigma}{d\Omega} = \frac{k'm}{m'k}|f(k,k',\theta)|^2 \tag{2.14}$$

In this expression, primed variables represent the values after the reaction process, relative to the outgoing flux. Note that $\hbar\mathbf{k}/m$ is the velocity and that for an elastic collision, where the mass and velocity norm remains the same after the collision, the factor in front of f elides.

As a consequence, every reaction channel will be characterized by its own scattering amplitude f. It is trivial to generalize equation 2.14 to express the differential cross section of the reaction channel $\alpha \to \beta$ [5]:

$$\left(\frac{d\sigma}{d\Omega}\right)_{\alpha\to\beta} = \frac{m_\alpha k_\beta}{m_\beta k_\alpha}|f_{\beta,\alpha}(k,k',\theta)|^2 \tag{2.15}$$

The connection between the Hamiltonian of the many-body nuclear system and the physical observable of the differential cross-section is now evident. It is clear that the observable itself is strongly dependent, not only on the kinematic conditions of the two nuclei but also on the interaction potentials and thus on the nuclear structure of the target and projectile nuclei.

In most experiments, the angular momentum projection is unknown, meaning that no beam and target polarization M_p, M_t is present and no polarization measurement of the reaction fragments M_{β_1}, M_{β_2} is performed. The overall cross section needs to be averaged over all possible angular momentum projections:

$$\frac{d\sigma}{d\Omega} = \frac{1}{(2J_p+1)(2J_t+1)}\sum_{M_p,M_t,M_{\beta_1},M_{\beta_2}}\left(\frac{d\sigma}{d\Omega}\right)_{\alpha\to\beta} \tag{2.16}$$

2.2.3 The Optical Potential

In the shell-model picture, nucleons generate a common mean-field which is contained in the nuclear Hamiltonian $\hat{H}_\alpha$. The residual of this interaction, as stated in equation 2.4, constitutes the potential V which is explicitly included in equation 2.3. Analogously to this idea, it is possible to imagine that the colliding nuclei will interact via a common potential $U(\mathbf{r}_\alpha)$ before any exchange of nucleons occurs. This central potential will depend only on the relative

coordinates of the nuclei and can be optimized, in this approximation, as the potential which best describes the elastic scattering process of the nuclei.

The central potential is unable to account for any nuclear structure in the colliding nuclei so that no other reaction channel can exist if the residual potential V is omitted. In other words, a direct reaction can be thought of as the result of perturbations in elastic scattering theory.

$$\left(\hat{T} + \hat{H}_\alpha + U_\alpha - E\right) \Psi_\alpha = (U - V)\, \Psi_\alpha \tag{2.17}$$

Considering the homogeneous version of equation 2.17 by setting $V = 0$ and the fact that the central potential U_α only depends on the relative coordinate, it is possible to separate the wave function in a component that accounts for the degrees of freedom (ϕ_α) and another component which describes the relative motion $\chi_\alpha(\mathbf{r}_\alpha)$, solution to the equation:

$$\left(\hat{T} + U_\alpha - E_\chi\right) \chi_\alpha(\mathbf{r}_\alpha) = 0 \tag{2.18}$$

The wave function of the initial state α has been expressed in terms of the components of the reaction channels by means of the overlap and *reconstructed* as the sum of all possible channels in equation 2.12. Consequently, part of the incident flux will be taken up by inelastic and transfer channels. Nevertheless, considering a hermitian Hamiltonian in equation 2.18 that, in turn, means a real potential U_α, it is impossible to correctly match the elastic channel as wished from the expectations of the potential. The way to reduce the flux is to consider the potential U_α which will generate some absorption of the incoming flux which will then be *distributed* to the various inelastic and transfer-reaction channels.

Since the relative-motion Schrödinger equation 2.18 presents a well-behaved central potential, it is possible to separate the solution in a spherical harmonic $Y_l^m(\theta, \phi)$ and radial component $f_l(k_\alpha, r_\alpha)$ [5]:

$$\chi_\alpha(\mathbf{r}_\alpha) = \frac{4\pi}{k_\alpha r_\alpha} \sum_{l,m} i^l e^{i\sigma_l} f_l(k_\alpha, r_\alpha) Y_l^{*m}(\hat{r}_\alpha) Y_l^m(\mathbf{k}_\alpha) \tag{2.19}$$

An angular-momentum dependent phase shift $e^{i\sigma_l}$ has been introduced to account for the Coulomb potential that, due to its asymptotic decay of $\frac{1}{r}$, does not decay fast enough at $r \to \infty$ to justify the asymptotic plane wave expansion. The expansion in the case of the Coulomb potential can be shown to introduce a non-zero phase shift. However, the scattering amplitude can be sum to the elastic component of the expansion. The radial component is defined as the solution to the following equation which now includes also the angular momentum quantum number l:

$$\left(\frac{\hbar^2}{2m_\alpha}\left(\frac{d^2}{dr^2} - \frac{l(l+1)}{r^2}\right) - U_\alpha + E_\alpha\right) f_l(k_\alpha, r_\alpha) = 0$$

A common parametrization of the potential U is given by the sum of a real and imaginary Woods-Saxon potential:

$$f(r;R,a) = \frac{1}{1+e^{\frac{r-R_V}{a_V}}}$$
$$U(r) = Vf(r;R_V,a_V) + iWf(r;R_W,a_W)$$

where the parameters V, R_V, a_V, W, R_W, a_W are defined (chosen) as those that best describe the elastic reaction channel in a given system of nuclei and at the proper reaction energy. It is also possible to formulate a realistic potential based on first principles of the nucleon-nucleon interaction and the overall nuclear model.

Similarly to the shell-model picture, the spin-orbit coupling is also expected in the mean potential and in the relative motion wave function χ_α. The presence of this additional term complicates the treatment of the optical potential:

$$U_{so}(r)(2\,\mathbf{l}\cdot\mathbf{s}) = (V_{so}+iW_{so})\left(\frac{\hbar}{m_\alpha c}\right)^2 \frac{1}{r}\frac{df(r;R_{so},a_{so})}{dr}(2\,\mathbf{l}\cdot\mathbf{s})$$

The introduction of the scalar product of the spin and angular momentum operators complicate the radial expression. In practice, it is necessary to couple the spherical harmonics in equation 2.19 to the spin wave function, since the new good quantum number is $\mathbf{j} = \mathbf{l} + \mathbf{s}$:

$$\left[Y_l(\theta) \otimes X_{1/2}(\sigma)\right]^m_j$$

2.2.4 DWBA Approximation and Spectroscopic Factors

Recalling equation 2.17, and integrating over the internal degrees of freedom ξ analogously to equation 2.5, the non-homogeneous version of the optical potential equation can be obtained. Thanks to the property of the potential U_α which does not depend on the internal degrees of freedom, it is possible to express the equation as follows:

$$(E-\epsilon_\alpha-\hat{T}_\alpha-U_\alpha)\,\psi_\beta(\mathbf{r}_\alpha) = \int d\xi\,\phi^*_\beta\,(V_\alpha-U_\alpha)\,\Psi_\alpha \tag{2.20}$$

This equation can be, once again, solved by means of Green's function procedure. However, in this case, no analytical solution of the radial wave function can be computed due to the presence of the potential U_α.

Defining χ_α as the relative motion solution to the homogenous version of equation 2.20, that is setting $V_\alpha - U_\alpha = 0$, the projected wave function ψ_α can be expressed in therms of the Green's function associated to equation 2.20 as:

$$\psi_\alpha = \chi_\alpha + \int d\mathbf{r}'\,G_\alpha(\mathbf{r},\mathbf{r}')\int d\xi\,\phi^*_\alpha\,(V_\alpha-U_\alpha)\,\Psi_\alpha \tag{2.21}$$

It is possible to show that the asymptotic expression of the *outgoing* Green's function G^+ far from the scattering center has the following form [5]:

$$G_\alpha^+(\mathbf{r},\mathbf{r}') \xrightarrow[r\to\infty]{} -\frac{m}{2\pi\hbar^2}\,\frac{e^{ik_\alpha r}}{r}\,\chi_\alpha^-(\mathbf{k}'_\alpha,\mathbf{r}') \quad \text{where}$$
$$\chi_\alpha^-(\mathbf{k}'_\alpha,\mathbf{r}') = \frac{4\pi}{k_\alpha r'}\sum_{l,m} i^{-l} f_l(k_\alpha,r') Y_l^{*\,m}(\hat{\mathbf{r}}') Y_l^m(\hat{\mathbf{k}}'_\alpha)$$

Which substituted in equation 2.21 gives the following asymptotic expression [5]:

$$\psi_\alpha = \chi_\alpha^+ - \frac{m_\alpha}{2\pi\hbar^2}\,\frac{e^{ik_\alpha r_\alpha}}{r_\alpha}\int d\mathbf{r}'\,d\xi\,\chi_\alpha^{*\,-}\,\phi_\alpha^*\,(V_\alpha - U_\alpha)\,\Psi_\alpha$$

From equation 2.10, it is known that χ_α^+, which is the solution to the radial component of the Hamiltonian with the optical potential U_α, can be expressed as the overlap with the solution to the free Hamiltonian ($U_\alpha = 0$):

$$\chi_\alpha^+(\mathbf{k}_\alpha,\mathbf{r}_\alpha) \xrightarrow[r\to\infty]{} -\frac{m_\alpha}{2\pi\hbar^2}\frac{e^{ik_\alpha r_\alpha}}{r_\alpha}\int d\mathbf{r}'\,e^{i\mathbf{k}'_\alpha\cdot\mathbf{r}'}U_\alpha(\mathbf{r}')\,\chi_\alpha(\mathbf{r}')$$

The scattering amplitude for the channel $\alpha \to \beta$ can be divided into two terms:

$$f_{\alpha,\beta}(\theta) = \left(\frac{m_\alpha}{2\pi\hbar^2}\int d\mathbf{r}'\,e^{i\mathbf{k}'_\alpha\cdot\mathbf{r}'}U_\alpha(\mathbf{r}')\,\chi_\alpha(\mathbf{r}')\right)\delta_{\alpha,\beta}$$
$$+\left(\frac{m_\alpha}{2\pi\hbar^2}\int d\mathbf{r}'d\xi\;\chi_\beta^{*\,-}\,\phi_\beta^*\,(V_\beta - U_\beta)\,\Psi_\alpha^+\right)$$

The DWBA approximation consists in considering the incoming initial wave function Ψ_α^+ as the product of the incoming radial function (distorted by the optical potential) and the nuclear structure component of the wave function:

$$\Psi_\alpha^+ \approx \phi_\alpha(\xi)\,\chi_\alpha^+(\mathbf{k}_\alpha,\mathbf{r}_\alpha)$$

This approximation can be understood by considering the exact wave function Ψ_α as the linear combination of the eigenstates of the Hamiltonian that only includes the optical potential U_α, which are a complete set. The integral in bra-ket notation contains the overlap of the basis states with Ψ_α:

$$|\Psi_\alpha\rangle = \sum_\gamma \langle\phi_\gamma\chi_\gamma|\Psi_\alpha\rangle\,|\phi_\gamma\,\chi_\gamma\rangle \tag{2.22}$$

Since the elastic channel is expected to possess the most significant overlap with the original wave function Ψ_α, to a first approximation, the coefficient $\langle\phi_\alpha\chi_\alpha|\Psi_\alpha\rangle$ should be the most important one, thus justifying the approximation.

In order to compute the differential cross section in the case of the DWBA approximation and in the case of the transfer channel, it is necessary the evaluation of the following integral:

$$\int d\mathbf{r}' d\xi \; \chi^{*-}_{\beta}(\mathbf{k}_\beta, \mathbf{r}_\beta)\, \phi^{*}_{\beta}(\xi)\, (V_\beta - U_\beta)\, \phi_\alpha(\xi)\, \chi^{+}_{\alpha}(\mathbf{k}_\alpha, \mathbf{r}_\alpha) \tag{2.23}$$

One of the simplest examples is the (d, p) transfer reaction. The following calculations will focus on this more straightforward case due to the presence of the structure-less proton. Nevertheless, it is possible to generalize the procedure to the (^{3}He,d) reaction considering the deuteron optical potential and structure. Figure 2.4 shows a conceptual schematic of the transfer reaction, where the intrinsic degrees of freedom and relative coordinates are shown.

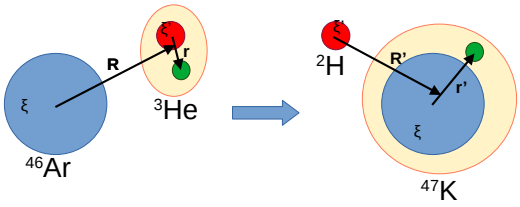

Figure 2.4: Schematic representation of the transfer reaction channel, in the specific case of the pickup reaction of interest. The proton is transferred to the inert ^{46}Ar core. In green is depicted the proton, in red the deuteron core and in blue the ^{46}Ar core.

In the case of a (d, p) reaction, the potential V_β is the sum of that of the proton and neutron and the proton and the final channel with A nucleons: $V_\beta = V_{pn} + V_{pA}$. The most common argument is that the potential V_{pA} should have the same effect of the optical potential U_p and that the difference of the remaining terms is approximately zero:

$$V_{pA} - U_p \approx 0 \tag{2.24}$$

The structure of the initial (with J_A and M_A) and final nuclei (with J_B and M_B) takes the form of:

$$\phi_\alpha = \phi^{M_A}_{J_A}(\xi)\, \phi^{d}(r) X^{\mu_d}_1(\sigma_p, \sigma_n)$$
$$\phi_\beta = \phi^{M_B}_{J_B}(\xi, \mathbf{r}_n)\, X^{\mu_p}_{1/2}(\sigma_p)$$

Here ξ refers to the nucleon coordinates, r the relative distance between neutron a proton in the deuteron radial wave function ϕ^d, X denotes the spin wave functions, and σ_i the proton and neutron spin coordinates. With the approximation of equation 2.24, the integration over the internal coordinates is independent of the relative ones, and equation 2.23 is significantly simplified.

Some considerations are necessary to perform the integration over the internal degrees of freedom between the nucleus before and after the transfer. The integral

over the internal degrees of freedom, extracted from the rest of the integration will have the following expression:

$$\int d\xi \, \phi_{J_B}^{*M_B}(\xi, \mathbf{r}_n) \phi_{J_A}^{M_A}(\xi) \tag{2.25}$$

The following step requires finding a way to express the nucleus after the transfer relative to the one before. This can be done with the so-called *coefficients of fractional parentage* β that can be used to obtain antisymmetric many-body states for identical particles [5, 9] here obtained with the operator $\mathcal{A}$. In particular, the A bodies normalized antisymmetric wave function can be obtained with a linear combination of the couplings of the $A-1$ normalized antisymmetric wave function coupled to the single body one:

$$\phi_{J_B}^{M_B}(\xi, \mathbf{r}_n) = \sum_{A',j,l} \beta_{j,l}(A+1, A') \, \mathcal{A}[\phi_{J_{A'}}(\xi) \otimes \varphi_{n,l,j}(\mathbf{r}_n)]_{J_B}^{M_B}$$

This expression consists in the so-called *parentage expansion* and is directly linked with the shell-model framework. In particular, the intent is to expand the nuclear wave function of a nucleus in terms of all possible coupling of the single-particle shell-model states with the core nucleus. In the specific case of the transfer of interest, it consists of an expression of the wave function ϕ_β of ^{47}K as the sum of all possible single-particle states coupled to the wave function ϕ_α of ^{46}Ar.

The presence of $\mathcal{A}$ represents the antisymmetrization operator and β the coefficients of fractional parentage, whose value depends on the structure of the nuclear wave function. The coupling is, as usual, carried out with the Clebsch–Gordan coefficients.

$$[\phi_{j_1}^{m_1} \otimes \varphi_{j_2}^{m_2}]_{j_3}^{m_3} = \sum_{m_2 \, m_2} \mathcal{C}_{m_1 \, m_2 \, m_3}^{j_1 \, j_2 \, j_3} \, \phi_{j_1}^{m_1} \varphi_{j_2}^{m_2}$$

and $\varphi_{n,l,j}^{m}$ represents the shell-model orbit:

$$\varphi_{n,l,j}^{m}(\mathbf{r}_n, \sigma_n) = \left[\varphi'_{n,l}(\mathbf{r}_n) \times X_{1/2}(\sigma_n)\right]_j^m \quad \text{and} \quad \varphi_{n,l}^{'m_l}(\mathbf{r}_n) = u_{n,l}(r_n) Y_l^{m_l}(\hat{\mathbf{r}_n})$$

As a consequence, the overlap integral 2.25 reduces to an expression of the angular momentum coupling coefficients, the amplitude $\beta_{j,l}(A-1, A)$ and the orbit of the transferred nucleon [5]:

$$\int d\xi \, \phi_{J_B}^{*M_B}(\xi, \mathbf{r}_n) \phi_{J_A}^{M_A}(\xi) = \binom{A+1}{1}^{-\frac{1}{2}} \sum_{j,l} \beta_{j,l}(A+1, A) \, \mathcal{C}_{M_A \, m_j \, M_B}^{J_A \, j \, J_B} \, \varphi_{nlj}^{*m_j}(\mathbf{r}_n, \sigma_n)$$

The binomial coefficient is introduced to account for the identical particle formalism that has not been introduced in the course of this introduction. The coefficient 1 stands for the transfer of a single nucleon. In the case of neutron

and protons treated as distinguishable particles, the binomial coefficients need to be substituted with the product of two binomial coefficients for protons and neutrons. In this calculation, the strong assumption is that the core nucleons are not affected by the transfer reaction. The square of the coefficient β is often referred to as the spectroscopic factor $\mathcal{S}_{lj}$.

$$\mathcal{S}_{lj}^{\frac{1}{2}} = \beta_{lj} = \binom{A+1}{1}^{\frac{1}{2}} \int d\xi \, d\mathbf{r}_n, \phi_{J_B}^{*M_B}(\xi)[\phi_{J_{A'}}(\xi) \otimes \varphi_{n,l,j}(\mathbf{r}_n)]_{J_B}^{M_B}$$

It consists of the integral of the overlap between the two wave functions, that of the final state and the initial state coupled to the single-particle orbit where the nucleon will be transferred.

Substituting the overlap integral in the DWBA amplitude (equation 2.23), it is possible to obtain the final cross section according to equation 2.15.

$$\left(\frac{d\sigma}{d\Omega}\right)_{J_A M_A m_d \to J_B M_B m_p} = \frac{m_\alpha k_\beta}{m_\beta k_\alpha} |f_{\beta,\alpha}(k, k', \theta)|^2$$

where $m_{\alpha,\beta}$ represent the reduced masses of the system. Moreover, the amplitude is the result of the angular momentum couplings:

$$f_{\beta,\alpha}|_{J_A M_A m_d \to J_B M_B m_p} = \sum_{l,j} \mathcal{C}^{J_A\, j\, J_B}_{M_A\, m_j\, M_B} \mathcal{C}^{1/2\, 1/2\, 1}_{m_p\, m_n\, m_d} \mathcal{C}^{l\, 1/2\, j}_{m_l\, m_n\, m_j} \left(i^l (2l+1)^{\frac{1}{2}} \mathcal{S}_{lj}^{\frac{1}{2}} \mathcal{B}_l^{m_l} \right)$$

At last, the coefficient $\mathcal{B}$ contains the relative motion component $\chi_{\alpha,\beta}$, the α index will stand for the deuteron and β for the proton. In this case, due to the simplification introduced by equation 2.24 it has the following form:

$$\mathcal{B}_l^{m_l} = i^{-l}(2l+1)^{-\frac{1}{2}} \frac{m_\beta}{2\pi\hbar^2} \times \int d\mathbf{r}_n \, d\mathbf{r}_p \, \chi_p^{*-}(\mathbf{k}_p, \mathbf{r}_p) \varphi_{nl}^{*m_l}(\mathbf{r}_n) V_{np}(r_n - r_p) \chi_d^{+}(\mathbf{k}_d, \mathbf{r}_d) \phi_d(r_n - r_p)$$

If the spin direction is not measured, as in the case of this experiment, the measured cross section is averaged over all possible M components, as introduced in equation 2.16 [5]:

$$\frac{d\sigma}{d\Omega} = \frac{1}{3(2J_A+1)} \sum_{M_B m_p M_A m_d} \left(\frac{d\sigma}{d\Omega}\right)_{J_A M_A m_d \to J_B M_B m_p} = \frac{1}{2} \frac{m_\alpha k_p}{m_\beta k_d} \frac{2J_B+1}{2J_A+1} \sum_{l\, m\, m_l} \mathcal{S}_{lj} \, |\mathcal{B}_l^{m_l}|^2$$

This expression divides the cross-section into two terms: the spectroscopic factor $\mathcal{S}$ dependent exclusively on the nuclear structure of the colliding nuclei and another term $\mathcal{B}$ which depends on the relative motion and the shape of the overlap between the populated states. Due to the presence of the Clebsch-Gordan coefficients, the selection rules for a reaction consist in the angular momentum conservation ($\mathbf{J}_B = \mathbf{J}_A + l + \frac{1}{2}$) and the parity conservation ($\pi_B = \pi_A\,(-1)^l$).

The part which includes $\mathcal{B}$ contains a strong dependence on the transferred angular momentum l. A more in-depth discussion of the effect of the angular momentum transfer in the specific case of this experiment will be discussed in Chapter 6.

The spectroscopic factor $\mathcal{S}$, on the other hand, represents a multiplication factor of the overall cross-section and in the shell-model picture represents the number of particles occupying a given j shell.

2.2.5 The Quenching of Spectroscopic Factors

The previous results can be generalized to the case of nucleon adding or removal. In practical terms, the spectroscopic factor $\mathcal{S}$ represents a multiplicative factor in front of the single particle (SP) differential cross section [1]:

$$\frac{d\sigma}{d\Omega} = g\mathcal{C}^2\mathcal{S}_i\frac{d\sigma^{SP}}{d\Omega}$$

The factor C consists of an additional isospin coefficient and is set equal to 1 in most cases [13] while the coefficient g represents the statistical factor dependent on the degeneracy of the state of interest labeled by i, which is set to $(2j+1)$ for nucleon addition and 1 for the removal.

The expectation, in the shell-model framework, is that the sum of all single-particle excitations with the same configuration should add up to the total degeneracy of the orbital. This expectation is contained in the sum rule, where adding all vacancies and occupations should amount to a factor of $2j+1$. In particular, the sum of all spectroscopic factors to a state of a given j value can be expressed as [1]:

$$(2j+1)N_j = \sum_j (2j+1)\mathcal{C}^2\mathcal{S}_j^+ + \sum_j \mathcal{C}^2\mathcal{S}_j^-$$

In the previous expression, the spectroscopic factors for nucleon adding ($\mathcal{S}^+$) and removing ($\mathcal{S}^-$) have been differentiated.

The total degeneracy $2j+1$ is modulated by the factor N_j that should be conceptually equal to one.

Extensive experimental studies have been performed for the study of this factor N. The investigation was motivated by the observed quenching of the single-particle strength in all experimental data when compared to the independent-particle shell-model limit.

In particular, Figure 2.5 presents the observed single-particle strength compared to the shell-model limit as a function of the separation energy

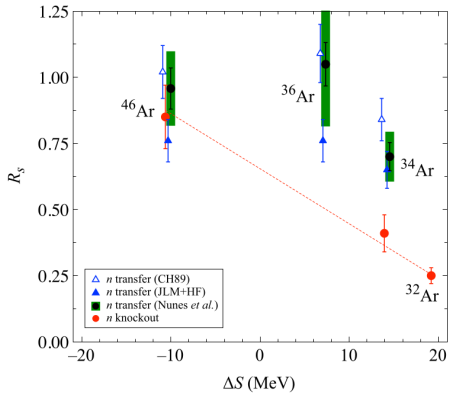

Figure 2.5: Ratio of measured single-particle strength over the independent-particle shell-model prediction as a function of the asymmetry of separation energy of protons and neutrons for argon isotopes. Experimental data of neutron-transfer (p,d) reactions (in black and blue) are compared with results from intermediate-energy knockout reactions (in red) [7, 11]. The green intervals represent the total experimental and theoretical uncertainty relative to the data shown with the black marker. Figure adapted from reference [1].

asymmetry between protons and neutrons. The data, consisting of transfer (p,d) reactions in some argon isotopes, is compared to intermediate-energy knockout reactions.

The quenching phenomenon reduces the single-particle strength by $30\% - 40\%$ compared to the shell-model prediction and is a ubiquitous feature of all experimental data. The general consensus is that the cause is correlations not accounted for in the model [1].

2.3 Conclusions

Spectroscopic factors and, in general, direct reactions appear as a powerful tool for the investigation of the nuclear structure of a nucleus. The underlying theory combines the reaction dynamics with the information on the nuclear structure, which requires the introduction of the spectroscopic factors. These coefficients cannot be considered observables directly, and it is their combination with nuclear models that allow one to extract physical insight. In the case of the current work, they are key elements to investigate the proton component of the ^{46}Ar wave function, which has been shown to present problematic aspects from the point of view of shell-model calculations [2]. This aspect will be discussed in the next chapter in subsection 3.2.3

Bibliography

[1] Aumann, T. et al. "Quenching of single-particle strength from direct reactions with stable and rare-isotope beams". In: *Progress in Particle and Nuclear Physics* vol. 118 (2021), p. 103847. DOI: https://doi.org/10.1016/j.ppnp.2021.103847. URL: https://www.sciencedirect.com/science/article/pii/S0146641021000016.

[2] Calinescu, S. et al. "Coulomb excitation of ^{44}Ca and ^{46}Ar". In: *Phys. Rev. C* vol. 93 (4 Apr. 2016), p. 044333. DOI: 10.1103/PhysRevC.93.044333. URL: https://link.aps.org/doi/10.1103/PhysRevC.93.044333.

[3] Caurier, E. et al. "The shell model as a unified view of nuclear structure". In: *Rev. Mod. Phys.* vol. 77 (2 June 2005), pp. 427–488. DOI: 10.1103/RevModPhys.77.427. URL: https://link.aps.org/doi/10.1103/RevModPhys.77.427.

[4] Duflo, J. and Zuker, A. P. "The nuclear monopole Hamiltonian". In: *Phys. Rev. C* vol. 59 (5 May 1999), R2347–R2350. DOI: 10.1103/PhysRevC.59.R2347. URL: https://link.aps.org/doi/10.1103/PhysRevC.59.R2347.

[5] Glendenning, N. K. *Direct Nuclear Reactions*. WORLD SCIENTIFIC, June 2004. DOI: 10.1142/5612. URL: https://doi.org/10.1142/5612.

[6] Heyde, K. *The nuclear shell model*. Berlin New York: Springer-Verlag, 1994.

[7] Lee, J. et al. "Neutron-Proton Asymmetry Dependence of Spectroscopic Factors in Ar Isotopes". In: *Phys. Rev. Lett.* vol. 104 (11 Mar. 2010), p. 112701. DOI: 10.1103/PhysRevLett.104.112701. URL: https://link.aps.org/doi/10.1103/PhysRevLett.104.112701.

[8] Mayer, M. G. "On Closed Shells in Nuclei. II". In: *Phys. Rev.* vol. 75 (12 June 1949), pp. 1969–1970. DOI: 10.1103/PhysRev.75.1969. URL: https://link.aps.org/doi/10.1103/PhysRev.75.1969.

[9] Moro, A. M. *Models for nuclear reactions with weakly bound systems*. 2019. arXiv: 1807.04349 [nucl-th].

[10] Nowacki, F. and Poves, A. "New effective interaction for $0\hbar\omega$ shell-model calculations in the $sd - pf$ valence space". In: *Phys. Rev. C* vol. 79 (1 Jan. 2009), p. 014310. DOI: 10.1103/PhysRevC.79.014310. URL: https://link.aps.org/doi/10.1103/PhysRevC.79.014310.

[11] Nunes, F. M., Deltuva, A., and Hong, J. "Improved description of ^{34,36,46}Ar(p, d) transfer reactions". In: *Phys. Rev. C* vol. 83 (3 Mar. 2011), p. 034610. DOI: 10.1103/PhysRevC.83.034610. URL: https://link.aps.org/doi/10.1103/PhysRevC.83.034610.

[12] Schwenk, A. and Zuker, A. P. "Shell-model phenomenology of low-momentum interactions". In: *Phys. Rev. C* vol. 74 (6 Dec. 2006), p. 061302. DOI: 10.1103/PhysRevC.74.061302. URL: https://link.aps.org/doi/10.1103/PhysRevC.74.061302.

[13] Wilkinson, D. *Isospin in nuclear physics*. Amsterdam: North-Holland Pub. Co, 1969.

Chapter 3

The problem of transition probabilities in ^{46}Ar

The evolution of the shell closure far from the so-called valley of β stability is an essential element to test our understanding of the nuclear structure properties and the occurrence of correlations in the shell-model picture of the nuclear many-body system.

The study of a shell closure is not a simple matter as there exists no direct observable related to a shell gap. Nevertheless, a shell gap can manifest itself and become evident from many observables. A good indication of a significant gap can be given by binding energies that are directly related to nucleon separation energies. A nucleus featuring a closed-shell configuration is expected to present high nucleon-removal energies when compared to an open-shell configuration. A sharp increase in binding energy along an isotopic (or isotonic) chain indicates that a shell closure has been reached.

Another indication of a substantial closed-shell configuration is given by transition probabilities. In this case, the configuration does not allow for strong correlations between nearly energy-degenerate orbitals, and the only possibility for nucleons is to jump the shell gap in order to produce an excited state. This generates a reduced overlap between the wave functions of the excited and ground states, which, in turn, translates to a reduced transition probability between the two states. On the other hand, highly correlated states feature many different combinations of configurations which translate to a significant overlap between the states and thus a large transition probability. The comparison between the excitation energy value of the 2_1^+ state or the transition probability and the systematic values of nearby isotopes is a complementary picture to the binding energy study for the evolution of a nuclear shell closure.

This chapter will describe how the study of the evolution of the $N = 28$ shell closure led to the discovery of nuclear structure properties at odds with theoretical models for ^{46}Ar. A brief introduction on the current knowledge of this neutron shell closure will be followed by a more in-depth picture from the nuclear structure point of view in the framework of nuclear models.

Figure 3.1 shows the landscape of the current nuclear chart with an insert on the particular region of ^{46}Ar, located in the neutron-rich side of the β stability valley.

Figure 3.1: Nuclide chart of the known isotopes. ^{46}Ar is located $-2p$ below the double magic ^{48}Ca isotope, along the $N = 28$ nuclear shell closure. Colored cells indicate the most likely decay for each kind of isotope: blue for β^-, red for β^+, yellow α emission, and green for spontaneous fission. The decay of ^{46}Ar occurs via β^- to ^{46}K ($T_{1/2} = 105$ s) with a half-life of $T_{1/2} = 8.4$ s, which in turn decays to ^{46}Ca. This particular calcium isotope can be, by most accounts, considered a stable isotope with a considerable lifetime of $T_{1/2} = 2.8 \cdot 10^{15}$ years, but will eventually decay via β^- emission to ^{46}Sc followed by ^{46}Ti.

3.1 The N=28 shell evolution

It is well known that the nearby $N = 20$ and $N = 28$ shell closures differ significantly both in nature and robustness.

On one side, the $N = 20$ gap is delimited by orbitals of different parities ($d_{3/2}$ below, positive and $f_{7/2}$ above, negative), which, together with sub-shell gaps in $Z = 14, 16$, hinders the onset of quadrupole correlations and generates stability to the removal of up to five protons [34].

On the other hand, the $N = 28$ separates orbitals of the same parity and experimental observables hint at a quick collapse of the gap with the removal of only a few protons [33].

In particular, this rapid breakdown of the shell gap is correlated experimentally by an enhancement of typical collective features not far from the doubly magic ^{48}Ca isotope that translate into reduced quadrupole excitation energy ($E(2^+)$) and high transition probabilities ($B(E2)$).

In particular, studies on the nuclear structure of ^{44}S associate this isotope with the onset of collectivity, pointing to a ground state mixed by spherical and deformed configurations. These considerations arise from large measured transition probabilities and point to a deformed ground state[14, 32]. Further information was provided by the decay of the isomeric 0_2^+ level [8] and its spherical nature, in contrast with the prolate nature of the ground state. Further investigation [4] led to the discovery of other low-lying states that are understood as combinations of deformed and spherical configurations.

The ^{46}Ar isotope features a relatively high excitation energy of the first 2^+ state, offering a first hint of the presence of the shell gap. A further indication is given by neutron knockout reactions that feature small cross sections for the population of the $3/2^-$ state in ^{45}Ar [10], signaling an empty $\nu p_{3/2}$ shell above $N = 28$. Nevertheless, other studies [11, 29] performed with direct (d,p) reactions suggest a progressive erosion of the shell gap. Further studies were performed aiming at characterizing the shell closure in this isotope via mass measurement and transition probabilities and will be discussed in detail in the dedicated subsections (3.2.3 and 3.2.1).

Other evidence of the evolution of the shell closure can be found in the lowering of the energy of the 0_2^+ state in ^{46}Ar [24] at 3695 keV to only 1365 keV in ^{44}S [16].

3.2 The case of ^{46}Ar

Various considerations have been made in the literature regarding the nuclear structure of this isotope, in particular, because it sits on the edge between magic and more collective nuclei. Many experiments and theoretical considerations focused on the study of the neutron component of the wave function in order to gain information on the neutron shell gap by means of knockout and transfer reactions (subsection 3.2.2) and mass measurements aimed at the study of neutron separation energies (subsection 3.2.1). These studies present, in general,

good agreement with theoretical predictions, proof of the ability of the interacting shell model and the various effective interactions developed for the *sd* and *pf* major shells to describe observables in this region.

On the other hand, transition probabilities are also significant for the study of the evolution of the shell closure. Measurement performed with Coulomb excitation methods (subsection 3.2.3) revealed a surprising discrepancy with the shell-model prediction that points at a sharp increase of the B(E2) value in correspondence of ^{46}Ar along the isotopic chain. The experimental data, differing by a factor of more than two, features a drop in correspondence to the $N = 28$ shell closure. Studies on the cause of this inconsistency have pointed out that something needs to be understood on the proton component of the wave function and will be explained in more detail in the following sections.

3.2.1 Neutron Separation Energies

The neutron separation energy is strongly correlated to the shell gap. When compared to other isotopes in the same region, a deeply bound nucleon will be associated with the presence of a shell closure and vice-versa.

Neutron separation energies consist of the comparison of the mass of a given isotope with respect to the lighter isotope. As a consequence, the comparison of the mass of ^{46}Ar with that of the nearby ^{47}Ar (^{45}Ar) isotope constitutes a direct indication of the energy necessary to add (remove) one neutron to (from) the ground state of ^{46}Ar. This comparison is able to probe the neutron component of the wave function directly and is thus closely correlated with the $N = 28$ shell gap.

If the pairing interaction were not present, this comparison would be sufficient. However, due to the significant effect of this interaction, a staggering is always observed in the binding energy trend of an isotopic chain, where odd nuclei show a decrease in binding energy if compared to even nuclei. In order to circumvent this effect, it is possible to remove it by considering the two-neutron separation energy. Measuring the mass excess (ME) of isotopes separated by two neutrons (with mass ME_ν), the two-neutron separation energy S_{2n} is defined as:

$$S_{2n}(Z, A) = 2 \cdot ME_\nu + ME(Z, A-2) - ME(Z, A)$$

The previous expression aims at removing the pairing contribution to the mass trend but introduces another strong dependency caused by the proton-neutron asymmetry in the mass formula (liquid-drop model). As a consequence, a progressive drop in the previous expression of S_{2n} is expected in the progression towards neutron-rich nuclei that combines with the sudden decrease in value as a shell closure is reached. The trend of S_{2n} for exotic nuclei is not always of straightforward interpretation due to these aspects [19].

Another observable related to mass measurement can be considered [3]: D_n, defined as a function of the one-neutron separation energy S_n:

$$D_N(Z, A) = (-1)^{N+1} \left[S_n(Z, A+1) - S_n(Z, A)\right]$$

This parameter (D_n) is expected to oscillate due to the pairing interaction, while a sudden increase in value would be indicative of a shell gap. In the shell-model picture, it can be understood as the progression of binding energy as a shell is filled with neutrons at different J_z values.

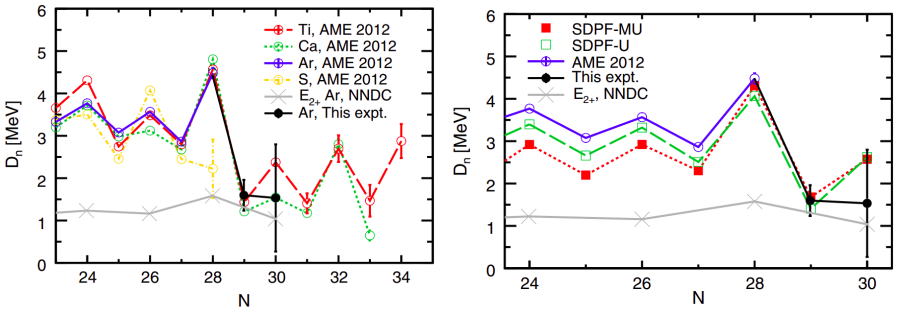

Figure 3.2: Trend of the parameter D_n along various isotopic chains, figure adapted from reference [19]. The graph indicates a large energy gap in ^{46}Ar which fades with the removal of two protons in the sulfur isotopes (left panel). Shell-model predictions with the SDPF-U effective interaction appear in close agreement with experimental data (right panel).

Two recent mass measurements of neutron-rich argon isotopes have been performed at the National Superconducting Cyclotron Laboratory at Michigan State University [19] and at ISOLDE/CERN [21]. Figure 3.2 shows the results of the parameter D_n in the case of the argon isotopic chain in comparison with some other significant nearby chains.

In particular, while the expected staggering is present, the most significant feature is the prominent increase of D_n for $N = 28$ that hints at a considerable shell gap in the case of the double magic ^{48}Ca, as well as ^{50}Ti ($+2p$) and ^{46}Ar ($-2p$). The removal of two more protons causes the $N = 28$ energy gap to fade, as shown for the sulfur isotopic chain, pointing to ^{46}Ar as the most neutron-rich even semi-magic isotope located along the $N = 28$ shell closure.

Shell-model calculations performed with the SDPF-MU [35] and SDPF-U [23] interactions are in close agreement with the experimental data, showing a remarkable precision in the prediction of the shell gap in ^{46}Ar.

The SDPF-U has been developed to suit calculations in the $sd - pf$ valence space. It is based on the phenomenology around the $N = 28$ shell closure and its weakening far from the stability and has been shown to predict with remarkable consistency many observables in the region. The authors of reference [23] remark that, in the development of the interaction, special attention was dedicated to the vanishing of the shell closure and on the evolution of the splitting of the $1/2^+$ and $3/2^+$ states in neutron-rich isotopes, hence the reason behind its use in this work.

3.2.2 Transfer and Knockout Reactions

Neutron transfer and knockout reactions have been both performed for ^{46}Ar.

In particular, the knockout reaction was performed at Coupled Cyclotron Facility at the National Superconducting Cyclotron Laboratory at Michigan State University [10]. The first indication of the shell closure persistence consists of the small observed spectroscopic factor, amounting to 0.2(2) for the $p3/2$ orbit. The authors deduce a spectroscopic factor of 4.9(7) for the population of the ground state of ^{45}Ar, in agreement with shell-model calculations with a valence shell dominated by the $f_{7/2}$ state.

The neutron transfer reaction was performed at GANIL with the MUST detector [12]. The authors inferred spectroscopic factors in full agreement with the shell-model predictions, providing further confirmation of the presence of the shell gap and pointing at a quenching of the p and f orbit splitting as the effect responsible for the weakening of the $N = 28$ gap. In particular, the spectroscopic factor relative to the state at 1791 keV (mainly $f_{7/2}$) amounts to 0.17 and can be compared to the ground state (mainly $p3/2$: 0.60) and the first excited state at 1184 keV (mainly $p1/2$: 0.93).

While the interest has been mainly focused on the neutron component of the wave function, as previously anticipated, the discrepancies start to arise in observables which are characterized by a strong contribution from the protons. The following chapters will focus on these cases, which offer the justification of the experiment described in this work.

3.2.3 Electromagnetic Transition Probabilities

The reduced-transition probability $B(Rl)$ between two states is related to the matrix elements that contain the overlap between initial and final state (α and β) by means of the electromagnetic operator $\hat{\Omega}_{l\mu}$:

$$B\left(Rl, J_\alpha \to J_\beta\right) = \frac{1}{2J_\alpha + 1} \sum_{M_\alpha M_\beta} \left| \left\langle \beta \left| \hat{\Omega}_{l\mu}(R) \right| \alpha \right\rangle \right|^2$$

Where R stands for electric (E) or magnetic (M), M_α and M_β the nuclear angular momenta projections, and J_α and J_β the total angular momenta. The reduced transition probability $B(Rl)$ is in turn related to the actual transition probability T_{fi} (which also corresponds to the inverse of the lifetime of two states) by the following expression [15]:

$$T_{fi}(l; R) = \frac{8\pi(l+1)}{l[(2l+1)!!]^2} \frac{k^{2l+1}}{\hbar} B\left(Rl, J_i \to J_f\right)$$

The expression depends on the energy of the emitted photon due to the wave-vector magnitude k and on the angular momentum l. In the case of an electric quadrupole transition probability, the explicit form for the equation is the following:

$$T(E2) = 1.223 \cdot 10^9 E^5 B(E2)$$

Where the quadrupole reduced transition probability ($B(E2)$) is expressed in $e^2\text{fm}^4$, and the energy E is in MeV.

From the definition of the matrix element, it is clear that both protons and neutrons participate in the transition, and only in particular cases, the approximation of a transition due only to protons or neutrons is effective. In the independent particle shell-model picture, the transition between two states is ascribed to the promotion of one nucleon from one orbit to another. In this simplified case of transition between single-particle states, the overlap can be computed in a simplified model to obtain the so-called Weisskopf estimates. These values offer insight into the nature of a nuclear transition when compared to values measured or calculated with more sophisticated models. In fact, they can be considered an assessment of the degree of collectivity of a given state, since the occurrence of more correlation will significantly increase the transition probability when compared to the single-particle case. Generally, a high value of the ratio between the measured transition probability and the Weisskopf estimate is indicative of a collective nature.

The analysis of the trend of transition probabilities along isotopic chains is a powerful insight into the evolution of the shells, with a sharp decrease in the case of a shell closure.

Transition probabilities are not a direct observable but can be extrapolated via two main methods: Coulomb excitation measurements and lifetime measurements. Each experimental methodology is affected by its own difficulties and advantages. Nevertheless, the duality and the correspondence between the two methodologies allowed the exploration of this physical quantity of nuclei far from stability.

A detailed description with a special focus on the methodology is presented in reference [7].

While the lifetime of a state is linked to the conceptually simple measurement of the number of transitions occurring in a given time interval, the idea behind the Coulomb excitation is somewhat less direct and yet still independent from any nuclear model. The idea behind this methodology lies in the probability of exciting a nucleus with a purely electromagnetic interaction. Thanks to this known interaction, it is possible to ensure that the probability of exciting a state is dependent only upon the initial and final wave function of the states of interest. As a consequence, it is expected that, in the presence of a nucleus with structure, the (elastic) Rutherford differential cross-section will be modulated by the probability of populating a given state:

$$\frac{d\sigma_{clx}}{d\Omega} = \frac{d\sigma_{Ruth}}{d\Omega} \cdot P(i \longrightarrow f)$$

The probability $P(i \longrightarrow f)$ is in turn proportional to the reduced transition probability [13]. A Coulomb excitation measurement translates in the assessment of the discrepancy between a structure-less Rutherford scattering with respect to the measured cross-section due to the population of the states of interest. The first measurements performed with this technique used electrons as projectiles. Due to the dependence on the projectile Z, the experimental techniques evolved for the use of heavy ions. A purely electromagnetic interaction was ensured

by limiting the maximum beam energy to allow a minimum approach distance between beam and target larger than the sum of the nuclear radii. The interest in performing Coulomb excitation measurements with radioactive beams to extract transition probabilities in exotic nuclei further pushed the experimental technique in using intermediate energy scattering. In this case, the kinematics of the reaction is exploited to limit the detection to angles that are associated with a maximum approach between target and beam larger than the nuclear radii. The analysis is thus limited to a portion of the solid angle as explained in detail in reference [13].

In the case of ^{46}Ar, both Coulomb excitation measurements, as well as lifetime experiments, have been performed.

In particular, two experiments took place at intermediate Coulomb excitation energies in 1999 [29] and 2003 [9] at the National Superconducting Cyclotron Laboratory at Michigan State University.

Further experimental efforts focused on the Coulomb excitation measurement at barrier energy at GANIL in 2016 [5].

An independent lifetime measurement was performed at Laboratori Nazionali di Legnaro [20], returning a transition probability at odds with the three Coulomb excitation values but compatible with the shell-model figure. The measurement, affected by low statistics and the impossibility of performing a Q-value gate on the magnetic spectrometer, obtained a lifetime of $0.8^{+0.3}_{-0.4}$ ps for the 2^+ state.

Table 3.1 presents a comparison of the values of the cited experiments. All Coulomb excitation experiments feature compatible transition probability values, while the lifetime measurement indicates a significant increase in value.

Reference	Coul. Ex. [29] (e^2fm^4)	Coul. Ex. [9] (e^2fm^4)	Coul. Ex. [5] (e^2fm^4)	Lifetime [20] (e^2fm^4)
B(E2) ↑	196(39)	218(31)	225(29)	570^{+335}_{-160}

Table 3.1: Comparison of $B(E2)$ transition probabilities as measured in the referenced papers for ^{46}Ar. Intermediate-energy Coulomb excitation measurements [5, 9, 29] return compatible values, at variance with the lifetime experiment [20].

Figure 3.3 compares the values obtained from the barrier-energy Coulomb excitation experiment with the shell-model prediction with the SDPF-U interaction and similar variations along the argon isotopic chain. The experimental data suggest a gradual increase in transition probability starting from $N = 20$, reaching the maximum value at $N = 24$ that follows a new minimum in correspondence with the $N = 28$ shell closure. The available data terminates with ^{48}Ar where an increase in transition probability can be observed once again. In particular, while the trend starting from ^{38}Ar presents a similar gradual increment in transition probability, in correspondence to the $N = 28$ shell closure, a prominent increase emerges, in contrast with the experimental data. The following data for ^{48}Ar indicates a convergence between the shell

model and the data. A noteworthy consideration can be made for the shell-model prediction for ^{46}Ar, where all tested effective interactions predict a similar value, which also corresponds to the highest transition probability in the neutron-rich argon isotopic chain.

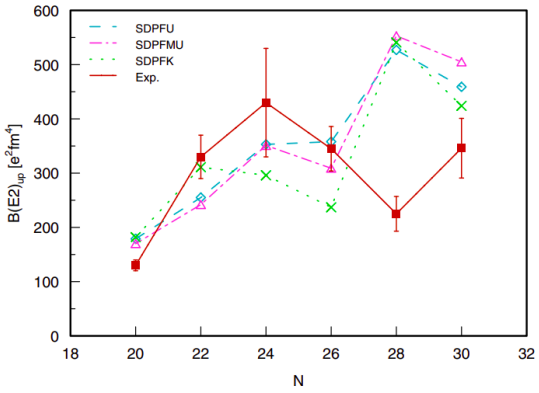

Figure 3.3: Evolution of transition probability of the argon isotopic chain for experimental data (red, solid line) and shell-model predictions with various SDPF effective interactions (green, magenta and cyan lines). Figure adapted from reference [5]

The authors in reference [5] provide a detailed study of the transition matrix elements by extrapolating the neutron (M_n) and proton (M_p) components by combining the Coulomb excitation data with the inelastic (p,p$'$) scattering. Figure 3.4 shows the evolution of the two components of the matrix elements along the argon isotopic chain in the case of two different values of polarization charges and can be compared with the SDPF-U interaction.

While a somewhat significant divergence with the shell-model prediction can be observed in the neutron component in correspondence to ^{44}Ar, the addition of two more neutrons finds the SDPF-U prediction in much closer agreement in correspondence to the shell closure. Regarding the proton component, however, a gradual decline of amplitude can be observed in both experimental data and theoretical prediction from the $N = 20$ shell closure up to ^{44}Ar with similar values and trends. In correspondence to ^{46}Ar, however, a small drop in amplitude in the data is opposed by a significant jump in the shell-model prediction. This difference in trend and, more specifically, the overestimation of the proton component of the matrix element has been proposed as a possible explanation of the large reduced transition probabilities predicted by the shell model.

Recent developments showed that this problem is not limited to ^{46}Ar, and is also existent in ^{44}S [18] ($-2p$ with respect the argon isotope along the $N = 28$ shell).

The authors show that intermediate-energy Coulomb excitation measurements are well in agreement with calculations performed with the SDPF-U interaction

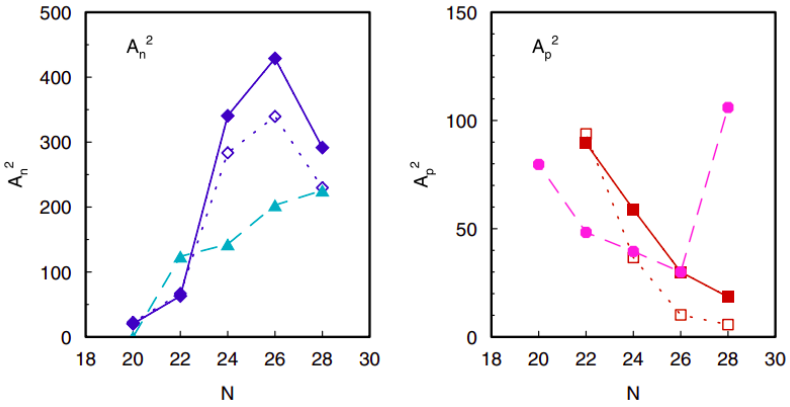

Figure 3.4: Squared values of the matrix elements for neutrons (left panel) and protons (right panel) along the argon isotopic chain. The experimental data is shown with the standard polarization charges $\delta_n = \delta_p = 0.5$ (solid line) and alternative values of $\delta_n = \delta_p = 0.2$ (dotted line). The SDPF-U interaction prediction (dashed line) shows a remarkable discrepancy of the proton component in correspondence to ^{46}Ar. Figure adapted from reference [5].

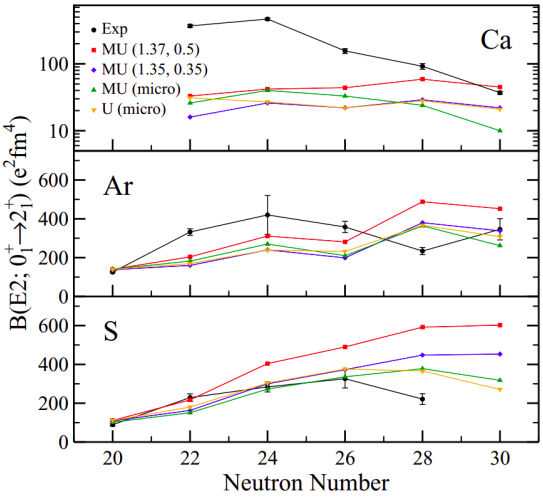

Figure 3.5: Evolution of transition probabilities along the ^{48}Ca (top panel), ^{46}Ar (middle panel) and ^{44}S (bottom panel) isotopic chain. The experimental data is compared with different values of neutron and proton polarization charges as well as a quantification of the effective charge based on the model space. Figure adapted from reference [18].

in ^{38,40,42}S. Nevertheless, reaching the shell closure in ^{44}S, the same deviation of the transition probability by a factor of two can be observed. A detailed study has also been performed to assess the dependence of the reduced transition probabilities from the polarization charge values (here summarized in Figure3.5). In particular, a model was introduced to quantify the charge dependence from the model space, effectively rendering the polarization charges dependent upon the nucleus and the state. While the description of the model is beyond the scope of this introduction, the authors conclude that the introduction of orbital dependence on the polarization charges is not sufficient to justify the discrepancy observed in ^{46}Ar and ^{44}S.

3.2.4 The Density Functional Theory (DFT) Picture

The ^{46}Ar isotope has been studied extensively also in the framework of models based on density functional theories, which consist in the natural evolution of Hartree Fock mean-field calculations [6]. These are based on the variational principle, applied to the energy functional with respect to the density matrix and pairing tensor [26] to extract the properties of the ground state.

Relativistic Hartree-Bogoliubov with finite-range pairing interaction calculations with the NL3 effective interaction were first performed in the $N = 28$ region to test the onset of deformation along the neutron-rich side of the valley of stability [17]. The model predicts a strong suppression of the energy gap with a progression of deformed ground states starting with the phenomenon of shape coexistence in ^{44}S and evolving to a deep oblate minimum in ^{42}Si. In the case of ^{46}Ar, a very flat potential energy surface was found, with the flat minimum extending from a value of 0 of the deformation parameter β to a negative value of $\beta = -1$, suggesting a soft oblate minimum.

Later studies exploiting the same theoretical framework found a similar trend for the potential energy surface [27, 28]. Figure 3.6 shows the evolution of the surface along the $N = 28$ shell, with the progressive onset of deformation, with the ^{46}Ar isotope presenting a minimum value spread over a large range of the deformation parameter.

Recently developed state-of-the-art mean-field (and beyond) techniques achieve a remarkable precision in the description of the nuclear matter density properties [2]. While the average density profile configuration is very similar for the great majority of isotopes in the Segrè chart, in some rare cases, DFT calculations predict a density depletion in the central region of some experimentally accessible isotopes. In particular, in the case of ^{46}Ar, independently performed relativistic mean-field calculations indicate a central depletion of proton density [30, 31]. Isotopes associated with this remarkable phenomenon have been named bubble nuclei, and the gathered theoretical and experimental interest from the nuclear structure community has been manifold. Knockout reactions have been used successfully as a tool to prove experimentally this peculiar property in ^{34}Si [22].

This central depletion, in terms of single-particle orbitals, translates into a suppressed population of $s_{1/2}$ orbitals that are characterized by a lower mean

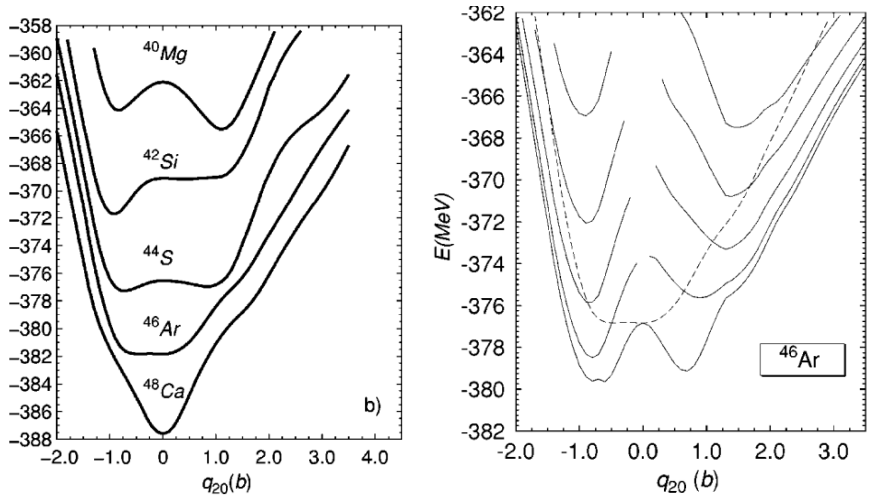

Figure 3.6: Mean field potential energy surfaces computed in the Hartree–Fock–Bogolyubov framework as a function of the deformation parameter, graph adapted from reference [27]. (left panel) The evolution along the $N = 28$ shell closure indicates a quick onset of deformation along the neutron rich side. (right panel) The angular momentum projected potential energy surface. The plotted solid curves indicate an angular momentum of $I = 0, 2, \ldots 8$, while the dashed curve indicates the mean field result.

squared radius, in turn, caused by the vanished centrifugal barrier with respect to higher angular momentum values. The candidate nuclei for the central depletion phenomenon considered in the theoretical study in reference [31] consist of those which are also neighboring even-even non-bubble nuclei, where the $s_{1/2}$ orbital is expected to be occupied.

Figure 3.7 shows the results of the relativistic mean-field calculations performed in reference [31] and compares the doubly-magic ^{48}Ca isotope with ^{46}Ar. In terms of neutron density, the profile is not affected significantly by the removal of two protons. In the case of the proton component, on the other side, an evident depletion is present in the central portion of the density profile. This is explained by the inversion of the $d_{3/2}$ and $s_{1/2}$ orbitals and by the drop in Fermi energy caused by the removal of the two protons that brings it between the energy of the two orbitals.

The results presented in Figure 3.7 also indicate the importance of measurement of observables strictly dependent on the proton component of the wave function. As a consequence, a direct proton transfer reaction can be considered a very effective tool to shed light on the peculiar aspect further.

Section 8.2 of the final chapter (8) will discuss this aspect with new results obtained with a Skyrme interaction. In particular, it will be discussed how the inversion of the orbitals can be described by the SLy5 interaction with the

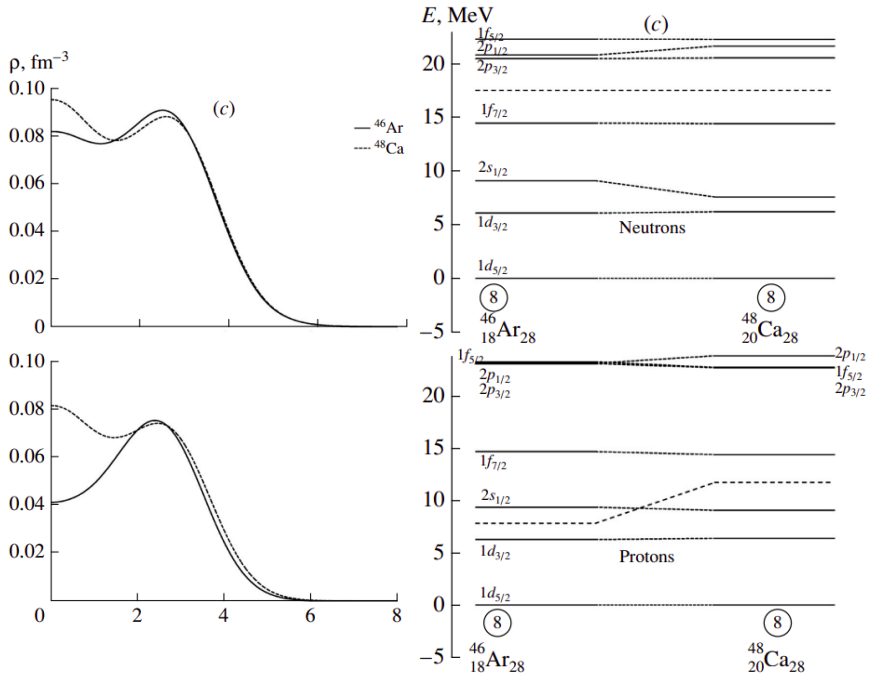

Figure 3.7: Relativistic mean field calculations of the evolution from ^{48}Ca to ^{46}Ar. (top left panel) Neutron density profile for ^{48}Ca (dashed line) and ^{46}Ar (solid line). (bottom left panel) Proton density profile showing a central depletion for ^{46}Ar. (top right panel) Single particle orbitals evolution for neutrons and Fermi energy (dashed line) (bottom right panel) Single particle orbitals evolution for protons and Fermi energy (dashed line). Adapted from reference [31]

introduction of a tensor component.

3.2.5 Shell-model calculations

In the course of this chapter, some results related to shell-model calculations have been presented. In particular, section 3.2.3 focused on the discrepancy between the transition probabilities calculated with the shell model with the SDPF-U interaction and the experimental data.

A more detailed discussion regarding the shell-model picture will be presented in Chapter 8 and specifically in section 8.1, where the results will be discussed and compared to the experimental outcome.

In a concise anticipation of the calculations discussed in the section, the shell model predicts a configuration of the ground state of ^{46}Ar where neither the $s_{1/2}$ nor the $d_{3/2}$ orbits are fully occupied. This, in turn, translates to similar spectroscopic factors relative to the population of the ground state ($1/2^+$) and first excited state ($3/2^+$) of ^{47}K.

3.3 Spectroscopy of ^{47}K by Means of Direct Reactions from ^{48}Ca

The single-particle states of ^{47}K can be understood as hole configurations in the closed-shell doubly-magic ^{48}Ca nucleus. Direct reactions studies are an insightful tool for the understanding of the nature of these excited states.

A ^{48}Ca($\overrightarrow{\mathrm{d}}$,^{3}He)^{47}K direct reaction was performed at the Indiana University multistage Cyclotron Facility (IUCF) with a beam of polarized deuterons at an energy of 79.2 MeV [1]. The polarized deuterons in conjunction with the measured angular distributions allowed the authors to distinguish not only different values of transferred angular momentum l, but also to determine the j transferred, discriminating the two cases: $j = l \pm \frac{1}{2}$.

A total of seventeen states were populated:

- $L = 0$: The transfer to the ground state ($1/2^+$) is associated with the pick-up of a $s_{1/2}$ proton in ^{48}Ca, and the spectroscopic factor amounts to $\mathcal{C}^2\mathcal{S} = 1.55$. A second $1/2^+$ state was observed at an excitation energy of 3.83 MeV with $\mathcal{C}^2\mathcal{S} = 0.28$. The two states exhaust 90% of the shell-model strength limit.

- $L = 1$: No transitions were observed. The justification found by the authors is twofold. On the one hand, the high surface absorption of the ^{3}He particles may hinder the probability of pick-up of a proton in the central $1p$ orbit. On the other hand, the strength of the $d_{5/2}$ orbital appears very fragmented and extends at higher excitation energies, above the neutron separation energy. Since the $1p$ protons are more bound, the relative hole states are expected to extend to even higher excitation energy.

- $L = 2$: These reaction were distinguished between $j = 3/2$ and $j = 5/2$. In the first case, the first excited state of ^{47}K was populated with $\mathcal{C}^2\mathcal{S} = 4.16$, thus reaching the shell-model limit. An additional higher-lying state was populated at 3.88 MeV with $\mathcal{C}^2\mathcal{S} = 0.70$. A total of ten $j = 5/2$ transitions were also observed at excitation energy ranging from 3.32 MeV to 8.02 MeV, and the sum of all spectroscopic factors amounted to 64% of the shell-model limit. The reason for the fragmented nature of these states has been found in terms of the coupling of a hole and a phonon relative to the collective 2^+ state of ^{48}Ca [36].

- $L = 3$: In a perfectly closed-shell configuration of ^{48}Ca, no $L = 3$ transition of proton pickup from the $f_{7/2}$ orbits are expected. Nevertheless, the presence of a low-lying $7/2^-$ state in ^{47}K indicates a small degree of shell braking, associated with a low spectroscopic factor of $\mathcal{C}^2\mathcal{S} \approx 0.08$. Although the simpler one-step DWBA calculation is able to reproduce well the measured angular distribution, the population of the state could also be attributed to a two-step process such as the proton pick-up from the $s_{1/2}$ coupled to a 3^- state of ^{48}Ca.

Another study conducted with a different direct reaction (^{48}Ca(t, α)^{47}K) at 33 MeV [25] confirmed these results on the low lying states of ^{47}K.

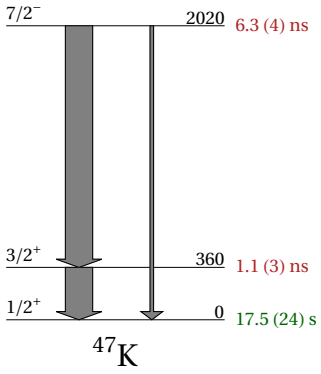

Figure 3.8: Experimental spectroscopic information of the low lying states of ^{47}K. The branching ratio for the $7/2^-$ state to the ground state amounts to only 11.7(17)%.

For completeness, Figure 3.8 presents the known spectroscopic information of the low lying levels of ^{47}K. Not only the spin and parity levels are assigned, but the lifetime of the excited states have also been measured. This spectroscopic knowledge of ^{47}K is of fundamental importance for the current experiments that will rely on this information for many experimental considerations.

3.4 Conclusions

This chapter introduced some of the experimental and theoretical efforts dedicated to the study of the region around ^{46}Ar and the $N = 28$ shell closure. This isotope emerges as an interesting study case due to the peculiar structure of the proton component of the wave function and its implications on the observables that are strongly dependent on it. While much experimental effort has been placed on the study of the neutron-dependent observables to shed light on the shell closure, this experiment aimed at a direct probe of the proton component of the nuclear structure of ^{46}Ar. This study was carried out by means of direct proton transfer reaction with the intent of assessing the relative $L = 2$ transfer to the $3/2^+$ state with respect to the $L = 0$ population of the ground state. The next chapters will focus on the experimental considerations and, more in general, on the analysis and outcomes.

Bibliography

[1] Banks, S. et al. "The 48Ca(d→, 3He)47K reaction at 80 MeV". In: *Nuclear Physics A* vol. 437, no. 2 (1985), pp. 381–396. DOI: https://doi.org/10.1016/S0375-9474(85)90096-X. URL: https://www.sciencedirect.com/science/article/pii/S037594748590096X.

[2] Bender, M., Heenen, P.-H., and Reinhard, P.-G. "Self-consistent mean-field models for nuclear structure". In: *Rev. Mod. Phys.* vol. 75 (1 Jan. 2003), pp. 121–180. DOI: 10.1103/RevModPhys.75.121. URL: https://link.aps.org/doi/10.1103/RevModPhys.75.121.

[3] Brown, B. A. "Nuclear Pairing Gap: How Low Can It Go?" In: *Phys. Rev. Lett.* vol. 111 (16 Oct. 2013), p. 162502. DOI: 10.1103/PhysRevLett.111.162502. URL: https://link.aps.org/doi/10.1103/PhysRevLett.111.162502.

[4] Cáceres, L. et al. "In-beam spectroscopic studies of the ^{44}S nucleus". In: *Phys. Rev. C* vol. 85 (2 Feb. 2012), p. 024311. DOI: 10.1103/PhysRevC.85.024311. URL: https://link.aps.org/doi/10.1103/PhysRevC.85.024311.

[5] Calinescu, S. et al. "Coulomb excitation of ^{44}Ca and ^{46}Ar". In: *Phys. Rev. C* vol. 93 (4 Apr. 2016), p. 044333. DOI: 10.1103/PhysRevC.93.044333. URL: https://link.aps.org/doi/10.1103/PhysRevC.93.044333.

[6] Colò, G. "Nuclear density functional theory". In: *Advances in Physics: X* vol. 5, no. 1 (2020), p. 1740061. DOI: 10.1080/23746149.2020.1740061. eprint: https://doi.org/10.1080/23746149.2020.1740061. URL: https://doi.org/10.1080/23746149.2020.1740061.

[7] Dewald, A., Möller, O., and Petkov, P. "Developing the Recoil Distance Doppler-Shift technique towards a versatile tool for lifetime measurements of excited nuclear states". In: *Progress in Particle and Nuclear Physics* vol. 67, no. 3 (2012), pp. 786–839. DOI: https://doi.org/10.1016/j.ppnp.2012.03.003. URL: https://www.sciencedirect.com/science/article/pii/S0146641012000713.

[8] Force, C. et al. "Prolate-Spherical Shape Coexistence at $N = 28$ in ^{44}S". In: *Phys. Rev. Lett.* vol. 105 (10 Sept. 2010), p. 102501. DOI: 10.1103/PhysRevLett.105.102501. URL: https://link.aps.org/doi/10.1103/PhysRevLett.105.102501.

[9] Gade, A. et al. "Detailed experimental study on intermediate-energy Coulomb excitation of ^{46}Ar". In: *Phys. Rev. C* vol. 68 (1 July 2003), p. 014302. DOI: 10.1103/PhysRevC.68.014302. URL: https://link.aps.org/doi/10.1103/PhysRevC.68.014302.

[10] Gade, A. et al. “Knockout from ^{46}Ar : $\ell = 3$ neutron removal and deviations from eikonal theory”. In: *Phys. Rev. C* vol. 71 (5 May 2005), p. 051301. DOI: 10.1103/PhysRevC.71.051301. URL: https://link.aps.org/doi/10.1103/PhysRevC.71.051301.

[11] Gaudefroy, L. et al. “Structure of the $N = 27$ isotones derived from the ^{44}Ar$(d, p)^{45}$Ar reaction”. In: *Phys. Rev. C* vol. 78 (3 Sept. 2008), p. 034307. DOI: 10.1103/PhysRevC.78.034307. URL: https://link.aps.org/doi/10.1103/PhysRevC.78.034307.

[12] Gaudefroy, L. et al. “Study of the N = 28 shell closure in the Ar isotopic chain”. In: *The European Physical Journal A* vol. 27, no. S1 (Mar. 2006), pp. 309–314. DOI: 10.1140/epja/i2006-08-047-0. URL: https://doi.org/10.1140/epja/i2006-08-047-0.

[13] Glasmacher, T. “COULOMB EXCITATION AT INTERMEDIATE ENERGIES”. In: *Annual Review of Nuclear and Particle Science* vol. 48, no. 1 (1998), pp. 1–31. DOI: 10.1146/annurev.nucl.48.1.1. eprint: https://doi.org/10.1146/annurev.nucl.48.1.1. URL: https://doi.org/10.1146/annurev.nucl.48.1.1.

[14] Glasmacher, T. et al. “Collectivity in 44S”. In: *Physics Letters B* vol. 395, no. 3 (1997), pp. 163–168. DOI: https://doi.org/10.1016/S0370-2693(97)00077-4. URL: https://www.sciencedirect.com/science/article/pii/S0370269397000774.

[15] Greiner, W. and Maruhn, J. A. *Nuclear Models*. en. 1996th ed. Berlin, Germany: Springer, Feb. 1996.

[16] Grévy, S. et al. “Observation of the 0_2^+ state in ^{44}S”. In: *The European Physical Journal A* vol. 25, no. S1 (July 2005), pp. 111–113. DOI: 10.1140/epjad/i2005-06-179-8. URL: https://doi.org/10.1140/epjad/i2005-06-179-8.

[17] Lalazissis, G. A. et al. “Relativistic Hartree+Bogoliubov description of the deformed $N = 28$ region”. In: *Phys. Rev. C* vol. 60 (1 June 1999), p. 014310. DOI: 10.1103/PhysRevC.60.014310. URL: https://link.aps.org/doi/10.1103/PhysRevC.60.014310.

[18] Longfellow, B. et al. “Quadrupole collectivity in the neutron-rich sulfur isotopes ^{38,40,42,44}S”. In: *Phys. Rev. C* vol. 103 (5 May 2021), p. 054309. DOI: 10.1103/PhysRevC.103.054309. URL: https://link.aps.org/doi/10.1103/PhysRevC.103.054309.

[19] Meisel, Z. et al. “Mass Measurements Demonstrate a Strong $N = 28$ Shell Gap in Argon”. In: *Phys. Rev. Lett.* vol. 114 (2 Jan. 2015), p. 022501. DOI: 10.1103/PhysRevLett.114.022501. URL: https://link.aps.org/doi/10.1103/PhysRevLett.114.022501.

[20] Mengoni, D. et al. “Lifetime measurements of excited states in neutron-rich ^{44,46}Ar populated via a multinucleon transfer reaction”. In: *Phys. Rev. C* vol. 82 (2 Aug. 2010), p. 024308. DOI: 10.1103/PhysRevC.82.024308. URL: https://link.aps.org/doi/10.1103/PhysRevC.82.024308.

[21] Mougeot, M. et al. “Examining the $N = 28$ shell closure through high-precision mass measurements of $^{46–48}$Ar”. In: *Phys. Rev. C* vol. 102 (1 July 2020), p. 014301. DOI: 10.1103/PhysRevC.102.014301. URL: https://link.aps.org/doi/10.1103/PhysRevC.102.014301.

[22] Mutschler, A. et al. “A proton density bubble in the doubly magic 34Si nucleus”. In: *Nature Physics* vol. 13, no. 2 (Oct. 2016), pp. 152–156. DOI: 10.1038/nphys3916. URL: https://doi.org/10.1038/nphys3916.

[23] Nowacki, F. and Poves, A. “New effective interaction for $0\hbar\omega$ shell-model calculations in the $sd - pf$ valence space”. In: *Phys. Rev. C* vol. 79 (1 Jan. 2009), p. 014310. DOI: 10.1103/PhysRevC.79.014310. URL: https://link.aps.org/doi/10.1103/PhysRevC.79.014310.

[24] Nowak, K. et al. “Spectroscopy of ^{46}Ar by the (t, p) two-neutron transfer reaction”. In: *Phys. Rev. C* vol. 93 (4 Apr. 2016), p. 044335. DOI: 10.1103/PhysRevC.93.044335. URL: https://link.aps.org/doi/10.1103/PhysRevC.93.044335.

[25] Ogilvie, C. et al. “Spectroscopy of 47K and proton core-excitations in 48Ca from the 48Ca(t, α)47K reaction”. In: *Nuclear Physics A* vol. 465, no. 3 (1987), pp. 445–460. DOI: https://doi.org/10.1016/0375-9474(87)90358-7. URL: https://www.sciencedirect.com/science/article/pii/0375947487903587.

[26] Ring, P. and Schuck, P. *The Nuclear Many-Body Problem*. Physics and astronomy online library. Springer, 2004. URL: https://books.google.it/books?id=PTynSM-nMA8C.

[27] Rodríguez-Guzmán, R., Egido, J. L., and Robledo, L. M. “Quadrupole collectivity in $N \approx 28$ nuclei with the angular momentum projected generator coordinate method”. In: *Phys. Rev. C* vol. 65 (2 Jan. 2002), p. 024304. DOI: 10.1103/PhysRevC.65.024304. URL: https://link.aps.org/doi/10.1103/PhysRevC.65.024304.

[28] S. Péru, M. Girod, and J.F. Berger. “Evolution of the N = 20 and N = 28 shell closures in neutron-rich nuclei”. In: *Eur. Phys. J. A* vol. 9, no. 1 (2000), pp. 35–47. DOI: 10.1007/s100500070053. URL: https://doi.org/10.1007/s100500070053.

[29] Scheit, H. et al. “New Region of Deformation: The Neutron-Rich Sulfur Isotopes”. In: *Phys. Rev. Lett.* vol. 77 (19 Nov. 1996), pp. 3967–3970. DOI: 10.1103/PhysRevLett.77.3967. URL: https://link.aps.org/doi/10.1103/PhysRevLett.77.3967.

[30] Sharma, M. K. et al. “Nuclear structure study of some bubble nuclei in the light mass region using mean field formalism”. In: *Chinese Physics C* vol. 39, no. 6 (June 2015), p. 064102. DOI: 10.1088/1674-1137/39/6/064102. URL: https://doi.org/10.1088/1674-1137/39/6/064102.

[31] Shukla, A., Åberg, S., and Bajpeyi, A. "Systematic study of bubble nuclei in relativistic mean field model". In: *Physics of Atomic Nuclei* vol. 79, no. 1 (Jan. 2016), pp. 11–20. DOI: 10.1134/s1063778816010191. URL: https://doi.org/10.1134/s1063778816010191.

[32] Sohler, D. et al. "Shape evolution in heavy sulfur isotopes and erosion of the $N = 28$ shell closure". In: *Phys. Rev. C* vol. 66 (5 Nov. 2002), p. 054302. DOI: 10.1103/PhysRevC.66.054302. URL: https://link.aps.org/doi/10.1103/PhysRevC.66.054302.

[33] Sorlin, O. and Porquet, M.-G. "Evolution of theN= 28 shell closure: a test bench for nuclear forces". In: *Physica Scripta* vol. T152 (Jan. 2013), p. 014003. DOI: 10.1088/0031-8949/2013/t152/014003. URL: https://doi.org/10.1088/0031-8949/2013/t152/014003.

[34] Utsuno, Y. et al. "Onset of intruder ground state in exotic Na isotopes and evolution of the $N = 20$ shell gap". In: *Phys. Rev. C* vol. 70 (4 Oct. 2004), p. 044307. DOI: 10.1103/PhysRevC.70.044307. URL: https://link.aps.org/doi/10.1103/PhysRevC.70.044307.

[35] Utsuno, Y. et al. "Shape transitions in exotic Si and S isotopes and tensor-force-driven Jahn-Teller effect". In: *Phys. Rev. C* vol. 86 (5 Nov. 2012), p. 051301. DOI: 10.1103/PhysRevC.86.051301. URL: https://link.aps.org/doi/10.1103/PhysRevC.86.051301.

[36] Wagner, G. J. et al. "Lifetime of nuclear hole states caused by phonon-hole coupling". In: *Physics Letters B* vol. 57 (1975), pp. 413–416.

Chapter 4

The Experimental Setup and Calibrations

4.1 The Production of the ^{46}Ar Radioactive Beam

The ^{46}Ar radioactive beam was provided by the Spiral 1 facility in GANIL (Grand Accélérateur National d'Ions Lourds), Caen, France [6].

This facility has been at the forefront of innovation in the development of the Isotope Separation On-Line (ISOL) techniques for radioactive beam production. Such a technique relies on the extraction and post acceleration of isotopes produced from reactions with a primary beam, thus allowing for beam optics properties comparable to those of stable beams.

The SPIRAL 1 facility relies on thick graphite targets on which a high-intensity primary heavy-ion beam impinges and on the subsequent diffusion of the produced ions from the hot target to the ion source. The ions are ionized by an ECR source (Nanogan III Electron Cyclotron Resonance) and are separated and injected in the post acceleration stage, consisting of the CIME cyclotrons (Cyclotron d'Ions à Moyenne Énergie). The radioactive beam is then delivered to the experimental hall of interest.

Figure 4.1 shows an extrapolation of the expected production of each isotope before the post acceleration section. Typically the intensities are reduced by two orders of magnitude to account for the losses in charge breeding and post acceleration. While all beams shown in the figure rely on the fragmentation mechanism for the production, heavier radioactive beams on the neutron-deficient side can also be produced via fusion evaporation as an alternative technique.

Figure 4.2 shows the layout of the SPIRAL 1 facility with the VAMOS hall, which hosted the experimental setup.

In the particular case of this experiment, a primary beam of ^{48}Ca impinged on the primary carbon target with a power ranging from 300 W to 600 W and energy of 60 MeV/u. The ^{46}Ar radioactive isotopes were extracted from the fragmentation products and post accelerated at an energy of 9.96 MeV/A and an average intensity of $4 \cdot 10^4$ particles per second.

Figure 4.3 pictures one of the CIME cyclotrons open for repair with one of the RF cavities extracted from the main body.

4.2 Experimental Apparatus

The overall setup of the experiment consists of the combination of multiple state-of-the-art detectors: MUGAST+AGATA+VAMOS, whose performance is documented in a separate publication[2].

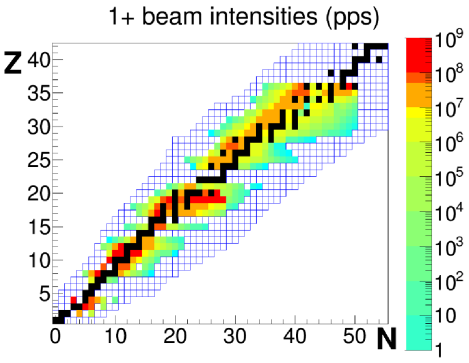

Figure 4.1: Extrapolation of the expected intensity and availability of isotopes produced by the SPIRAL 1 setup, before the post acceleration procedure. Figure adapted from reference [6].

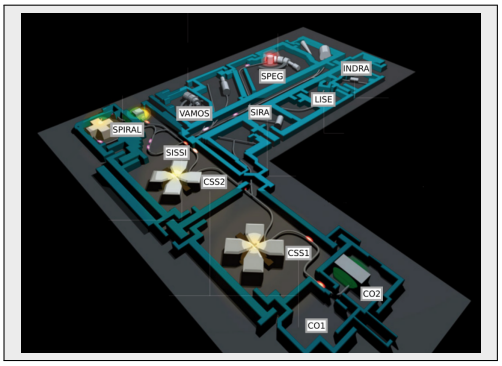

Figure 4.2: The facility for the production of post-accelerated radioactive beams in GANIL. Adapted from reference [17].

The radioactive beam, entering the reaction chamber after passing through the beam tracker CATS [13], impinges on a cryogenic ^{3}He target [7]. The light reaction fragments are detected by the position-sensitive silicon detectors MUGAST [2] at backward angles with respect to the beam and by MUST2 [14] at forward angles.

The heavy fragments are identified by the magnetic spectrometer VAMOS [16, 18, 19] placed in its zero degrees configuration. Gamma rays emitted by the de-excitation of the reaction fragments are detected by the segmented high purity germanium array AGATA[1] placed ad backward angles.

A sketch of the experimental setup is shown in Figure 4.4, with a schematic view of the direction of emission of the reaction fragments.

Each component of the setup has a particular purpose which and be detailed in the following dedicated sections of the current chapter:

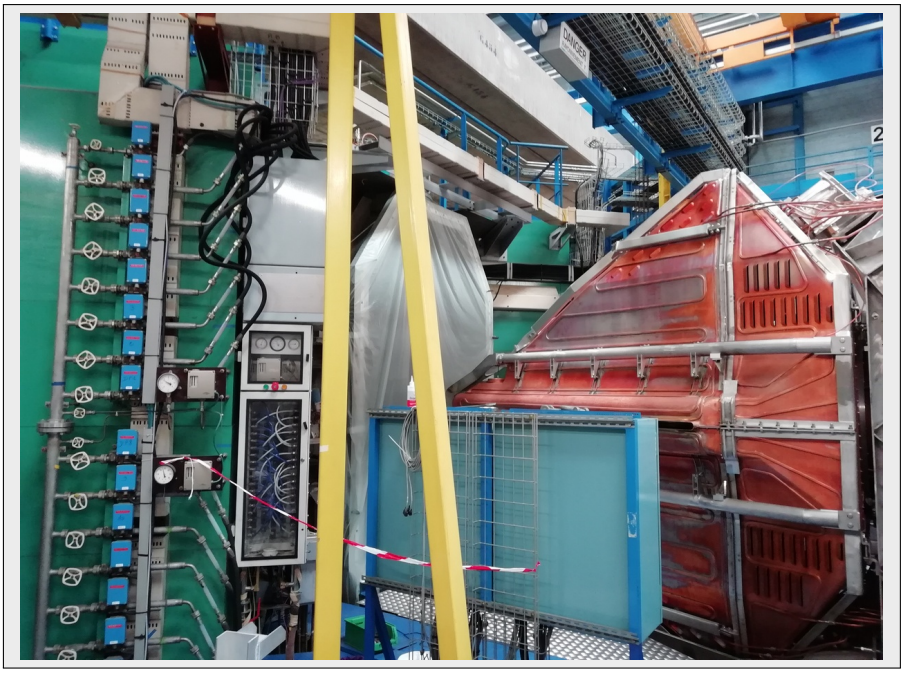

Figure 4.3: Picture of CSS1, one of the post-acceleration cyclotrons, open for inspection. The copper block consists of one of the four accelerating cavities.

- VAMOS (section 4.3):
  1. Identify the reaction fragment (^{47}K) on an event-by-event basis
  2. Monitor the target thickness over time by measuring the magnetic rigidity ($B\rho$) of the beam over time
  3. Measure the recoiling-fragment β for an event-by-event Doppler correction of the emitted γ rays
  4. Track the beam current over time on the focal plane of the detector
- CATS2 (section 4.5):
  1. Provide the position of entrance of the beam for the focusing procedure and general beam monitoring
  2. Track the incoming beam intensity
  3. Measure the time of flight for the silicon detectors and the magnetic spectrometer
- AGATA (section 4.7):
  1. Measure the γ rays emitted by the excited reaction products such as ^{47}K, populated by the ^{46}Ar(^{3}He,d)^{47}K channel

2. Detect the γ rays emitted by the inelastic excitation of the beam, ^{46}Ar

- MUGAST and MUST2 (section 4.6):

1. Identify the light particles
2. Measure the energy and position of the emitted particles

Appendix C shows a schematic of the electronics chain of the setup.

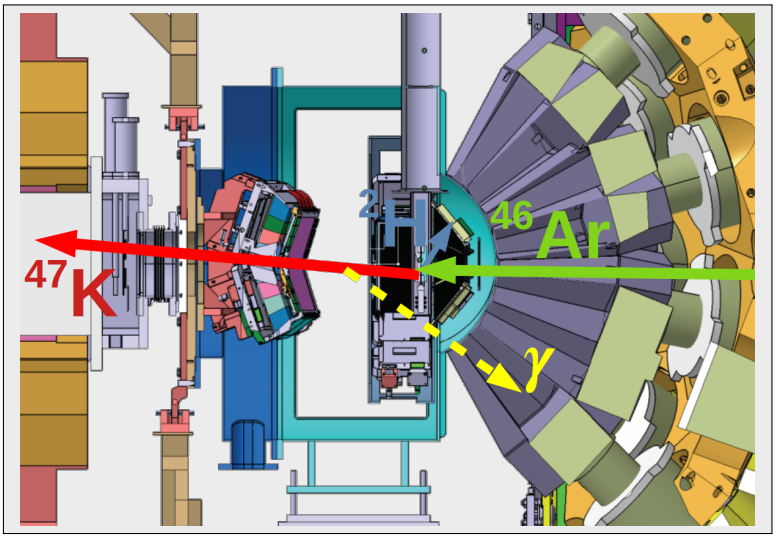

Figure 4.4: View of the experimental setup showing the target, the silicon detectors, the γ-ray detector, and the entrance of the magnetic spectrometer. Arrows indicate a typical reaction event in terms of the direction of the emitted particles.

4.2.1 The Kinematics of the Reaction

The reaction consists in a ^{46}Ar(^{3}He,d)^{47}K proton-pickup direct reaction. As a consequence of the kinematics of the process, the deuteron is emitted and detected at backward angles in the laboratory frame of reference with the largest cross section.

The beam energy in the center of the target, which corresponds to the average reaction energy, requires detailed calculations due to the thickness of the target. Table 4.1 presents the amount of energy lost by the argon ions in the various layers between the beam tracker and the entrance of the magnetic spectrometer.

The selected charge state of the beam is 9^{+}, which corresponds to a (measured) magnetic rigidity value of $B\rho = (2.328 \pm 0.002)$ Tm.

Beam position	**Eff. Thickness** (mg/cm^2)	**En. middle** (MeV)	**En. after** (MeV)
Entrance	-	-	458.2
CATS2	0.84 ($H_8C_{10}O_4$)	453.3	448.3
Ice Deposition	1.38 (H_2O)	427.3	405.8
Havar	3.15 ($Co_{42}Cr_{20}Ni_{13}Fe_{19}W$)	392.6	379.3
^{3}He	2.27 (^3He)	357.2	334.1
Havar	3.15 ($Co_{42}Cr_{20}Ni_{13}Fe_{19}W$)	319.7	305.0
Ice Deposition	1.38 (H_2O)	378.5	250.5
VAMOS	-	271.2	-

Table 4.1: Energy of the beam while passing through different materials. Ice thickness is assumed of 35 μm, while the target thickness is averaged over the beam shape of 3.72 mm with a density of 0.0045 g/cm^3. Further details on the density of the ^{3}He gas are presented in Appendix A.

The (relatively) low energy of the beam and the various layers of material (documented in Table 4.1) lead to a distribution of charge states (cf. subsection 4.3.6) that is higher on average compared to the original one, allowing the magnetic spectrometer, with its maximum magnetic rigidity of 1.6 Tm[19], to bend the trajectory of the beam ions within its focal plane.

The exponential-like decay of the cross-section in the center of mass frame of reference is shown in Figure 4.5. Since the highest portion of the cross-section for the direct reaction is contained at low angles, most of the deuterons will be emitted at backward angles in the laboratory due to the frame of reference transformation. The conversion between the angles in the laboratory is shown in Figure 4.6, where small angles in the center-of-mass frame correspond to backward angles, with respect to the beam direction, in the laboratory. The energy and angle of emission of particles relative to a two-body reaction are tied by the conservation of the four-momentum. For the reaction of interest, the relation between angle and energy in the lab is presented in Figure 4.7. The kinematics of the ^{47}K ions is restricted within values of momentum and angle that are always contained by the acceptance of the magnetic spectrometer, as discussed in detail in subsection 5.2.7. The light deuteron fragments are detected by MUGAST at angles between $118° - 172°$ which correspond to $2° - 23°$ in the center of mass frame of reference.

As it is apparent from Figure 4.5, the $L = 0$ transfer presents a clear signature if compared to other transferred angular momenta (such as $L = 2$ and $L = 3$), as it appears strongly peaked at the lowest angles in the center of mass frame of reference. In the laboratory frame of reference, this peculiarity translates to a high expected number of counts in the annular detector, which is placed at the most backward angles in the case of a high $L = 0$ transfer cross-section.

Another relevant aspect for the analysis is the position of the first $L = 2$ peak compared to the $L = 0$ distribution as it appears in correspondence to the

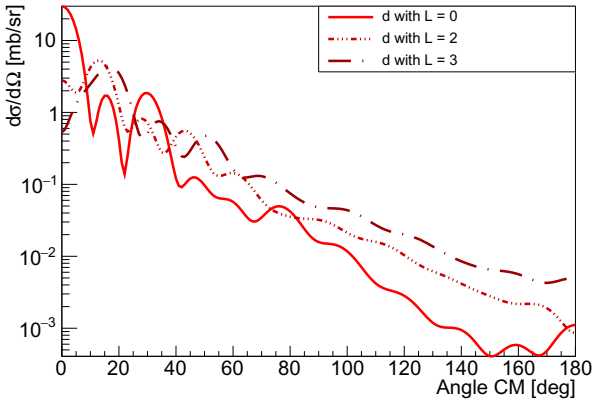

Figure 4.5: Center-of-mass angular distributions with different types of transfers and unitary spectroscopic factor for the proton-transfer direct reaction ^{46}Ar(^{3}He,d)^{47}K.

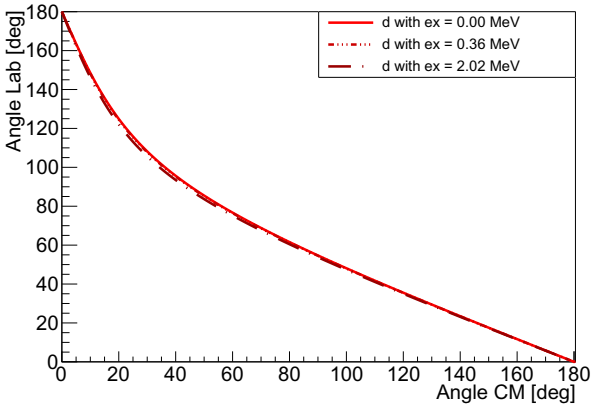

Figure 4.6: Angle conversion between center of mass and laboratory frame of reference for the light particle, the deuteron.

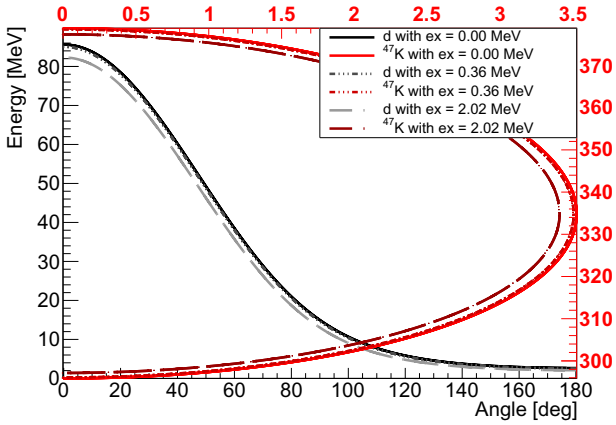

Figure 4.7: Kinematics of the light and heavy reaction fragments superimposed with different scales. Due to the Lorentz boost, the heavy reaction fragment is limited in a cone of maximum angle of aperture of 3.5 degrees.

minimum of the former, further differentiating the two distributions.

The objective of the experiment is to assess the relative amount of $L = 0$ and $L = 2$ transfer cross sections via a measurement of the $L = 0 + L = 2$ angular distributions. The analysis strategy relies on the deconvolution of the total distribution into the constituent ones, relative to the two different values of transferred angular momentum, because the $1/2^+$ and $3/2^+$ states of ^{47}K are too close in energy to be distinguished by measuring the energy of the light reaction fragments.

The region of sensitivity of the MUGAST detector in the center of mass reference falls in the interval $[2°, 24°]$, where the first two peaks of the $L = 0$ distribution are present and can be compared to the first peak of the remaining $L = 2, 3$ distributions. It is also evident that the number of deuterons measured in the annular detector, where the first peak of the $L = 0$ distribution is present, and the other distributions provide negligible contributions, will fix the overall amount of counts that can be present in the second peak at around 18°.

Given the low binding energy of the deuteron (2224.566(1) keV), the deuteron-breakup reaction channel is also open with a significant cross section. This process consists of a three-body reaction where after the transfer of one proton from the target to the beam ion, the deuteron breaks in its constituent nucleons. This reaction does produce ^{47}K, which can be identified in the magnetic spectrometer, while the protons can be detected and distinguished from the deuterons by the silicon detectors. The magnetic spectrometer is not able to measure the emission angle on the vertical plane with a resolution high enough to perform angular distribution or spectroscopy on the heavy beam-like fragment so that a full reconstruction of the three-body reaction ^{46}Ar(^{3}He,pn)^{47}K is not possible in the current experiment.

4.3 The magnetic spectrometer: VAMOS

VAMOS[16, 18, 19], the VAriable MOde high acceptance Spectrometer, is a large solid-angle ray-tracing magnetic spectrometer able to fully identify the reaction fragments.

Its main components are schematically depicted in Figure 4.8. They consist of two quadrupole magnets which focus the recoiling reaction fragments first in the y then in the x directions, and a dipole, which separates the ions on the dispersion (x) axis based on their magnetic rigidity $B\rho$:

$$B\rho = \frac{p}{q} \approx C\frac{A}{q}\beta\gamma \quad \text{where} \quad C = \frac{c}{eN_a} \approx 3.105\ T{\cdot}m \quad , \quad \gamma = \left(1-\beta^2\right)^{-\frac{1}{2}} \tag{4.1}$$

This expression contains a dependence of the magnetic rigidity from the charge state q, the atomic mass A, Avogadro's number N_a, the speed of light c, and electric charge e. As a consequence of the optics of the spectrometer, ions with different magnetic rigidity will follow different trajectories. Thanks to the detectors located in the focal plane of the spectrometer, it is possible to reconstruct the path undertaken and measure the magnetic rigidity of each fragment [15] to perform a full identification of the reaction fragments on an event-by-event basis.

The spectrometer is exploited for several purposes in the analysis of the experiment and is essential for the full reconstruction of the nuclear reaction as well as other aspects such as beam monitoring (through the $B\rho$) and the detection of the velocity β of the recoiling fragment for the Doppler correction.

The spectrometer was set in the zero degrees configuration. Thanks to its high acceptance both in momentum and in solid angle, and due to the kinematics of the reaction (cf. 4.2.1), virtually [1] all beam ions and reaction fragments are accepted within the spectrometer (cf. 5.2.7).

The spectrometer is capable of an angular acceptance of $\pm 7°$ in the polar angle and $\pm 10°$ in the azimuthal angle while the momentum acceptance is of $\pm 30\%$.

In the focal position of the spectrometers, located 7600 mm from the target and along the z-axis, several detectors are present:

1. Multi-Wire Parallel Plate Avalanche Counter (subsection 4.3.1)
2. Drift Chambers (subsection 4.3.2)
3. Ionization Chamber (subsection 4.3.3)

The overall active area of these detectors consists of a 1000 mm × 150 mm surface and allows for the measurement of the observables inherent to the reaction fragments, which will be described in the following subsections.

[1] Monte Carlo Geant4 simulations, discussed in subsection 5.2.7, indicate that more than 99% of ions emitted in each reaction fall within the acceptance of the spectrometer.

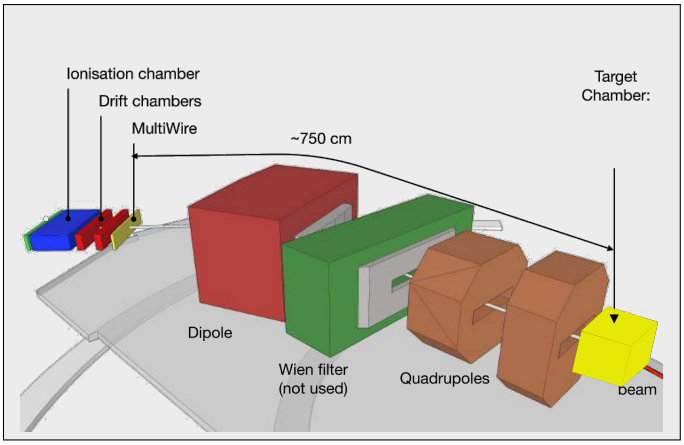

Figure 4.8: Schematic of the main components of the VAMOS magnetic spectrometer. The focal plane detectors are placed 760 cm after the target and behind the quadrupole and dipole magnets. Picture adapted from reference [17].

Throughout the experiment, the magnetic rigidity ($B\rho$) was gradually decreased in order to account for the progressively lowering of the energy of the emitted ions due to the growing ice deposition (cf. subsection 4.4.2). The magnetic field on the dipole was initially set to obtain a reference $B\rho$ value of 1.05 Tm, which was later lowered to 0.95 Tm and kept at 0.9 Tm in the last phase of the experiment.

4.3.1 The Multi-Wire Parallel Plate Avalanche Counter (MWPPAC)

The first of the focal plane detectors, located precisely in the focal plane position (7600 mm from the target in the z direction), consists of a Multi-Wire Parallel Plate Avalanche Counter.

Its main purpose is to provide a high-resolution measurement of the Time of Flight (TOF) of the fragments, which is necessary for the velocity vector (β) measurement. It serves as a start signal for the Time to Amplitude Converter (TAC) that is, in turn, stopped by the delayed signal from CATS2, the beam tracker (presented in Section 4.5). The choice to invert start and stop is a common occurrence justified by the difference in rates observed by the two detectors. In particular, the beam tracker is expected to reach a higher trigger rate compared to the multiwire as not all events which cross the tracker will eventually reach the multiwire, which would lead to many events where the start signal will not be stopped. Conversely, if the MWPPAC acts as the start signal, only events of interest will trigger the start of the TAC module allowing for a lower dead time in the acquisition system.

With the same total active area of 1000 mm $\times$ 150 mm of the other focal-plane detectors, the MWPPAC is composed of a central cathode and two anodes separated by 2.2 mm each.

The cathode is polarized at −450 V and consists of wires spaced 0.5 mm apart, while the anode is grounded and is composed of wires spaced by 1 mm.

The chamber containing the MWPPAC is filled by isobutane (C_4H_{10}) at a pressure of 7 mbar, contained by a Mylar window of 0.9 μm, supported by multiple nylon wires of 100 μm diameter placed every 50 mm.

The ions crossing the detector ionize the gas along the trajectory; the free electrons are accelerated by the electric field gradient and drift towards the anodes generating an avalanche in the proximity of the wires, where the field is more intense. The charge associated with the electron avalanche is collected in the central cathode and read out by 20 electronically-independent sections that provide 20 time signals. This segmentation allows for a reduced capacitance, which in turn allows for a faster rise time of the signals and an improved time resolution which has been measured at around 500 ps.

4.3.2 The Drift Chambers

The two drift chambers (DC) of VAMOS serve the purpose of detecting both the horizontal and vertical crossing positions of the recoiling ion. By stacking multiple drift chambers one after the other, it is possible to detect also the direction of the velocity vector. The information provided will then be used to compute the velocity (β), which depends on the reconstructed path and on the time of flight. The former is computed by the trajectory reconstruction procedure (briefly described in subsection 4.3.4). Additionally, this procedure also allows for the reconstruction of the angles of emission with respect to the target, making use of the observables provided by the drift chambers.

Each drift chamber detects an x position by measuring the maximum of the induced charge distribution on the pads and a y position by measuring the drift time of the electrons from the wire placed transversely.

The direction of the recoil can be extracted only if more than one drift chamber detects the ion, while the position information requires a single measurement.

The drift chambers, located after the MWPPAC detector, are enclosed in Mylar windows and contain isobutane (C_4H_{10}) at 7 mbar, exploiting the good quenching properties of this gas.

Each drift chamber can be conceptually divided into two volumes: a drift and an amplification volume. The former is the active volume where the crossing ion produces a trail of primary electrons from the ionization of the gas. The charges start the drift towards the Frisch grid [9] to later enter the amplification region where the higher electrical field generates an avalanche which increases the overall induced charge on the pads.

The cathode in the drift portion of the volume is placed in the upper part of the chamber and is polarized at −500 V, while the Frisch grid is placed at ground potential.

The Frisch grid effectively shields the induction pads from all charges in the drift volume that has two important effects: renders the charge induced on the pads independent of the position of primary ionization while also shielding the

positive charges (characterized by a significantly lower drift velocity) from the pads thus increasing the time resolution of the signal (shorter rise time).

The amplification volume increases the induced charge via secondary ionization by means of a plane of 8 wires placed 15 mm below the Frisch grid and spaced 10 mm apart from each other.

The cathode plane is placed at the bottom of the amplification volume and consists of two rows of 160 staggered pads aligned along the dispersion plane (x axis) made of gold-plated strips. The staggered disposition of the pads has the objective of minimizing the chance of a loss of induced charge due to a trajectory in correspondence of the segmentation between two pads. The strips are arranged to cover the total surface for a total area coverage of 6.02×40 mm^2 each and a pitch of 6.4 mm.

The drift chambers are physically and effectively connected to the MWPPAC (subsection 4.3.1); as a consequence, the same low-pressure gas circulates between them. At the final extremity of the detector array (MWPPAC+DC) a single 2.5μm Mylar window contains the isobutane gas supported by 32 vertical nylon wires while separating it from the ionization chamber that features higher pressures.

The amplification wires provide the (fast) timing signal (t_d) which is essential to determine the drift velocity v_d when compared to the time signal of the MWPPAC (t_{MWPPAC}) from which the y axis position can be extrapolated:

$$y = v_d(t_d - t_{MWPPAC}) \quad \text{where} \quad v_{d_{isobutane}} \approx 5.528\text{cm}/\mu\text{s}$$

The x axis position, on the other hand, can be computed with a much higher resolution, exploiting the induced charge on the pads. The choice of a higher precision on the dispersion plane (x-axis) is justified by the strong correlation of this value with the magnetic rigidity of the reaction fragment, which is, in turn, essential for the identification in A/Q.

A common high-performance method to predict the charge distribution induced from a point charge is the so-called *Hyperbolic secant squared* method (SECHS) [10]. The same technique is also applied for the CATS2 beam tracker 4.5. It is possible to observe [10] that the charge distribution from a point source on pads of width w can be approximated by a squared secant function, allowing for a position resolution higher than the discrete position of the center of the pad. The induced charge Q on the pad in position x is given by:

$$Q(x) = \frac{a_1}{\cosh^2\left(\frac{\pi(x-a_2)}{a_3}\right)}$$

This approximation is convenient as the centroid position (a_2) has an analytical expression, function of the induced charge on the nearby strips (Q_{M-1}, Q_{M+1}) of the highest induced charge strip Q_M:

$$\begin{cases} a_2 = \frac{a_3}{\pi} \tanh^{-1} \sqrt{\frac{\sqrt{Q_M/Q_{M-1}} - \sqrt{Q_M/Q_{M+1}}}{2\sinh(\pi w/a_3)}} \\ a_3 = \frac{\pi w}{\cosh^{-1} \frac{1}{2}\left(\sqrt{Q_M/Q_{M-1}} + \sqrt{Q_M/Q_{M+1}}\right)} \end{cases}$$

A systematic error as a function of the inter-strip position is present and characterized in reference [10]. It is possible to exploit the cited characterization to correct the position offset and recover an improved position resolution.

The nominal position resolution achieved by the described setup is 0.27 mm in the x axis and of 0.35 mm in the y axis.

The stack of multiple drift chambers allows for the measurement of a total of four parameters: $x_f(y_f)$, the position in the horizontal(vertical) direction, and $\theta_f(\phi_f)$, the angle with respect to the horizontal(vertical) plane. The focal plane angles, which will be often cited in the course of this section, must not be confused with spherical coordinate angles (θ_f^{S}, ϕ_f^{S}) as they consist in the angles with respect to the plane in the x and y directions. The following transformation relates the two different coordinates:

$$\begin{cases} \theta_f = \theta_f^{\mathrm{S}} \sin(\phi_f^{\mathrm{S}}) \\ \phi_f = \theta_f^{\mathrm{S}} \cos(\phi_f^{\mathrm{S}}) \end{cases}$$

4.3.2.1 Detector Calibration

The calibration necessary for an accurate position reconstruction with the SECHS procedure consists in the gain matching of all the different pads to a reference value with a simple quadratic dependence:

$$Q_i^{match} = A_i + B_i Q_i + C_i Q_i^2$$

A reference pulse signal is injected in the electronics of each pad simultaneously to allow for the gain matching procedure.

4.3.3 The Ionization Chamber

The Ionization Chamber (IC) of VAMOS consists of an active gas volume of 1000 x 150 x 579 mm^3, with a drift cathode in the upper part and a segmented anode shielded by a Frisch grid. The anode segmentation is transverse with respect to the beam entrance in order to allow for an energy loss measurement in each of the six segments. The IC was filled with carbon tetrafluoride (CF_4) at a pressure of 120 mbar to allow for the beam to stop in the 4^{th} segment, relying on the first segments to measure the partial energy loss. The pressure was set to allow the beam and the reaction fragments to stop fully within its active volume.

While the Frisch grid is kept at ground potential, the anode and cathode are polarized at respectively 900 V and -2250 V.

The comparison between partial and total energy loss allows for discrimination in Z of the reaction fragments.

4.3.3.1 Isotope identification

The linear stopping power of a charged ion passing through matter is strongly dependent on many parameters. At the energies involved in this experiment, the main cause of energy loss is the interaction of the ion with the electrons of

the absorbing material, although nuclear losses also come into play at the lowest energies. A well known parametrization of the (mean) mass stopping power $-\left\langle \frac{dE}{dx} \right\rangle$, in the range of $0.1 < \beta\gamma < 1000$, is given by the Bethe equation[8]:

$$-\left\langle \frac{dE}{dx} \right\rangle = Kz^2 \frac{Z}{A} \frac{1}{\beta^2} \left(\frac{1}{2} \ln \frac{2m_e c^2 \beta^2 \gamma^2 W_{max}}{I^2} - \beta^2 - \frac{\delta(\beta\gamma)}{2} \right) \tag{4.2}$$

With the following notation:

- $K = 4\pi N_A r_e^2 m_e c^2$ is the coefficient
- z the charge number of the incident ion
- Z the atomic number of the absorber
- A the atomic mass of the absorber
- $\beta = \frac{v}{c}$ the velocity
- γ the Lorentz factor
- m_e the electron mass
- c the speed of light
- $W_{max} = \frac{2m_e c^2 \beta^2 \gamma^2}{1+2\gamma m_e/M+(m_e/M)^2}$ is the maximum possible energy transfer to an electron in a single collision
- I the mean excitation energy
- δ the density effect correction to ionization energy loss for relativistic ions
- N_A the Avogadro's number
- $r_e = \frac{e^2}{4\pi\epsilon_0 m_e c^2}$ the classical electron radius
- ϵ_o the vacuum permittivity
- M the incident ion mass in W_max

The linear stopping power S also includes ρ, the density of the material:

$$S = \rho \left\langle \frac{dE}{dx} \right\rangle$$

In the limit of low ion energy ($\beta\gamma < 1$), it is possible to derive from equation 4.2 the dependence of the energy loss in a common absorber as a function of the kinetic energy of the incident charged particle E, its mass M and the charge number [9]:

$$S = C_1 \frac{Az^2}{E} \ln C_2 \frac{E}{M}$$

Where the C_1, C_2 constants depend on the material and all other constants previously described. We expect then to be able to differentiate particles based on their z and M values in a 2-dimensional plot of partial deposited energy and total deposited energy. In practice, and in the specific case of the described

ionization chamber and the reaction fragments of interest, the discrimination in mass would require a higher resolution due to its higher absolute value.

More sophisticated models and parametrizations are used in real-world applications compared to the standard Bethe equation (eq. 4.2), however, the dependence on z and the energy trend remains qualitatively the same. Nuclear stopping power is also often considered, although it appears only relevant at low energies.

Figure 4.9 shows an example of the dependence on Z of the stopping power in the case of the ^{3}He gas contained in the target. The evaluation of the energy loss of the ions in the gas is important for the reaction kinematics reconstruction.

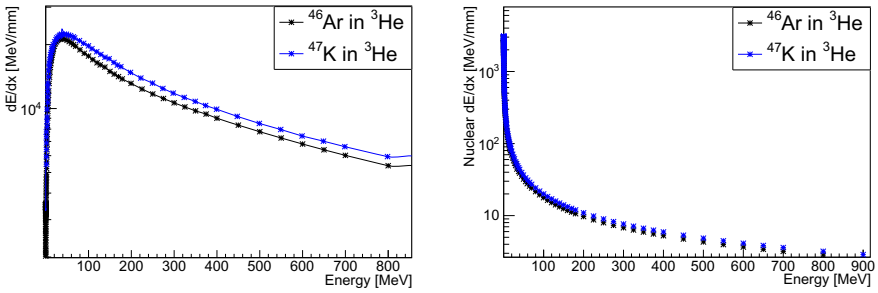

(a) Total stopping power

(b) Nuclear stopping power

Figure 4.9: Stopping power as a function of the ion energy (^{46}Ar and ^{47}K) in the case of a gaseous ^{3}He target with a pressure of $4.5 \cdot 10^{-3}$ g/cm^3 which amounts to $9.0 \cdot 10^{20}$ atoms/cm^3 [23]. The electronic stopping power in the energy range of interest is several orders of magnitude more relevant in the stopping process.

4.3.3.2 Detector Calibration

An effective process to refine the calibration of the ionization chamber is to compare the energy deposited in one segment with respect to the next. A 2-dimensional plot shows that the data possess significant features which are highly dependent on the energy loss parameters of the system (such as atomic charge of the ion, density of the gas, thickness of the anode pads). This procedure is discussed in section 5.1, where the calibration takes advantage of the comparison with the simulated data.

The final atomic number selection is performed exploiting the correlation of partial and total energy deposited, shown in Figure 4.10. In particular, the partial energy deposition can be evaluated either in the first or in the first two segments of the ionization chamber. Both cases are shown and lead to comparable resolutions.

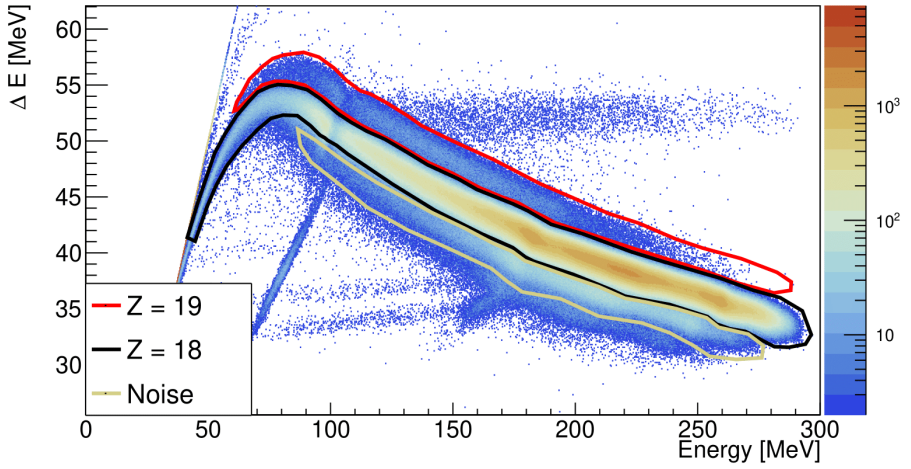

(a) First Ionization Chamber segment

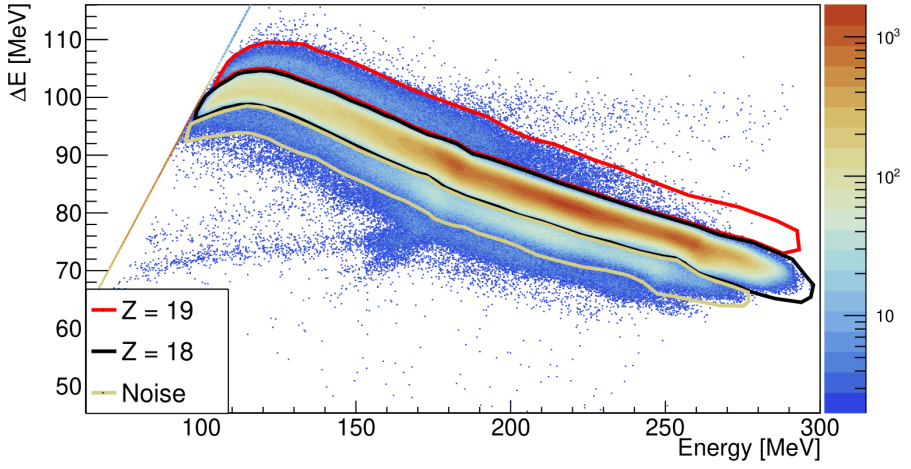

(b) First two ionization chamber segments

Figure 4.10: Partial deposited energy (ΔE) vs total energy matrices for the ionization chamber of VAMOS. The absence of counts in the punch-through region indicates that the beam and all reaction fragments are stopped within the active volume. Most of the statistics are due to ^{46}Ar, the beam ($Z = 18$), while the upper line corresponds to $Z = 19$.

4.3.4 Trajectory Reconstruction

The idea behind the trajectory reconstruction of a magnetic spectrometer resides behind the concept that there exists an (invertible) transformation Ω^{-1} that maps the final hyper coordinates of the outgoing ion to a set of coordinates which is not known a priori.

In this context, the effect of the magnetic field of the quadruples and of the dipole on the trajectory of the particle can be fully synthesized in the transformation Ω which maps the emission angles with respect to the target (θ_t and ϕ_t) and the magnetic rigidity $B\rho$ and path l to the coordinates measured by the focal plane detectors: the position (x_{fp} and y_{fp}) and the angles with respect to the plane (θ_{fp} and ϕ_{fp}). The transformation Ω would depend on the $B\rho$ value set on the spectrometer, nevertheless, it is simpler to remove the dependence by expressing the magnetic rigidity and the path length as a discrepancy from a reference value. A new coordinate $\delta = B\rho/B\rho_0$ is introduced as the ratio between the magnetic rigidity of the fragment and the reference value set on the dipole magnet $B\rho_0$. The scaled coordinate is $l = Path/Path_0$, where its value refers to the nominal path from the target to the focal plane position along the most central trajectory. This transformation relates the measured coordinates on the focal plane to the remaining coordinates of interest as:

$$(x_{fp}, \theta_{fp}, y_{fp}, \phi_{fp}) \xrightarrow{\Omega^{-1}} (\theta_t, \phi_t, l, \delta) \tag{4.3}$$

Due to the presence of the quadrupole magnets and the inhomogeneities of the magnetic fields, the use of algorithms dependent on the transfer map is not a viable option.

On the other hand, thanks to the high-resolution mapping of the magnetic field produced by the magnets performed during their design and production, an approach relying on multi-particle tracking codes emerged as a better option. In particular, the initial coordinate reconstruction makes use of the numerical integration of the Newton-Lorentz equation performed in the ZGOUBI[12] code.

The trajectory reconstruction algorithm consists of the most recent developments on the original procedure described in reference [19]. The integration of the equations is performed with a total of 20000 particles, covering the whole acceptance (in angle and momentum) of the spectrometer and storing initial and final coordinates presented in equation 4.3. A matrix of the mapping is thus produced, making an interpolation and the approximation of the transformation Ω possible. Once the mapping is known, it is possible to reconstruct a trajectory by identifying the closest mapped final coordinates to the measured ones. The *closeness* relation is selected with a parameterized root mean square distance ($D^2 = \alpha_1(x_m - x_f)^2 + \alpha_2(\theta_m - \theta_f)^2 + \alpha_3(y_m - y_f)^2 + \alpha_4(\phi_m - \phi_f)^2$) and its parameters chosen by a χ^2 minimization. A finer precision can be achieved by interpolating the grid of the mapping.

The stored set of coordinates (initial+final) could be used for a multivariate Taylor expansion to map the measured coordinates to the parameters of interest:

$$\delta = \sum_{i,j,k,t=0}^{i+j+k+t=7} C_{ijkt}^{(\delta)} \cdot x_{fp}^{i} \cdot \theta_{fp}^{j} \cdot y_{fp}^{k} \cdot \phi_{fp}^{t}, \tag{4.4}$$

$$\theta = \sum_{i,j,k,t=0}^{i+j+k+t=7} C_{ijkt}^{(\theta)} \cdot x_{fp}^{i} \cdot \theta_{fp}^{j} \cdot y_{fp}^{k} \cdot \phi_{fp}^{t} \tag{4.5}$$

$$\phi = \sum_{i,j,k,t=0}^{i+j+k+t=7} C_{ijkt}^{(\phi)} \cdot x_{fp}^{i} \cdot \theta_{fp}^{j} \cdot y_{fp}^{k} \cdot \phi_{fp}^{t}, \tag{4.6}$$

$$l = \sum_{i,j,k,t=0}^{i+j+k+t=7} C_{ijkt}^{(l)} \cdot x_{fp}^{i} \cdot \theta_{fp}^{j} \cdot y_{fp}^{k} \cdot \phi_{fp}^{t} \tag{4.7}$$

Where the coefficients C_{ijkt}^{i} are computed on a set of trajectories simulated by the tracking code (ZGOUBI). While a simultaneous fit of all trajectories might seem like a sensible procedure, it can easily lead to systematic errors.

Avoiding a global fit of the whole parameter space, a two-step procedure leads to improved results. The steps are dictated by the significant difference in position resolution on the x- and y-axis of the spectrometer (corresponding respectively horizontal and vertical plane). The discrepancy in resolutions stems from the higher resolution of the x-position measurement that is computed from the induced charge on the drift chamber's pads if compared with the vertical position, which depends on the drift time of the charge carriers in the gas.

The first step consists of the determination of the x position coordinates first, with a scanning of the trajectories with an interval that is finer than the position resolution in x of the focal plane detectors. The scanning fixes with good precision the x value leaving the remaining parameters to be fixed. An interpolation of the y-axis trajectories (with fixed x) with an expansion similar to equation 4.7 is computed and used to extract the initial coordinates.

The extracted values of $B\rho$ and $Path$ are essential for the reconstruction of the mass and charge state of the reaction fragment (cf. 4.3.5).

4.3.5 Fragment Identification

The values of β and γ are computed based on the ion path reconstruction D and the time of flight of the fragment TOF:

$$\beta = \frac{D}{TOF \cdot c}$$

Where the distance D is the path crossed by the ion between the target and the point of crossing of the focal plane of VAMOS. Since the multiwire is placed behind the nominal focal plane position, the overall distance is the sum of the reconstructed distance $Path$ (as described in subsection 4.3.4) with the addition of an offset corrected by the angle between the focal plane and the ion trajectory:

$$D = \frac{\text{Path}}{\cos(\phi_{fp})} + \frac{D_{FP}^{MW}}{\cos(\theta_{fp})\cos(\phi_{fp})}$$

At the same time, also the time of flight must be computed accounting for the offset introduced by the time that the beam ions take to reach the target starting from the CATS2 tracker. Since the MWPPAC in the focal plane of the spectrometer acts as a start signal for the delayed stop of CATS2, the timing value returned by the TDC (Time to Digital Converter) must be inverted and offset by a constant amount, $Offs$:

$$TOF = Offs - t_{TDC} \tag{4.8}$$

The term $Offs$ contains both the electronic delay in the logic start signal as well as the time from the beam to reach the target, which is a constant value since the beam is monochromatic.

With the values of the magnetic rigidity ($B\rho$) and velocity (β), it is possible to compute the ratio A/Q according to equation 4.1.

Given the velocity and the total deposited (kinetic) energy E_k, it is possible to extract the mass of the ion with the relativistic expression:

$$E = E_k + m_0 = \gamma m_0 c^2 \Longrightarrow m_0 = \frac{E_k}{(\gamma - 1)c^2}$$

Which expressed in atomic mass units can be converted to:

$$A = \frac{E_k}{(\gamma - 1)u} \quad \text{where} \quad u = 931.494\text{MeV}/c^2 \tag{4.9}$$

The value of total energy needs to be coherent with the measured velocity (β), on which depends the Lorentz factor γ. The velocity β depends on the time of flight measured by the MWPPAC, while the total energy depends on the ionization chamber. However, between the two detectors, the ion experiences an energy loss in the drift chambers, and, as a consequence, the two values of E_k and γ are not completely coherent. In order to correct for this aspect, it is necessary to compute the amount of energy not measured between the two detectors with the aid of a Monte Carlo simulation, as described in subsection 5.1.2. The amount of lost energy is estimated through its linear dependence on the energy deposited in the first layer of the ionization chamber.

Combining the trajectory reconstruction (subsection 4.3.4) for the extrapolation of the magnetic rigidity with the velocity vector, equation 4.1 allows the measurement of the ratio A/q, which is completely independent of the ionization chamber data.

The charge state can then be found as the ratio of $A/(A/q)$ referring to equations 4.1 and 4.9.

4.3.5.1 A/Q Optimization

The ratio A/Q depends on the time of flight of the fragment and on the $B\rho$ reconstruction, as shown in equation 4.1 and in particular depends on the time of flight measured by the MWPPAC. This focal-plane detector is composed of multiple wire sections and each is characterized by an intrinsic offset $Offs$ (cf. equation 4.8) that can vary with respect to the nearby wires.

Since the wires are placed along the x-axis direction (in the dispersion plane of the spectrometer), a dependence of A/Q with respect to the focal-plane x position can be observed in Figure 4.11a. The A/Q values are not perfectly aligned with the expected values of the charge states of the beam ($A = 46$, $Q = [18, 14]$). As a consequence, it is possible to introduce a shift on the value of the offset dependent on the MWPPAC wire which has triggered. Figure 4.11b shows the effect of this optimization. Nevertheless, a further deviation is present in the comparison between the expected A/Q value as a function of the position on the dispersion plane. This aberration is likely due to small deviations in the $Path$ reconstruction. Once again, it is possible to introduce a focal plane position-dependent correction to align the A/Q states to the correct values, as shown in Figure 4.11c. The applied correction was implemented with a spline of third-degree polynomials that quantified the amount of shift in the $Path$ variable as a function of the dispersion plane position.

The same dependence of the deviation upon the focal plane position was not observed in the y-axis direction, where in the totality of the y focal plane acceptance, the mean of the point corresponded to the expected value.

While the correction has been extracted by computing the profile of the beam charge states, the same values of shifts are also valid in the case of $Z = 19$ reaction fragments, as shown in Figure 4.12. The A/Q values appear aligned, and no systematic trend is present.

4.3.5.2 Further Optimizations

If the charge state Q and the mass of an ion M are both identified, it is possible to compute the (kinetic) energy E_k from its magnetic rigidity ($B\rho$) with the following expression:

$$E_k = \sqrt{\left(\frac{B\rho c}{Q}\right)^2 + M^2} - M$$

It is expected that the energy computed from the $B\rho$ value and the energy measured by the ionization chamber E_{IC} summed with the non-measured energy $E_{n.m.}$ should coincide with the energy measured with the previous $B\rho$ expression.

By considering the $Q = 17$ charge state of the ^{46}Ar beam, a linear correction was applied to the total energy ($E_{IC} + E_{n.m.}$) with the following expression:

$$E = (E_{IC} + E_{n.m.})\, p_1 + p_0 \tag{4.10}$$

It is possible to observe a time dependence of the charge state and the mass of the ion. This is likely due to slight fluctuations of the pressure of the chamber

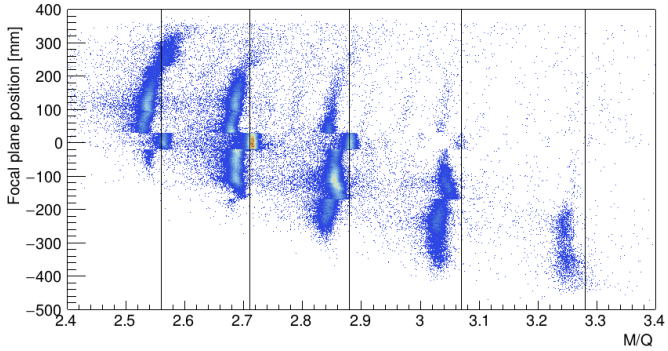

(a) Correlation between focal plane x position and A/Q with no corrections applied.

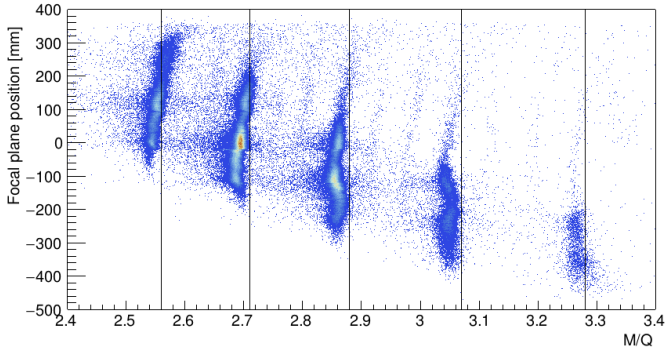

(b) Correlation after the MWPPAC time offset shift.

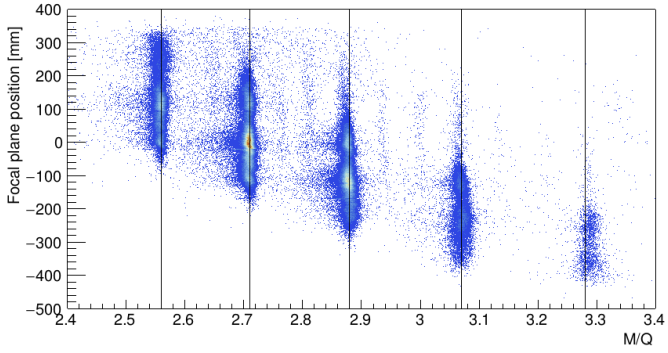

(c) Correlation with x-focal plane position dependent correction on the *Path* value

Figure 4.11: Aberration in the A/Q values dependent on the dispersion focal plane position (x-axis) in different stages of the corrections applied. No selection in atomic number Z has been applied for the current plot.

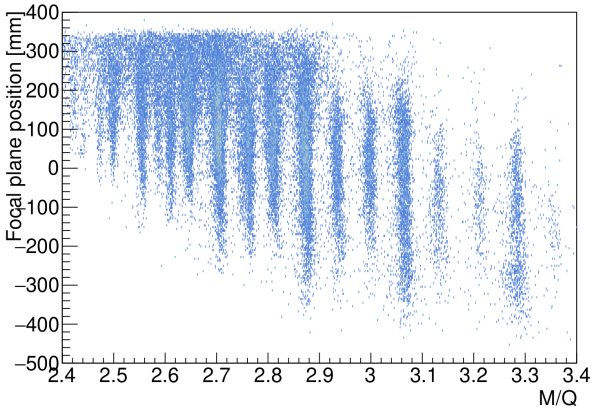

Figure 4.12: Correlation graph between A/Q values with selected atomic number $Z = 19$ after the correction procedure. No systematic trend is evident.

over time which in turn causes a broadening of the mass and charge state peaks. A time-dependent shift has been introduced in the total energy of the ionization chamber to minimize this effect. Figure 4.13 shows the successful effect of the procedure.

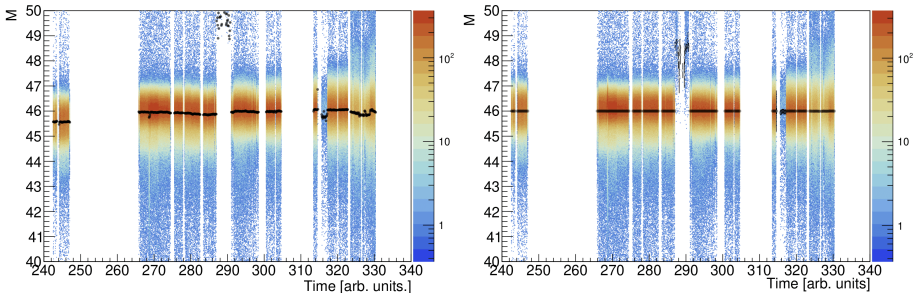

Figure 4.13: Mass for the atomic number $Z = 18$ as a function of time before and after the alignment.

4.3.6 Charge State Distribution

The energies involved in the experiment, between 9 MeV/u and 5 MeV/u, do not guarantee a fully stripped ion, and a charge state distribution is expected as the ion crosses the material layers. While the ^{46}Ar ion is delivered to the experimental hall with a 9^+ charge state, this value quickly increases as layers of material are crossed.

The effect of a charge state distribution on the data is related to the $B\rho$ acceptance of the spectrometer, which is discussed more in detail in the simulation subsection 5.2.7. A wide charge state distribution has a negative effect on the acceptance of the spectrometer as it increases the $B\rho$ spread of the reaction fragments of interest. Nevertheless, a broad distribution is typical of isotopes much higher in mass compared to ^{47}K and ^{46}Ar.

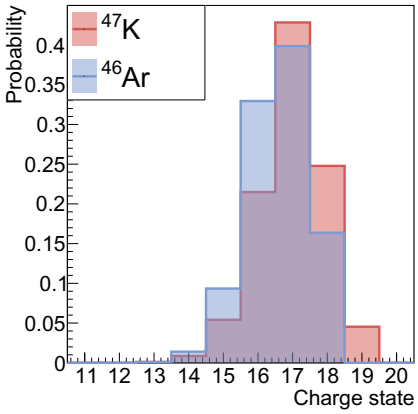

Figure 4.14: Charge state distribution measured for ^{46}Ar (in blue) and ^{47}K (in red).

Figure 4.14 shows the measured distribution for both ^{46}Ar and ^{47}K. While 17^+ charge state is the most prominent state in both cases, it is clear that most of the statistics are contained within a few charge states, making the impact on the overall acceptance minimal.

The high acceptance of the spectrometer, together with a combination of similar $B\rho$ values for the ^{47}K reaction fragments as well as the beam, allows the detection of the majority of the events. The efficiency figure in excess of 99% estimated from the Monte Carlo simulation (section 5.2) is relative to the focal plane detectors and does not consist in an absolute value.

4.3.7 Event Selection

Every event in the magnetic spectrometer is selected with a graphical cut in the ΔE versus E matrix shown in Figure 4.10. An event is associated with a given Z value if it occurs within the 2-dimensional cut on the correlation matrix of partial and total energy.

A further selection with graphical cuts is then performed in the charge versus mass-over-charge matrix (Figure 4.15), where the selections are placed in correspondence with the peaks relative to different values of the charge state and their A/q ratio. This methodology has been considered advantageous as it helps to reduce contamination from nearby peaks and takes advantage of the

limited dataset of produced isotopes. The reduction in contamination is justified by the fact that the selection is performed in two dimensions and follows the features of the matrix in Figure 4.15. A one-dimensional selection would also produce an unwanted increase in the overlap of the tails of the distributions.

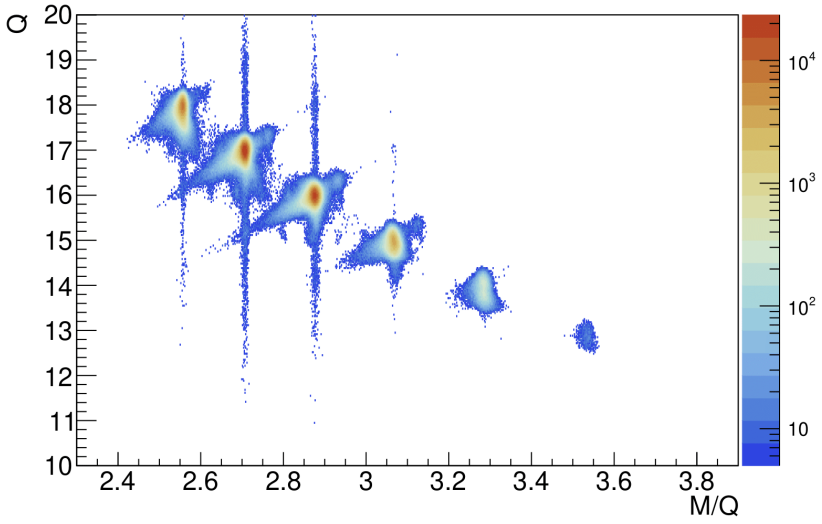

(a) $Z = 18$

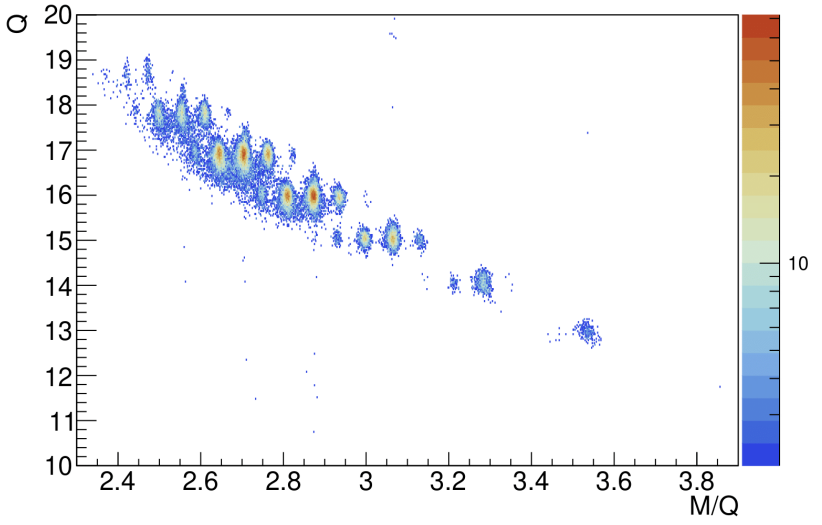

(b) $Z = 19$

Figure 4.15: Matrix of mass over charge state (x-axis) and charge state (y-axis) with different selections in atomic number (Z). $Z = 18$ corresponding to argon (top panel) and $Z = 19$, corresponding to potassium (bottom panel).

4.4 HeCTOr: The Cryogenic Target

The cryogenic target [7] (HeCTOr, the ^{3}He Cryogenic Target of Orsay) has been developed to allow the study of direct reactions in inverse kinematics with weak radioactive beams. It is able to cool the gas contained in its closed loop down to temperatures around $(5-6)$ K and achieve an overall effective thickness of $\approx 10^{20}$ atoms/cm^2.

The cooled gas is contained within two 3.8 μm thick Havar [5] windows in a target cell exposed to the beam and placed in the reaction chamber 25 mm behind the nominal target position. The target cell, shown in Figure 4.16 consists of a solid copper support with a conic flange characterized by a 130° aperture and a diameter of 16 mm of the smaller base.

The pressure can be set to a maximum of 1 bar, which causes a measured transverse deformation of the Havar containment windows of 0.7 mm at room temperature.

The gas contained in the target circulates in a closed-loop system while the refrigerating medium consists of Liquid Helium (LHe), which is injected in the upper part of the cryostat and reaches the target cell by means of gravity. An additional thermal shield, cooled to liquid nitrogen temperatures, is placed before the cold surfaces to decrease the overall LHe consumption.

Figure 4.16: Picture of the copper target cell. The aperture cone faces backward angles towards the beam. A thermal shield is placed around the structure to offer insulation from the radiated heat from the surroundings. Figure adapted from reference [7].

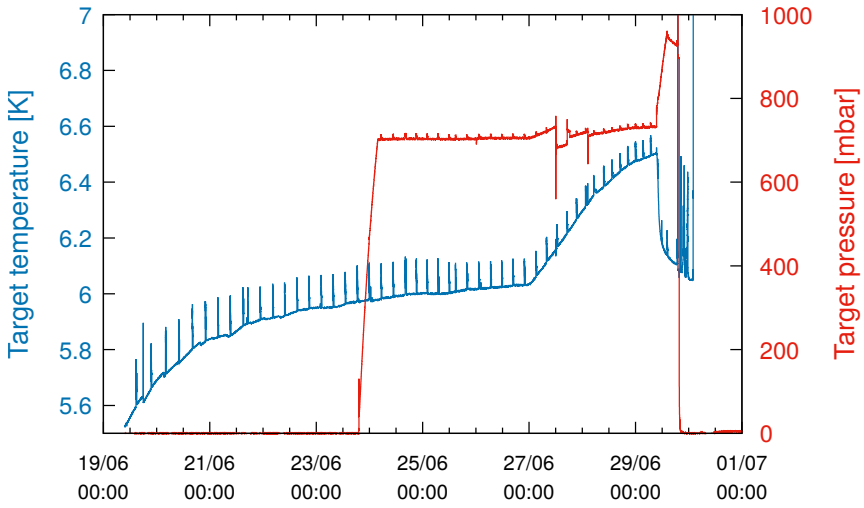

Figure 4.17: Temperature and pressure in the cryogenic target over time, the fast increase in pressure corresponds to the filling of the target. The average pressure achieved was 705 mbar and remained constant during the experiment. Spikes observable in the temperature value correspond to the cyclic filling of the refrigerating ^{4}He.

4.4.1 The Deformation of the Target

The deformation of the target occurs as a response to the pressure difference between the contained ^{3}He and the reaction chamber vacuum. Using the material properties of Havar and the (circular) boundary conditions of the surface, it is possible to compute the predicted deformation given a pressure difference and the radius of the support. Exploiting the results in reference [20], it is possible to compute a deformation profile given the known experimental conditions.

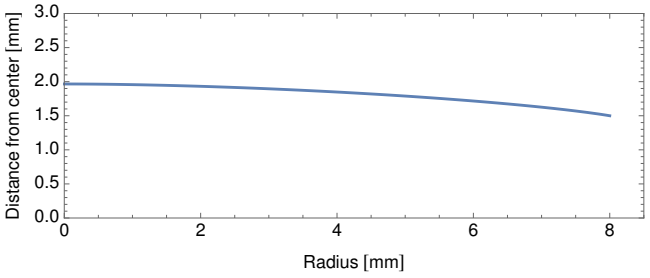

Figure 4.18: Target deformation profile, with a pressure of 700 mbar.

The membrane deformation model aims at finding a map between a two

dimensional un-deformed body Ω (in $\mathcal{R}^2$) into a manifold in $\mathcal{R}^3$:

$$\Phi(\Omega) : \mathcal{R}^2 \longrightarrow \mathcal{R}^3$$

The relation between the differential pressure p_0, the Cauchy stress tensor T and the unit normal to the surface $\hat{m}$ is given by the equation [20]:

$$-p_0\hat{m} = \nabla \cdot T \tag{4.11}$$

Exploiting the symmetry of the system, it is possible to assign polar coordinates to the original un-deformed surface Ω and cylindrical coordinates of the deformed surface. In the case of small deformations, the model can be further simplified by considering a linear mapping of the strain tensor to the stress tensor T.

The following expansion parameter ϵ related to the strain can be defined [20]:

$$\varepsilon = \frac{\left(1-\nu^2\right) R\, p_0}{Y\, h} \tag{4.12}$$

Where the symbols appearing in the equation and the adopted values are:

- h is the membrane thickness ($3.8 \cdot 10^{-3}$ mm)
- p_0 is the pressure differential ($7.0 \cdot 10^4$ Pa)
- R the boundary radius (8 mm)
- ν the Poisson's ratio (0.28)
- Y the elastic modulus in tension ($2.10 \cdot 10^1 1$ Pa)

The final value of the expansion parameter is small ($\epsilon = 6.8 \cdot 10^{-4}$), thus justifying the procedure of approximation.

A fractional expansion in terms of ϵ of the coordinates mapping is necessary due to the fact that the deformation perpendicular to the plane is of a different order ($O(\varepsilon)$) compared to the deformation within the plane. The 1/3 fractional exponent is chosen by the authors of reference [20] for mathematical reasons.

$$\begin{aligned} r &= \rho + \varepsilon^{1/3} r_1 + \varepsilon^{2/3} r_2 + O(\varepsilon), \\ \theta &= \varphi + \varepsilon^{1/3}\theta_1 + \varepsilon^{2/3}\theta_2 + O(\varepsilon) \\ z &= \varepsilon^{1/3} z_1 + \varepsilon^{2/3} z_2 + O(\varepsilon) \end{aligned} \tag{4.13}$$

It is possible to prove that $r_1 = \theta_1 = 0$ which simplifies the previous transformation. Equation 4.11 translates to the following boundary value problem, which can be easily solved with dedicated software such as Mathematica [22].

$$\begin{cases} \frac{1}{\rho}\frac{d}{d\rho}\left[\rho\left(\frac{dr_2}{d\rho} + \nu\frac{r_2}{\rho} + \frac{1}{2}\left(\frac{dz_1}{d\rho}\right)^2\right)\right] - \frac{\nu}{\rho}\left(\frac{dr_2}{d\rho} + \frac{1}{2}\left(\frac{dz_1}{d\rho}\right)^2\right) - \frac{r_2}{\rho^2} = 0 \\ \frac{1}{\rho}\frac{d}{d\rho}\left[\rho\left(\frac{dz_1}{d\rho}\right)\left(\frac{dr_2}{d\rho} + \nu\frac{r_2}{\rho} + \frac{1}{2}\left(\frac{dz_1}{d\rho}\right)^2\right)\right] = -1 \end{cases} \tag{4.14}$$

The differential equation problem features the following conditions on the boundaries of the membrane and an additional condition on the symmetry of the system given by the gradient at the center of the membrane:

$$\begin{cases} r_2(1) & = 0 \\ z_1(1) & = 0 \\ \frac{dz_1}{d\rho}\Big|_0 & = 0 \\ r_2(0) & = 0 \end{cases} \tag{4.15}$$

Once a solution $\{r_1(\rho), z_1(\rho)\}$ has been found, the profile of the deformation can be simply found by the inverse of the transformation in equation 4.14.

Figure 4.18 shows the result of the calculation in the case of a set pressure of 700 mbar, as set during the experiment.

Setting a pressure of 1000 mbar on the model returns a maximum deformation of 0.7 mm, which is in full agreement with the deformation measured and quoted in reference [7].

A deformation translates into an increased thickness which is dependent on the angle of emission with respect to the target. In general, the effective thickness of the material that the ion crosses depends on the emission angle as the inverse of its cosine. This is no longer true in the case of a deformed target which presents an increased thickness for smaller angles relative to that of a *flat* target, as shown in Figure 4.19.

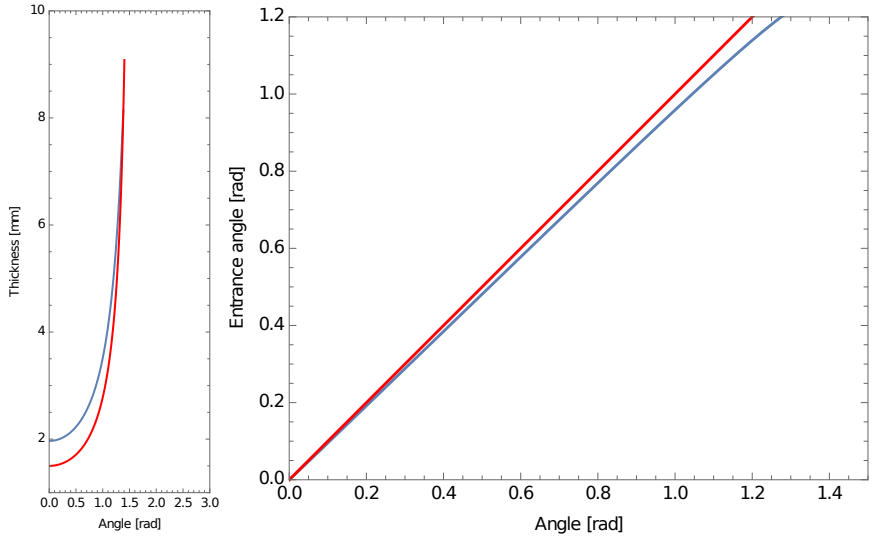

Figure 4.19: Effective thickness in ^{3}He as a function of the emission angle (left panel) and angle of entrance on the HAVAR window (right panel). In red the curve relative to a flat target and in blue a deformed target.

Another effect of the target deformation is that the entrance angle on the HAVAR windows is also different compared to the *flat* counterpart. This effect, shown in Figure 4.19, also affects the effective thickness of the ice deposition layer (cf. subsection 4.4.2).

These aspects, which imply a modification of ^{3}He gas, HAVAR, and ice crossed by the charged particles, have been accounted for using the measured data on the position of emission of the reaction fragment combined with the results of this deformation model.

4.4.2 The Ice Growth on the HAVAR Windows

The target itself, due to its many cold surfaces, acts as a cryogenic pump in the vacuum of the reaction chamber. The HAVAR containment windows have shown considerable ice deposition during the course of the experiment, consistent with a linear increase of about 22.5 μm per day in total.

This phenomenon could be closely monitored thanks to the presence of the spectrometer that returns a $B\rho$ value for the beam and can be used to extract an estimate of the ice thickness by measuring the energy loss of the beam as it passes through the target.

The evaluation of the ice growth in the course of the experiment is necessary to correct for the energy loss of the outgoing deuterons in the reaction kinematic calculations.

The ice layer can be thought of and analyzed as an additional layer with a thickness measured as described in the current subsection and with the same shape as the HAVAR window, being adherent to it.

Figure 4.20 shows the evolution of the magnetic rigidity ($B\rho$) during the experiment. The filling of the target cell is highlighted in the red shaded region, where a rapid decrease of the $B\rho$ value indicates an increase in thickness that can also be observed in Figure 4.17. A gradual and less rapid decrease in magnetic rigidity is also present in correspondence to a stable pressure in the remainder of the experiment as a result of ice growth.

4.5 The Beam Tracker: CATS2

The detector [13] consists of a low-pressure multiwire proportional chamber designed specifically for radioactive beams. Two cells with a common anode and an overall effective area of (70×70) mm^2 are present. The anode is composed of $10 - \mu$m-thick golden tungsten wires spaced 1 mm apart that contribute to the low 1% opacity of the system.

The wires are polarized at a tension of 800 V and located between two perpendicularly segmented cathode planes at a distance of 3.2 mm. The cathodes are made up of 28 strips of evaporated gold on $1.5 - \mu$m-thick Mylar with a thickness of 200 nm, a pitch of 2.54 mm, and an inter-strip of 0.2 mm.

Additional supporting Mylar foils are placed on each side of the beam tracker for additional support.

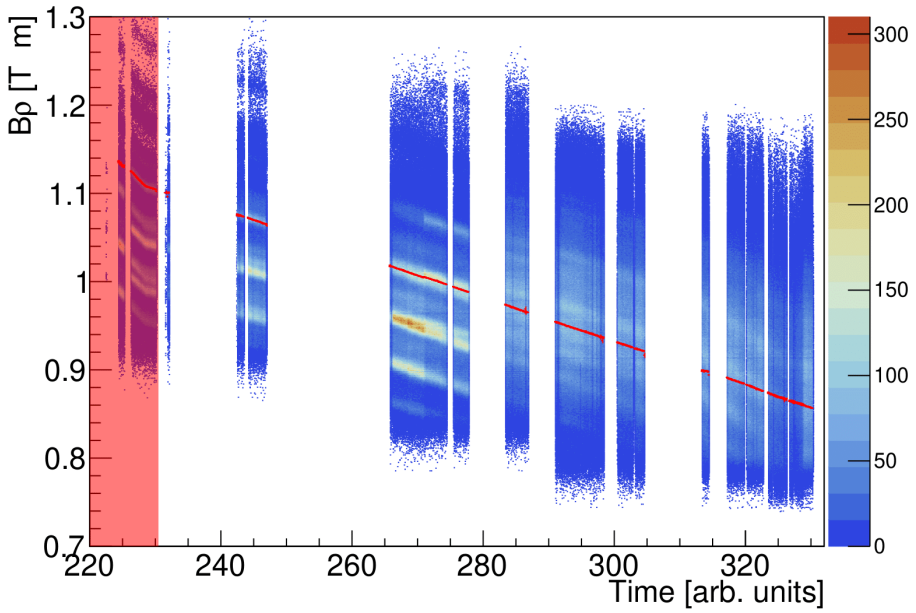

Figure 4.20: Magnetic rigidity ($B\rho$) evolution over time. The shaded region represents the filling of the ^{3}He target, while the remaining portion of the graph represents the progression of the experiment. The superimposed red line represents the value relative to the beam ions with charge state $Q = 16$.

The detector is filled with pure isobutane (C_4H_{10}) to exploit its quenching properties and minimize the chances of the detector tripping due to higher rates.

The beam tracker is placed inline of the beam, 2.045 m before the nominal target position.

An additional tracker, placed at a distance of 0.5 m inline from the other one, can also be inserted. Their combination allows to obtain the direction of the incident ion to improve the kinematics reconstruction.

In this particular experiment, the second beam tracker was removed to limit the angular straggling, which would have hindered the performances of VAMOS.

4.5.1 Calibration and Performance

The gain on each strip, which is read out independently, is matched by injecting a pulser signal on the wires and aligning the collected charge to a reference.

Various position finding algorithms are available; however, the one used in the course of the analysis is the squared secant method, already mentioned in the subsection regarding the theory of operation of the drift chambers of VAMOS 4.3.2.

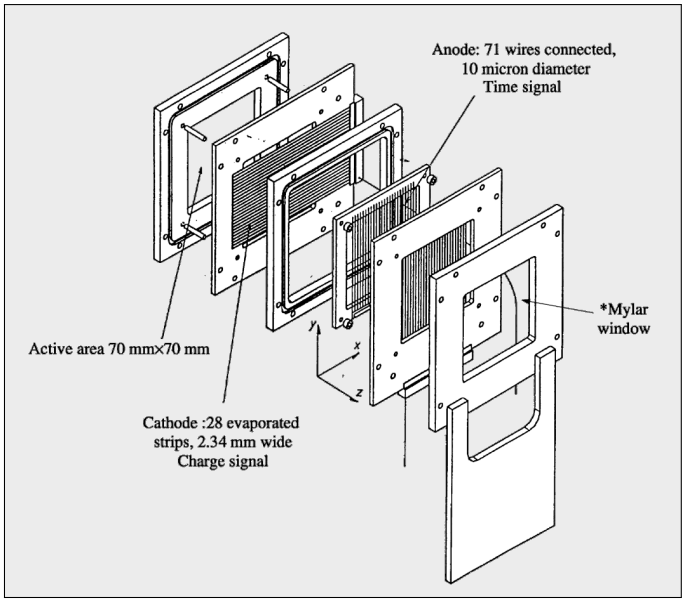

Figure 4.21: Schematic view of the beam tracking detector CATS2. Image adapted from reference [13]

The overall nominal resolution achieved is of 300 μm on the X direction and of 500 μm on the Y direction. In-beam tests show an $X(Y)$ position resolution of 240μm (390 μm) with a beam intensity of $1.6 \cdot 10^5$ pps which decreases to 440μm (750 μm) in the case of a higher counting rate of $1.4 \cdot 10^6$ pps. The counting rate throughout the experiment was maintained within the first intensity limit.

The timing information is obtained by the wire signals, the anode, and is expected to be in the order of 400 ps with an efficiency of virtually 100%.

A safe rate that can be sustained by the detector for long periods of time is around 10^5 pps.

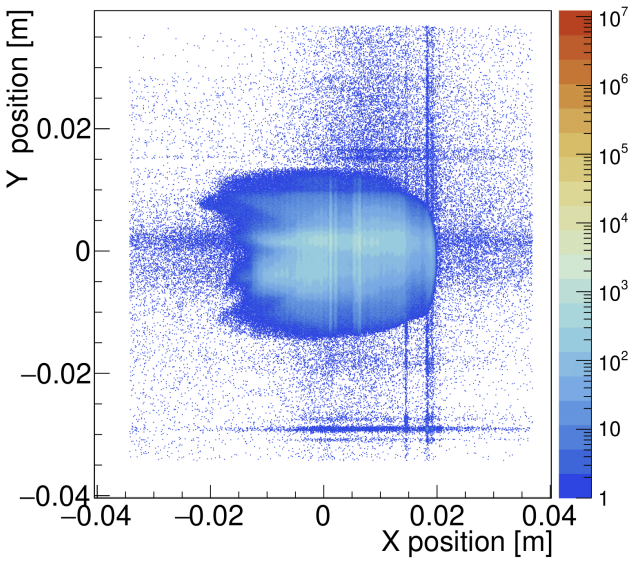

Figure 4.22: Beam profile on the CATS2 detector, placed 2.045 m before the nominal target position. All statistic is shown in the plot.

4.6 The MU(ST) GAS(PARD) T(RACE) (MUGAST) and MUST2 Detectors

4.6.1 MUGAST

The MUGAST project is the combination of the silicon detectors of a future array (GRIT) combined with the well-established electronics of MUST2 [14]. In total, around 3000 independent electronic channels need to be read out for the full detector, consisting of energy and time of all strips on both sides of the silicon detectors.

The array [2, 3] will be composed of a total of 8 square and 8 trapezoid Double-Sided Silicon Strip Detectors (DSSD), covering most of the backward portion of the solid angle of emission from the target. As shown in the technical drawing in Figure 4.24 and in the experimental data of Figure 4.23, the solid angle is covered by square (placed on the 90° ring) and trapezoid detectors (covering angles of 105° to 155° with respect to the forward beam direction). At last, a ring-shaped (annular) detector covers the most backward angles (159° to 2.95°).

The detectors are placed 130 mm from the target nominal position that differs from the cryogenic target position, as the latter is shifted by 25 mm in the beam direction and towards the magnetic spectrometer.

The trapezoid detectors are 500 − μm-thick Neutron-Transmutation Doped

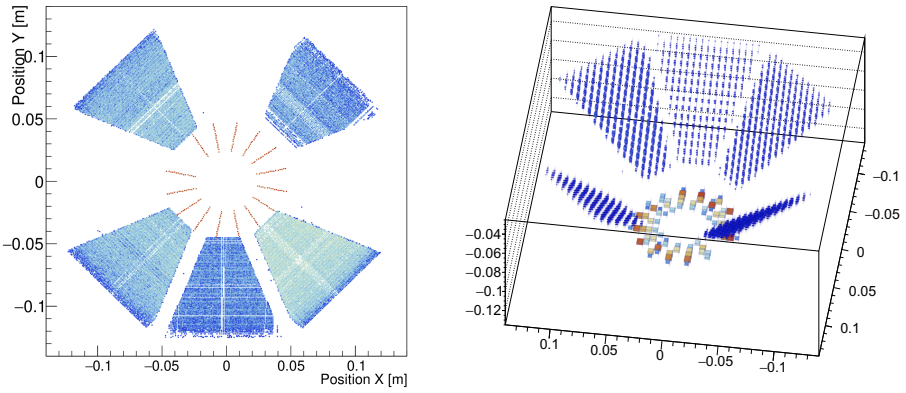

Figure 4.23: Graph of the hit pattern on the silicon detector in the course of the whole experiment. No particle gate has been applied. (left panel) x- and y-axis position. (right panel) Three-dimensional plot, bigger boxes indicate a higher amount of hits.

(NTD) silicon wafers with each side divided in 128 strips (710 μm (front) 760 μm (rear) pitch) perpendicular to each other. They are placed with the ohmic side facing the target to improve the performance of the pulse shape discrimination techniques.

The annular detector is a 500 μm thick float zone wafer divided into 4 quadrants with 16 rings on the junction side and 4 sectors on the ohmic side. The fine segmentation allows for an angular resolution of approximately 0.4° with respect to the nominal target position.

The electronics are placed along a ring-shaped support structure located at 90° with respect to the beam direction as shown in Figure 4.24. They consist of boards containing 9 ASICs and MUFEE boards each, with the capability of readout of 256 strips, corresponding to one entire detector[2]. The ASICs deliver a multiplexed stream of data combining energy time and leading-edge discriminator to the MUVI boards that allow the slow control and data processing of the detector.

Figure 4.23 shows the overall statistics as a function of the position of the whole array in the course of the experiment. It is possible to identify regions of missing strips that are more common for some detectors, such as trapezoid number 7. Another aspect worthy of note is the poor resolution in phi of the position of the annular detector if compared to the one achieved in theta. This aspect is related to the experimental interests in the sensitivity of the detector since an angular distribution is dependent only on the angle with respect to the beam trajectory.

MUST2[14], placed at forward angles in this particular configuration, is an array of four 300 μm DSSD detectors backed by 16 CsI crystals read by

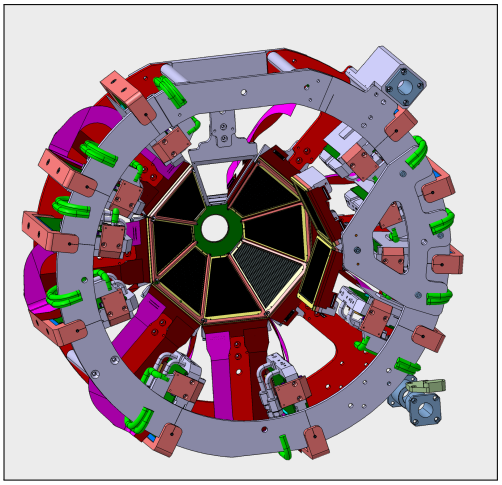

Figure 4.24: Technical drawing in 3D of the MUGAST detectors and the relative support structure placed at backward angles. The incoming beam passes through the annular detector pictured in green. Image adapted from reference [2].

photodiodes.

The combination of scintillators and thin position-sensitive silicon detectors allows for an accurate particle discrimination with the partial energy deposition procedure (ΔE vs E), similarly to the one performed in the ionization chamber of the magnetic spectrometer in subsection 4.3.3. The MUST 2 detector is placed at forward angles where the differential cross section of the reaction of interest is minimal. Additionally, fusion-evaporation reactions on the target materials cause the emission of light charged particles in the forward cone that overlaps with the angular coverage of MUST2. As a consequence, little information was extracted from the array in the analysis of the experiment. Additionally, while some ^{3}He ions are detected in MUST2, they do not align with the kinematic line of the elastic scattering reaction (^{46}Ar(^{3}He, ^{3}He)^{46}Ar). This is not surprising considering the reduced angular coverage of MUST2 near 90°, where the cross section of this reaction is maximized.

4.6.2 Energy Calibration

The energy calibration of the setup consists in the alignment of all 128 strips of both sides of the trapezoids and annular with an alpha source (in this case ^{239}Pu, ^{241}Am and ^{244}Cm whose energies are reported in table 4.2).

The strips are read out by the MUFEE boars that incorporate a 14 bit ADC. The total bit depth is shared between the two sides of the silicon detector. In particular, the first 2^{13} bits are reserved to the ohmic side (Y-strips, negative polarity), while the remaining 2^{13} ones are kept for the junction side (X-strips, positive polarity). The pedestals of all strips are therefore aligned to the channel

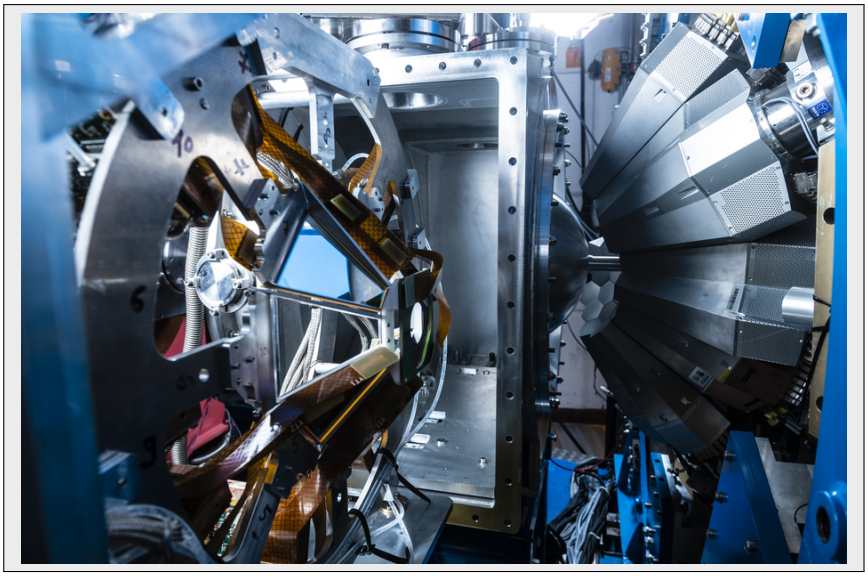

Figure 4.25: Picture of MUGAST while being mounted in the reaction chamber. Photo by ©P. Stroppa/CEA

Nuclei	**Energy (MeV)**	**Intensity**	Half-life (years)
^{239}Pu	5.15659(14)	70.77(14)	$2.411 \cdot 10^4$
	5.11443(8)	17.11(14)	
	5.1055(8)	11.94(14)	
^{241}Am	5.48556(12)	84.8(5)	432.2
	5.44280(13)	13.1(3)	
	5.38823(13)	1.66(2)	
^{244}Cm	5.80477(5)	76.40(12)	18.1
	5.76264(3)	23.60(12)	

Table 4.2: Triple alpha emission energies, intensities and half-lives.

number 8192 before the calibration procedure.

The peaks are fitted with Gaussian distributions that also include the satellite peaks. The reference value of the transition energy, shown in Table 4.2, is modified to account for the energy loss of the alpha particle in the 0.3μm aluminum dead-layer. A zero-extrapolation procedure is performed to align the zero energy value with the electronics pedestal by modifying the dead-layer thickness [11]. At last, a linear calibration is applied to the ADC channel value to obtain the reference energy value.

Figure 4.26 shows the calibration applied in the case of the 128 strips of

detector 1. Aside from the calibration, a re-mapping of the electronic channels is also performed in order to align adjacent strips with adjacent numbers.

The analysis procedure requires a match of 1 MeV between the energy measured on both layers in order to suppress spurious events. The final energy of each event consists of the calibrated value of the X-side of the silicon (junction side).

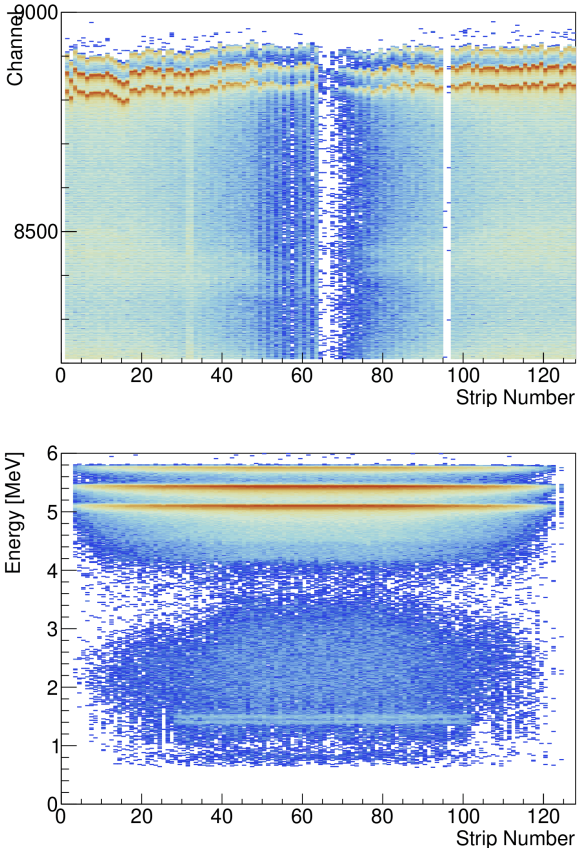

Figure 4.26: Spectra of MUGAST's trapezoid MG1 acquired with a triple-alpha source: ^{239}Pu, ^{241}Am and ^{244}Cm before (top panel) and after (bottom panel) the calibration. On the x axis are shown all the 128 X strips of the detector while the y axis shoes the amplitude of the signal (top panel) or the energy (bottom panel). Between the indexes of the strips is also present a mapping, as the first index given by the electronics is mapped to a new index which respects the spatial positioning of the strip.

Figure 4.27 shows the energy spectrum of the ^{241}Am peaks measured with the sum of all X-strips of detector 1. The total FWHM of 0.44 MeV, obtained

according to the resolution model in appendix B, is a good indication of the correct alignment of all strips. The resolution model consists of a Gaussian distribution convoluted with an exponential to account for losses in charge collection that generate a left tail on the peaks.

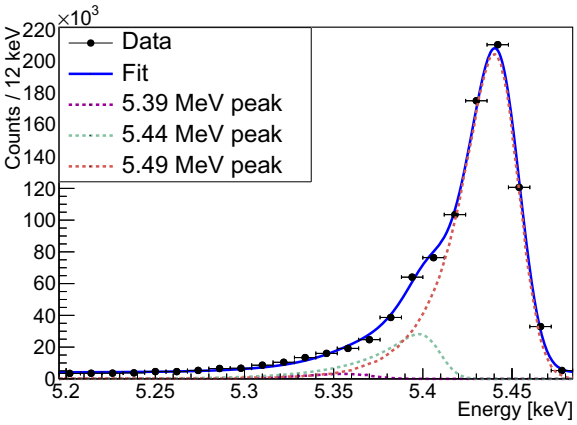

Figure 4.27: Fit of the energy spectrum of all X strips of MUGAST trapezoid MG1. The fit, performed according to the model in appendix B returned the following values $\tau = (3.227 \pm 0.007) \cdot 10^{-2}$MeV, $\sigma = (9.60 \pm 0.03) \cdot 10^{-3}$MeV which amount to FWHM=0.044 MeV. The energies of the triple alpha source are characterized in Table 4.2 and the peak is relative to ^{241}Am.

4.6.3 Time Calibration

The calibration of the silicon detectors in both energy and time is necessary to perform particle discrimination with the Energy Time-of-Flight method, which will be briefly illustrated in subsection 4.6.4.

The time calibration is performed with a time calibrator which injects a start and stop signal randomly at fixed intervals of $N \times \tau$. The value of N is a random integer, and the time value of $\tau = 20$ ns is chosen to span the whole TDC (Time to Digital Converter) range of 640 ns. The calibration fits the discretized peaks, separated by 20 ns and aligns them to the correct timing value with a second-order polynomial, as shown in Figure 4.28. The procedure calibrates the relative time but not the absolute value, which is sufficient for the particle identification procedure that will be discussed in subsection 4.6.4.

The operation is performed both on the X- and Y-axis strips so that the timing information can be obtained from both sides of the silicon detector.

The final time information in the analysis procedure is taken from the Y-strips side (ohmic side), which is facing the target and is first irradiated by the particles.

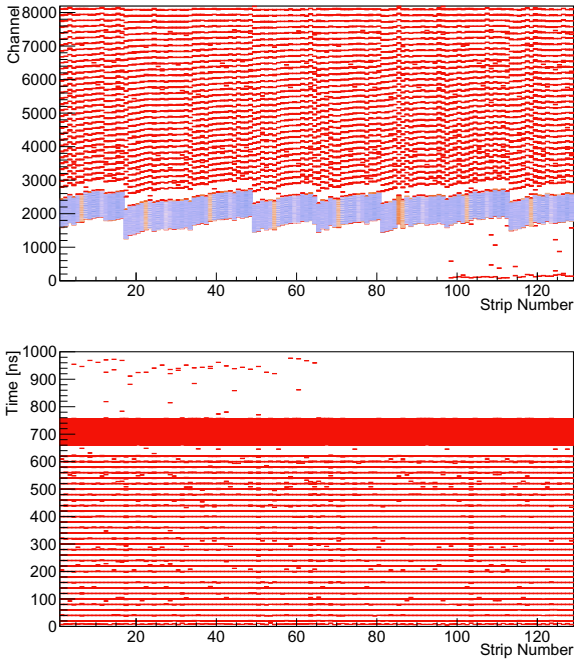

Figure 4.28: Strip-time calibration of MUGAST. Several start and stop signals are sent randomly and aligned to the correct time interval with a second-order polynomial function. The graph shows the result before (top panel) and after (bottom panel) the time alignment for each Y-axis strip of one of the trapezoids (MG1).

4.6.4 Particle Discrimination: Energy-Time of Flight Technique

Assuming that the flight path of the particle Δx to be a constant, the relation between kinetic energy E_k and time of flight Δt of a particle of mass m_0 is the following:

$$E_k(m_0; \Delta t) = \frac{m_0}{\sqrt{1 - (\Delta x/\Delta t))^2}} - m_0$$

The Time Of Flight (TOF) is measured with a calibrated Time to Amplitude Converter (TAC) with a start given by MUGAST and the stop obtained by the delayed signal of CATS2. As a consequence, the total time between start and stop is correlated to the time of flight of the ion with the simple equation $\Delta t = delay - TOF$. Additionally, the constant $delay$ contains not only the signal delay set but also the (constant) time of flight of the beam ions from the beam tracker to the target position. The energy dependence of the E-TOF curve follows the relation:

$$disc(m_0) = E_k(m_0; delay - TAC) \quad \text{with } \Delta t > 0$$

and can be seen for different masses in Figure (4.29). In practice, different particles are discriminated on the basis of this correlation between time and energy. The main limitations of this procedure consist in the overall time and energy resolution and the possible overlap of different particles in the punch-through region at large energies.

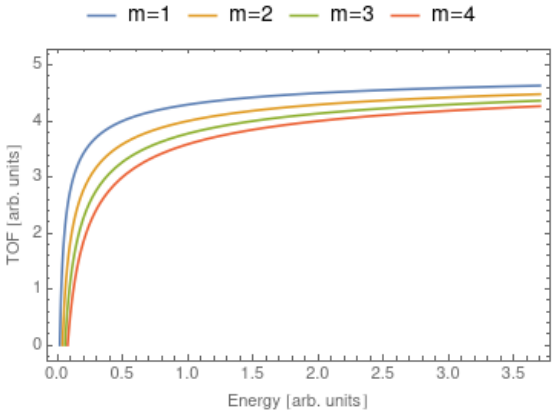

Figure 4.29: Example of particle discrimination based on time of flight and energy measurement, shown in the cases of masses multiples of and arbitrary mass of 1.

Due to the time walk of the start signal given by the silicon detector, there exists a further correlation between energy and time of flight which deviates the measure E-TOF curve from the theoretical shape in Figure 4.29. As a consequence, the experimental curve cannot be directly compared to the theoretical one shown in the figure.

Figure 4.30 shows the energy time-of-flight selection of trapezoid 4 and the annular detector. The black dots in the figure represent all the acquired statistics in the course of the experiment. Three lines are present and correspond to the detection of protons, deuterons, and alpha particles. Most of the statistics are associated with the detection of protons emitted from the deuteron breakup channel or fusion-evaporation reactions.

Fusion-evaporation reactions occur on heavy elements contained in the HAVAR windows where elements such as cobalt and other metals are present. On the other hand, fusion-evaporation on the light components of the target, such as ^{3}He and the ice deposition, is rarely associated with the emission of light particles at backward angles due to the significant Lorentz boost in the kinematics. Due to the high statistics acquired for protons in comparison to the other particles, a considerable amount of these particles is present in the punch-through tail of the distribution.

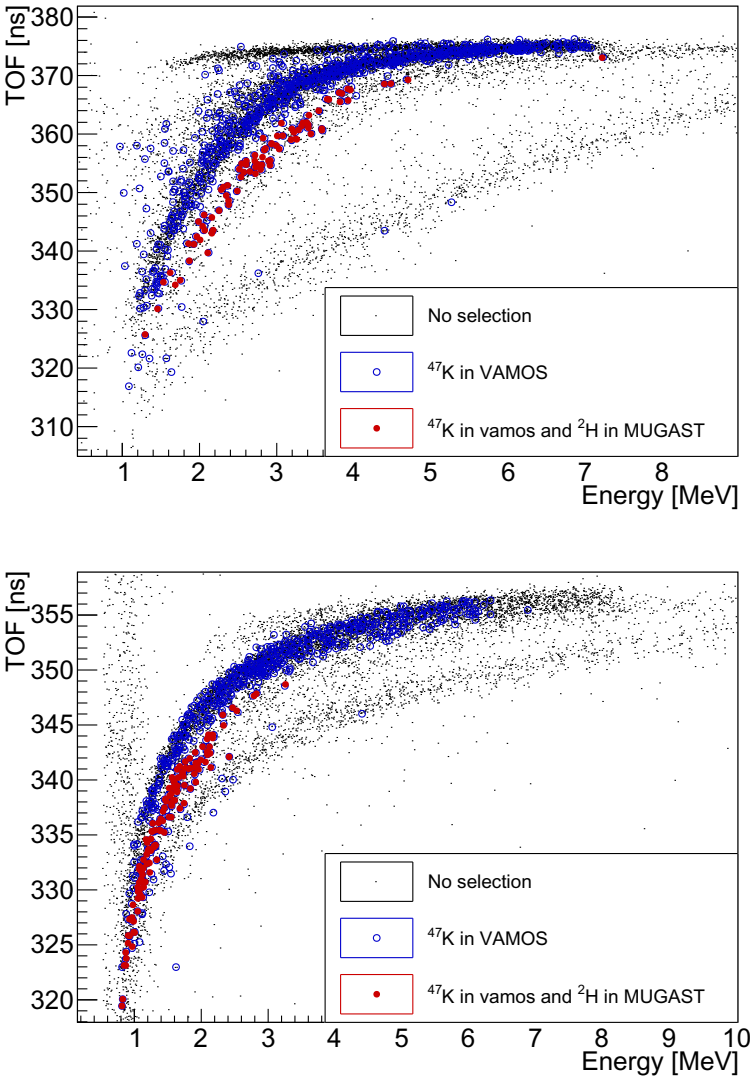

Figure 4.30: Energy time-of-flight for the MUGAST trapezoid number 4 with angular coverage $[117° - 160°]$ (top panel) and the annular detector with angular coverage $[163° - 171°]$ (bottom panel). The graph shows the whole acquired statistics in the case of no event selection (black dots), with a selection of ^{47}K in VAMOS (blue circles) and selecting also deuterons in MUGAST (solid red circles).

Only protons and deuterons are clearly present with the condition of the detection of ^{47}K in VAMOS in Figure 4.30.

Other significant considerations can be made regarding the average and the maximum energies of both light particles. In particular, a two-body reaction associates to an angle of emission a definite energy in the laboratory frame of reference. While the energy measured by the silicon detector is affected by the emission-angle dependent energy loss, a correlation between angle and energy offers an indication of this kind of reaction.

Compared to the case without any selection, protons in coincidence with VAMOS are always fully stopped in the silicon detector (no punch-through tail is present) in the trapezoids and are limited to a maximum energy of about 6.5 MeV in the annular detector that is placed at more backward angles. While deuterons are emitted with a seemingly continuous distribution in the case of no selection on the spectrometer, once the condition on the reaction fragment of interest is applied, the maximum energy is limited to ≈ 4.2 MeV in the case of the trapezoids and ≈ 2.5 MeV in the case of the annular. Another aspect that further supports this argument is the lower average energy of deuterons detected in the annular detector in comparison to the trapezoids, which corresponds to angles, in the laboratory, closer to 180°.

4.6.5 Energy Loss Correction

While the energy shown in Figure 4.30 consists of the energy measured by the silicon detector, in order to reconstruct the kinematics, it is necessary to recover the energy after the reaction and before all the energy losses in the target. In order to operate an energy loss reconstruction, it is essential to know the amount of material crossed by the charged particle. Figure 4.19 shows how the amount of ^{3}He is strongly dependent on the emission direction, as well as how the angle of incidence is affected by a deformed target which, in turn, changes the effective thickness that the ion crosses in the window and in the ice layer.

The energy loss process, as introduced in Section 4.3.3.1, is a stochastic process: as a consequence, there is no one-to-one correspondence between the energy before and after the material layer. Given a definied initial value, the energy after the crossed layer will be characterized by a probability distribution that has a well-defined mean and a width (variance) which increases as the layer thickness expands. As a consequence, the best effort in correcting for energy losses will consist in adding the average energy loss after having computed the material thickness according to the target deformation profile and the angle of entrance in the window. It is, however, impossible to correct for the significant energy straggling due to the variance of the distribution.

The energy before and after the correction is presented in Figure 4.31 as a function of the angle of emission. The average energy increases while the distribution appears more compact.

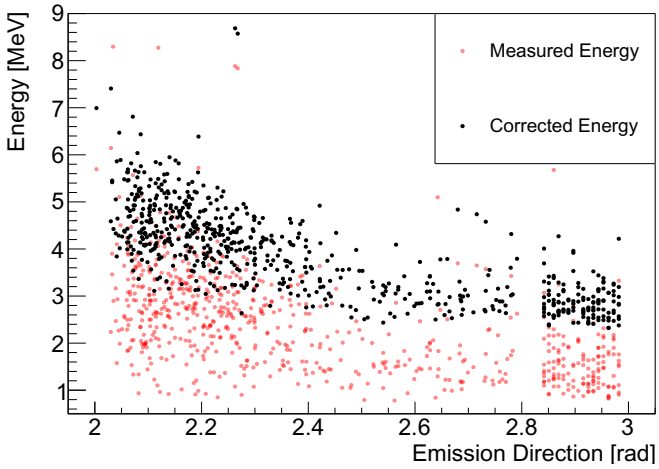

Figure 4.31: Deuteron energy before and after the energy loss correction as a function of the angle of emission. The calculations are based on the considerations made on the shape of the target in subsection 4.4.1.

4.7 The Gamma-Ray Detector: AGATA

The AGATA (Advanced GAmma Tracking Array) detector [1] consists of a state-of-the-art γ-ray tracking array composed of High Purity Germanium (HPGe) crystals.

Its peculiarity is the ability to estimate the position of interaction of the photon within 4 mm [1] by relying on the pulse shape measured by its electrically segmented anodes. This allows the exploitation of γ-ray tracking algorithms that are able to reconstruct γ ray scattering Compton events, thus reducing the background and increasing the overall efficiency. The detector is widely considered the next technological evolution compared to the previous generation of γ-ray detectors that rely on scintillators surrounding each germanium detector to suppress the background caused by Compton events. While a tracking array aims at reconstructing events with multiple interactions, a Compton suppressed detector vetoes any event with a germanium-scintillator time coincidence. In the case of AGATA, the overall efficiency per solid angle is increased by the removal of the Compton shields and the substitution with sensitive HPGe material. Other advantages include an improvement of the Doppler correction capability due to the high resolution of the position of interaction figure and all the benefits derived from the position sensitivity. Moreover, the high degree of segmentation could allow achieving a higher counting rate compared to conventional detectors of comparable size.

Figure 4.32 shows the detector in the honeycomb support structure for the configuration during the experimental campaign of 2019 in GANIL.

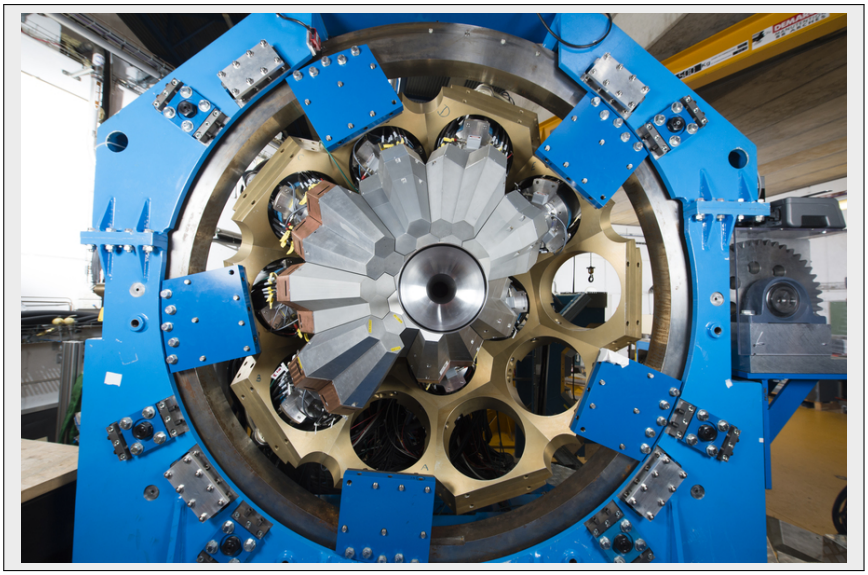

Figure 4.32: Picture of the AGATA tracking- HPGe γ-ray detector. Photo by ©P. Stroppa/CEA

All germanium crystals are arranged in triple clusters that share a common flange and liquid Nitrogen Dewar. Each crystal is segmented radially and longitudinally in 6 sectors, for a total of 36 sectors each. A common central contact is present in the center of the semiconductor crystal. All segments differ in shape due to the geometry of the detector, as shown in Figure 4.33.

The position reconstruction algorithm is based on a pulse shape analysis (PSA) procedure which minimizes the discrepancy between the signals measured in each segment and a basis of signals which associates to a position of interaction a set of signals in each segment. Figure 4.34 shows the sensitivity of normalized signals to the position of interaction of the γ ray. Discriminating features are the difference in drift time between electrons and holes that cause a difference in slope of the charge collection, as well as a kink in the signal rise curve whose position is dependent on the distance between the interaction point and the collection anode (cathode). Another source of discrimination between different positions of interaction is due to the charge induced in the neighboring segments, which is higher for interactions segments closer to the point of interaction. A grid search of a figure of merit (χ^2) computed from the energy-normalized signal and the signal bases is able to achieve a remarkable position resolution of ≈ 4 mm [21].

A total of 39 crystals were fully operational during the experiment, for a total of 13 triple clusters and one double cluster, amounting to only two detectors that were mounted but not operating correctly.

The coupling of the AGATA detector, which exploits the GTS trigger and synchronization system (cf. [1]), with the remaining detectors, relies on the

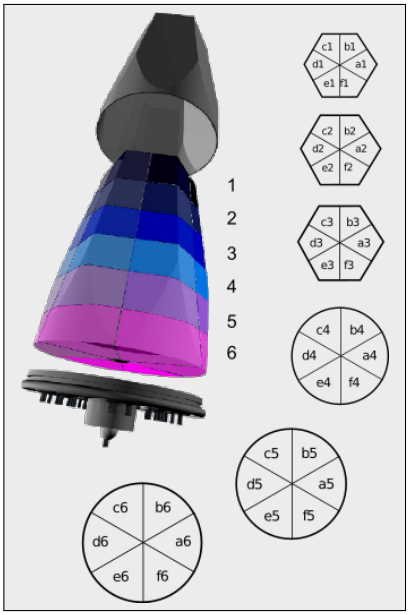

Figure 4.33: Segmentation of one HPGe crystal in different segments. Figure adapted from reference [1].

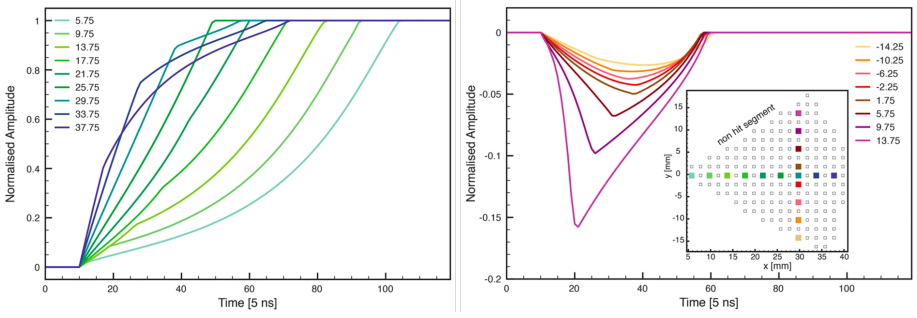

Figure 4.34: Signals simulated for a segment located 40.25 mm from the front face. The graph shows the core signal (left panel) of the hit segment and the and the charge-induced signal on a the neighboring segment (right panel). Figure adapted from reference [4]

AGAVA (AGATA VME Adapter) interface. As a consequence, the array can operate in *standalone mode* allowing the measurement of any γ-ray event in the course of the experiment, without any trigger request from the ancillary detectors. This trigger condition was chosen in the case of the present experiment due to the low intensity of the radioactive beam and overall reduced background. A coincidence (prompt) event of AGATA and any of the ancillaries must have a condition on the difference of the AGATA time stamp and that of the AGAVA module. Figure 4.35 shows the difference in timestamps of the AGATA and the ancillaries. A condition must be set on the difference of timestamps according to the coincidence peak to ensure proper prompt events. The timing condition, shown in Figure 4.35 is a 100 ns window.

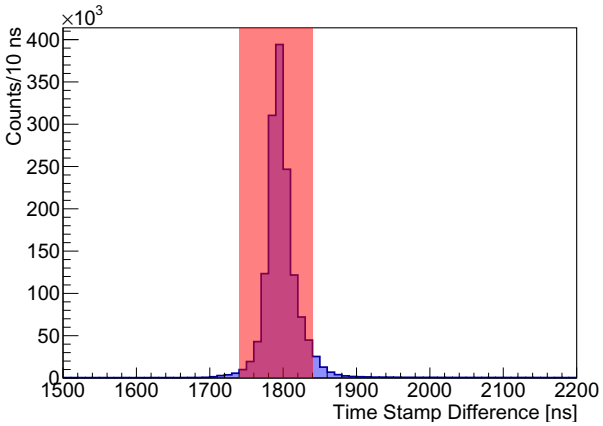

Figure 4.35: Coincidence peak of AGATA with the ancillary detectors, with the red shaded region correspollnding to the gate window of 100 ns.

4.7.1 Detector Calibration

The calibration of the array demands the energy alignment of the 36 segments and the central contact (core) of each HPGe crystal. The calibration of all segments requires a considerable amount of statistics if compared to the core spectra due to their limited spatial size. As a consequence, the segments were calibrated with a ^{60}Co source. The core spectra, characterized by higher efficiency, allowed the calibration to be performed with a ^{152}Eu source.

In this experiment, the low energy of the γ rays of interest, only 360 keV, makes the use of the tracking algorithm not necessary as Compton scattering in crystals far from each other is unlikely. The optimal choice resides on the add-back procedure, where the energy measured by the core of neighboring crystals is added together, and the position of the incoming γ ray is chosen as the one relative to the most energetic hit. The add-back procedure also has

the added benefit of a straightforward efficiency estimation through the Geant4 simulations (an aspect which is treated in section 5.3).

Figure 4.36 shows the ^{152}Eu source spectra produced by each core after the calibration procedure. Each crystal appears well aligned and the performance of the array in terms of resolution in the energy region of interest around 360 keV appears satisfactory.

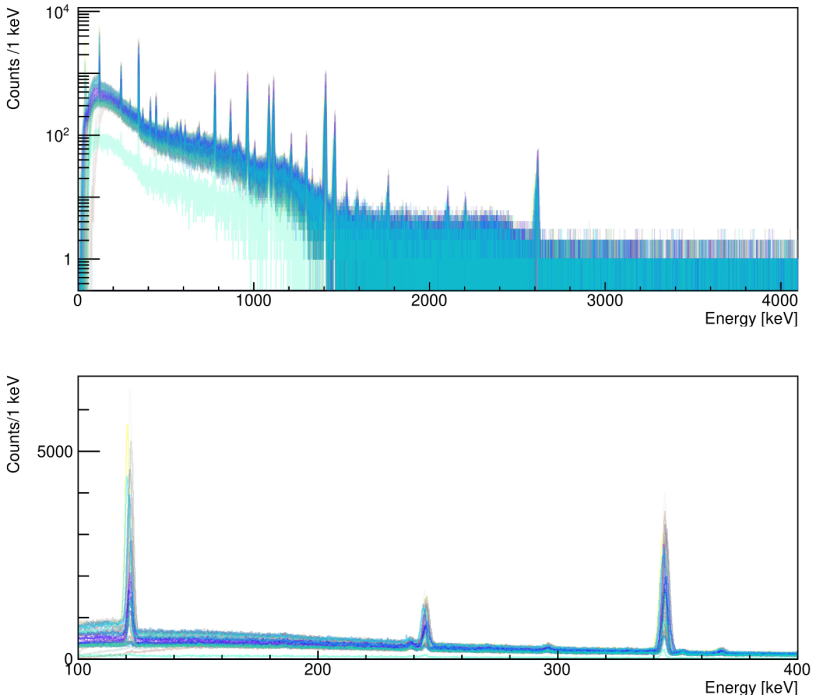

Figure 4.36: Calibrated core spectrum of a source of ^{152}Eu source placed 85 mm behind the target position of all detectors present. The full range (top panel) and the energy region of interest around 360 keV (bottom panel) are shown. The Europium lines appear well matched in all crystals.

Since the detector was operating in standalone mode, in the course of the whole experiment, many γ rays originated from the decay chain of ^{46}Ar isotopes implanted in the reaction chamber were observed. Figure 4.37 shows the final spectrum acquired and Figure 4.38 the hit pattern with all operational crystals.

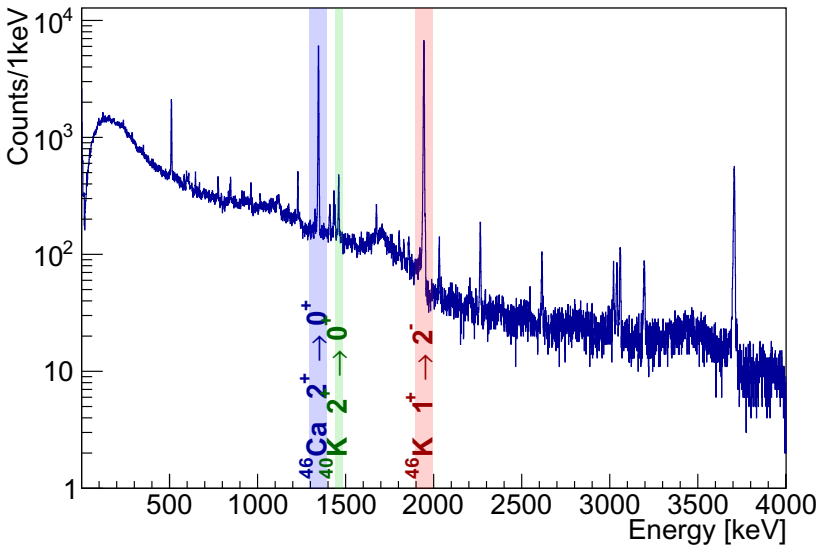

Figure 4.37: Total spectrum acquired in the course of the experiment in standalone mode. Peaks observed correspond to the decay chain of ^{46}Ar due to implantation in the reaction chamber.

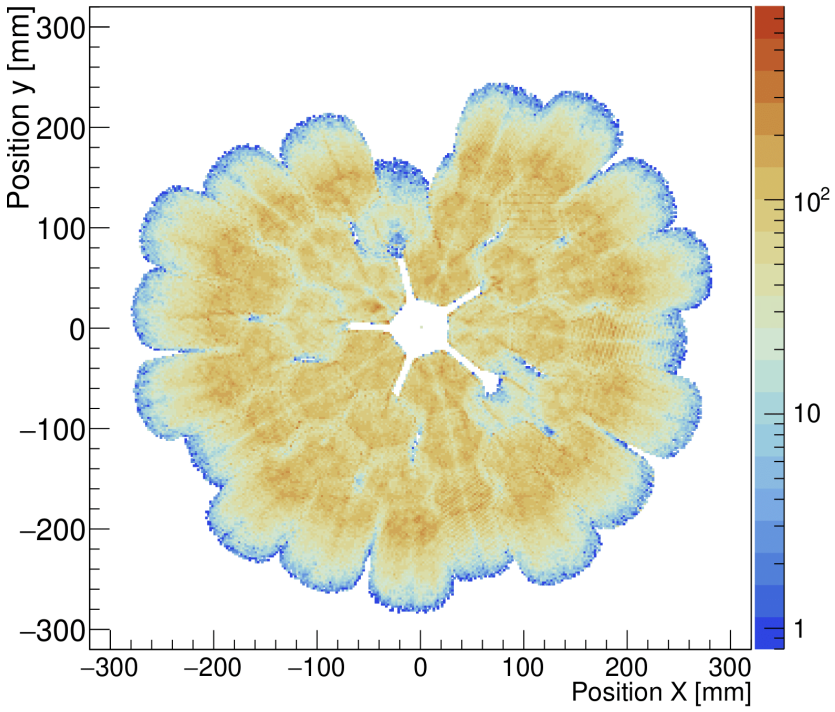

Figure 4.38: Hit pattern on the HPGe tracking array in the course of the whole experiment, showing the solid angle covered by the operational crystals.

Bibliography

[1] Akkoyun, S. et al. "AGATA—Advanced GAmma Tracking Array". In: *Nuclear Instruments and Methods in Physics Research Section A: Accelerators, Spectrometers, Detectors and Associated Equipment* vol. 668 (Mar. 2012), pp. 26–58. DOI: 10.1016/j.nima.2011.11.081. URL: https://doi.org/10.1016/j.nima.2011.11.081.

[2] Assié, M. et al. "The MUGAST-AGATA-VAMOS campaign: Set-up and performances". In: *Nuclear Instruments and Methods in Physics Research Section A: Accelerators, Spectrometers, Detectors and Associated Equipment* vol. 1014 (2021), p. 165743. DOI: https://doi.org/10.1016/j.nima.2021.165743. URL: https://www.sciencedirect.com/science/article/pii/S0168900221007282.

[3] Beaumel, D. "The GASPARD project". In: *Nuclear Instruments and Methods in Physics Research Section B: Beam Interactions with Materials and Atoms* vol. 317 (2013). XVIth International Conference on Electro-Magnetic Isotope Separators and Techniques Related to their Applications, December 2–7, 2012 at Matsue, Japan, pp. 661–663. DOI: https://doi.org/10.1016/j.nimb.2013.05.047. URL: https://www.sciencedirect.com/science/article/pii/S0168583X13006113.

[4] Bruyneel, B., Birkenbach, B., and Reiter, P. "Pulse shape analysis and position determination in segmented HPGe detectors: The AGATA detector library". In: *The European Physical Journal A* vol. 52, no. 3 (Mar. 2016). DOI: 10.1140/epja/i2016-16070-9. URL: https://doi.org/10.1140/epja/i2016-16070-9.

[5] Davis, J. R. *ASM specialty handbook: nickel, cobalt, and their alloys*. ASM International, 2000.

[6] Delahaye, P. et al. "New exotic beams from the SPIRAL 1 upgrade". In: *Nuclear Instruments and Methods in Physics Research Section B: Beam Interactions with Materials and Atoms* vol. 463 (2020), pp. 339–344. DOI: https://doi.org/10.1016/j.nimb.2019.04.063. URL: https://www.sciencedirect.com/science/article/pii/S0168583X19302472.

[7] Galtarossa, F. et al. "HeCTOr: the 3He Cryogenic Target of Orsay for direct nuclear reactions with radioactive ion beams". In: *Nuclear Instruments and Methods in Physics Research Section A: Accelerators, Spectrometers, Detectors and Associated Equipment* vol. 1018 (2021), p. 165830. DOI: https://doi.org/10.1016/j.nima.2021.165830. URL: https://www.sciencedirect.com/science/article/pii/S0168900221008159.

[8] Group, P. D. et al. “Review of Particle Physics”. In: *Progress of Theoretical and Experimental Physics* vol. 2020, no. 8 (Aug. 2020). 083C01. DOI: 10.1093/ptep/ptaa104. eprint: https://academic.oup.com/ptep/article-pdf/2020/8/083C01/34673722/ptaa104.pdf. URL: https://doi.org/10.1093/ptep/ptaa104.

[9] Knoll, G. F. *Radiaction Dedection and Measurement*. John Wiley, 2020.

[10] Lau, K. and Pyrlik, J. “Optimization of centroid-finding algorithms for cathode strip chambers”. In: *Nuclear Instruments and Methods in Physics Research Section A: Accelerators, Spectrometers, Detectors and Associated Equipment* vol. 366, no. 2 (1995), pp. 298–309. DOI: https://doi.org/10.1016/0168-9002(95)00604-4. URL: https://www.sciencedirect.com/science/article/pii/0168900295006044.

[11] Matta, A. “Etude du noyau très riche en neutrons 10He par réaction de transfert d’un proton 11Li(d,3He)”. Theses. Université Paris Sud - Paris XI, Feb. 2012. URL: https://tel.archives-ouvertes.fr/tel-00684544.

[12] Méot, F. “The ray-tracing code Zgoubi”. In: *Nuclear Instruments and Methods in Physics Research Section A: Accelerators, Spectrometers, Detectors and Associated Equipment* vol. 427, no. 1 (1999), pp. 353–356. DOI: https://doi.org/10.1016/S0168-9002(98)01508-3. URL: https://www.sciencedirect.com/science/article/pii/S0168900298015083.

[13] Ottini-Hustache, S. et al. “CATS, a low pressure multiwire proportionnal chamber for secondary beam tracking at GANIL”. In: *Nuclear Instruments and Methods in Physics Research Section A: Accelerators, Spectrometers, Detectors and Associated Equipment* vol. 431, no. 3 (1999), pp. 476–484. DOI: https://doi.org/10.1016/S0168-9002(99)00380-0. URL: https://www.sciencedirect.com/science/article/pii/S0168900299003800.

[14] Pollacco, E. et al. “MUST2: A new generation array for direct reaction studies”. English. In: *European Physical Journal A* vol. 25, no. SUPPL. 1 (2005). Cited By :95, pp. 287–288. URL: www.scopus.com.

[15] Pullanhiotan, S. et al. “Improvement in the reconstruction method for VAMOS spectrometer”. In: *Nuclear Instruments and Methods in Physics Research Section B: Beam Interactions with Materials and Atoms* vol. 266, no. 19 (2008). Proceedings of the XVth International Conference on Electromagnetic Isotope Separators and Techniques Related to their Applications, pp. 4148–4152. DOI: https://doi.org/10.1016/j.nimb.2008.05.024. URL: https://www.sciencedirect.com/science/article/pii/S0168583X08006952.

[16] Pullanhiotan, S. et al. “Performance of VAMOS for reactions near the Coulomb barrier”. In: *Nuclear Instruments and Methods in Physics Research Section A: Accelerators, Spectrometers, Detectors and Associated Equipment* vol. 593, no. 3 (2008), pp. 343–352. DOI: https://doi.org/10.1016/j.nima.2008.05.003. URL: https://www.sciencedirect.com/science/article/pii/S0168900208007080.

[17] Ramos, D. “Fragment Distributions of Transfer- and Fusion-Induced Fission from ^{238}U+ ^{12}C Reactions Measured Through Inverse Kinematics”. PhD thesis. Universidade De Santiago De Compostela, 2016.

[18] Rejmund, M. et al. “Performance of the improved larger acceptance spectrometer: VAMOS++”. In: *Nuclear Instruments and Methods in Physics Research Section A: Accelerators, Spectrometers, Detectors and Associated Equipment* vol. 646, no. 1 (2011), pp. 184–191. DOI: https://doi.org/10.1016/j.nima.2011.05.007. URL: https://www.sciencedirect.com/science/article/pii/S0168900211008515.

[19] Savajols, H. “VAMOS: A variable mode high acceptance spectrometer for identifying reaction products induced by SPIRAL beams”. In: *Nuclear Instruments and Methods in Physics Research Section B: Beam Interactions with Materials and Atoms* vol. 204 (2003). 14th International Conference on Electromagnetic Isotope Separators and Techniques Related to their Applications, pp. 146–153. DOI: https://doi.org/10.1016/S0168-583X(02)01908-0. URL: https://www.sciencedirect.com/science/article/pii/S0168583X02019080.

[20] Strikwerda, J. C. and Considine, J. M. “Deformation of a Membrane Under Uniform Static Pressure”. In: (Jan. 1994). URL: https://www.researchgate.net/profile/John_Considine2/publication/2695043_Deformation_of_a_Membrane_Under_Uniform_Static_Pressure/links/55e4648708aede0b573516eb/Deformation-of-a-Membrane-Under-Uniform-Static-Pressure.pdf.

[21] Söderström, P.-A. et al. “Interaction position resolution simulations and in-beam measurements of the AGATA HPGe detectors”. In: *Nuclear Instruments and Methods in Physics Research Section A: Accelerators, Spectrometers, Detectors and Associated Equipment* vol. 638, no. 1 (2011), pp. 96–109. DOI: https://doi.org/10.1016/j.nima.2011.02.089. URL: https://www.sciencedirect.com/science/article/pii/S016890021100489X.

[22] Wolfram Research, I. *Mathematica, Version 13.0.0*. Champaign, IL, 2021. URL: https://www.wolfram.com/mathematica.

[23] Ziegler, J. F., Ziegler, M., and Biersack, J. “SRIM – The stopping and range of ions in matter (2010)”. In: *Nuclear Instruments and Methods in Physics Research Section B: Beam Interactions with Materials and Atoms* vol. 268, no. 11 (2010). 19th International Conference on Ion Beam Analysis, pp. 1818–1823. DOI: https://doi.org/10.1016/j.nimb.2010.02.091. URL: https://www.sciencedirect.com/science/article/pii/S0168583X10001862.

Chapter 5

Geant4 Simulations for the Response of the Experimental Apparatus

Geant4 [1, 2, 3] is a toolkit that allows the simulation of the interaction between particles and matter based on Monte Carlo methods. It is developed in C++ and is able to simulate a considerable energy range from a few hundreds of eV to several TeV.

The toolkit supports many physical processes such as particle decays, optical electromagnetic, and hadronic processes, with the ability to include arbitrarily complex geometries and materials.

Physical events can be obtained with generators by sampling the probability density functions which characterize the process. An event generator for in-beam nuclear reactions will create an event randomly, accounting for the experimental distribution of the incoming beam in momentum, position, and angle. The reaction will then be produced in a randomized position between the start and the end of the target. The reaction fragments will be, in turn, emitted with an angular distribution sampled from the differential cross section and emitted with the relative momentum.

The simulation toolkit has proven essential for the simulation of the response of the detectors to the particular experimental conditions that will be discussed in the course of this Chapter.

5.1 The VAMOS Ionization Chamber Simulation

A Monte Carlo Geant4 simulation of the response of the ionization chamber of the magnetic spectrometer (VAMOS) has been implemented in order to characterize the detector and refine the data analysis.

In particular, the simulation includes the layers of material preceding the ionization chamber, such as the Mylar containment windows of the MWPPAC and the drift chambers. The detector response characterization is also useful for precise calibration of each of the subsequent layers (pads) of the chamber.

In order to simulate the loss of charge in the junction between different pads, a dead layer of 1 mm was added between the different rows of the ionization chamber.

Figure 5.1 shows the three-dimensional representation of the detector with a simulated ion of 400 MeV passing through the various layers and depositing energy in the CF_4 gas contained in the ionization chamber.

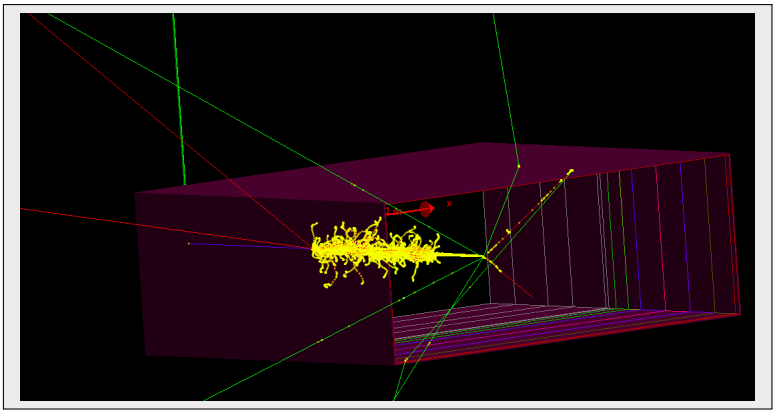

Figure 5.1: Geant4 visualization of the ionization chamber with a ^{46}Ar beam. The position of the beam is fixed while the energy varies between 400 MeV and 200 MeV. The energy deposited is measured in the ionization chamber segments.

Using the Geant4 General Particle Source (GPS), it is possible to simulate the emission of ^{46}Ar and ^{47}K ions with a uniform distribution ranging from 400 MeV to 200 MeV, thus exceeding the experimental values. The necessity of high energy data is necessary for the calibration procedure described in subsection 5.1.1. The resolution obtained in each segment of the ionization chamber was measured and verified both in the simulation and the experiment to verify the match for ^{46}Ar ions. Angular straggling was also included in the generation of events to simulate the increased energy deposited for trajectories that are not perfectly longitudinal with respect to the ionization chamber.

5.1.1 Ionization Chamber Calibration

The simulation can be exploited to optimize the ionization chamber calibration. While an initial calibration of the ionization chamber was performed by matching the expected deposited energy of the beam ions in each layer, significant energy straggling is present and hinders the outcome of the result. Additionally, a systematic bias could be introduced if the layers that the ion passes are not considered correctly. In order to remove this problem, it is possible to exploit the correlation of the energy deposited in adjacent segments of the ionization chamber (shown in Figure 5.2). The physical argument behind this process relies on the continuity of the stopping power of a material (presented in subsection 4.3.3.1). The ratio $R_{1,2}$ between the energy deposited in adjacent segments of length Δx, can be approximated with the following ratios of the stopping power, already introduced in subsection 4.3.3.1:

$$R_{1,2} = \frac{\int_{x_1-\Delta x_1/2}^{x_1+\Delta x_1/2} \left\langle \frac{dE}{dx} \right\rangle dx}{\int_{x_2-\Delta x_2/2}^{x_2+\Delta x_2/2} \left\langle \frac{dE}{dx} \right\rangle dx}$$

$$\approx \frac{\left\langle \frac{dE}{dx} \right\rangle\Big|_{x=x_1}}{\left\langle \frac{dE}{dx} \right\rangle\Big|_{x=x_2}} \frac{\Delta x_1}{\Delta x_2}$$

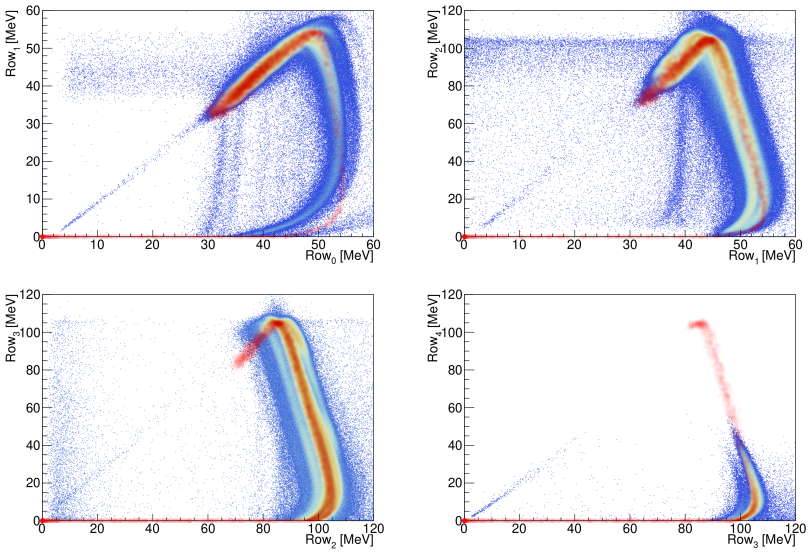

Figure 5.2: Correlation graph between the energy deposited on a row (x-axis) and the energy deposited on the next row (y-axis). The simulation in the case of ^{46}Ar emitted in the geometrical center of the ionization chamber with a uniform energy distribution from 50 MeV to 400 MeV is overlayed on the data with no Z selection.

If the energy is high enough to be far from the Bragg peak, the stopping power curve can be approximated with a linear dependence and, as a consequence, also the ratio of energy deposition is expected to preserve the linearity with a constant coefficient $R_{1,2}$. Figure 5.2 shows this linear region with the addition of far more complex features which are ascribed to lower energies of the ion, where this approximation no longer holds true. Nevertheless, the simulation is able to reproduce the correlation accordingly. Another feature that can be observed in the correlation graph is the punch-through energy which corresponds to the maximum energy that can be deposited in a segment and is strictly dependent on the thickness of the material.

Since the beam is fully stopped within segment 4 of the chamber, the correlation shapes are strongly dependent on the Bragg peak position. In particular, when the energy of the charged ion is low enough, the stopping power increases greatly (as introduced in subsection 4.3.3.1), generating an exponential-like energy release in a short distance. Due to this abrupt energy release in a small portion of the detector, a small change in the geometry will potentially create a great change in the detector response. In particular, if the Bragg peak

occurs near the junction between two pads, the matching between simulation and real-world data is scarce. This effect is also caused by experimental aspects which are not accounted for in the simulation, such as the non-linearity of the pre-amplifiers that is more evident at low energies [12], or other effects such as charge sharing between nearby pads. This aspect becomes clear in Figure 5.2, where, in the "Bragg tail" region of the correlation plot, there is not a perfect overlay between simulation and data.

Since no selection was applied in the correlation plot, it is possible to observe how other values of atomic number, namely $Z = 17$, are also present in the graph.

5.1.2 Estimate of the Not-Measured Energy

In order to estimate the amount of energy lost by the ion in the material which precedes the ionization chamber, it is possible to exploit the linearity of the energy released in subsequent layers when the ion is far from the Bragg peak. This linearity assumption has been argued in the previous subsection and only holds for the first segments of the ionization chamber. In particular, the reaction fragment of interest (the ^{47}K ion emitted in the direct reaction as well as ^{46}Ar) is expected to be stopped in the third or fourth rows of the ionization chamber. As a consequence, it is possible to assume that in the first row, the energy is still high enough to be far from the Bragg peak leading to a linear correlation between the energy lost in the layers preceding the ionization chamber and the energy lost in the first segment.

Since the Geant4 simulation includes all the material layers between the MWPPAC detector and the IC, it is possible to extract this linear correlation between the non-measured energy ($\Delta E_{n.m.}$) and the energy deposited in the first layer (ΔE_0):

$$\Delta E_{n.m.} = p_0 + p_1 \Delta E_0$$

The correlation coefficients are, to a first approximation, independent from the value of Z, so that it is possible to exploit the linear dependence in the case of both argon and potassium.

Figure 5.3 shows the correlation plot with argon and potassium ions, as well as the result of the linear fit performed in the region far from the Bragg peak region. Even if it is clear that the dependence on Z of the extracted parameters is negligible given the energy resolution, the adopted values are the average of the extracted numbers.

It is interesting to observe how, outside the linear zone, the Z dependence dominates, and ions with different atomic numbers trace different correlation figures.

This correction of the charge state is necessary to extract the value of the total energy of the ion presented in subsection 4.3.5.2.

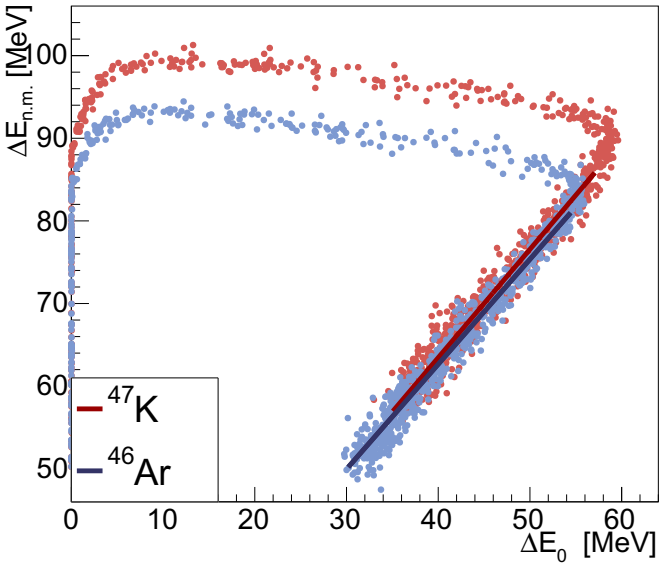

Figure 5.3: Not measured energy vs Energy loss in the first ionization chamber row. Average of linear fits far from the Bragg peak: $p0 = 11.44$, $p1 = 1.290$. Simulation of 1000 events with emission at an energy from 50 MeV to 400 MeV of ^{46}Ar and ^{47}K.

5.2 The MUGAST Simulation

The simulation of the silicon detector arrays (MUGAST+MUST2) is carried out with the NPTOOL toolkit [11] which is based on both ROOT [5] and Geant4. The overall code handles the generation of events and the simulation of the response of the detectors and has been extensively tested in the course of past experiments. Modifications to the distributed codebase were performed in order to further extend it to the case of the described experiment and will be briefly discussed in this section.

Figure 5.4 shows a rendering of some events simulated with the setup of interest.

The Monte Carlo simulation of the silicon detectors is essential in order to correct for the solid angle efficiencies and to assess the effect of many experimental aspects on the response of the detector, such as missing strips or the growing thickness of the ice deposition on the HAVAR windows of the target.

The simulation implements the predictable and observed experimental conditions in order to extract the response of the array to the different reactions. This response assessment will be used in the data analysis statistical considerations reported in Chapter 7.

The main aspects considered in the simulation, which will be discussed in

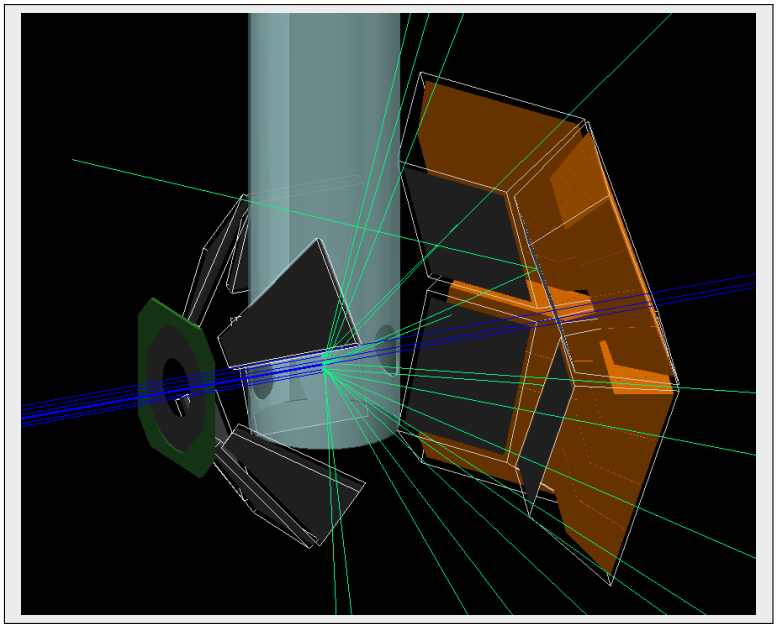

Figure 5.4: Geant4 visualization of the MUGAST setup with the transfer reaction.

this section, are the following:

- Center-of-mass angular distribution
- Gaussian-distributed beam profile on target with specified sigma on X or Y and mean position
- Beam angular straggling
- Beam energy spread
- Angular distribution dependence on the energy due to ice growth

- Accounting for dead strips
- Adjust thresholds strip by strip to match the data to characterize the response at low energy
- Account for the effect of ice growth
- Dead layers

5.2.1 Geometry of the Array

The simulated detectors include both MUST2 and MUGAST, as well as the cryogenic target. An additional sensitive detector that measures energy and position of interaction is placed at forward angles to estimate the acceptance of VAMOS and will be discussed in more detail in subsection 5.2.7.

The geometry of the target is modified to include the (deformed) cryogenic target, composed of the ^{3}He gas at the experimental density, the deformed Havar windows, and the Ice deposition.

A thin layer of aluminum is also added to the front faces of the detectors to simulate the loss in deposited energy due to the passivated layer and a possible slightly incomplete depletion of the silicon. The thickness of the aluminum passive layer was extrapolated from the calibration procedure and changes for each detector, according to the extrapolation performed in subsection 4.6.2.

The aluminum thickness ranged from $0.33\,\mu$m to $0.40\,\mu$m for the trapezoid detectors and was set to 0.68μm for the annular.

5.2.2 Event Generation

The beam optics can be simulated by including standard distributed spread in kinetic energy, position on the target and angle. Once the beam ion has been traced, a reaction occurs along its path in the target material (^{3}He). Heavy and light reaction fragments are then emitted with angle and energy given by the two-body kinematics with a suited excitation energy. The angle of emission is randomly sampled according to the angular distribution provided in the center-of-mass reference frame. Once the particles are emitted, if a sensitive detector is reached, the events will be recorded.

Due to the kinematics of the reaction, which consists of the addition of a proton to the beam ion, the light particle, the deuteron, will be emitted at mostly backward angles where MUGAST is located (cf. subsection 4.2.1).

5.2.3 The Missing Strips

Each DSSD contains a total of 128 strips on each side. However, a fraction of these channels can fail to the extent that no events will ever be recorded for a given strip. This aspect is expected and can be induced by many factors, such as damages accumulated during the previous experiments or a malfunctioning contact. A strip can be considered fully functional if both the energy and the time of flight are within the expected specifications.

A missing strip will cause a loss in efficiency that can be reproduced in the Geant4 simulation. If a strip has been detected as non-operational, it will be excluded in the analysis of the simulation in order to obtain the same detector response of the experiment.

For the data analysis, a strip is considered fully functional if it has measured at least one proton in the time span of the experiment, which means that both the energy as well as the time of flight were properly computed for the strip.

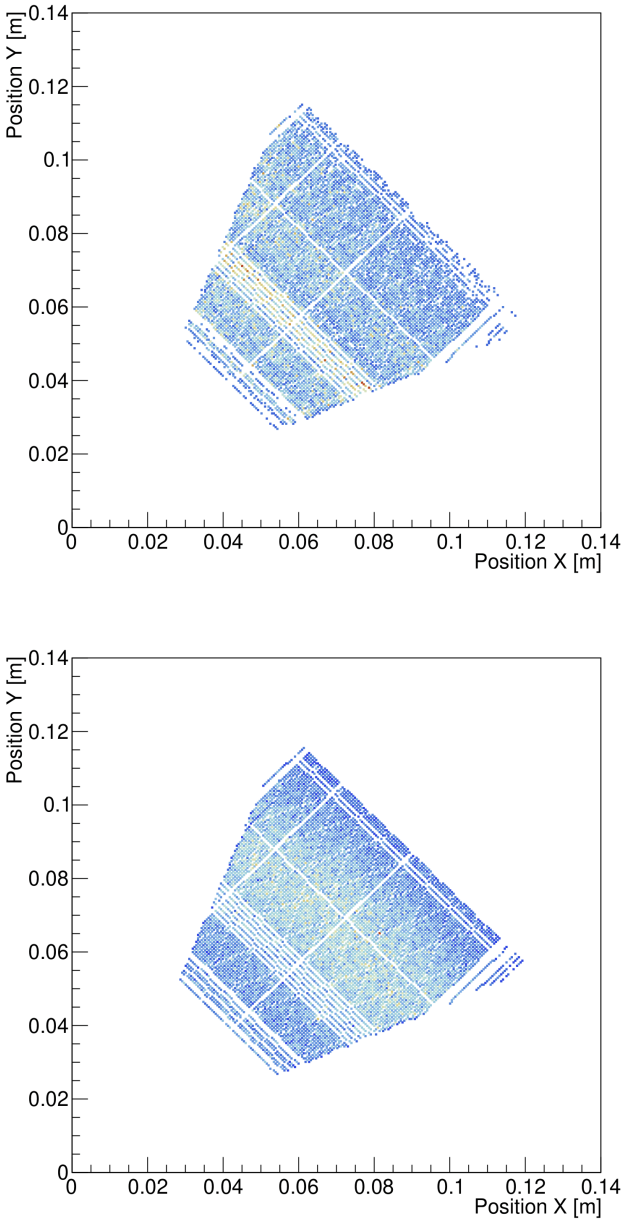

Figure 5.5: Comparison of MUGAST trapezoid number 7 which had the most of the missing strips between data (top panel) and simulation (bottom panel). The number of events in the trapezoid amounted to $8.4 \cdot 10^4$ and in the data to $3.2 \cdot 10^4$.

This is a sensible choice due to the large number of protons measured by each strip of the detector. At last, it is important to note that this choice will not include any bias since a functional strip that by chance has not measured any proton (a very unlikely occurrence) will simply be considered dead in both the data and the simulation. This will not introduce systematic errors as it will only slightly decrease the sensitivity of the detector without harming the comparison.

Trapezoid number 7 was by far the most affected by missing strips, an aspect which is evident in Figure 5.5 and (4.23) where in many cases, no energy signal was measured by the detector in the course of the experiment. In order to verify the correspondence between simulation and acquired data visually, various simulations with different angular momentum transfers and different ice thicknesses (cf. subsection 5.2.5) were combined to obtain the response in Figure 5.5 (right). Comparing the graphs, it is possible to validate the simulation, and in particular, the loss of statistics in correspondence to the missing strips.

5.2.4 Electronic Thresholds

All the DSSD strips are read out by individual electronics channels [4], as a consequence, each will be characterized by a threshold that might be not negligible in the case of low energy deuterons that are emitted at the most backward angles according to the kinematics of the reaction (cf. subsection 4.2.1). This effect can be included in the simulated data by recording the minimum energy measured by each strip in the experiment and applying a threshold condition on the measured energy.

5.2.5 Ice Deposition on the Target Windows

Another experimental aspect that can be quantified with the simulation concerns the ice deposition over time on the HAVAR windows of the cryogenic target.

Due to the kinematics of the reaction, which implies lower energy for deuterons emitted at backward angles, a gradual increase in the detection threshold is expected.

The observation of this phenomenon has been discussed in subsection 4.4.2. Since the amount of ice is known thanks to the magnetic spectrometer $B\rho$ measurement, it is possible to quantify the number of deuterons measured within a given ice thickness interval, effectively binning the number of deuterons according to the amount of the ice.

A $5\,\mu$m interval (bin) is considered spanning from $20\,\mu$m to $55\,\mu$m, thus covering all the whole experimental range of different thicknesses of the ice. For each bin value, a simulation was performed in the case of different angular momentum transfer angular distributions ($L = 0, 2, 3$) with the correct excitation energy as well as for the case of a uniform angular distribution with the three possible excitation energies ($Ex = 0\,\text{MeV}$, $0.360\,\text{MeV}$, $2.02\,\text{MeV}$) corresponding to the excited states of ^{47}K.

For each transferred angular momentum, simulations with a total of 70000 events each relative to different ice thickness geometries are added together

proportionally to the number of deuterons detected in each ice interval. This allows one to obtain a response of the detector to each of the three types of transfer $L = 0, 2, 3$.

The value of the fine binning interval of $5\,\mu$m is chosen so that simulations relative to adjacent bins show an almost undetectable effect on the response of the setup. In particular, a simulation with a given ice thickness shows marginal differences in excitation energy and angular distribution when compared to the same simulation with the ice increased by $5\,\mu$m. As a consequence, it is possible to conclude that the effect of the binning, if compared to a continuous change of the thickness, has no impact on the simulation results.

5.2.6 Other Aspects

Other experimental aspects included in the simulation concern beam optics. In particular the beam energy, position of incidence, and direction angle are sampled from a Gaussian distribution with standard deviation respectively of $\sigma = 10$ MeV, $\sigma = 0.1$ mrad, and $\sigma = 2.5$ mm. The values represent common parameters for post accelerated radioactive beams, while the energy straggling is justified by the presence of the beam tracker.

The increase of ice deposition has the effect of modifying the mid-target beam energy and can reflect on a variation of the angular distribution. The DWBA differential cross-section calculations presented in Chapter 6 showed marginal variations in terms of the computed angular distributions. Nevertheless, each simulation performed with a given ice thickness is associated with an angular distribution calculated with the correct mid-target energy.

5.2.7 The Acceptance of VAMOS

Each deuteron measured by MUGAST is correlated with a heavy ion detected in VAMOS since the presence of ^{47}K is required for each event. It is clear that, due to the two-body kinematics, the light and heavy fragments are strongly correlated in angle and energy, and hence a bias could be introduced in the data if the acceptance of the heavy fragment is not taken into account. Due to the kinematics of this particular reaction and the significant Lorentz boost in the laboratory frame of reference, the great majority of the fragments emitted are expected to be accepted in the spectrometer (cf. 4.2.1). Nevertheless, a Monte Carlo simulation is able to include effects due to the energy and the angular straggling, making the quantification of this aspect possible.

A valid event in VAMOS translates to the emission of the heavy fragment within the acceptance of the spectrometer in terms of $B\rho$ and angle of emission, as it is dependent on the optics of the magnetic elements and on the focal plane detectors coverage. In the case of VAMOS, the high-resolution mapping of the magnetic fields allows for the tracking of ions from the emission after the target to the focal plane position, as briefly illustrated in subsection 4.3.4. The same mapping can be used to compute if the heavy fragment detected in the simulation by the simple detector at forward angles falls within the acceptance

of the spectrometer. This detector measures both the energy and angles of emission.

In order to determine the $B\rho$ value, a charge state is randomly sampled in the simulation according to the charge state distribution and together with the ion (kinetic) energy E_k determines the magnetic rigidity according to the following equation as a function of the mass M and charge state Q:

$$B\rho = \frac{1}{Q\,c}\sqrt{E_k^2 + 2E_k\,Mc}$$

The reference value of $B\rho$ of the spectrometer was modified multiple times due to the ever-decreasing beam energy caused by the increase in ice thickness. In the simulation, each interval of ice thickness was associated with the experimental reference setting of $B\rho_0$.

The three coordinates of interest are determined on an event-by-event basis, computing the emission angles with respect to the target: θ_t, ϕ_t and the ratio of magnetic rigidity: $\delta = B\rho/B\rho_0$.

In order to speed up the calculations, a first acceptance calculation is performed to verify if the three coordinates are within the global maximum and minimum values of the accepted trajectories. If this is not the case, the event is rejected.

If all three parameters are within limits, the acceptance is not yet assured, and the following procedure must be performed for each parameter.

Since the acceptance presents itself as a three dimensional matrix $M_{i,j,k}$, where each element contains a number of values which correspond to the final coordinates, when it is necessary to compute the acceptance of a parameter i, the closest values of parameters j and k must be found to check if the value of parameter i is within the accepted range.

It appears the necessity of definition of a metric to determine the closest trajectory. In a similar way to the procedure described in subsection 4.3.4, the *closeness* relation between different points is defined by the distance $d = \sqrt{(p_j/c_j)^2 + (p_k/c_k)^2}$. In this case, the scaling constants c_j, c_k are defined by the difference between maximum and minimum value of each parameter.

If the measured (simulated) parameter $i_{measured}$ is compared to the maximum i_{max} and minimum i_{min} values of the same parameter in the matrix, an event is accepted if the following condition holds true:

$$M_{i_{min},j_c,k_c} < M_{i_{measured},j_c,k_c} < M_{i_{max},j_c,k_c} \tag{5.1}$$

The fragment is accepted if it falls within range of all three parameters (θ_t, ϕ_t, δ).

Figure 5.6 shows the acceptance of the spectrometer (namely the matrix $M_{i,j,k}$) in the case of the projections on two axis. It is clear that it is not possible to consider the acceptance of each parameter independently from the others. This argument is even more evident in the case of the three-dimensional graph in Figure 5.7 which clearly shows that some combinations of parameters are

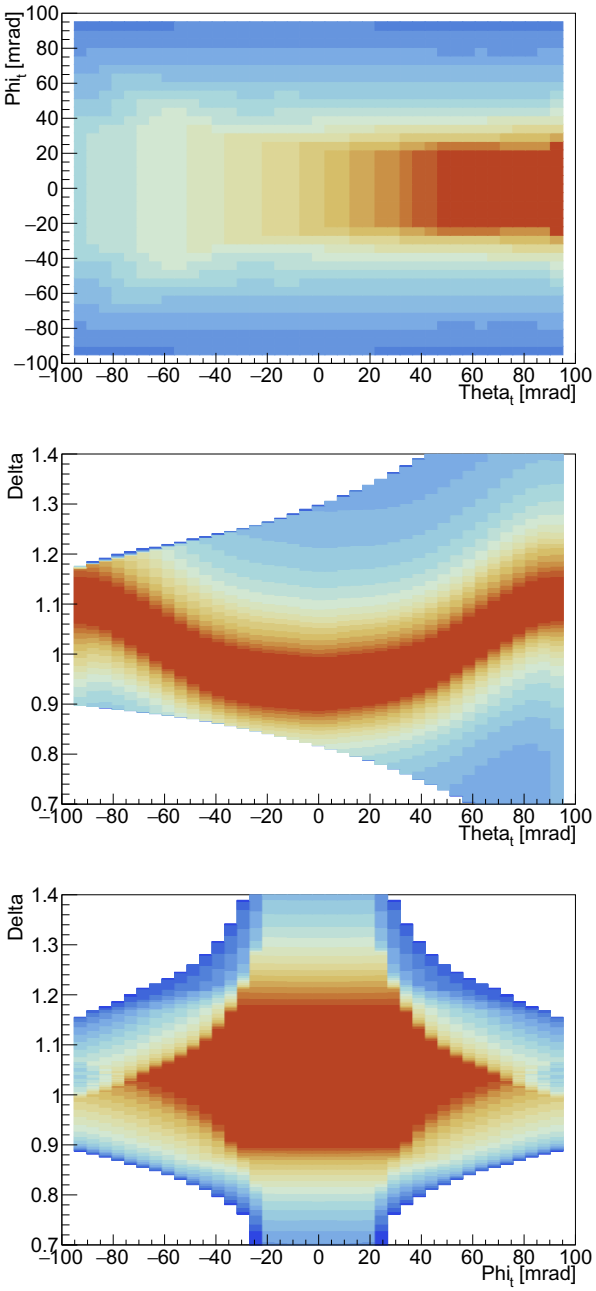

Figure 5.6: Two dimensional projections of the acceptance of each combination of the three parameters: θ_t, ϕ_t and δ. Bins closer to red in gradient represent a higher number of trajectories.

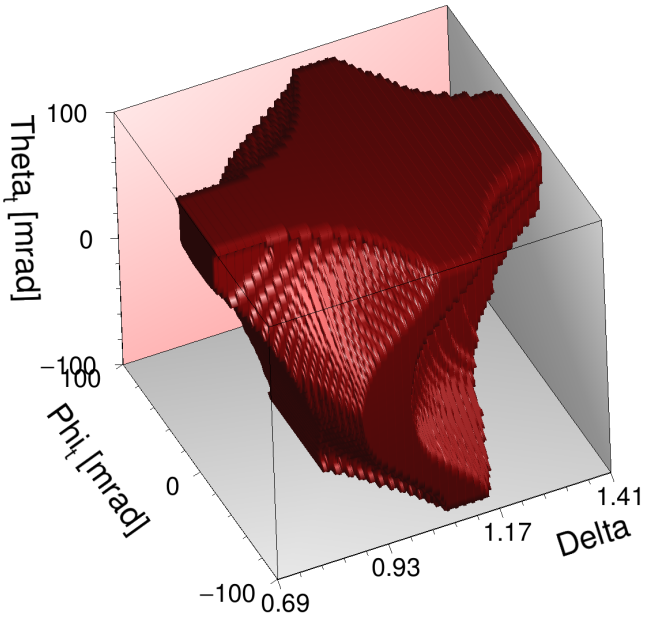

Figure 5.7: Three dimensional acceptance of the magnetic spectrometer, based on the three parameters θ_t, ϕ_t and δ. An event is accepted if it falls within the volume delimited by the pictured three-dimensional surface.

impossible to accept. In simple terms, an event that is contained within the pictured surface is an event that can be accepted by the spectrometer.

5.3 The AGATA Simulation

Gamma rays are observed in coincidence with ^{47}K in the magnetic spectrometer in correspondence to 360 keV and 1660 keV. A direct $L = 2$ transfer to the $3/2^+$ state would imply the emission of a 360 keV γ ray with a lifetime of 1.1 ns. At the same time, direct feeding of the $7/2^-$ state would imply the emission of two γ rays (most of the time) of 360 keV and 1660 keV with a lifetime of the state of 6.3 ns (cf. the ^{47}K level scheme in Figure 3.8).

As a consequence, direct feeding to the two states will produce different responses on the tracking array. In particular, it is possible to verify if the intensity of the two peaks at 360 keV and 1660 keV are compatible with the results obtained from the analysis of the angular distribution.

In order to achieve this goal, it is necessary to account for all the geometrical aspects of the experimental setup (absorption due to the various materials) as well as to simulate the reaction and the emission of the γ rays based on the

lifetime of the states. The latter is crucial since a long-lived state will decay behind the cryogenic target, where γ-ray absorption is large.

The simulation of the HPGe γ-ray detector array relies on the Monte Carlo Geant4 simulation code developed and maintained by the AGATA collaboration [7] with supplementary features implemented for this experiment.

The cryogenic target is included as an additional ancillary detector that can be added to the geometry of the array. The target was implemented by reconstructing the geometry of the target cell [8], whose main material consists of a relatively thick copper structure (as described in reference [8]). The accuracy of the target cell geometry is essential to reproduce the real-world data correctly as it is placed between the HPGe array and a nucleus decaying behind the target. The target cell is supported from the top by additional metallic material and encapsulated in a thin copper shielding box. The target and its support structure are complemented by the MUGAST reaction chamber included in the simulation in the GDML format. A block of iron placed in correspondence to the entrance quadrupole of VAMOS completes the setup to simulate the potential Compton background. The geometry of the complete setup is shown in Figure 5.8. The emission from a ^{152}Eu source positioned behind the target cell is shown. In Figure 5.9, green lines indicate the emission of γ rays, red lines of electrons, and blue lines of positrons. A close inspection of Figure 5.9 shows the shielding effect caused by the target where two γ rays are deflected by Compton scattering and one γ ray is fully absorbed in the copper structure.

A total of 39 fully operating crystals are placed in the simulation (13 triple cluster and one double cluster with two non-operational detectors overall). In order to reconstruct the γ-ray efficiency from the simulation, it is necessary to include the intrinsic efficiency of each crystal which is a parameter that ranges from 70% to 88% as documented in reference [10].

5.3.1 Source Measurement Validation

A ^{152}Eu source run was performed at the end of the experiment in order to validate the simulation. The source was centered in the x and y position and placed 85 mm behind the target cell towards the magnetic spectrometer. As a result, the target structure stands between the source and the HPGe array, effectively shielding part of the emitted γ rays. This position was chosen to evaluate the response to the emission of a γ ray from a long-lived state of the recoiling nucleus. The efficiency of the detector depends not only on the distance between the detector and the source but also on the amount of solid angle covered by the target structure and the attenuation factor, which is dependent on the energy.

As a consequence, two effects are to be expected:

- A reduction of the efficiency in absolute values due to the absorption of some of the emitted γ rays by the (relatively) thick target cell

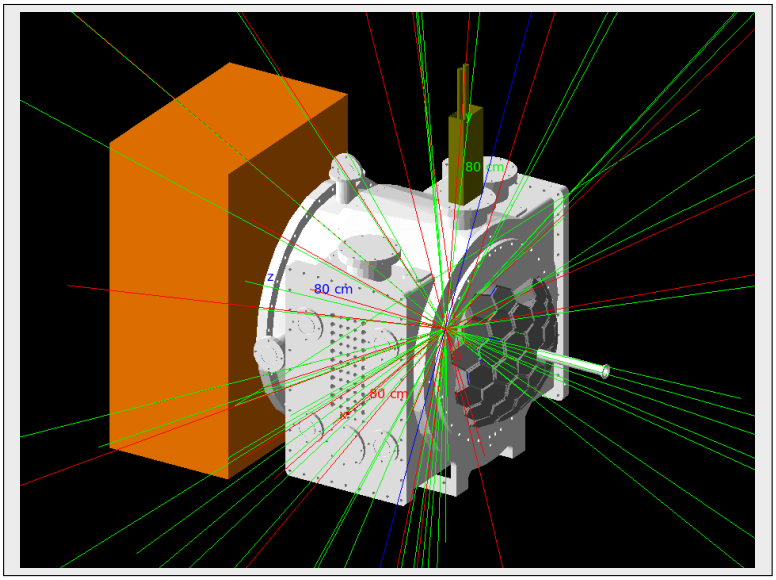

Figure 5.8: Visualization of the source simulation with the full reaction chamber, cryogenic target and AGATA.

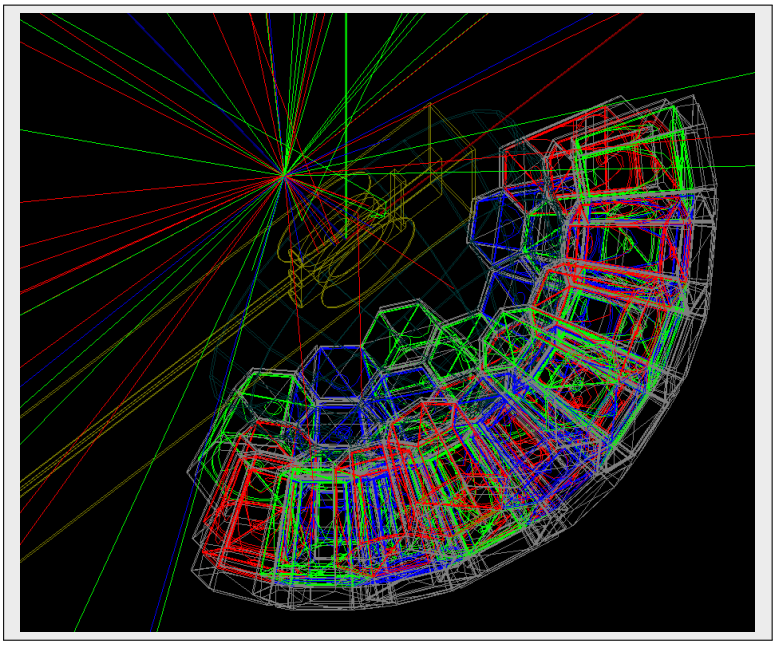

Figure 5.9: Simulation of the ^{152}Eu source placed 85 mm behind the target. In green the γ-ray trajectories, in blue e^+ and in red e^-. The reaction chamber and all nearby objects have been removed for visualization purposes.

- The modification of the usual efficiency curve of a γ-ray detector due to the energy dependence of the absorption coefficient. In particular, low energy γ rays are expected to be affected more by the interposed material if compared to higher energy photons. This aspect is dependent on the material, mainly copper, as well as its thickness.

Figure 5.10 shows the comparison between simulation and experimental data that appear in close agreement with each other. The fit procedure on the experimental spectra has been performed using the resolution model described in Appendix B and by using the integral of the distribution with the derived statistical uncertainty. The model is introduced to account for the loss in charge collection caused by neutron damage on the crystalline structure of the germanium crystal, which manifests itself with the presence of a low energy (left) tail on the peaks of the spectra [6].

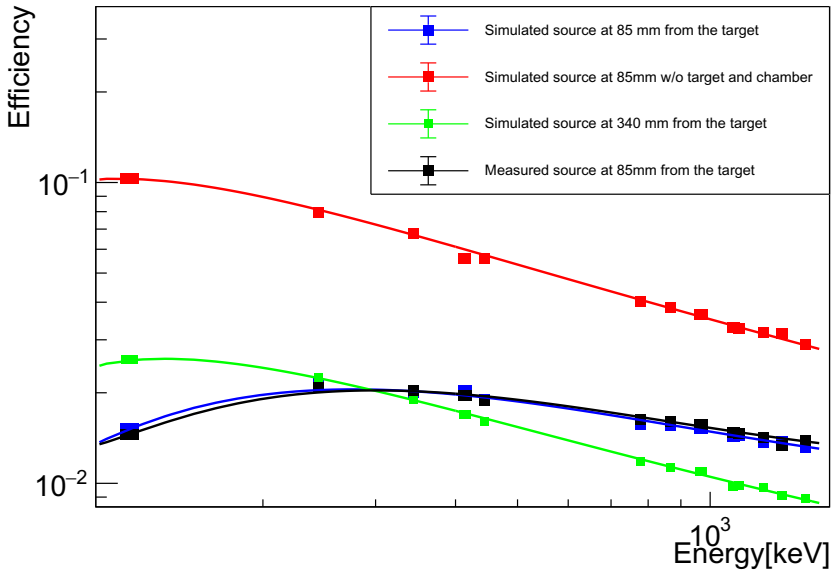

Figure 5.10: Comparison of Geant4 simulation and data of core detection efficiency of AGATA with a ^{152}Eu source. The solid lines correspond to a fit of the efficiency curve parametrization performed according to reference [9]. Statistical errors on the fit are present but not visible due to their low relative value. The presented curves are relative to the simulation (blue) and experimental data (black), with the source placed 85 mm behind the target cell. The efficiency curve with the same position but without the reaction chamber and the cryogenic target (red) shows the γ-ray absorption. The efficiency with the source placed further away from the spectrometer (green) shows the impact of a reduced solid angle coverage.

Comparing the efficiency curve at 85 mm (in black) with the simulation of the same setup with the target and the reaction chamber removed, it is clear how the presence of these structures affects the overall shape of the curve in absolute terms as well as in terms of trend. In fact, the black line appears more attenuated for low energy γ rays with respect to the red one, indicating the presence of an absorber material. In the same figure, a simulation of the emission far from the target structure (340 mm) shows how the diminished solid angle covered by the germanium array negatively affects the efficiency. Nevertheless, another interesting aspect can be observed, as the shape of the (red) curve relative to the absence of the target structure is somehow recovered. This is due to the fact that, in relative terms, the solid angle covered by the target cell has decreased more if compared to that of the detector, making the absorption effect on the curve less important.

A further consideration is necessary concerning the effect of the efficiency from the AGATA analysis methodology. A γ-ray spectrum can be generated using the AGATA cores (as in the case of the efficiency curves considered in Figure 5.10), exploiting the add-back procedure or the tracking algorithm. In order to reconstruct the efficiency of each analysis procedure from the simulated data, the first two methods simply require the energy deposition evaluation of Geant4. The efficiency of the tracking algorithm, on the other hand, also relies on the positions of interactions. As a consequence, the efficiency figure can be considered reliable only in the case of accurate correspondence of the position of interaction of the data and the simulation. While in the case of the data, the position figure depends on a χ^2 minimization that searches for at the most a single interaction within a segment, in the simulation, many more interactions are present on average. This aspect is dealt with by *packing* close interaction points by considering them as a single interaction with energy equal to the sum of all energy and with the position equal to the energy-weighted average position of all interactions. As a consequence of this further step, in order to remove the potential introduction of systematic errors, only the case of core and add-back spectra will be considered.

5.3.2 Event Generation and Reaction Simulation

While the efficiency as a function of the position of emission has been verified with measured data, an additional step is necessary in order to simulate the response of the detector in the course of the experiment.

In particular, an event must be generated with the correct physical properties. On the one hand, the two-body kinematics and the energy losses need to be considered to allow for the correct energy of emission of the ^{47}K fragment. The energy of emission affects the Doppler correction as well as the broadening of the peaks observed. On the other hand, an event must be simulated with the correct decay characteristics of the states of interest, namely the lifetime of the states. A long-lived state of a few nanoseconds will decay far from the nominal central position of the array, thus producing a broadening of the observed peaks. The broadening of the Doppler corrected peaks can be understood starting from

the Doppler formula that relates the energy of a γ ray emitted in the frame of reference at rest (E_{γ_0}) with respect to the energy (E_γ) in another frame of reference which is moving at a velocity β with respect to the former:

$$\frac{E_\gamma}{E_{\gamma_0}} = \frac{\sqrt{1-\beta^2}}{1-\beta\cos\vartheta_\gamma}$$

where ϑ_γ indicates the angle between the velocity vector and that of the γ ray. The source of the broadening can be broken down in its main constituents: the uncertainty on the angle of emission $\Delta\vartheta_\gamma$, the uncertainty on the recoil velocity $\Delta\beta$ and the intrinsic resolution ΔE_{intr}:

$$\left(\frac{\Delta E_{\gamma_0}}{E_{\gamma_0}}\right)^2 = \left(\frac{\beta\sin\vartheta_\gamma}{1-\beta\cos\vartheta_\gamma}\right)^2 \times (\Delta\vartheta_\gamma)^2 + \left(\frac{\beta-\cos\vartheta_\gamma}{(1-\beta^2)\,(1-\beta\cos\vartheta_\gamma)}\right)^2 \times (\Delta\beta)^2 + \left(\frac{\Delta E_{\text{intr}}}{E_\gamma}\right)^2$$

The first aspect to observe is that $\Delta E_{\gamma 0}$ is proportional to the energy of the transition, making the broadening more evident for higher-energy γ rays. The second uncertainty is related to the angle between the velocity vector (or β) and the angle of emission of the photon. While for a short-lived state and thanks to the high position resolution of AGATA (nominally 4 mm), this effect is often negligible, in the case of interest, the emission consists in a stochastic process where the photon can be emitted along the trajectory of the ion in a position which follows the typical exponential distribution (in the case of one single excited state). While the direction of β is measured by the magnetic spectrometer, the angle of emission is affected by a large uncertainty in $\Delta\vartheta_\gamma$ due to this uncertainty on the position of emission.

Figure 5.11 shows the response of the detector in the case of feeding to three different states: the $3/2^+$ and $7/2^-$ states in the level scheme presented in Figure 3.8 as well as another short-lived state. Various aspects can be noted from the difference between the spectra. On one side, the broadening of the 1660 keV peak is very significant if compared to the intrinsic resolution of the detector of a few keV. On the other hand, also the centroid of the 360 keV peak is shifted, and its overall integral appears to be also affected by the different feeding due to the delayed emission in the case of the population to the $7/2^-$ state.

Table 5.1 shows the effect of the population to different states on the total efficiency of AGATA. As expected, the detection of 360 keV γ rays decreases significantly in the case of the feeding to the $7/2^-$ state.

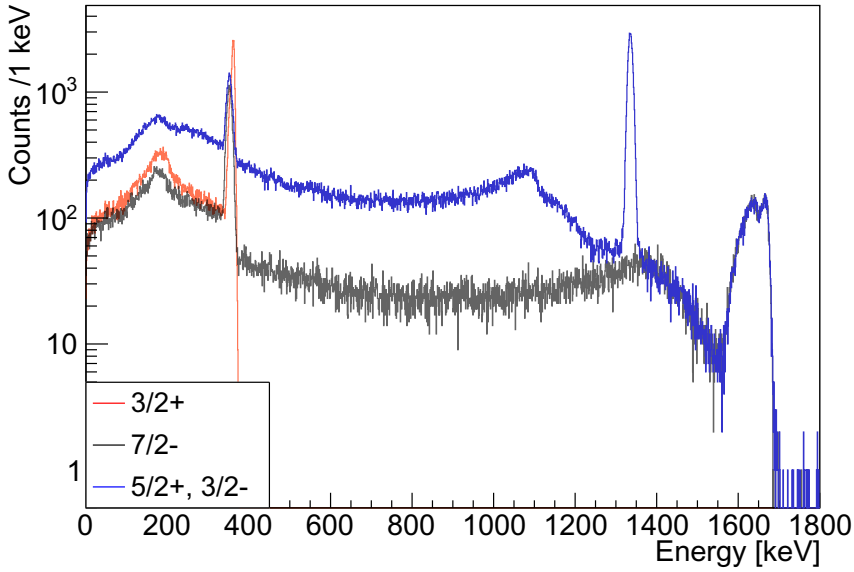

Figure 5.11: Simulated and Doppler corrected γ-ray spectra of 10^6 reactions in the case of three different populated states. The broadened peak around 1660 keV is caused by the long lived $7/2^-$ state.

	Feeding to $3/2^+$	**Feeding to** $7/2^-$
360 keV efficiency	2.7%	1.3%
1660 keV efficiency	-	0.99%

Table 5.1: Simulated efficiency in the case of different populated states, including reaction kinematics and lifetime of the populated states.

Bibliography

[1] Agostinelli, S. et al. "Geant4—a simulation toolkit". In: *Nuclear Instruments and Methods in Physics Research Section A: Accelerators, Spectrometers, Detectors and Associated Equipment* vol. 506, no. 3 (2003), pp. 250–303. DOI: https://doi.org/10.1016/S0168-9002(03)01368-8. URL: https://www.sciencedirect.com/science/article/pii/S0168900203013688.

[2] Allison, J. et al. "Geant4 developments and applications". In: *IEEE Transactions on Nuclear Science* vol. 53, no. 1 (2006), pp. 270–278. DOI: 10.1109/TNS.2006.869826.

[3] Allison, J. et al. "Recent developments in Geant4". In: *Nuclear Instruments and Methods in Physics Research Section A: Accelerators, Spectrometers, Detectors and Associated Equipment* vol. 835 (2016), pp. 186–225. DOI: https://doi.org/10.1016/j.nima.2016.06.125. URL: https://www.sciencedirect.com/science/article/pii/S0168900216306957.

[4] Assié, M. et al. "The MUGAST-AGATA-VAMOS campaign: Set-up and performances". In: *Nuclear Instruments and Methods in Physics Research Section A: Accelerators, Spectrometers, Detectors and Associated Equipment* vol. 1014 (2021), p. 165743. DOI: https://doi.org/10.1016/j.nima.2021.165743. URL: https://www.sciencedirect.com/science/article/pii/S0168900221007282.

[5] Brun, R. et al. *root-project/root: v6.18/02*. Version v6-18-02. Aug. 2019. DOI: 10.5281/zenodo.3895860. URL: https://doi.org/10.5281/zenodo.3895860.

[6] Bruyneel, B. et al. "Correction for hole trapping in AGATA detectors using pulse shape analysis". In: *The European Physical Journal A* vol. 49, no. 5 (May 2013). DOI: 10.1140/epja/i2013-13061-4. URL: https://doi.org/10.1140/epja/i2013-13061-4.

[7] Farnea, E. et al. "Conceptual design and Monte Carlo simulations of the AGATA array". In: *Nuclear Instruments and Methods in Physics Research Section A: Accelerators, Spectrometers, Detectors and Associated Equipment* vol. 621, no. 1 (2010), pp. 331–343. DOI: https://doi.org/10.1016/j.nima.2010.04.043. URL: https://www.sciencedirect.com/science/article/pii/S0168900210008922.

[8] Galtarossa, F. et al. "HeCTOr: the 3He Cryogenic Target of Orsay for direct nuclear reactions with radioactive ion beams". In: *Nuclear Instruments and Methods in Physics Research Section A: Accelerators, Spectrometers, Detectors and Associated Equipment* vol. 1018 (2021), p. 165830. DOI: https://doi.org/10.1016/j.nima.2021.165830. URL: https://www.sciencedirect.com/science/article/pii/S0168900221008159.

[9] Gray, P. and Ahmad, A. "Linear classes of Ge(Li) detector efficiency functions". In: *Nuclear Instruments and Methods in Physics Research Section A: Accelerators, Spectrometers, Detectors and Associated Equipment* vol. 237, no. 3 (1985), pp. 577–589. DOI: https://doi.org/10.1016/0168-9002(85)91069-1. URL: https://www.sciencedirect.com/science/article/pii/0168900285910691.

[10] Ljungvall, J. et al. "Performance of the Advanced GAmma Tracking Array at GANIL". In: *Nuclear Instruments and Methods in Physics Research Section A: Accelerators, Spectrometers, Detectors and Associated Equipment* vol. 955 (2020), p. 163297. DOI: https://doi.org/10.1016/j.nima.2019.163297. URL: https://www.sciencedirect.com/science/article/pii/S0168900219315475.

[11] Matta, A. et al. "NPTool: a simulation and analysis framework for low-energy nuclear physics experiments". In: *Journal of Physics G: Nuclear and Particle Physics* vol. 43, no. 4 (Mar. 2016), p. 045113. DOI: 10.1088/0954-3899/43/4/045113. URL: https://doi.org/10.1088/0954-3899/43/4/045113.

[12] Ramos, D. "Fragment Distributions of Transfer- and Fusion-Induced Fission from ^{238}U+ ^{12}C Reactions Measured Through Inverse Kinematics". PhD thesis. Universidade De Santiago De Compostela, 2016.

Chapter 6

DWBA Calculations of Proton-Transfer Cross-Sections

A thorough treatment of the nuclear reaction dynamics is essential in order to extrapolate the nuclear structure information that is crucial for the outcome of the experiment. This chapter will discuss some of the considerations and calculations for the extraction of the angular distributions, which are in turn necessary to extrapolate the final relative spectroscopic factors.

All nuclear reaction calculations are carried out with the Fresco code [12], a program developed in Fortran to perform nuclear coupled-channel reaction calculations. While Fresco includes a multitude of reaction calculations procedures that can quickly reach high levels of complexity, the following chapter will focus on simple finite range 1-step DWBA calculations. Due to the presence of the structure of the cryogenic target, angles towards 90 degrees, where most of the statistics are expected, were shadowed by the support structure, thus preventing the measurement of the elastic scattering reaction (^{46}Ar(^{3}He, ^{3}He)^{46}Ar). This reaction is often used to extract the parameters of the optical potential in the entrance channel.

Nevertheless, the validity of the optical potentials considered in the following chapter can be verified by comparison with other experimental data on direct reactions.

In the case of the transfer reaction on ^{46}Ar considered in this work, the optical potentials necessary for a precise calculation are the following:

- **Incoming scattering**: ^{46}Ar-^{3}He
- **Outgoing scattering**: ^{47}K-^{2}H
- **Core-core**: ^{46}Ar-^{2}H
- **Binding**: ^{46}Ar-^{1}H
- **Helium potential**: ^{1}H-^{2}H

Various global optical potentials will be considered, tested, and compared to experimental data in the following sections. Global optical potentials consist of parametrizations of the Wood-Saxon function with respect to some parameters that often correspond to the atomic number and mass as well as the incident energy. They are generally obtained with a minimization procedure from the angular distributions computed for the elastic channel with respect to the experimental data. Consequently, their validity is often restricted within a specific energy range and region of the Segrè chart. Due to this minimization

procedure, the amount of available data influences the performances of the global potentials. The optical potential, modeled with the Wood-Saxon function, is composed by the following terms:

$$V(r) = V_R(r) + V_{SO}(r) + V_C(r) + i\left[W_D(r) + W_S(r) + W_{SO}(r)\right]$$

The imaginary part of the potential is related to the absorption of the incoming flux. The terms consist in the Coulomb potential V_c, the real (imaginary) part of the potential well V_r (W_S), the real (imaginary) spin-orbit component V_{SO} (W_{SO}) and the surface absorption W_D. Each term needs three constants that can be parametrized with respect to the energy or the scattering nucleus: The depth of the well V, the radius r, and the diffusivity parameter a.

Following along the line of the global deuteron potential developed by Han et al. [6], the volume components for both real V_R and imaginary W_S terms will have a simple shape described by:

$$V_R(r) = -\frac{V_R(E)}{1 + \exp\left(\frac{r - R_R}{a_R}\right)}$$

The surface absorption W_D, on the other hand, will depend on the derivative of the Wood-Saxon function so that it will reach a maximum of absorption along the surface of the potential well:

$$W_D(r) = -4W_D(E)\frac{\exp\left(\frac{r - R_D}{a_D}\right)}{\left[1 + \exp\left(\frac{r - R_D}{a_D}\right)\right]^2}$$

The spin-orbit components V_{SO} and W_{SO} will also be related to the derivative and proportional to the spin-orbit scalar product:

$$V_{SO}(r) = -\left(\frac{\hbar}{m_\pi c}\right)^2 (\vec{L}\cdot\vec{S})\frac{V_{SO}}{a_{SO} r}\frac{\exp\left(\frac{r - R_{SO}}{a_{SO}}\right)}{\left[1 + \exp\left(\frac{r - R_{SO}}{a_{SO}}\right)\right]^2}$$

The Coulomb component V_C is often parameterized with the simple Coulomb potential outside the radius R_C and considering a constant charge distribution inside:

$$V_C(r) = \begin{cases} C_1 \frac{Z_d Z}{R_C}\left(3 - \frac{r^2}{R_C^2}\right) & \text{if } r < R_C \\ C_2 \frac{Z_d Z}{r} & \text{if } r \geqslant R_C \end{cases}$$

The region of sensitivity of the experiment, in the center-of-mass reference frame, is between 2° and 23° (cf. Figure 7.8). In this region, the shape of the angular distribution is dominated by the angular momentum matching between the beam and target nuclei, while the optical parameters of the potential are of secondary importance [5].

In the following sections, this will be apparent by a close match between the calculated angular distribution for small angles and the progressive distancing at larger angles. In particular, the absorption component of the potential will dominate the decay at large angles in the center of mass so that a fine-tuning of the parameters relative to the imaginary volume part is necessary to achieve a good agreement for large angles.

6.1 Elastic Scattering

6.1.1 The Deuteron Potential

The deuteron potential consists in the exit channel for the reaction of interest on ^{46}Ar. Some global optical potentials have been parametrized in order to describe elastic scattering data between deuterons and heavy nuclei; in the current section, three potentials will be considered:

- An et al. [1]: global optical potential obtained from data ranging from ^{12}C to ^{238}U with energies of less than 183 MeV
- Han et al. [6]: global optical potential for nuclear masses ranging from $A = 12$ to $A = 209$ with an energy of up to 200 MeV
- Bojowald et al. [4]: global potential produced with a reduced amount of data for nuclear masses ranging from $A = 27$ to $A = 208$ and energies comprised between 50 MeV to 80 MeV.

The elastic scattering data are available from a recent experiment performed in GANIL at the SPIRAL1 facility for the study of the ^{47}K(d,p)^{48}K direct reaction in inverse kinematics with a radioactive beam of ^{47}K at 7.52 MeV/u [11]. The experiment took advantage of the same experimental setup with the addition of DSSD square detectors placed at 90 degrees with respect to the target, thus allowing the measurement of the elastic scattering reaction channel (^{47}K(d,d)^{47}K). The elastic channel is of vital importance for this work as it corresponds to the exit channel of the transfer reaction and is in a similar energetic range.

Figure 6.1 shows the comparison between the elastic data with the DWBA calculations performed with three optical potentials developed by An et al. [1], Han et al. [6], and Bojowald et al. [4]. While all three global potentials considered are in good agreement with the data in the range of sensitivity 2°-23°, the potentials parametrized by Han et al. show impressive compatibility in the whole experimental range.

While no other public data exists for elastic scattering of deuterons on ^{47}K, it is possible to test the same optical potential parametrizations with the experimental data of reference [2]. The authors studied the spectroscopy of ^{47}K via direct reaction from the stable isotope ^{48}Ca: ^{48}Ca(d,^{3}He)^{47}K. Moreover, the authors were also able to measure the elastic scattering reaction channel (^{48}Ca(d,d)^{48}Ca) with bombarding energy of 79.2 MeV. While this energy is

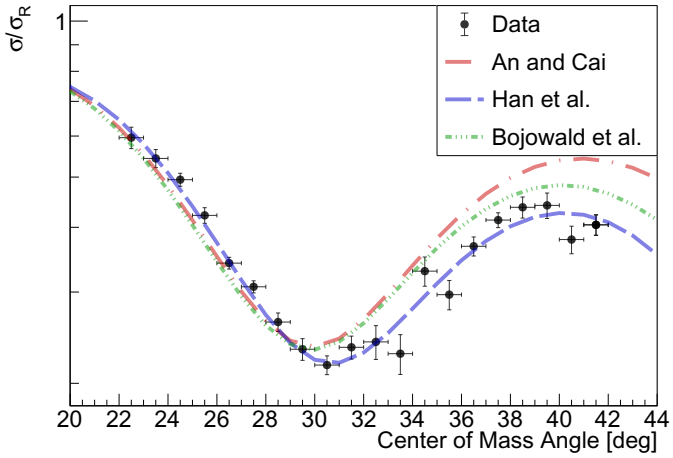

Figure 6.1: Ratio of the elastic over the Rutherford differential cross sections. Comparison of DWBA reaction calculations with different optical potentials for the elastic scattering reaction ^{47}K(d,d)^{47}K at 7.52 MeV/u in inverse kinematics.

significantly higher than the one of this work, it can still serve as a qualitative benchmark of the potential parameters. Figure 6.2 shows the same potentials considered in Figure 6.1 with updated values for the reaction of interest and bombarding energy. The agreement between experimental data and the DWBA theoretical distribution is satisfactory for angles closer to zero degrees and diverges for larger values.

6.1.2 The $A = 3$ Potential

The optical potential for ^{3}He represents the entrance channel, and while no elastic scattering was measured for the present experiment, some considerations can still be carried out. The global optical potentials considered in the case of ^{3}He consist in:

- Trost et al. [13]: ^{3}He global optical potential for nuclei with mass range from 10 to 208 and energies from 10 MeV to 220 MeV
- Li et al. [8]: ^{3}H global optical potential for nuclei from ^{48}Ca to ^{232}Th with energies of less than 40 MeV
- Hyakutake et al. [7]: ^{3}He potential for nuclei in the vicinities of ^{60}Ni in an energy range from 90 MeV to 120 MeV
- Becchetti et al. [3]: Global potential for ^{3}H and ^{3}He with bombarding energies of less than 40 MeV

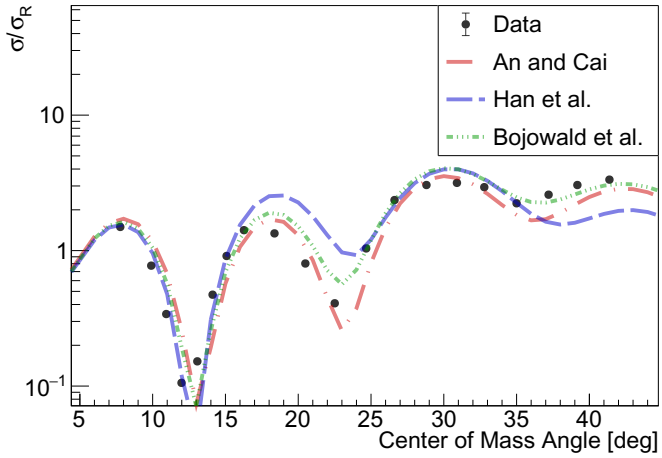

Figure 6.2: Ratio of the elastic over the Rutherford differential cross sections. The DWBA calculations are compared to the experimental data with different optical potentials for the elastic scattering reaction ^{48}Ca(d,d)^{48}Ca at 79.2 MeV in direct kinematics [2].

- Liang et al. [9]: Global ^{3}He optical potential for nuclei from ^{9}Be to ^{208}Pb with energies of less than 270 MeV

Although, no experimental data exists in the case of elastic scattering on ^{3}He, the work by Becchetti et al. offers the parametrization of the optical potential for both tritons and ^{3}He. Experimental data of elastic scattering of tritons on ^{48}Ca exists in literature [10] with a beam energy of 33 MeV in direct kinematics, close to the energy of interest. The similarity of the parametrization of tritons and ^{3}He justifies some of the presented calculations, where the ^{3}He parametrization was tested on the elastic scattering of triton isotopes.

Figure 6.3 shows the experimental angular distribution compared to the DWBA calculations performed with the previous optical potentials. The comparison is favorable for angles in the angular range of interest with a progressively increasing divergence for angles above $\approx 35°$. Similarly to the previous cases, the optical potentials often fail at reproducing the absorption component for increasing angles while still reproducing the positions of maxima and minima of the distribution.

6.2 Proton Transfer Reactions

In transfer reaction calculations, the final and initial partitions differ due to the transfer of one nucleon. As a consequence, also the optical potentials before and after the transfer are different. One-step finite-range DWBA calculations are performed for the following calculations and will be benchmarked with existing

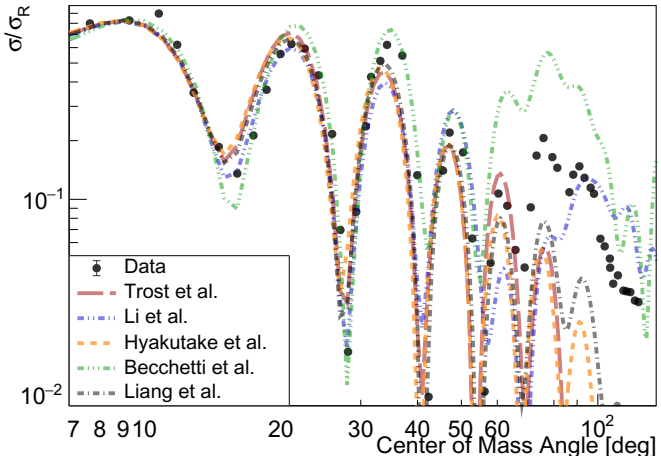

Figure 6.3: Ratio of the elastic over the Rutherford differential cross sections. Scattering of ^{48}Ca on tritons [10]: ^{48}Ca(t,t)^{48}Ca at 33 MeV (direct kinematics). The x-axis is shown in logarithmic scale to accentuate the angular region of interest which ranges from 0° to ≈ 23° in the center of mass frame of reference.

experimental data on the (^{48}Ca(d,^{3}He)^{47}K) reaction, although at the much higher energy of 79.2 MeV in direct kinematics [2].

6.2.1 ^{48}Ca(d,^{3}He)^{47}K

The calculation was performed using Wood-Saxon potentials to describe the overlaps between incoming ^{48}Ca ground state and the states of interest of ^{47}K, $\langle^{48}\text{Ca}|^{47}\text{K}\rangle$. The calculations are made to reproduce the experimental data of reference [2] which focuses on the study of the direct reaction using a (polarized) deuterium beam on a ^{48}Ca target. While a total of seventeen states of the potassium isotope were populated, the current work aims to reproduce the observed $L = 0$ and $L = 2$ transfers to $1/2^+$ and $3/2^+$ states of ^{47}K. The authors provide a parametrization of the optical potentials, which has also been included in these calculations. A comparison between some of the global potentials is shown in Figure 6.4, where the calculations account for the spectroscopic factors inferred in the cited article.

In particular, two $L = 0$ reaction channels were observed for the proton transfer to the ground state and to a level located excitation energy of 3.8 MeV. The latter higher-lying state was shown to absorb a small amount of the $j = 1/2$ strength, amounting to a spectroscopic factor $C^2S = 0.28$, which needs to be compared with the value of $C^2S = 1.55$ relative to the ground state.

As far as the $L = 2$ reaction channels are concerned, a total of twelve different channels were observed. Nevertheless, while the $j = 5/2$ strength appears to be very fragmented since the sum of the ten measured spectroscopic factors amounts

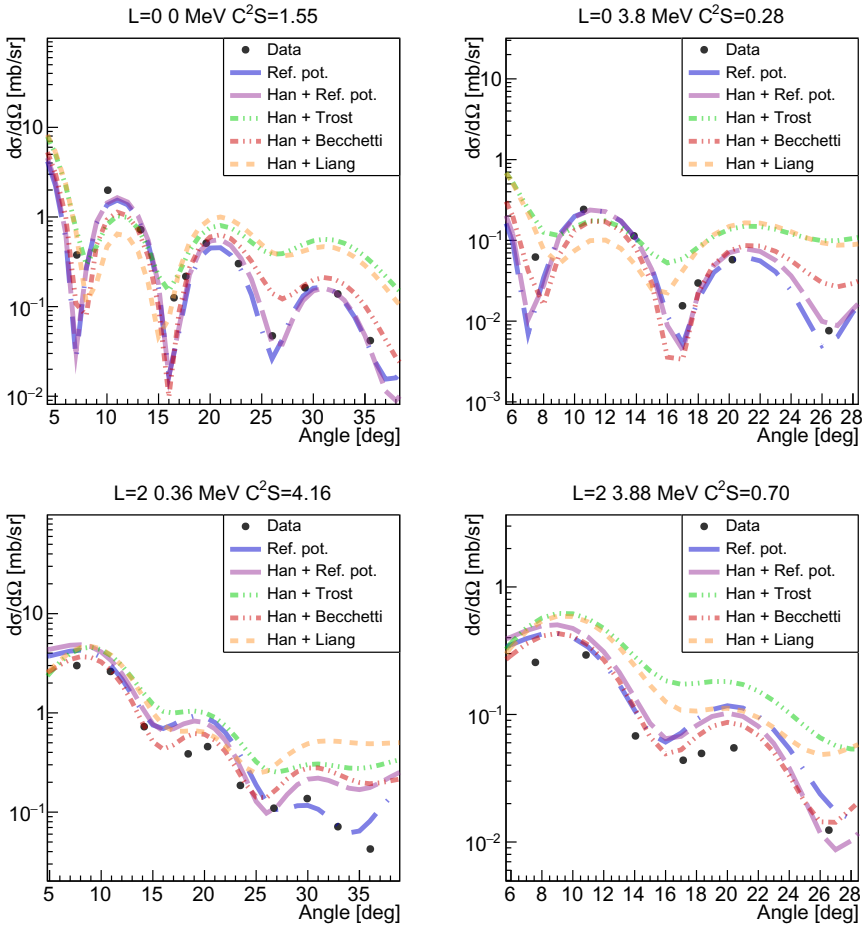

Figure 6.4: Comparison of single-step finite range DWBA calculations performed with Fresco and the available experimental data for the direct reaction ^{48}Ca(d,^{3}He)^{47}K at 79.2 MeV in direct kinematics [2]. The reference potential, in blue, consist in the parametrization identified by the authors in reference [2] to better reproduce the data, while the other combinations are the global optical potentials considered in the current work.

to 64% of the shell-model limit, the case for the $j = 3/2$ state is different. The $j = 3/2$ strength appears to be exhausted by only two states in ^{47}K: the first excited state at 0.36 MeV and the higher-lying state at 3.88 MeV. The first state takes up most of the strength with a spectroscopic factor of $C^2S = 4.16$, while the second only amounts to $C^2S = 0.7$.

Since in the direct reaction with ^{46}Ar, no evidence of populating the $j = 5/2$ states was observed, the calculations are shown only for $j = 1/2$ and $j = 3/2$, which also correspond to the states of interest to this work.

In order to assess the performance of the optical potentials, various combinations of parametrizations in the entrance and exit channels have been considered. With the intent of limiting the number of cases, only two distinct deuteron optical potentials have been considered. The calculation has also been performed with the parameters presented by the authors in reference[2] to compare the results with the global potential by Han et al.. Their performance in the deuteron channel of interest has been proved in Figure 6.1. The combination of the global potential by Han et al. with the parameters cited in the article for the exit channel (^{3}He) offers further confirmation of its efficacy. The distribution considering the ^{3}He potential by Becchetti et al. shows remarkable results, especially in the sensitivity range up to 23°, predicting correctly the position of maxima and minima as well as the attenuation and relative intensity of the peaks. The remaining combinations of the potential by Han et al. and Liang et al. or Trost et al. show a similar trend but fail to reproduce the data as closely as the other cases. More specifically, although the maxima and minima of the distribution appear well-positioned, the attenuation of the angular distribution is not accurately reproduced.

Further confirmation of the parametrization by Becchetti et al. is offered by its ability to reproduce both tritons and ^{3}He, which is proven by the performance in the experimental range of interest in the elastic scattering on tritons in Figure 6.3.

The considerations carried out according to the calculations presented in Figure 6.3 and 6.4 for the ^{3}He potential as well as Figure 6.1 for the deuteron potential clearly point to the combination of Becchetti et al. and Han et al. as the most most effective choice in modeling the reaction of interest.

6.2.2 ^{46}Ar(^{3}He,d)^{47}K

Given the previous remarks regarding the performance of the optical potentials, the direct reaction on ^{46}Ar has been computed with a singe step finite-range DWBA calculation with two potentials for the entrance channel (Trost et al. and Becchetti et al.) and two other potentials for the outgoing channel (An et al. and Han et al.). Every combination of the selected potential has been used to compute the angular distribution for the proton transfer channel do the ground state ($s_{1/2}, L = 0$), the first excited state at 360 keV ($d_{3/2}, L = 2$) and the state at 2.02 MeV ($f_{7/2}, L = 3$). While the angular distributions shown in Figure 6.4 hint at a sub-optimal performance of the potential of Trost et al., the

calculations are included in the current section to quantify the dependence of the final experimental result linked to the choice of the optical potential.

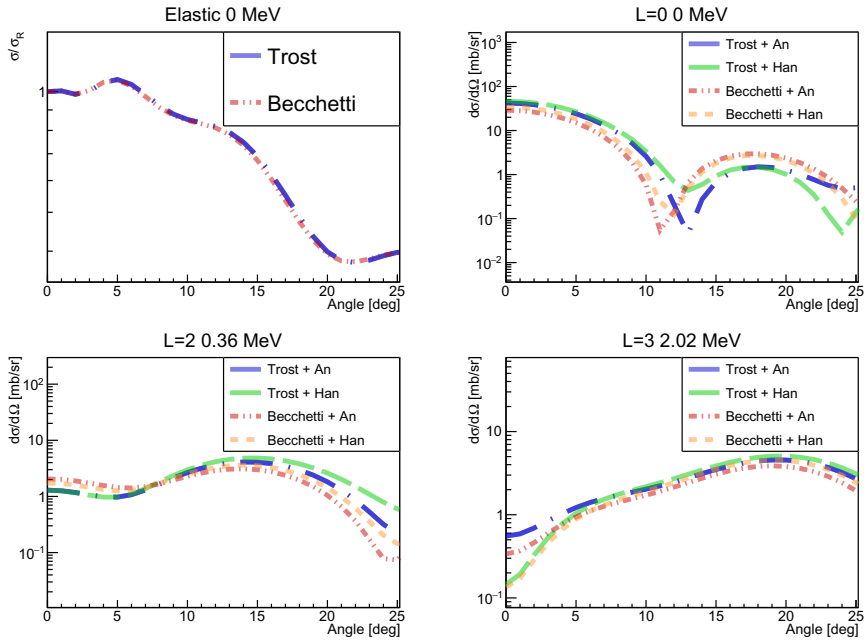

Figure 6.5: Angular distribution for the ^{46}Ar(^{3}He,d)^{47}K direct reaction with a ^{46}Ar radioactive beam with an energy of 357.2 MeV (corresponding to the mid target energy with an ice thickness of 35 μm. Combinations of different optical potentials are shown in the region of sensitivity of the experiment. (top left panel) Elastic reaction channel. (top right panel) $L = 0$ transfer to the ground state. (bottom left panel) $L = 2$ transfer to the $d_{3/2}$ state at 0.36 MeV. (bottom right panel) $L = 3$ transfer the state at 2.02 MeV.

Figure 6.5 shows the proton transfer reaction channels with the elastic scattering on ^{3}He in the angular range of experimental sensitivity. The ratio between the elastic cross-section and the Rutherford cross-section shows a close agreement between the two ^{3}He optical potentials by Trost et al. and Becchetti et al.. The transfer reaction channels, which are also dependent on the deuteron optical potentials, show great similarity between the combinations of Becchetti + An and Becchetti + Han. The only observed discrepancy stemming from the change of the deuteron potential resides in the $L = 3$ angular distribution at zero degrees. Nevertheless, comparing the cross-section value, it is clear that such a slight difference is undetectable since it lies in an angular range where the $L = 0$ transfer cross-section is more than two orders of magnitude higher.

Concerning the combinations with the ^{3}He optical potential by Trost et al., all reaction channels show similar angular distributions both in overall shape as well as absolute value with the exception of the $L = 0$ transfer channel.

In this case, the position of the maxima of the distributions is coherent with those produced by Becchetti et al.. Nevertheless, the attenuation, similarly to Figure 6.4, appears to be reproduced in a systematically different manner, while the position of the first minimum of the $L = 0$ is also shifted by $\approx 3°$ in the two combinations.

Figure 6.6 shows the same calculation in the whole angular range, where discrepancies are more evident for angles closer to 180°. In the graph relative to the elastic channel, it is also possible to observe the absorption component of the optical potential developed by Trost et al. and Becchetti et al. show a similar trend.

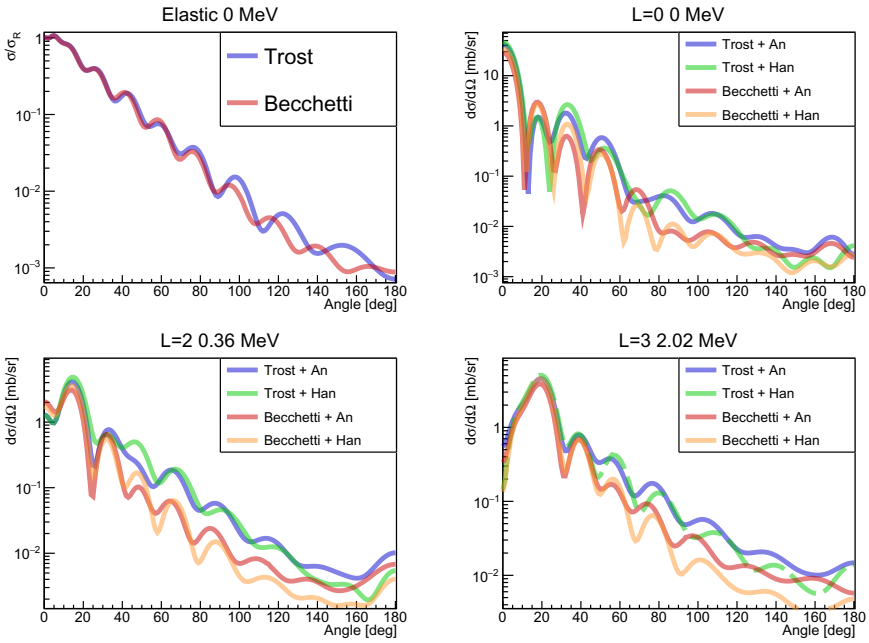

Figure 6.6: Angular distributions of Figure 6.5 in the full range. Discrepancies progressively increase for angles far from zero degrees. (top left panel) Elastic reaction channel. (top right panel) $L = 0$ transfer to the ground state. (bottom left panel) $L = 2$ transfer to the $d_{3/2}$ state at 0.36 MeV. (bottom right panel) $L = 3$ transfer the state at 2.02 MeV.

Bibliography

[1] An, H. and Cai, C. "Global deuteron optical model potential for the energy range up to 183 MeV". In: *Phys. Rev. C* vol. 73 (5 May 2006), p. 054605. DOI: 10.1103/PhysRevC.73.054605. URL: https://link.aps.org/doi/10.1103/PhysRevC.73.054605.

[2] Banks, S. et al. "The 48Ca(d→, 3He)47K reaction at 80 MeV". In: *Nuclear Physics A* vol. 437, no. 2 (1985), pp. 381–396. DOI: https://doi.org/10.1016/S0375-9474(85)90096-X. URL: https://www.sciencedirect.com/science/article/pii/S037594748590096X.

[3] Becchetti Jr, F. D. and Greenlees, G. W. "General set of ^{3}He and triton optical-model potentials for A > 40, E < 40 MeV." In: *pp 682-3 of Polarization Phenomena in Nuclear Reactions. / Barschall, H. H. (ed.). Madison, Wis. Univ. of Wisconsin Press (1971).* (Jan. 1971). URL: https://www.osti.gov/biblio/4753391.

[4] Bojowald, J. et al. "Elastic deuteron scattering and optical model parameters at energies up to 100 MeV". In: *Phys. Rev. C* vol. 38 (3 Sept. 1988), pp. 1153–1163. DOI: 10.1103/PhysRevC.38.1153. URL: https://link.aps.org/doi/10.1103/PhysRevC.38.1153.

[5] Catford, W. N. "What Can We Learn from Transfer, and How Is Best to Do It?" In: *Lecture Notes in Physics* (2014), pp. 67–122. DOI: 10.1007/978-3-642-45141-6_3. URL: http://dx.doi.org/10.1007/978-3-642-45141-6_3.

[6] Han, Y., Shi, Y., and Shen, Q. "Deuteron global optical model potential for energies up to 200 MeV". In: *Phys. Rev. C* vol. 74 (4 Oct. 2006), p. 044615. DOI: 10.1103/PhysRevC.74.044615. URL: https://link.aps.org/doi/10.1103/PhysRevC.74.044615.

[7] Hyakutake, M. et al. "Elastic scattering of 119 MeV 3He particles and energy and mass-number dependence of optical potential parameters". In: *Nuclear Physics A* vol. 333, no. 1 (1980), pp. 1–12. DOI: https://doi.org/10.1016/0375-9474(80)90013-5. URL: https://www.sciencedirect.com/science/article/pii/0375947480900135.

[8] Li, X., Liang, C., and Cai, C. "Global triton optical model potential". In: *Nuclear Physics A* vol. 789, no. 1 (2007), pp. 103–113. DOI: https://doi.org/10.1016/j.nuclphysa.2007.03.004. URL: https://www.sciencedirect.com/science/article/pii/S0375947407002291.

[9] Liang, C.-T., Li, X.-H., and Cai, C.-H. "Global3He optical model potential below 270 MeV". In: *Journal of Physics G: Nuclear and Particle Physics* vol. 36, no. 8 (July 2009), p. 085104. DOI: 10.1088/0954-3899/36/8/085104. URL: https://doi.org/10.1088/0954-3899/36/8/085104.

[10] Ogilvie, C. et al. “Spectroscopy of 47K and proton core-excitations in 48Ca from the 48Ca(t, α)47K reaction”. In: *Nuclear Physics A* vol. 465, no. 3 (1987), pp. 445–460. DOI: https://doi.org/10.1016/0375-9474(87)90358-7. URL: https://www.sciencedirect.com/science/article/pii/0375947487903587.

[11] Paxman, C. and the e793s collaboration. Private communication. 2021.

[12] Thompson, I. *Nuclear Reactions for Astrophysics : Principles, Calculation and Applications of Low-Energy Reactions*. Cambridge: Cambridge University Press, 2009.

[13] Trost, H.-J., Lezoch, P., and Strohbusch, U. “Simple optical model treatment of the elastic 3He scattering”. In: *Nuclear Physics A* vol. 462, no. 2 (1987), pp. 333–357. DOI: https://doi.org/10.1016/0375-9474(87)90551-3. URL: https://www.sciencedirect.com/science/article/pii/0375947487905513.

Chapter 7

Experimental Results

7.1 Analysis Strategy

The aim of the experiment is to measure the amount of $L = 2$ transfer to the first excited $(3/2^+)$ state in ^{47}K relative to the $L = 0$ transfer to the ground state $(1/2^+)$ (cf. Figure 3.8). This chapter will focus on the procedure to extract the needed information from the measured angular distribution.

In the case of nuclear states well separated in energy, the excitation energy spectrum allows the determination of the integral of each peak corresponding to an excited state. The states of interest of ^{47}K are separated by 360 keV, well below the experimental resolution in excitation energy. The resolution is hindered by the energy straggling on the target materials and the considerable thickness of the ^{3}He target. Nevertheless, exploiting the significant difference in angular distribution between the $L = 0$ and $L = 2$ transfer, it is possible to extract this ratio from a fit of the data. In particular, the $L = 0$ transfer to the ground state is characterized by a prominent peak at angles close to zero degrees in the center of mass frame of reference, which corresponds to backward angles in the lab (cf. Figure 4.6 and Figure 6.5). On the other hand, the first maximum of the $L = 2$ transfer occurs at approximately 15°, between the first and second peak of the $L = 0$ distribution. In the laboratory frame of reference, the first and second peaks are located respectively in correspondence to the annular and trapezoid detectors. Consequently, the measured data is sensitive to the first and second peaks of the $L = 0$ distribution and the first peaks of the $L = 2, 3$ transfers. Considering the differential cross sections integrated with respect to the solid angle covered by the annular detector, only the $L = 0$ transfer is expected to contribute to the measured deuterons significantly in this detector. Practically, this array component will fix the amount of $L = 0$ transfer, which will then be compared to the measured counts in the trapezoid detectors that will determine the amount of higher L transfer.

The simulations introduced in Chapter 5 included many experimental conditions which need to be considered not to introduce any bias in the comparison between the simulations and the data.

Figure 7.1 presents a schematic view of the interplay between experimental data and simulations and summarizes the analysis strategy that will be presented in the current chapter. The goal is to compare the simulated response of the setup to the different types of transferred angular momentum ($L = 0, 2, 3$) with experimental data to perform a maximum likelihood fit. The central role is played by the experimental data (in red), from which the conditions related to the setup can be extracted. These aspects concern electronic thresholds, missing strips, or target thickness and have been introduced in Chapter 5 and included in

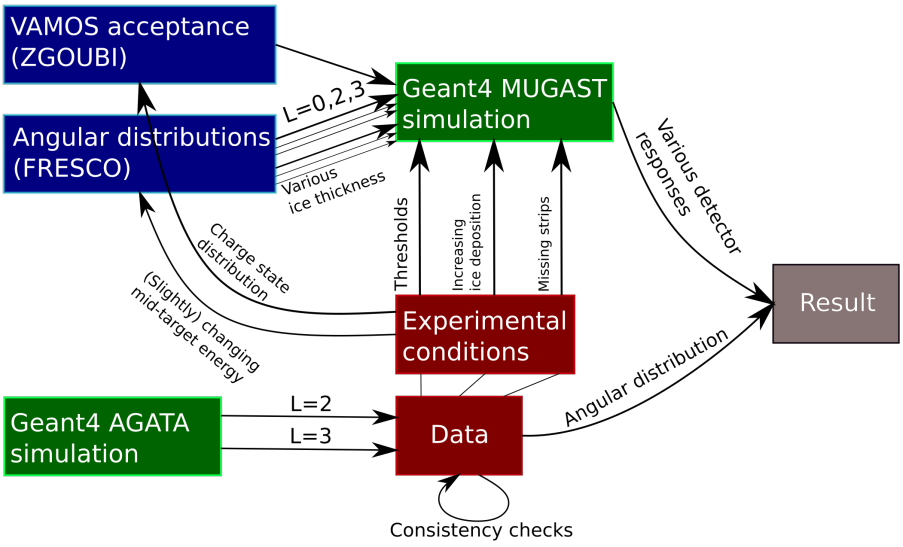

Figure 7.1: The response of the experimental apparatus has been characterized with Geant4 Monte Carlo simulations (Chapter 5) in order to operate the de-convolution of the transfer components ($L = 0, 2, 3$).

the Monte Carlo Geant4 simulation (in green). The geometry of the simulation is changed to increase the amount of ice deposited on the HAVAR windows of the target. The number of deuterons measured in the experimental data is binned in 5 μm intervals of ice thickness; simulations performed for each bin are added together with a number of events proportional to the number of deuterons measured. To each ice layer bin, its own angular distribution is associated. The DWBA calculations are performed with Fresco (cf. Chapter 6) and account for slight changes in the reaction dynamics caused by the gradual decrease in mid-target beam energy.

The final result is obtained by comparing the response of the simulation to the experimental data analyzed with the same procedure. Section 7.3 will present the procedure of extraction of the relative spectroscopic factors $(\mathcal{C}^2\mathcal{S}[L = 2]/\mathcal{C}^2\mathcal{S}[L = 0])$ based on the comparison of the experimental response with the simulated one.

Additional external calculations are necessary for the prediction on the acceptance of the magnetic spectrometer (VAMOS), which also depends on the experimental charge state distribution. The simulation of AGATA offers the possibility of consistency checks on the data and will be presented at the end of the chapter in section 7.5.

The main goal of this section is to extract this ratio of spectroscopic factors from the maximum likelihood fit of the experimental response of the setup.

7.2 Excitation Energy Spectrum

In all previous considerations concerning the energy loss of charged particles in the target layers, an equal repartition of the total ice thickness, extrapolated from the magnetic rigidity of the beam, has been assumed. To strengthen this assumption, it is possible to exploit the peculiarity of the $L = 0$ angular distribution, which is concentrated in the solid angle covered by the annular detector. There, it is crucial to know the amount of ice deposited on the target face, being the deuterons emitted at very low energy in the backward-most angles. Due to the low integrated differential cross-section of the other distributions in this angular range, it is possible to assume that all counts in the annular detector should be relative to excitation energy equal to 0 MeV. The percentage of ice on one face of the target relative to the other will effectively influence the position of the excitation energy peak. In particular, with an increase in the amount of ice on the backward face, the average energy loss correction applied to the deuterons will increase, which, in turn, will amount to a decrease in the mean excitation energy distribution. The excitation energy distribution measured by the sole annular detector can be fitted with a Gaussian distribution, and the extracted mean value and error can be compared to zero to verify if the ice repartition on the target faces is consistent with the data.

The amount of ice facing the spectrometer was set, in the energy loss calculations of the analysis procedure, in a range of values between 70% to 130% of the other side. The optimal value has been found to correspond to the equal repatriation of the total ice thickness among the two sides of the target. The total deuteron counts in the annular detector amounted to 135, and were fitted a Gaussian. With an equal repartition on the two windows, the mean of the excitation energy distribution is compatible with zero with a χ^2 minimization (-0.04 ± 0.16) or likelihood maximization (0.19 ± 0.34).

The excitation energy peak, shown in Figure 7.3, appears shifted at higher excitation energy values, despite being centered in the annular detector. This shift is generated by the counts in the trapezoid detectors at angles closer to 90°. It is attributed to the non-uniformity of the ice layer, which will be discussed in subsection 7.2.1 and can also be observed in the simulated data in Figure 7.7.

In order to further the resolution of the excitation energy peak, two trial procedures have been tested, both inherent to the beam optics and focalization. The following paragraphs will focus on the two approaches.

7.2.0.1 Position Reconstruction with the Beam Tracker

The possibility of reconstructing the position of incidence of a ^{46}Ar ion on the target on an event-by-event basis will be considered in the current section. This procedure usually requires the presence of two CATS2 beam tracker detectors, usually separated by a distance of 0.5 m and placed 2 m before the nominal target position. The measurement of the incidence of the charged ion on both detectors allows the reconstruction of the position on the target exploiting the measurement of the direction of the particle. In this particular experiment, the

choice to insert in the beam trajectory only one of the two detectors was made to reduce the straggling. Consequently, an event-by-event reconstruction requires important assumptions that can be verified by the effect of the applied correction on the excitation energy peak. Assuming that the beam focal point occurs in a position slightly offset with respect to the target nominal location along the longitudinal direction, the position measured by CATS2 will be proportional to the position on the target. The assumptions for this argument to hold are two: that the focal point of the beam is centered in the x-y plane and that no optical elements are present in the trajectory after the beam tracker. While the second hypothesis is certainly verified, the first will be considered in the next subsection 7.2.0.2.

The position on the target (x_T and y_T) can be reconstructed from the position on CATS2 (x_C and y_C) with the simple linear relation:

$$\begin{cases} x_T = C_x\, x_C \\ y_T = C_y\, y_C \end{cases}$$

A minimization procedure will identify two coefficients C_x and C_y, which best fit the experimental data.

Considering the former relation, it is possible to modify the standard calculations for the kinematic reconstruction, now assuming that the direction of the velocity and the position on the target are known from the beam position measured by the tracker. This will cause a (slightly) variation of the angle of emission and energy loss corrections. This correction is affected by the amount of ^{3}He gas crossed as well as the angle of incidence on the target windows.

In fact, the overall ^{3}He thickness crossed by the particle will depend on the position of incidence of the beam on the target and the emission direction of the deuterons measured by the silicon detector. Since the beam does not hit the target in its center, no longitudinal symmetry is present, the length of the collision vector from the reaction point to the target edge is computed with a minimization procedure. Aside from the total distance crossed in the gas medium, the angle with the normal vector of the surface of HAVAR and the ice deposit will modify the effective thickness of these materials.

A figure of merit has been defined to verify the outcome of each combination of scaling parameters C_x and C_y. During the experiment, three states have been populated, located at excitation energies of 0 MeV (corresponding to the $1/2^+$ state), 0.36 MeV ($3/2^+$) and 2.02 MeV ($7/2^-$). Anticipating the results presented in the course of this chapter, little evidence of $L = 2$ transfer to the $3/2^+$ state has been observed from the angular distribution. As a consequence, in order to limit the number of free parameters in the fit, only two Gaussian distributions were considered, corresponding to the two remaining states of ^{47}K. A possible choice for the figure of merit can be identified in the chi-square (χ^2) value for each parameter $\{C_x, C_y\}$ combination. In order to correlate the observed χ^2 and the number of degrees of freedom k with a probability, the following integral can be considered:

$$p(X > x|H) = \int_x^\infty dx' \, \mathrm{PDF}_{\chi^2}(x'; k) \tag{7.1}$$
$$\text{where} \quad \mathrm{PDF}_{\chi^2}(x; k) = \frac{1}{2^{k/2}\Gamma(k/2)} x^{k/2-1} e^{-x/2}$$

In this case, $p(X > x|H)$ represents the probability of obtaining a χ^2 value higher than the one measured (x), given the hypothesis H of a Gaussian model with a specific set of coefficients $\{C_x, C_y\}$. The highest the probability, the most likely for a set of coefficients to be correct.

A simple two-dimensional grid search for the coefficients C_x and C_y is tested, with possible values ranging from -1.1 to 1.1 for a total of 10 points in each dimension. For reference, a coefficient of 1 would indicate no focusing at all, while a coefficient of ± 1.1 indicates a diverging beam. Positive coefficients smaller than one, on the other hand, are indicative of a focal point located behind the nominal position of the target, while negative greater than -1 coefficients are relative to a spot preceding the target.

Figure 7.2 (top panel) shows the results of the grid search procedure with respect to the χ^2 figure of merit. With the extent of the available statistics, it is not possible to identify a single local maximum of probability. Nevertheless, the broad peak around $\{C_x, C_y\} = \{0.3, 0.1\}$ appears as the most likely choice, with probability values (according to equation 7.1) ranging around 50%, the optimal value. On the other hand, regions with unlikely coefficients (close to 1) are penalized by a low probability score, well below 10%.

7.2.0.2 Beam-Spot Position

Another option can be considered regarding the beam optics: the case of a focal point not aligned with respect to the nominal position of the target in the x-y plane. This aspect is justified by the observation, in previous experiments [4], of a beam-spot position out of the nominal center. Similar considerations to the previous chapter can be applied in this case. In particular, a grid-search scan of various possibilities can be performed, updating the energy loss and reaction kinematic calculations to account for the case of a beam colliding in a specific portion of the target.

The scan for the beam spot position ranges between -5 mm to 5 mm for each dimension (x and y plane), for a total of 10 points in each direction.

The results with the figure of merit presented in equation 7.1 are presented in Figure 7.2 (bottom panel). A broad peak in probability emerges in the region around $\{x, y\} = \{1\,\mathrm{mm}, 1\,\mathrm{mm}\}$. This value is consistent with a good fit in the nearby region, while more extreme values of beam-spot position are penalized by low probabilities.

While the amount of statistics limits the results that can be achieved by this procedure, the presented figures still serve as a further confirmation of the good beam optics throughout the experiment.

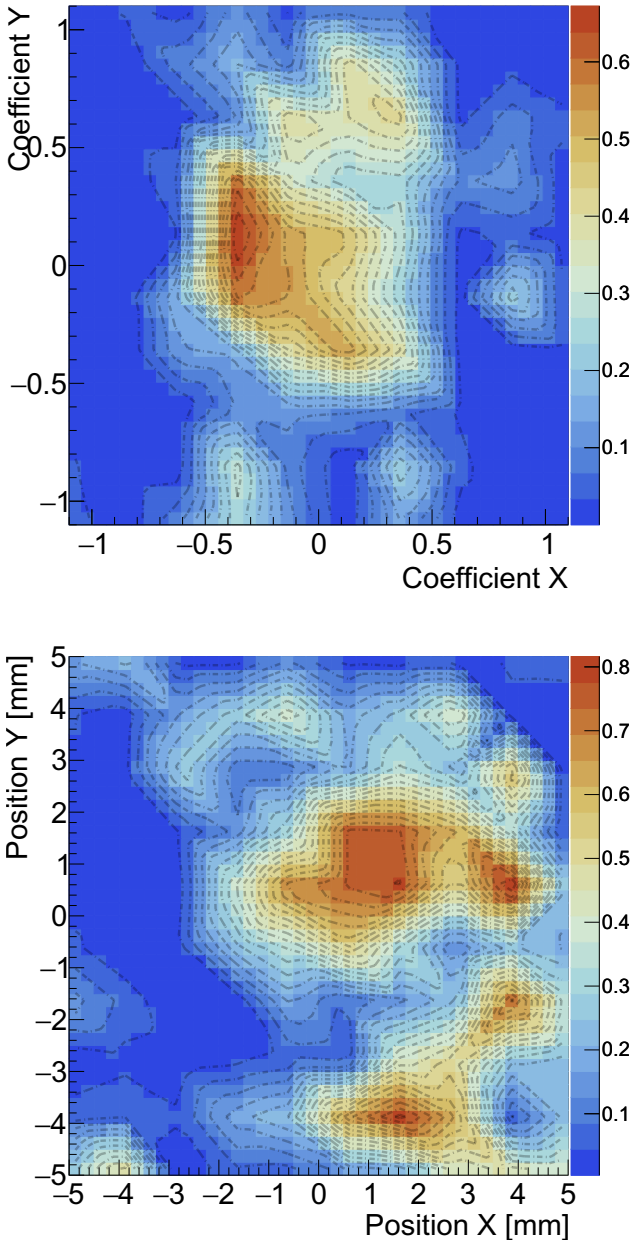

Figure 7.2: Grid search for a optimal excitation energy spectrum according to the figure of merit in equation 7.1. (top panel) Position of incidence on the target according the position on the beam tracker. (bottom panel) Beam spot position in the x-y plane.

Due to the absence of a unique relative minimum for both procedures and the fact that none of them showed a significant advantage, all future excitation energy spectra will assume a centered beam spot.

7.2.1 Ice Layer Uniformity

Due to the crystalline structure of the ice, the layer deposited on the HAVAR windows cannot be expected to possess a uniformity similar to that of a stretched metallic target. This aspect manifests in a poor resolution in the reconstruction of the excitation energy, where the energy-loss correction is essential in order to reconstruct the kinematics of the reaction. In particular, in a Geant4 simulation, a physical volume will feature uniform surfaces, not accounting for the energy straggling introduced by this aspect.

In order to account for a non-uniform thickness, a random value Δx has been sampled from a Landau distribution:

$$\Delta x = \frac{1}{\pi c} \int_0^\infty dt\, e^{-t} \cos\left(t\, \frac{x-\mu}{c} + \frac{2t}{\pi} \log\left(\frac{t}{c} \right) \right)$$

where c represents the scaling parameter and μ the location parameter. Due to the considerable tail of the distribution, the mean and variance integrals do not converge. This particular distribution is chosen because it is used for the description of fluctuations in the energy loss of a charged particle passing through a thin material layer.

The thickness of the layer Δx in the energy-loss calculations of the analysis of the simulated data is sampled on an event-by-event basis using for μ the expected thickness. The scaling c is set to match the left tail of the experimental data and is found to be $c = 0.2 * \mu$.

Figure 7.3 shows a comparison between the measured excitation energy and the simulated data. The two peaks are not completely resolved; nevertheless, the presence of the two components is evident. Due to the presence of prominent tails, the distributions do not resemble a Gaussian function, making a fit not a simple endeavor.

The maxima of the peaks appear not aligned to 0 MeV and 2.02 MeV and are shifted by the same amount to higher values. This is likely caused by the assumption of a consistent ice thickness on the HAVAR window. In particular, the peak in the annular detector appears well aligned with the expected value of 0 MeV, and the remaining counts are mainly introduced by the trapezoids that shift the peak to higher values.

Another aspect worthy of note regards the excitation energy points at negative energies. These experimental points can partly be attributed to the prominent tail of the distribution caused by the non-uniform thickness of the ice layer, while the remainder could be caused by a small proton contamination which will be discussed in subsection 7.4.2.

It is important to note that the results obtained from the angular distribution are independent of the energy loss reconstruction procedure since no selection is applied on this distribution.

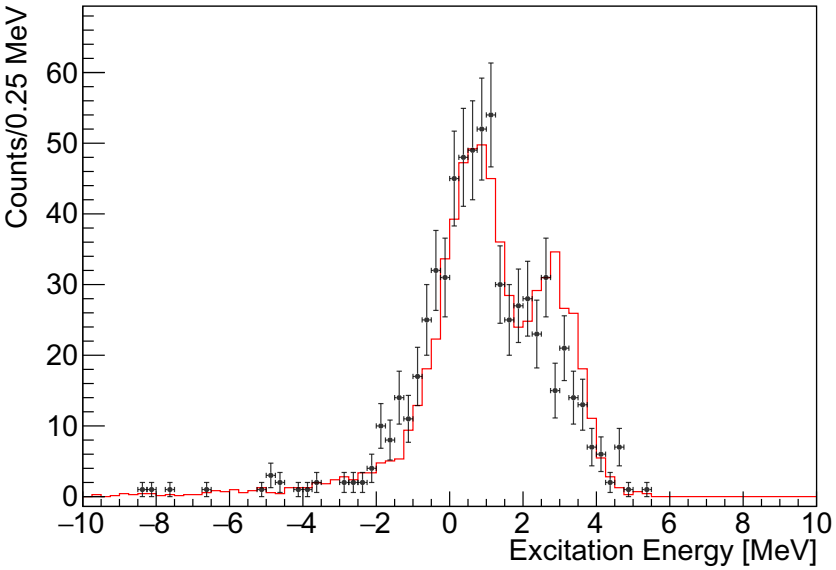

Figure 7.3: Comparison of the experimental excitation energy spectrum (in black) with the simulated spectrum (in red). The amount of counts in each peak is added according to the results of the fit performed in subsection 7.3.2. The prominent left tail of the distributions is caused by (and simulated as) the non-uniformity of the ice layer. The shift at higher excitation energy values is generated by counts in the trapezoids and is attributed to the non-uniformity of the ice layer, discussed in subsection 7.2.1. The same shift is present in the simulated data and can be observed in Figure 7.7.

7.3 Angular Distribution Deconvolution

7.3.1 An Introduction to the Procedure

The aim of this experiment is to extract the spectroscopic factors with a parametrization of the probability density function of the angular distribution.

This section will focus on the procedure to extract the relative spectroscopic factors in the framework of the maximum likelihood. The following definitions will be used in the course of this section:

- θ: the distribution parameter (in the parameter vector space) i.e. the spectroscopic factors of interest
- x : the measured dataset (i.e. the histogram and its bins)

In probabilistic terms, the correct figures for the spectroscopic factors will maximize the value of $p(\theta|x)$ which is the probability that the set of parameters corresponds to θ given the dataset x [5].

It is possible to reformulate the problem as a function of $p(x|\theta)$, the probability of obtaining the dataset x with parameters θ (the *likelihood* for θ), exploiting Bayes's theorem:

$$p(\theta|x) = \frac{p(x|\theta)p(\theta)}{p(x)}$$

In this case, $p(\theta)$ the so-called *prior probability*. It represents the probability of the set of parameters θ before the data x is taken into account. The choice of the prior probability can significantly alter the results, and for this analysis, the choice of a constant prior probability has been applied. A hard restrain on positive spectroscopic values has been introduced for physical reasons by limiting the maximization in this region.

On the other hand, $p(x)$ represents the probability of obtaining the measured dataset without accounting for any hypothesis, often referred to as *model evidence*. This factor is constant in a given measurement and represents a simple multiplicative (normalization) factor that is elided in any ratio of probabilities.

A more complete treatment of the concepts introduced here can be found in the Particle Data Group [6] and references therein.

It is possible to relate this expression to the set of experimental observables: $\{x_i\} = \{N, n_i\}$, where N is the total number of counts and n_i are the number of counts per bin. The likelihood for the parameters θ will now consist in $p(x|\theta) \equiv p(n \cap N|\theta)$:

$$p(n \cap N|\theta) = p(n|N, \theta)p(N|\theta) \tag{7.2}$$

The second term in equation 7.2 represents the probability dependence of obtaining N events given the parameter set θ. Assuming a Poisson point process, the probability of obtaining N counts amounts amounts to:

$$p(N|\theta) = \frac{\mu^N}{N!}e^{-\mu}$$

where μ corresponds to the average amount of events in the Poisson process in unit time and N to the number of occurrences. Focusing on the remaining term in the productory of equation 7.2 ($p(n_i|N, \theta) = \mathcal{L}(n_i|N, \theta)$), which represents the probability of having n_i counts in bin i if N is the total number of events, the correct choice is the multinomial distribution:

$$\mathcal{L}(n_i|N, \theta) = N! \left(\prod_i n_i!\right)^{-1} \left(\prod_i (p_i^\theta)^{n_i}\right) \tag{7.3}$$

With the condition on the total number of counts:

$$N = \sum_i n_i \quad \text{and} \quad 1 = \sum_i p_i^\theta$$

The probability factor p_i^θ represents the probability of obtaining a count in bin i and depends on the percentage of each type of transfer, as will be explained in subsection 7.3.2. This probability will be extracted from the Geant4 simulation. Three possible transfer channels are considered ($L = 0, 2, 3$) and the corresponding angular momentum will be labeled with index k. The simulation is produced with a number of events with a factor of more than 10^4 with respect to the experimental data in order to reduce statistical uncertainties.

Concerning the estimate of statistical uncertainties, in the case of a large data sample, the inverse of the covariance matrix $(cov(\theta_i, \theta_j)^{-1}_{i,j})$ is related to the hessian of the likelihood:

$$cov(\theta_i, \theta_j)^{-1}_{i,j} = - \left. \frac{\partial \ln \mathcal{L}}{\partial \theta_i, \theta_j} \right|_{\theta_{max}}$$

This expression is valid under some assumptions on the sample size; however, in the case of the following analysis, this approximation is not necessary due to the limited dimension of the parameters space θ which amounts to only two. A better estimation of the errors can be identified in the (hyper)surface defined by θ containing the maximum likelihood point described by:

$$\ln \mathcal{L}(\theta) = \ln \mathcal{L}(\theta_{max}) - \frac{s^2}{2} \tag{7.4}$$

where s represents the multiplication factor of a standard deviation confidence interval for the parameters. In the simple case of two parameters, the standard error (hypersurface) will consist in level curves of the likelihood surface (which will be presented in Figures 7.4 and 7.5).

It is also possible to show that in the limit of a large sample, the likelihood will approximate a Gaussian shape so that its logarithm will have a (hyper)parabolic trend. In other words, if the shape of the likelihood is similar enough to a Gaussian, the treatment of standard Gaussian errors is justified.

In the case of independent measurements x_i Gaussian distributed around the expected value p_i^θ and with known variance σ_i, the log likelihood maximization corresponds to the χ^2 minimization by a scaling and a constant:

$$\chi^2(\theta) = -2 \ln \mathcal{L}(\theta) + \text{constant} = \sum_{i=1}^{N} \frac{(x_i - p_i^\theta)^2}{\sigma_i^2} \tag{7.5}$$

As a consequence, the set of parameters that maximizes the likelihood corresponds to that that minimized the χ^2.

7.3.2 Comparison of Simulated Distributions

As presented in Chapter 2 the single particle differential cross section σ^{SP} and its experimental counterpart σ can be related as [2]:

$$\frac{d\sigma_k}{d\Omega} = g\, \mathcal{C}^2 \mathcal{S}_k \, \frac{d\sigma_k^{SP}}{d\Omega} \tag{7.6}$$

where k labels the populated state of interest (with a given angular momentum l and a given j) [2]. As presented in subsection 2.2.5, C stands for an isospin coefficient and is set equal to 1 in most cases, while g is the statistical factor dependent on the degeneracy of the state of interest and is set to $(2j+1)$ for nucleon addition and 1 for the removal.

This expression separates the reaction dynamics part (included in the differential single-particle cross-section) from the nuclear structure, which is contained in the spectroscopic factor $\mathcal{S}_i$ and consists in the integrated overlap between the wave-functions of the nucleus before and after the nucleon transfer.

In order to formalize the procedure from the statistical point of view, it is necessary to extract the dependence of the probabilities (p_i of equation 7.3) of having counts in each bin with respect to the spectroscopic factors which will act as the fit parameters. It is possible to decompose the problem in two events A_k and B_i:

$\mathbf{A}_k$	$\mathbf{B}_i$
Deuteron from reaction k is detected	Count falls in bin i

The values p_i correspond to the probability of having a count in bin i: $p(B_i)$, which needs to be computed with the so-called law of total probability:

$$p(B_i) = \sum_k p(B_i|A_k)p(A_k)$$

The two factors on the right-hand side of the equation can be computed as a result of the Monte Carlo Geant4 simulation presented in section 5.2.

The probability of the reaction labeled by k to occur is proportional to the cross-section since all other parameters remain constant. The total number of reactions N can be obtained by summing the exclusive cross-sections:

$$N_k = K \sum_k \int_{4\pi} d\Omega \, \frac{d\sigma_k}{d\Omega} = K \sum_k \mathcal{C}^2 \mathcal{S}_k \int_{4\pi} d\Omega \, \frac{d\sigma_k^{SP}}{d\Omega}$$

The constant K in the expression represents simply the experimental conditions which are constant for each value of transferred angular momentum and each bin:

$$K = I_{beam} \, n_{target} \, \Delta t \, \Delta x$$

where I_{beam} is the intensity in particles per second, n_{target} is the numerical target density (per unit of volume), Δt the acquisition time, and Δx the target thickness.

Having associated the number of events to a given reaction σ_k, and considering that the value of K is constant for all k, the probability that one particular reaction generates an event is straightforward to compute. The probability $p(\sigma_k)$

of each reaction labeled by k to occur is related to the ratio of the number of events relative to one particular reaction N_k over the sum of all events. Exploiting the constant value of K, the expression is the following:

$$p(\sigma_k) = \frac{\sigma_k}{\sum_{k'} \sigma_{k'}} = \frac{\mathcal{C}^2 \mathcal{S}_k \sigma_k^{SP}}{\sum_{k'} \mathcal{C}^2 \mathcal{S}_{k'} \sigma_{k'}^{SP}}$$

The event of interest $p(A_k)$ refers to the detection of a deuteron and thus depends on the detector efficiency ϵ_k in terms of solid angle coverage and other experimental factors. As a consequence, the probability has the following expression:

$$p(A_k) = \frac{\mathcal{C}^2 \mathcal{S}_k \sigma_k^{SP} \epsilon_k}{\sum_{k'} \mathcal{C}^2 \mathcal{S}_{k'} \sigma_{k'}^{SP} \epsilon_k} \tag{7.7}$$

The expression is normalized by ($p(\bigcup_k A_k) = \sum_k p(A_k) = 1$). On the other hand, it is also possible to compute the probability of having a count in bin i of the angular distribution which subtends a solid angle $\Delta\Omega_i$ with the following integrals:

$$p(B_i|A_k) = \left(\int_{\sum_{i'} \Delta\Omega_{i'}} d\Omega \, \frac{d\sigma_k}{d\Omega} \epsilon_k(\Omega) \right)^{-1} \int_{\Delta\Omega_i} d\Omega \, \frac{d\sigma_k}{d\Omega} \epsilon_k(\Omega) \tag{7.8}$$

$$= \left(\int_{\sum_{i'} \Delta\Omega_{i'}} d\Omega \, \frac{d\sigma_k^{SP}}{d\Omega} \epsilon_k(\Omega) \right)^{-1} \int_{\Delta\Omega_i} d\Omega \, \frac{d\sigma_k^{SP}}{d\Omega} \epsilon_k(\Omega) \tag{7.9}$$

where the factor $\epsilon_k(\Omega)$ has been introduced to account for the detection efficiency, which depends on the coordinates $\Omega = (\theta, \phi)$. The efficiency is not constant and depends on aspects such as the detector coverage or missing strips. At the same time, it also changes with the reaction type (thus the presence of the index k). Different reactions have a different probability of emission on the solid angle covered by the detector, and different excitation energies have different detection probability due to the presence of electronic thresholds.

In equation 7.9, the definition of the single-particle differential cross section (eq. 7.6) was used. The spectroscopic factors present in the numerator and denominator elide from the expression.

Also in this case the normalization is the following: $p(\bigcup_i B_i|A_k) = \sum_i p(B_i|A_k) = 1$. A Monte Carlo simulation which includes, in principle, all experimental conditions, will perform the ratio of integrals of equation 7.9 accounting correctly for the efficiency factor ϵ.

If $n_{k,i}^S$ represents the number of counts in bin i of the simulation relative to the reaction labeled by k, and N_k^S the total number of ejectiles detected in the simulation, expression 7.9 reduces to a simple ratio:

$$p(B_i|A_k) = \frac{n_{k,i}^S}{N_k^S} \tag{7.10}$$

Similarly, the efficiency of detecting a deuteron from a reaction k is tied to the simulation by the ratio between the total number of simulated events $N^S_{\rm tot}$.

$$\epsilon_k = \frac{1}{\sigma^{SP}_k}\int_{\Delta\Omega_i} d\Omega \frac{d\sigma^{SP}_k}{d\Omega}\epsilon_k(\Omega) = \frac{N^S_k}{N^S_{\rm tot}} \tag{7.11}$$

Summing all reactions with different transferred angular momentum (sum running over k), it is possible to obtain the expression for the probability of a count in bin i ($p(B_i)$) by combining equations 7.7, 7.9, 7.10, and 7.11:

$$p(B_i) = \frac{1}{\sum_{k'} \mathcal{C}^2\mathcal{S}_{k'}\sigma^{SP}_{k'}\epsilon_k}\sum_k \frac{n^S_{k,i}\mathcal{C}^2\mathcal{S}_k\sigma^{SP}_k\epsilon_k}{N^S_k} \tag{7.12}$$

The normalization condition using the expression for the total number of counts is: $N^S_k = \sum_i n^S_{k,}$.

If the main interest is related to relative spectroscopic factors, it is possible to express each spectroscopic factor relative to the reference one. For simplicity, the reference spectroscopic factor will be labeled by the index $k = 0$ and will be relative to the $L = 0$ transfer. Therefore, the set of fit parameters which was previously indicated by the set θ_k will be related to the spectroscopic factors as the ratio:

$$\theta_k = \frac{\mathcal{C}^2\mathcal{S}_{k'}}{\mathcal{C}^2\mathcal{S}_0}$$

The previous equation 7.12 can be transformed as:

$$p(B_i) = \frac{1}{\sum_{k'} \theta_{k'}\sigma^{SP}_{k'}\epsilon_k}\sum_k \frac{n^S_{k,i}\theta_k\sigma^{SP}_k\epsilon_k}{N^S_k} \tag{7.13}$$

being $\theta_0 = 1$ by definition. Since the interest is limited at the relative spectroscopic factor, the dimension of the parameter space is 2 (θ_0 is constrained to a unitary value).

7.3.3 The Experimental Outcome

Following the discussion in chapter 6, the analysis has been performed in the case of two combinations of optical potentials:

- Becchetti et al. [3] (^{3}He) and Han et al. [7] (deuteron)
- Trost et al. [8] (^{3}He) and An et al. [1] (deuteron)

The first combination is the most promising one as it is able to reproduce the differential cross section of the elastic scattering best. Nevertheless, the analysis has also been performed with the same procedure with the combination of the potentials by Trost et al. and An et al. in order to quantify the error introduced by the optical potential parametrization.

The maximization of the likelihood, due to the presence of a total of two parameters, has been performed with a simple grid search, allowing to observe the whole parameter space. Figure 7.4 (top left panel) presents the likelihood value as a function of the relative spectroscopic factors: $\mathcal{C}^2\mathcal{S}[L=2]/\mathcal{C}^2\mathcal{S}[L=0]$ (x-axis) and $\mathcal{C}^2\mathcal{S}[L=3]/\mathcal{C}^2\mathcal{S}[L=0]$ (y-axis). The likelihood is also compared to the χ^2 value in the same range (top right panel). The two procedures return compatible values for the amount of $\mathcal{C}^2\mathcal{S}[L=2]/\mathcal{C}^2\mathcal{S}[L=0]$ and $\mathcal{C}^2\mathcal{S}[L=3]/\mathcal{C}^2\mathcal{S}[L=0]$ relative transfers, with the second one showing smaller statistical errors. In both cases, the results hint at a suppressed $L=2$ transfer, with a ratio of spectroscopic factors that is compatible with zero. The red curves represent the statistical error computed according to equation 7.4 and 7.5.

The gradients of both the likelihood and the χ^2 in correspondence to the minimum are also shown in Figure 7.4 (bottom panel). The shapes closely resemble a parabolic one, justifying the treatment of errors in terms of standard deviation. Only one minimum is present in the whole parameter space, while the two fitted parameters appear anti-correlated. Table 7.1 presents the results and statistical errors.

Figure 7.5 shows the same procedure applied to the simulation of the other optical potential parametrization (Trost et al. + An et al.). The position of the $L=2$ relative transfer appears in the same location as the previous case, with similar statistical errors and correlation. On the other hand, a shift of the $L=3$ can also be observed. Similarly to the previous case, the results of the likelihood maximization and χ^2 minimization return statistically compatible results, with the latter presenting reduced statistical errors.

The result of the fit performed in the laboratory reference frame is shown in Figure 7.6 (left panel). Each component of the overall fit (in red) is also shown independently, while the residues are presented in the right panel of the figure. In order to be consistent with the described procedure, the assigned statistical errors correspond to the variance of the multinomial distribution. The reduced χ^2 value corresponds to $\chi^2/NDF = 0.83$, and is associated with a probability of 0.79 according to equation 7.1. The fit residues show no systematic trend along the angular range and appear evenly distributed around the zero value.

Experiments with thin targets and well-defined beam energy show clear kinematic lines in the correlation plot between energy and angle in the laboratory frame of reference. In the case of this experiment, the reaction energy is not fixed due to the gradual increase in thickness of the ice layer. As a consequence, little information can be conveyed by the energy and angle correlation plot. Nevertheless, a plot of excitation energy as a function of the laboratory angle will remove the dependence from the beam energy since all kinematic calculations are performed accounting for this aspect. Figure 7.7 shows the two quantities for the experimental data (left panel) and the simulation (right panel) for the case of the identified maximum of the likelihood (Figure 7.4). Despite the limited statistics, the peaks that arise from the maxima of the $L=0$ and $L=3$ distribution are evident and appear well reproduced by the simulated data.

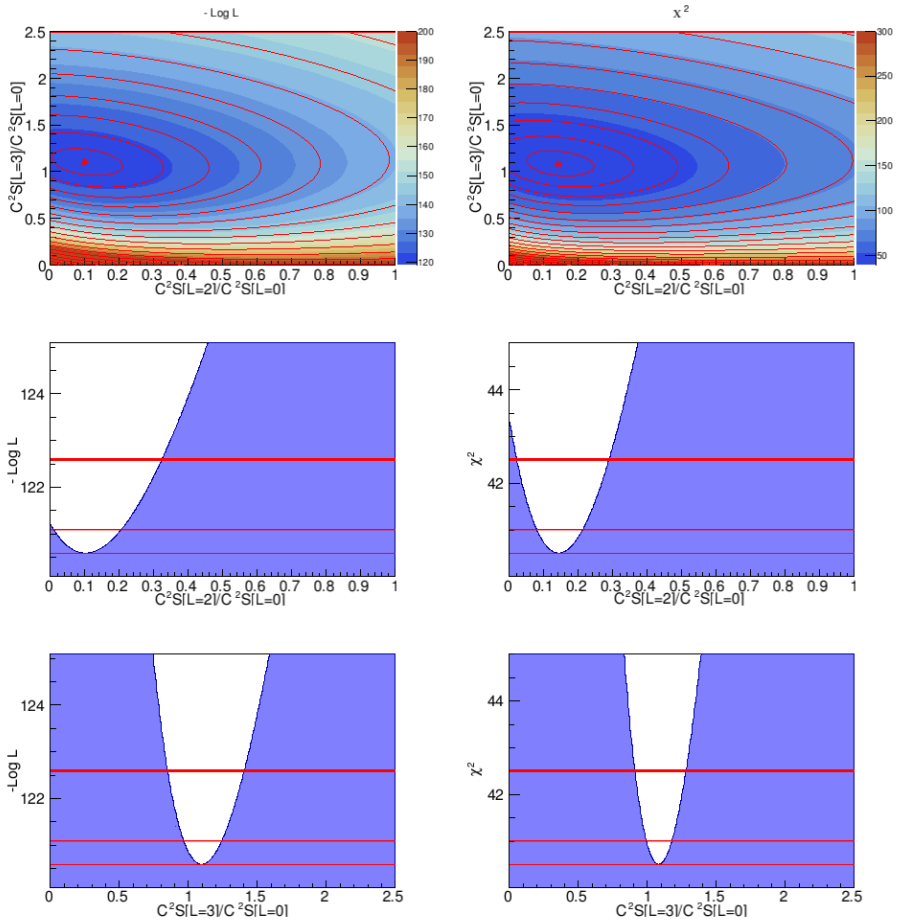

Figure 7.4: Fit parameter search based on the likelihood (left panel) and χ^2 (right panel). The fit is performed in the laboratory frame with a binning of 1 degree per bin. The parametrization of the optical potentials is by Becchetti et al. [3] (^{3}He) and Han et al. [7] (deuteron). The fit, presented in Figure 7.6 is indicative of a suppressed $L = 2$ transfer. For ease of comparison the likelihood $\mathcal{L}$ is presented as $-\ln \mathcal{L}$. Red lines indicate progressive values of the standard error (1σ, 2σ). The middle and bottom panels represent respectively the profile of the gradients in correspondence to the minimum for the $L = 2$ and $L = 3$ components.

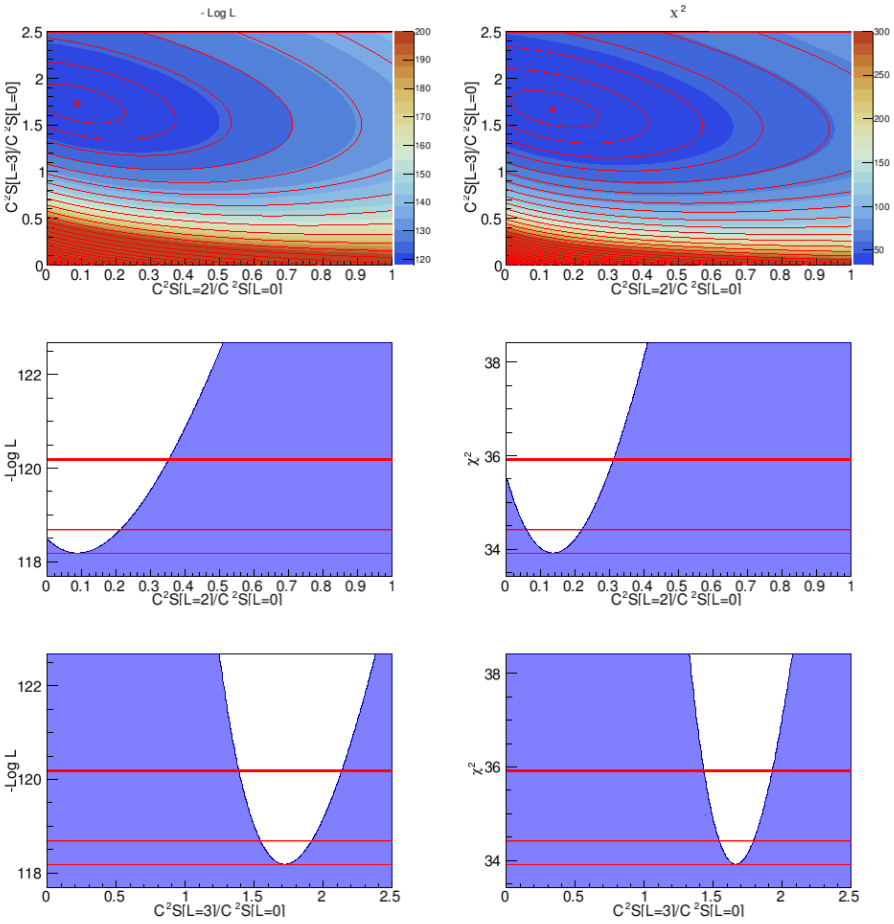

Figure 7.5: Fit results for the optical potential parametrization by Trost et al. [8] (^{3}He) and An et al. [1] (deuteron). All panels correspond to a similar procedure as Figure 7.4.

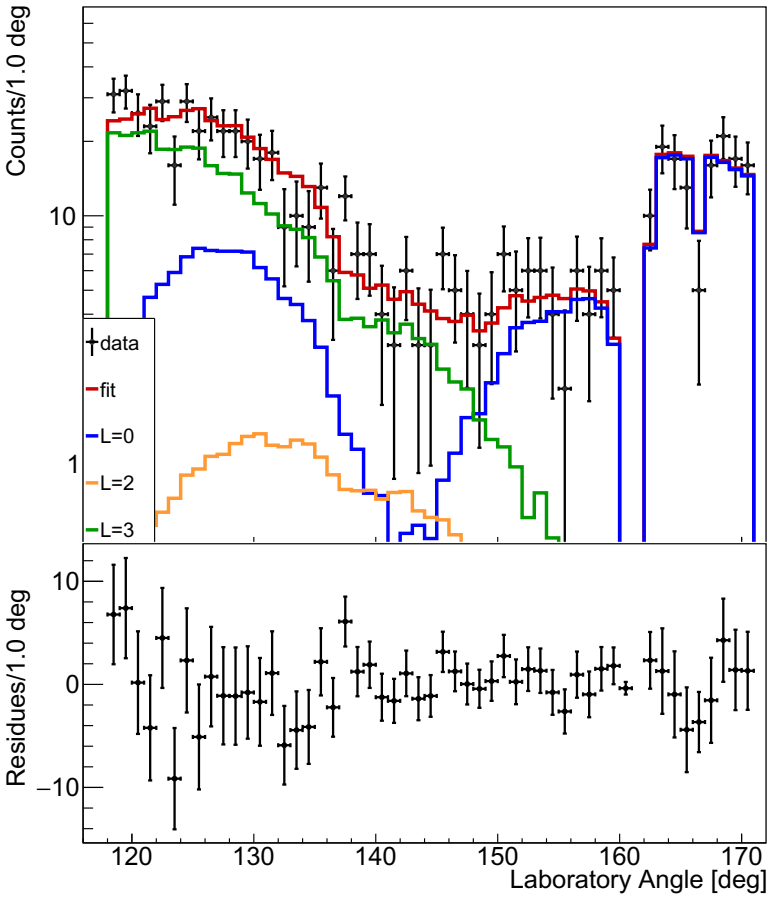

Figure 7.6: (top panel) Fit result on the laboratory count distribution relative to the maximization of the likelihood shown in Figure 7.4. The various components of the overall fit (red line) are shown, indicating a reduced amount of $L = 2$ transfer. (bottom panel) The residues with respect to the fitted distribution indicate no systematic trend.

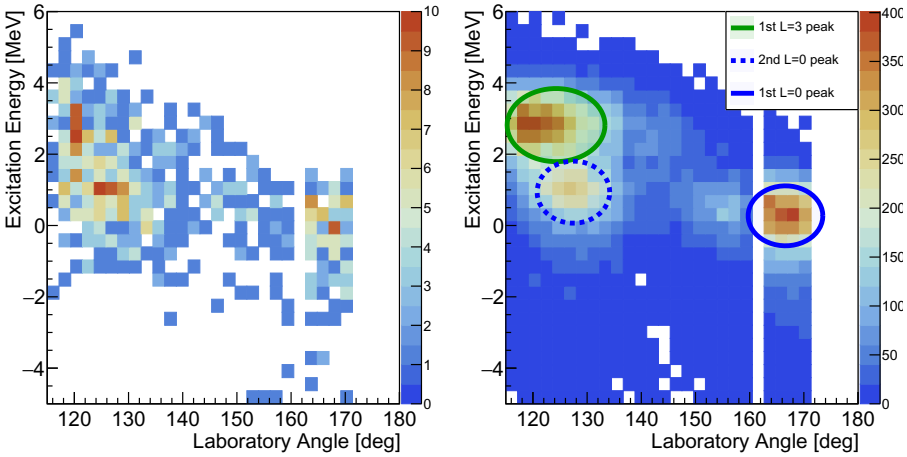

Figure 7.7: Correlation of Laboratory angle and excitation energy for the experimental data (left panel) and simulation (right panel). The latter has been computed based on the maximization of the likelihood shown in Figure 7.4. The accumulation of points appears reproduced in the experimental data.

7.3.4 Comparison with Theoretical Differential Cross Sections

7.3.4.1 Binned Angular Distributions

The experimental data consist of a binned distribution, i.e. a sampling of the angular distribution in intervals of the polar angle, considering a cylindrical symmetry.

It is indeed possible to obtain a center of mass distribution by applying an inverse Lorentz boost to the reaction fragments since it is customary to represent the angular distribution in this frame of reference, which removes some macroscopic effects which are only due to the kinematics of the reaction but not to the reaction channel properties.

In general, the number of counts in a binned angular distribution will depend on the differential cross-section as:

$$n_i \propto \sum_k \int_{\partial\Omega_i} d\Omega \frac{d\sigma_k}{d\Omega} \epsilon_k(\Omega) \tag{7.14}$$

This expression is similar to those introduced in the previous section, where the index i represents a given bin in θ, relative to a solid angle with boundaries represented by $\partial\Omega_i$. The efficiency ϵ_k has been introduced to account for experimental aspects. Index k expresses the various reaction channels. The proportionality constant is the same for all bins and reactions and depends on the integrated luminosity and can be neglected for the following reasoning.

Since the aim is to express the angular distribution as a function of only θ (and not ϕ), it is necessary to normalize the solid angle coverage in ϕ with the help of a simulation where the reaction fragment is emitted isotropically in the center of mass frame of reference.

The isotropic emission corresponds to the simulation of a constant differential cross-section in equation 7.14:

$$n_i^{\mathrm{ISO}} \propto \int_{\partial\Omega_i} d\Omega\, \epsilon_k(\Omega) \tag{7.15}$$

If it is safe to assume that the binning is fine enough for the differential cross-section to remain constant within the integration boundary $\partial\Omega$, it is possible to approximate equation 7.14 as a simple integration on the solid angle alone, assuming the differential cross-section as constant.

On a first approximation, the efficiency relative to a given bin i does not depend on the reaction label k in the case of isotropic emission. A small dependence can be present due to detection thresholds which depend on the excitation energy. While this aspect will be discussed later, taking the ratio of equation 7.14 and 7.15, it is possible to obtain an approximated expression of the measured differential cross section:

$$\frac{n_i}{n_i^{\mathrm{ISO}}} \propto \frac{\sum_k \int_{\partial\Omega_i} d\Omega \frac{d\sigma_k}{d\Omega}\, \epsilon(\Omega)}{\int_{\partial\Omega_i} d\Omega\, \epsilon(\Omega)} \approx \frac{\sum_k \frac{d\sigma_k}{d\Omega}\big|_{\theta_i,\phi_i} \int_{\partial\Omega_i} d\Omega\, \epsilon(\Omega)}{\int_{\partial\Omega_i} d\Omega\, \epsilon(\Omega)} = \sum_k \frac{d\sigma_k}{d\Omega}\bigg|_{\theta_i,\phi_i} \tag{7.16}$$

In summary, it is possible to observe that the ratio between the data and the simulated isotropic emission represents the differential cross-section in the case of a fine binning. This approximation does not hold if the angular distribution varies steeply within a bin.

Figure 7.8 shows the comparison between the calculated angular distributions and the experimental data obtained with the described procedure. The approximation of a constant value of ϵ_k in the case of isotropic emission depends on the excitation energy of the reaction. As a consequence, it is possible to remove this correlation by adding multiple isotropic simulations at the three different excitation energies: $0, 0.36$, and 2.02 MeV. The amount of events in each simulation is proportional to the reaction cross section, which depends on the spectroscopic factors obtained from the likelihood fit. The isotropic distributions are also obtained by adding numerous simulations performed at different ice thicknesses values.

The theoretical distributions have been computed with a weighted average of the angular distributions at different mid-target beam energy values. The weights applied are proportional to the number of deuterons measured at a given reaction energy caused by the presence of the ice.

The convolution of the distribution appears well reproduced by the experimental data. The most notable aspect is the correspondence of the maximum of the $L = 2$ differential cross section to the minimum of the measured

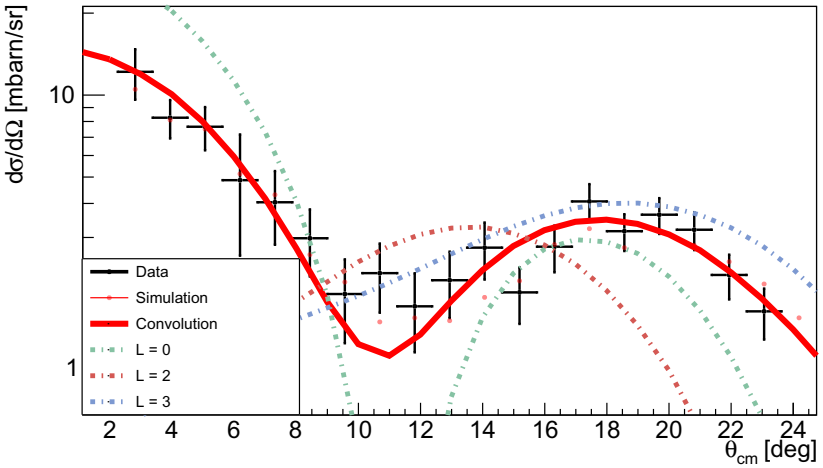

Figure 7.8: Comparison of the angular distribution in the center of mass with the DWBA calculations of subsection 6.2.2. All distributions are shown together with the convolution obtained from the maximization of the likelihood relative to Figure 7.4.

distribution. This aspect points towards the sensitivity of the experiment to the $L = 2$ transfer, which is then concluded to be very weak.

7.4 Evaluation of Systematic Errors

7.4.1 Optical Potential Dependence

An unavoidable source of uncertainty derives from the parametrization of the optical potential. Section 6.2.2 focused on the characterization of the impact of different parametrizations on the resulting angular distribution. A strong argument was made for the combination of the optical potential by Becchetti et al. for the incoming flux and by Han et al. for the outgoing channel. Nevertheless, to quantify the error introduced by the choice of the potential is possible to consider a different model, such as the combination of the parametrization by Trost et al. and An et al..

While the distributions obtained by the two different combinations present a difference in intensity of the first and second peaks of the $L = 0$ distribution (cf. subsection 6.2.2), their position remains unvaried.

Figure 7.9 presents the contour generated by the 1σ and the minimum values for the two potentials.

The effect of the different parametrization is to shift the $\mathcal{C}^2\mathcal{S}[L = 3]/\mathcal{C}^2\mathcal{S}[L = 0]$ relative spectroscopic factor to higher values, while maintaining a similar value for the amount of $\mathcal{C}^2\mathcal{S}[L = 2]/\mathcal{C}^2\mathcal{S}[L = 0]$. The statistical errors and the

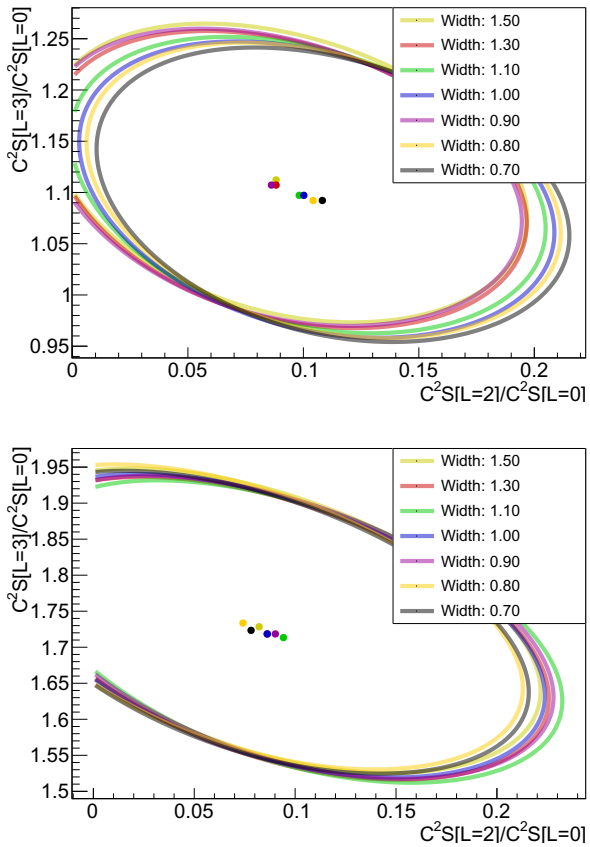

Figure 7.9: Two dimensional standard error contour based on the maximization of the likelihood with the combination of optical potentials relative to Figure 7.4(top panel) and 7.5(bottom panel). Different angular bin widths have been tested to estimate potential systematic errors. The widths, expressed in degrees range from 0.7° to 1.5° and return similar results.

correlation appear similar. A further test on the possibility of the introduction of systematic errors with different angular bin widths has also been verified in both cases. All results appear compatible and no systematic trend emerges by varying the angular bin width.

7.4.2 Proton Background Contribution

Further systematic uncertainty could be introduced by a contamination of protons in the selection of the deuterons in the energy time-of-flight correlation matrix (cf. Figure 4.30). This possibility has been tested by shifting the time of flight of particles detected in MUGAST by 5 ns. This change allows for most of the protons from the deuteron breakup reaction channel (^{46}Ar(^{3}He,pn)^{47}K) to be considered as deuterons. As a consequence, in the analysis, the detected particles will be a combination of protons and deuterons. The same selection algorithm is applied for the selection in the magnetic spectrometer, effectively processing protons as if they were deuterons. This implies that all the reaction kinematic calculations and energy loss correction are also computed for the protons.

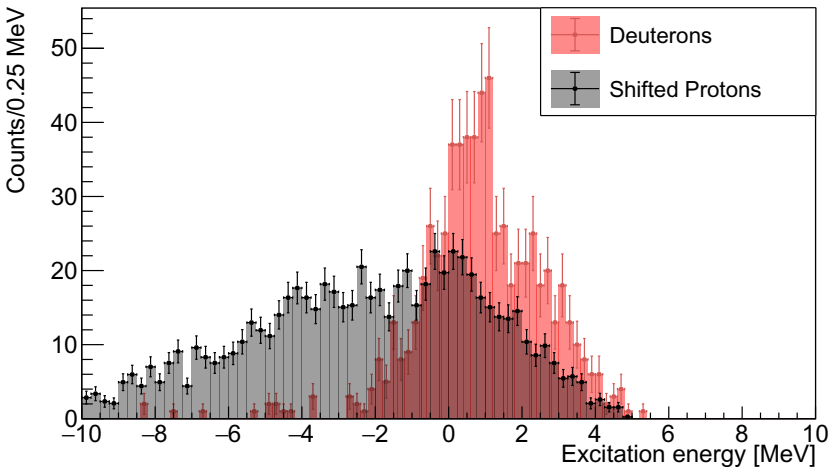

Figure 7.10: Comparison of the experimental excitation energy with the same analysis performed by shifting the time of flight of the particles by 5 ns. The procedure effectively allows protons to enter the selection of deuterons and are processed as such.

Figure 7.10 shows the outcome of the procedure on the excitation energy peak. The excitation energy distribution for the combination of protons and deuterons (in black) has been normalized to the integral of the experimental distribution (in red). Protons lose less energy in a medium with respect to deuterons; as a consequence, the energy loss correction tends to apply higher values of correction. Moreover, protons are tied to the three-body reaction

^{46}Ar(^{3}He,pn)^{47}K (since the gate on ^{47}K in VAMOS is present), so that the correlation between energy and angle is no longer significant. This procedure estimates that a large contribution of protons would entail a high amount of counts at excitation energies between -5 to 0 MeV, which are not observed in the experimental data. In fact, only a few counts are present at very negative energies, indicating a contamination lower than 2%.

7.5 The Gamma-Ray Spectrum

In coincidence with ^{47}K, a considerable amount of protons is detected. These counts are associated with the deuteron breakup reaction channel, consisting of the three-body reaction ^{46}Ar(^{3}He,pn)^{47}K.

Figure 7.11 shows the γ-ray spectrum in coincidence with ^{47}K tagged in VAMOS. Events are Doppler corrected on an event-by-event basis, using the velocity vector provided by the magnetic spectrometer. Although the position sensitivity of AGATA combined with the high resolution of HPGe detectors usually allows a finer binning, the uncertainty introduced by the long-lived states of ^{47}K and presented in subsection 5.3.2, has the effect of broadening the peaks, justifying a width of 8 keV.

A considerable amount of γ-rays at 360 keV are present, while an accumulation of counts can also be observed at $\approx$ 1660 keV. This spectrum constitutes a complementary picture of the previous considerations regarding the angular distribution. As a consequence, it is of interest to investigate the origin of these peaks.

The $7/2^-$ state at 2020 keV has a 88(9)% branching ratio to the 360 keV state so that most of the counts at 1660 keV should correspond to the emission of a 360 keV photon.

The efficiency curve will modulate significantly the integral of the two peaks that are far apart in energy. Further differences in efficiency are caused by the half-lives of the two states: 1.1(3) ns in the case of the $3/2^+$ state and 6.3(4) for the $7/2^-$.

The Geant4 simulation presented in section 5.3 contains both aspects and can be used to interpret the experimental response in the case of two different types of feeding. The background shown in Figure 7.11 is calculated by scaling the Doppler corrected spectrum outside the coincidence peak of AGATA (cf. Figure 4.35). The comparison indicates that the number of counts in the peak at 360 keV is compatible with the feeding to the $7/2^-$ state.

An accumulation of counts is also present around 1500 keV and corresponds to the emission of a 1345(3) keV photon by isotopes of ^{46}K implanted in the chamber. These isotopes are, in turn, part of the decay chain of ^{46}Ar. The emission of the γ-ray occurs at rest, generating a broadening of the peak in the Doppler-corrected spectrum. This aspect has been verified by comparison with the spectrum without any Doppler correction.

The same consideration can be made for the distribution located near 550 keV that can be ascribed to the 511 keV photons.

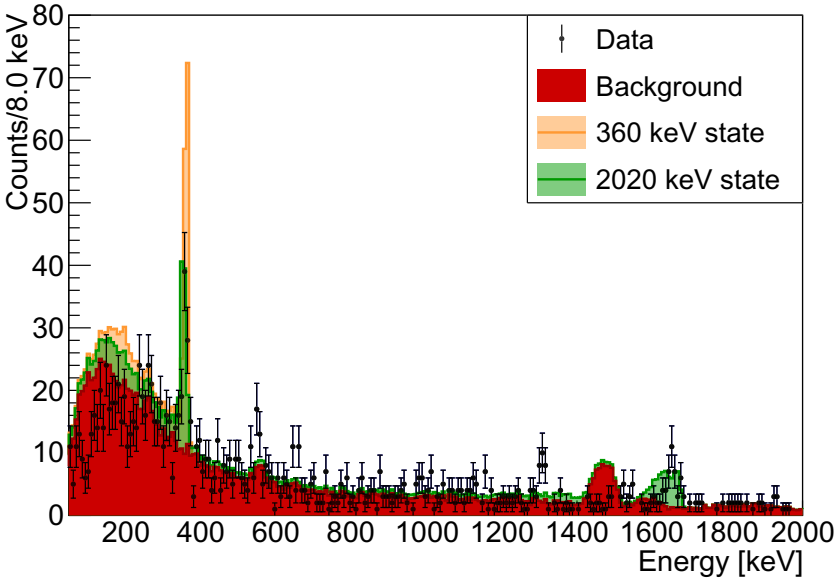

Figure 7.11: Comparison of add-back γ-ray spectrum in coincidence with ^{47}K in VAMOS. The experimental data is compared with simulated data in the case of direct feeding to the $3/2^+$ state and the $7/2^-$ state.

Another accumulation of points is observed around 1319 keV, consistent with the population of a ^{47}K state at 3350(30) keV $(5/2^+, 3/2^+)$, which decays to the $7/2^-$ state.

To quantify the previous results in terms of spectroscopic factors, it is possible to observe that the ratio between the amount of γ rays emitted at 360 keV (N_{360}) and at 1660 keV (N_{1660}) is given by the following expression:

$$\frac{N_{360}}{N_{1660}} = \frac{\sigma_2^{SP}\mathcal{C}^2\mathcal{S}[L=2]\,\epsilon_{360,2} + \sigma_3^{SP}\mathcal{C}^2\mathcal{S}[L=3]\,\epsilon_{360,3}\,BR}{\sigma_3^{SP}\mathcal{C}^2\mathcal{S}[L=3]\,\epsilon_{1660,3}\,BR}$$

where $2, 3$ label respectively the $3/2^+$ and $7/2^-$ states, σ_i the single-particle cross sections, ϵ the detection efficiencies at the labeled energy and relative to the indexed reaction and BR the branching ratio from the $7/2^-$ to the $3/2^+$ state.

Rearranging the expression, the ratio of spectroscopic factors can be determined from the ratio of γ rays count:

$$\frac{\mathcal{C}^2\mathcal{S}[L=2]}{\mathcal{C}^2\mathcal{S}[L=3]} = \frac{BR * \sigma_3 \left(\epsilon_{1660,3}\,\frac{N_{360}}{N_{1660}} - \epsilon_{360,3}\right)}{\sigma_2\,\epsilon_{360,2}}$$

The efficiency values can be found in table 5.1 in the case of a reaction populating the $7/2^-$ or the $3/2^+$ state. The branching ratio is set to $BR = 0.883$

and the single-particle cross sections amount to: $\sigma_2 = 1.67$ mbarn/srad and $\sigma_3 = 3.13$ mbarn/srad. These values are obtained by averaging the cross sections relative to different ice thicknesses with weights proportional to the number of deuterons measured at a given mid-target beam energy. The integrals of the two peaks amount to: $N_{360}/N_{1660} = 1.48 \pm 0.52$ which leads to a ratio of spectroscopic factors of: $\mathcal{C}^2\mathcal{S}[L=2]/\mathcal{C}^2\mathcal{S}[L=3] = 0.10 \pm 0.36$. The error is large due to the limited amount of statistics; nevertheless, it is compatible with the experimental value extracted from the angular distribution.

7.5.1 Triple Coincidences

A triple coincidence event requires the detection of a ^{47}K reaction fragment in VAMOS, a deuteron in MUGAST, and a γ ray in AGATA. The efficiency of the combined setup, being the product of all efficiencies, significantly reduces the statistics. Nevertheless, the high energy resolution of the HPGe detectors allows for a precise gate on the photon energy, thus reducing the amount of background in the time coincidence.

Figure 7.12 shows the Excitation energy spectrum of MUGAST in coincidence with a detected 360 keV γ-ray. The spectrum shows a collection of points around 2 MeV, consistent with a $L = 3$ transfer. The left tail of the distribution resembles the one observed in subsection 7.2.1 and was attributed to the ice thickness non-uniformity.

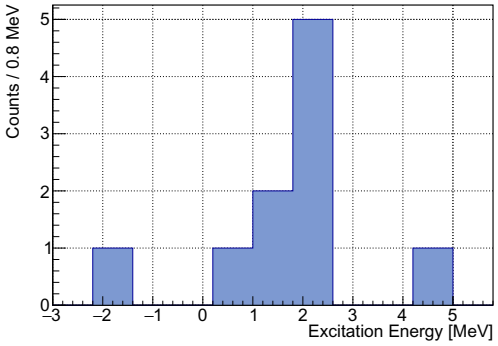

Figure 7.12: Excitation energy spectrum with triple coincidences relative to the detection of ^{47}K by VAMOS, a deuteron by MUGAST and a γ ray within a 40 keV interval around 360 keV in AGATA. The counts accumulate around 2 MeV, indicating that most counts are relative to the direct population of the state at 2020 MeV.

The γ-ray spectrum in coincidence with deuterons is shown in Figure 7.13, where the peak a 360 keV corresponds to the counts shown in Figure 7.12.

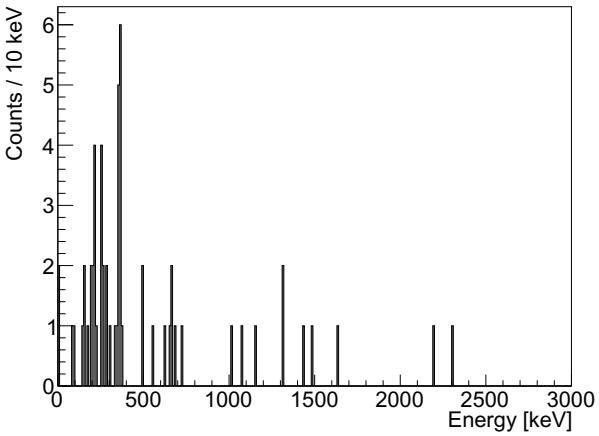

Figure 7.13: Addback spectrum in coincidence with ^{47}K in VAMOS and deuterons in MUGAST.

7.6 Conclusions of the Analysis

In conclusion, a reduced $L = 2$ transfer has been observed and the consistency among the experimental data has been tested. Table 7.1 summarizes the results obtained by the statistical considerations and the evaluation of the systematic errors. The statistical correlation coefficient $\rho_{1,2}$ between the relative spectroscopic factors has been estimated as [5]:

$$\rho_{1,2} = \frac{\mathrm{cov}[\theta_1, \theta_j]}{\sigma_1 \sigma_2} = -0.35$$

The choice of the optical potential, discussed in subsection 6.2.2, does not affect the result relative to the $L = 2$ transfer, lowering the ratio of spectroscopic factors ($\frac{\mathcal{C}^2\mathcal{S}[L=2]}{\mathcal{C}^2\mathcal{S}[L=0]}$) by 0.02, a value that corresponds to one fifth of the statistical error.

The discrepancy with the values produced by shell-model calculations will be discussed in Chapter 8 in the framework of current theoretical models.

	Value	**Statistical Uncertainty**	**Binning Uncertainty**
$\frac{\mathcal{C}^2\mathcal{S}[L=2]}{\mathcal{C}^2\mathcal{S}[L=0]}$	0.10	$^{+0.10}_{-0.10}$	$^{+0.02}_{-0.01}$
$\frac{\mathcal{C}^2\mathcal{S}[L=3]}{\mathcal{C}^2\mathcal{S}[L=0]}$	1.10	$^{+0.15}_{-0.13}$	$^{+0.03}_{-0.02}$

Table 7.1: Final experimental results for the relative spectroscopic factors: $\frac{\mathcal{C}^2\mathcal{S}[L=2]}{\mathcal{C}^2\mathcal{S}[L=0]}$ and $\frac{\mathcal{C}^2\mathcal{S}[L=3]}{\mathcal{C}^2\mathcal{S}[L=0]}$. The uncertainties introduced in section 7.4 and 7.3.3 are reported.

Bibliography

[1] An, H. and Cai, C. "Global deuteron optical model potential for the energy range up to 183 MeV". In: *Phys. Rev. C* vol. 73 (5 May 2006), p. 054605. DOI: 10.1103/PhysRevC.73.054605. URL: https://link.aps.org/doi/10.1103/PhysRevC.73.054605.

[2] Aumann, T. et al. "Quenching of single-particle strength from direct reactions with stable and rare-isotope beams". In: *Progress in Particle and Nuclear Physics* vol. 118 (2021), p. 103847. DOI: https://doi.org/10.1016/j.ppnp.2021.103847. URL: https://www.sciencedirect.com/science/article/pii/S0146641021000016.

[3] Becchetti Jr, F. D. and Greenlees, G. W. "General set of ^{3}He and triton optical-model potentials for A $>$ 40, E $<$ 40 MeV." In: *pp 682-3 of Polarization Phenomena in Nuclear Reactions. / Barschall, H. H. (ed.). Madison, Wis. Univ. of Wisconsin Press (1971).* (Jan. 1971). URL: https://www.osti.gov/biblio/4753391.

[4] Girard-Alcindor, V. "Above barrier narrow resonances in fluorine-15". PhD thesis. Normandie Université, 2020.

[5] Group, P. D. et al. "Review of Particle Physics". In: *Progress of Theoretical and Experimental Physics* vol. 2020, no. 8 (Aug. 2020). 083C01. DOI: 10.1093/ptep/ptaa104. eprint: https://academic.oup.com/ptep/article-pdf/2020/8/083C01/34673722/ptaa104.pdf. URL: https://doi.org/10.1093/ptep/ptaa104.

[6] Group, P. D. et al. "Review of Particle Physics". In: *Progress of Theoretical and Experimental Physics* vol. 2020, no. 8 (Aug. 2020). 083C01. DOI: 10.1093/ptep/ptaa104. eprint: https://academic.oup.com/ptep/article-pdf/2020/8/083C01/34673722/ptaa104.pdf. URL: https://doi.org/10.1093/ptep/ptaa104.

[7] Han, Y., Shi, Y., and Shen, Q. "Deuteron global optical model potential for energies up to 200 MeV". In: *Phys. Rev. C* vol. 74 (4 Oct. 2006), p. 044615. DOI: 10.1103/PhysRevC.74.044615. URL: https://link.aps.org/doi/10.1103/PhysRevC.74.044615.

[8] Trost, H.-J., Lezoch, P., and Strohbusch, U. "Simple optical model treatment of the elastic 3He scattering". In: *Nuclear Physics A* vol. 462, no. 2 (1987), pp. 333–357. DOI: https://doi.org/10.1016/0375-9474(87)90551-3. URL: https://www.sciencedirect.com/science/article/pii/0375947487905513.

Chapter 8

Theoretical Considerations and Conclusions

This section will discuss the experimental results in the framework of nuclear models. The ^{46}Ar isotope lies in a region where density functional theory, ab initio, and shell-model calculations prove to be a powerful tool for the investigation of the nuclear structure. In particular, theoretical models seem to indicate that the experimental result observed in the previous chapter could be explained by a structure property of the ground state of ^{46}Ar. Since the landscape of nuclear models is vast, this chapter has no intent of a detailed description of the calculations but merely aims at offering a bigger picture in the discussion of the experiment in terms of current theoretical frameworks in this field.

8.1 Shell-Model Calculations

The current section will present shell-model calculations performed to further investigate the nature of the discrepancy with the experimental data and gain a clear panoramic of the problem in terms of the model.

They were performed [11] with the m-scheme shell-model code ANTOINE[4, 5]. The code, developed in FORTRAN in 1999, allows for the treatment of so-called giant matrices exploiting the Lanczos diagonalization method. The necessity to operate with high dimensional matrices directly reflects the necessity of a large valence space to obtain spectroscopic information comparable with real-world data. The proliferation of the basis dimension is easy to grasp with a simple calculation. Defining D_π (D_ν) as the valence space for protons (neutrons), and n_π (n_ν) the number of valence protons (neutrons), the dimension N of the basis is given by the product of two binomial coefficients:

$$N = \begin{pmatrix} D_\pi \\ n_\pi \end{pmatrix} \times \begin{pmatrix} D_\nu \\ n_\nu \end{pmatrix} \tag{8.1}$$

The calculations were performed with a neutron valence space spanning the entire $sd - pf$ shell and protons restricted to the sd shell. The truncation in the m-scheme allowed the excitation of up to 4 jumps across the $N = 28$ gap ($4p - 4h$ configurations). Proton and neutron effective charges were set to the standard value of $\delta_p = 0.5$, $\delta_n = 1.5$, similarly to the calculations performed in reference [10] and [12].

According to equation 8.1, the dimension of the basis for the considered valence space would amount to $N = 14902327440$, which in the case of $M = 0$ Slater determinants with truncation reduces to an effective dimension of $N = 4784329$.

Table 8.1 presents the results for the spectroscopic information of interest concerning the ground state and the first excited states of ^{46}Ar and ^{47}K. In particular, the energy of the first excited state is close to the calculated value. The same consideration cannot be made for the transition probability of ^{46}Ar that features the discrepancy already presented in the dedicated subsection 3.2.3.

	Energy (keV)	**B(E2)↓** (e^2fm^4)
^{46}Ar (Experimental)	1577(1)	43.2(44)
^{46}Ar (SDPF-U)	1652	104
^{46}Ar (Alternative)	1632	103
^{47}K (Experimental)	360(1)	-
^{47}K (SDPF-U)	324	40.5
^{47}K (Alternative)	302	45.0

Table 8.1: Comparison of the energy and transition probabilities of the first excited state of ^{46}Ar and ^{47}K from the literature and the shell-model calculations with the SDPF-U interaction and an alternative interaction.

A complementary calculation has also been performed with the NATHAN code and an alternative interaction to test the stability of the shell-model results. This interaction has been generated starting from the SDPF-U by changing the monopoles between the protons in the pf shell and the neutrons. This alternative interaction has been used for calculations involving the $7/2^-$ state in ^{47}K, thus opening the pf space for protons. The interaction predicted the first $(3/2^+)$ state in ^{47}K at an excitation energy of 302 keV using the same valence space of the SDPF-U calculations. Opening the $Z = 20$ core for protons (with configurations of up to $4p-4h$) allowed the calculation of the $7/2^-$ state that is predicted at an energy of 2066 keV, in close correspondence with its experimental counterpart. As far as ^{46}Ar is concerned, this modified interaction returned an energy value of 1632 keV for the 2^+ state and a transition probability of $103\,e^2\mathrm{fm}^4$, consistent with the SDPF-U value.

The experimental electric quadrupole reduced transition probability ($B(E2)$) for the $3/2^+$ state of ^{47}K is not known since no mixing ratio for the decay to the $1/2^+$ ground state has been measured experimentally. Nevertheless, combining the shell-model values for the magnetic ($B(M1) = 0.9 \cdot 10^{-4}\,\mu_N^2$) and electric ($B(E2) = 45\ e^2\mathrm{fm}^4$) reduced transition probabilities, it is possible to extract a theoretical lifetime of $\tau = 0.92$ ns that can be compared to the experimental value of 1.59(40) ns. Increasing the number of basis states to include eight particles and eight holes configurations has no effect on the calculated values, implying that the truncation scheme does not affect the physical outcomes. The theoretical value is well within two standard deviations with respect to the measured lifetime, hinting at a satisfactory description of the nature of the two states of ^{47}K in the shell-model framework.

The spectroscopic factors for the direct proton-transfer reaction (^{46}Ar(^{3}He,d)^{47}K) can be computed with the SDPF-U interaction. The calculation was performed with the same truncation scheme with $4p-4h$ configurations. Table 8.3 presents the results of the calculation. Neither the $s_{1/2}$ nor the $d_{3/2}$ orbitals appear completely filled in ^{46}Ar. The spectroscopic factor of 0.94 relative to the $7/2^-$ state is an indication that a good description of the first two states of ^{47}K can be achieved by limiting the valence space of protons to the *sd* shell, or, in other words, that the $N = 20$ is a strong shell closure.

Energy	$\frac{1}{2}^+$ state (keV)	$\frac{3}{2}^+$ state (keV)	$\frac{7}{2}^-$ state (keV)
^{47}K (SDPF-U)	g.s.	324	-
^{47}K (Alternative)	g.s.	302	2066
^{47}K (*ab initio*)	g.s.	2511	6106
^{47}K (Experiment)	g.s.	360.0(10)	2020.0(15)

Table 8.2: Excitation energy of the low lying states of ^{47}K. The results are presented for different models: the shell-model with the SDPF-U interaction and an alternative interaction derived from it, as well as *ab initio* calculations.

C^{2}S	$\frac{1}{2}^+$ state	$\frac{3}{2}^+$ state	$\frac{7}{2}^-$ state
^{46}Ar$(d,p)^{47}$K (SDPF-U)	0.41	0.26	-
^{46}Ar$(d,p)^{47}$K (Alternative)	0.36	0.30	0.94
^{46}Ar$(d,p)^{47}$K (*ab-initio*)	0.66	0.025	0.69

Table 8.3: (Absolute) spectroscopic factors for the direct proton-transfer reaction (^{46}Ar(^{3}He,d)^{47}K) for the population of the ground state ($\frac{1}{2}^+$), the first excited state ($\frac{3}{2}^+$) and the $\frac{7}{2}^-$ state of ^{47}K. The results are presented for different models: the shell-model with the SDPF-U interaction and an alternative interaction derived from it, as well as *ab initio* calculations.

The occupation numbers of the orbitals for the ground state of ^{46}Ar and the first two excited states of ^{47}K are presented in Figure 8.1. According to the calculation, in the argon isotope, the $1s_{1/2}$ and $0d_{3/2}$ orbitals are occupied respectively 58% and 76%. In the case of ^{47}K, however, the shell-model picture points at a ground state ($1/2^+$) where the only non-filled orbital is the $1s_{1/2}$ with an occupation of 55%, while the first excited state ($3/2^+$) is of completely different nature with the $0d_{3/2}$ featuring an occupancy of only 76%. This is consistent with the identification of these levels as single-particle proton holes in the doubly-magic isotope ^{48}Ca.

In the independent-particle picture, the probability of filling the $s_{1/2}$ or $d_{3/2}$ orbital, given these occupancy figures, is roughly equally shared between the two

$\mathbf{C^2S}[L]/\mathbf{C^2S}[L=0]$	$\frac{3}{2}^+$ state	$\frac{7}{2}^-$ state
^{46}Ar$(d,p)^{47}$K (SDPF-U)	0.63	-
^{46}Ar$(d,p)^{47}$K (Alternative)	0.83	2.6
^{46}Ar$(d,p)^{47}$K (*ab initio*)	0.038	1.045
^{46}Ar$(d,p)^{47}$K (Experiment)	$0.10^{+0.11}_{-0.12}$	$1.10^{+0.18}_{-0.15}$

Table 8.4: Comparison of experimental and theoretical relative spectroscopic factors according to some of the nuclear models discussed in this Chapter. The results are presented for different models: the shell-model with the SDPF-U interaction and an alternative interaction derived from it, as well as *ab initio* calculations.

options. In particular, filling the first orbit will lead to the population of the $3/2^+$ state ($L = 2$ transfer), and placing the proton on the $d_{3/2}$ orbit implies populating the ground state ($L = 0$ transfer). This intuition is justified by the single-particle nature of these low lying states of ^{47}K.

The neutron component of the wave function, on the other hand, shows minor differences with only a slight decrease in occupation of the $f_{7/2}$ orbital. This effect is not surprising given the progressive breakdown of the shell gap in lower-Z isotopes along the $N = 28$ shell closure. The SDPF-U interaction, as introduced in the previous paragraphs, can correctly account for the evolution of the shell, and it is in agreement with experimental data in indicating ^{46}Ar as the last isotope where this gap is still significant.

Concerning the relative spectroscopic factors in ^{46}Ar, the values relative to the SDPF-U interaction are not compatible with the experimental data. In particular, they are at a distance of more than 3 standard deviations plus systematic errors with respect to the experimental data (cf. Table 8.4).

As a remark, the large figure given by the shell-model calculations for the relative spectroscopic factor of the $7/2^-$ state with the alternative interaction is skewed by the low value of the calculation for the ground state case. In order to remove this dependency, it is possible to define a new quantity $R[L]$, the spectroscopic factor relative to that of the $1/2^+$ and $3/2^+$ states:

$$R[L=3] = \frac{C^2S[L=3]}{C^2S[L=0] + C^2S[L=2]}$$

A simple rearrangement of the terms shows that the same quantity can be obtained for relative spectroscopic factors $\theta[L] = C^2S[L]/C^2S[L=0]$ with the following expression:

$$R[L=3] = \frac{\theta[L=3]}{\theta[L=2]+1}$$

The shell-model calculation achieves a value of $R[L = 3] = 1.4$, to be compared with the experimental result of $R[L = 3] = 1.0(2)$ for the optical

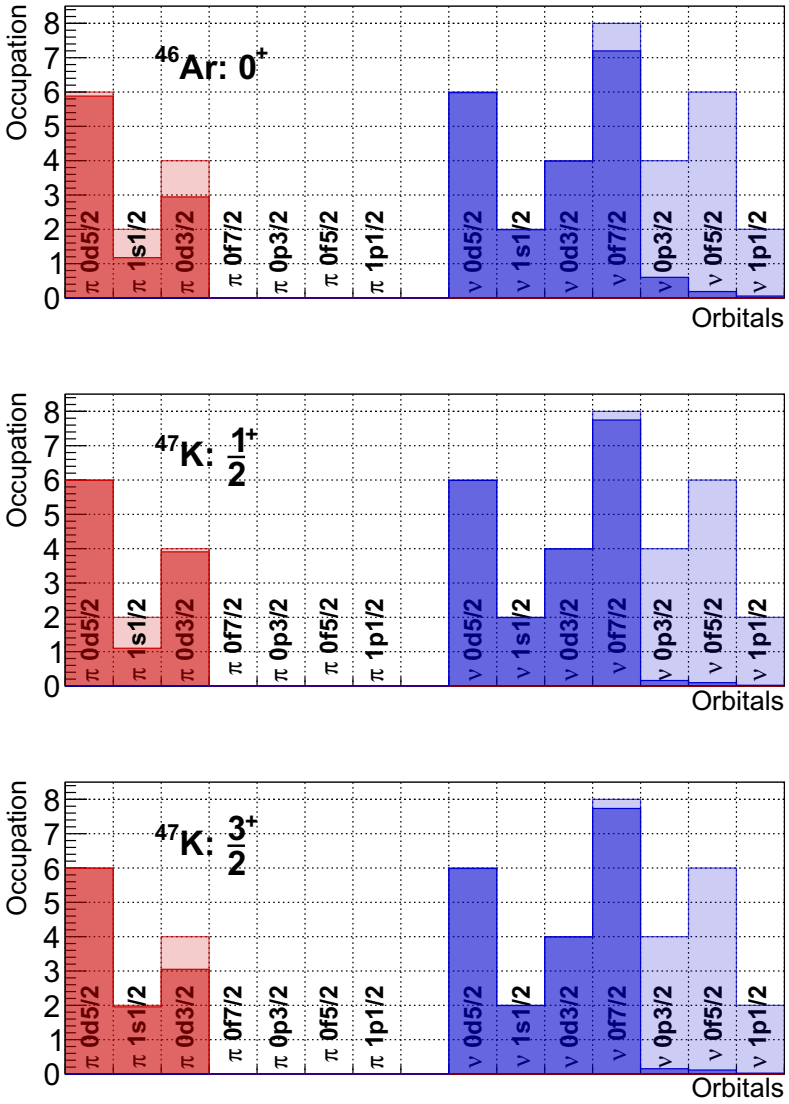

Figure 8.1: Occupation numbers of orbits computed with the SDPF-U interaction. The lighter shade indicates the orbital degeneracy and the darker color indicates the calculated occupation of the states of interest.

potential of Becchetti et al. and $R[L = 3] = 1.5(2)$ for that of Trost et al. (cf. subsection 7.4.1).

This value, together with the theoretical excitation energy of the $7/2^-$ state not too far off the experimental value, hints at a good shell-model description of this state as a proton excited to an empty $\pi f_{7/2}$ orbital.

At the same time, these results are a further indication of the failure of this model to account for the physical properties of the ground state of ^{46}Ar in terms of the $\pi s_{1/2} - \pi d_{3/2}$ wave function components.

8.2 The Density Functional Theory (DFT) Picture

Calculations of the ground state of ^{46}Ar have also been performed by means of DFT methods by G. Colò and collaborators [7].

The suppressed $L = 2$ transfer to the $d_{3/2}$ orbital indicates its large occupancy. This aspect, in turn, reflects the depletion of the $s_{1/2}$ orbital that is more localized in the inner part of the nucleus due to the vanishing of the centrifugal barrier of the central potential. If the depletion effect is sufficiently large, a void in the central portion of the density profile can emerge. This effect has been mentioned in the introductory chapter in section 3.2.4. In order to correctly describe this phenomenon, the theoretical model needs to be able to correctly describe the inversion of the two orbitals, which leads to the filling of the $d_{3/2}$ before the more central $s_{1/2}$.

The calculations were performed using a fully self-consistent Skyrme Hartree-Fock with the inclusion of the tensor interaction, similarly to those performed in reference [1].

A zero range tensor term in the Skyrme force is introduced, dependent on two tensor strength parameters, T and U (cf. reference [1] and references therein). The contact dependence (zero range) is due to the presence of the delta function $\delta(\mathbf{r})$.

$$\begin{aligned} V^T =& \frac{T}{2}\left\{\left[\left(\boldsymbol{\sigma}_1\cdot\mathbf{k}'\right)\left(\boldsymbol{\sigma}_2\cdot\mathbf{k}'\right)-\frac{1}{3}\left(\boldsymbol{\sigma}_1\cdot\boldsymbol{\sigma}_2\right)\mathbf{k}'^2\right]\delta(\mathbf{r})\right. \\ &\left.+\delta(\mathbf{r})\left[\left(\boldsymbol{\sigma}_1\cdot\mathbf{k}\right)\left(\boldsymbol{\sigma}_2\cdot\mathbf{k}\right)-\frac{1}{3}\left(\boldsymbol{\sigma}_1\cdot\boldsymbol{\sigma}_2\right)\mathbf{k}^2\right]\right\} \\ &+\frac{U}{2}\left\{\left(\boldsymbol{\sigma}_1\cdot\mathbf{k}'\right)\delta(\mathbf{r})\left(\boldsymbol{\sigma}_2\cdot\mathbf{k}\right)+\left(\boldsymbol{\sigma}_2\cdot\mathbf{k}'\right)\delta(\mathbf{r})\left(\boldsymbol{\sigma}_1\cdot\mathbf{k}\right)\right. \\ &\left.-\frac{2}{3}\left[\left(\boldsymbol{\sigma}_1\cdot\boldsymbol{\sigma}_2\right)\mathbf{k}'\cdot\delta(\mathbf{r})\mathbf{k}\right]\right\}. \end{aligned} \tag{8.2}$$

In the previous expression, the operators $k = (\nabla_1 - \nabla_2)/2i$ acts on the right and k' acts on the right. The tensor terms affect the spin-orbit potential U_{SO}:

$$U_{\mathrm{SO}} = \frac{W_0}{2r}\left(2\frac{d\rho_q}{dr}+\frac{d\rho_{q\prime}}{dr}\right)+\left(\alpha\frac{J_q}{r}+\beta\frac{J_{q\prime}}{r}\right) \tag{8.3}$$

The label q indicates protons or neutrons and ρ stands for the density while J represents the spin-orbit density. The parameters α and β are constituted by

two terms ($\alpha = \alpha_C + \alpha_T$) each representing the central exchange and the tensor contribution.

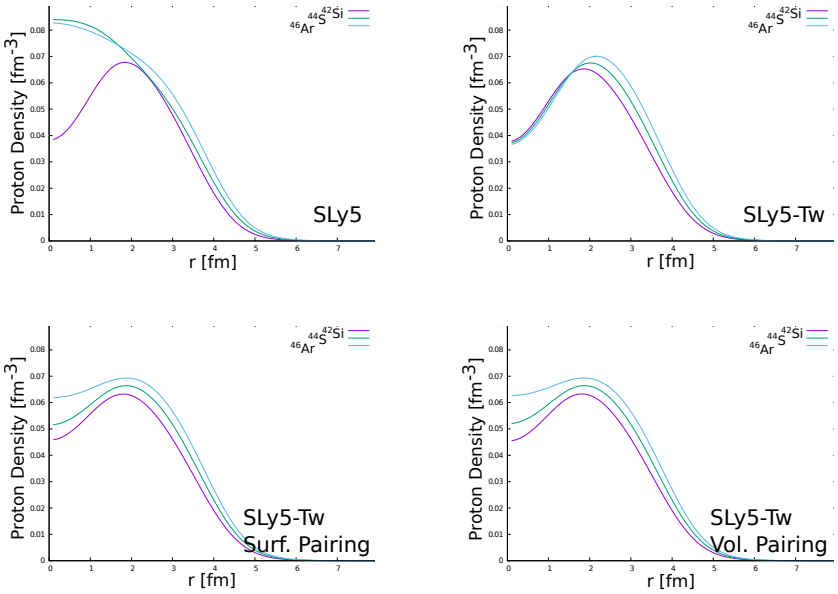

Figure 8.2: DFT calculation with the SLy5 force, a Skyrme-like interaction [7]. In light blue is shown the ^{46}Ar isotope, in green ^{44}S and in violet ^{42}Si. The x-axis presents the radius in fm and the y-axis the proton density in fm^{-3}. (top left panel) No bubble structure is present in ^{46}Ar as holes are located in the $d_{3/2}$ orbital, while protons occupy the more central $s_{1/2}$. (top right panel) Adding the more refined SLy5+Tw interaction, introduced in reference [1] generates a central depletion caused by the inversion of the two orbitals. (bottom left panel) Adding a surface pairing interaction the depletion is less pronounced and yet still present, also for ^{46}Ar. (bottom right panel) Similar effects can also be observed in the case of a volume pairing.

Figure 8.2 shows the result of the SLy5 parametrization (top left panel) in comparison with the SLy5+Tw (top right panel), thus introducing a tensor component to the interaction. The parametrization of the tensor terms of the latter is obtained perturbatively on top of the previous SLy5 force [1] and predicts a different proton density profile.

In particular, the SLy5 force hints at the presence of the bubble structure only in ^{42}Si, while the SLy5+Tw force finds an analogous structure also for ^{44}S and ^{46}Ar. The Sly5 interaction behaves similarly to alternative energy density functionals in predicting a standard ordering of the orbitals and, as a consequence, no central depletion. The introduction of a tensor component with the SLy5+Tw interaction is one of the cases where the inversion is present while

the energy is high enough to counterbalance the effect of the pairing interaction.

The description of the inversion of the orbitals in itself is not sufficient, as the bubble structure is weakened by the pairing correlation effect that tends to promote nucleons above the Fermi energy.

Consequently, the energy gap between the two orbitals needs to be sufficiently large to reduce the effect of the pairing correlation. This aspect can be clearly seen in Figure 8.2, where the introduction of the pairing force tends to fill the central depletion (bottom row) with respect to the bubble structure observed with no pairing interaction (top right panel). Two different types of pairing have been tested, a surface pairing and a volume pairing. The volume pairing interaction is a contact interaction of the form:

$$V_{vol} = V_0 \delta(\mathbf{r})$$

Where V_0 defines its strength, while the surface term has the analogous expression:

$$V_{surf} = V_0 (1 - \frac{\rho}{\rho_0}) \delta(\mathbf{r})$$

As expected, the addition of this interaction in both the volume and surface case has the effect of partially filling the central depletion. Nevertheless, the central density does not appear completely saturated in all three isotopes.

In terms of occupation probabilities, the calculation before the introduction of the pairing interaction predicts an occupation of 0 for the $s_{1/2}$ and 1 for the $d_{3/2}$. The effect of the pairing is to increase the occupation of the $s_{1/2}$ to 0.54 and decrease that of the $d_{3/2}$ to 0.78 [7] (equivalent values are obtained for the surface and volume pairing).

Independent calculations with a different Skyrme force performed in the framework of Skyrme Hartree Fock Bogoliubov, including a volume or surface pairing interaction (and a combination of them), hints at a similar bubble structure formation in ^{46}Ar [16]. Different strengths of the pairing interaction are tested based on values derived by the empirical pairing energy gap. These values are associated with a (low) probability of occupation of the $s_{1/2}$ orbit that ranges from 0.056 (in the case of mixed surface and volume pairing) to 0.269 for a stronger pairing force.

These results, observed in independent calculations and with different trials of pairing interaction, in combination with the experimental result that finds a low occupation of the $s_{1/2}$ orbital, corroborate the hypothesis of this peculiar structure in ^{46}Ar.

Coincidentally, the ^{44}S isotope presents a similar structure. This particular isotope has been shown (subsection 3.2.3) to present the same discrepancy in terms of transition probabilities, similar to the ^{46}Ar case.

8.3 *Ab initio* Calculations

The development of the *ab initio* framework relies on the extensive effort of deriving an effective theory from the underlying symmetries of quantum chromodynamics. Recent developments on these techniques opened the possibility of calculations not limited to light nuclei, pushing the frontier to the medium-mass region of the Segrè chart.

The quantum chromodynamics, which governs the strong force, can be treated by perturbative expansion only in the high energy scale. At low energies, relevant for nuclear physics phenomenons, the coupling constant is too large to justify the use of perturbation theory. Nevertheless, the vast amount of degrees of freedom that would constitute the treatment in terms of single quarks can be diminished in virtue of the confinement of quarks by considering composite particles such as nucleons and pions. This simplification allows the development of an effective Lagrangian, composed of effective interactions that still contain the same symmetries as the original QCD Lagrangian. A perturbative expansion can be introduced in terms of the coupling parameter Q/Λ. In this case, Q represents the momentum scale of the typical physical process and Λ the breakdown scale. The effective Lagrangian cannot describe physics with energies beyond this parameter; typical values are around $\Lambda \approx 1$ GeV. From the Lagrangian, it is possible to extract progressive expansions of the nuclear interactions where the next leading order presents more vertices of interaction with respect to the leading order. Each vertex is proportional to a constant that is identified by fitting nucleon-nucleon scattering data in the current practice.

Ab initio calculations have been performed [2] for ^{46}Ar using the NNLO$_{\mathrm{SAT}}$ interaction [9] with the self consistent Green's function method [6, 8, 13, 14].

While a full explanation of the calculation is beyond the scope of this work, the outcome of the calculation is presented to offer further insight into the experiment.

In particular, the same bubble profile density structure introduced in the previous section (8.2) has also been predicted in ^{46}Ar with the NNLO$_{\mathrm{SAT}}$ calculation [2]. This, in turn, translates to the spectroscopic factors shown in Table 8.3, which results in a reduced value of $C^2S = 0.025$ for the transfer to the $3/2^+$ state of ^{47}K, in line with the fact that the $\pi d_{3/2}$ orbit is almost full in the ground state of ^{46}Ar.

The comparison with the experimental data (Table 8.4) indicates that the results are fully compatible. In particular, the relative spectroscopic factor to the $3/2^+$ state appears well within error. The same consideration can be made for the $7/2^-$ state that appears within the statistical error. Table 8.2 presents the excitation energy of the states of interest in ^{47}K according to the calculations. The reason behind the significant dilatation of the energy spectrum is found in the nature of the underlying principles of the *ab initio* methodology. In particular, the interactions obtained from prime principles are able to reproduce the single-particle energies with uncertainties around $1 - 2$ MeV. These discrepancies stem from the theoretical uncertainty on the nuclear interaction.

Following the same considerations of the shell-model calculations, the value

of the $L = 3$ transfer over the sum of the $L = 0$ and $L = 2$ returns a value of $R[L = 3] = 1.01$, compatible with the experimental data ($R[L = 3] = 1.0(2)$). This is not surprising since both the relative figures are in agreement.

8.4 Summary and Conclusions

An impressive amount of experimental and theoretical effort has been dedicated in the past and recent times for the study of nuclear structure around the $N = 28$ shell closure. In particular, the study of the shell evolution and its demise far from the valley of stability has never failed to attract the interest of the nuclear structure scientific community. Much of the experimental effort has been focused on studying the neutron energy gap with the intent of assessing its presence or progressive fading in the most neutron-rich isotopes. The experimental data on the matter are manifold, ranging from neutron removal energies to (neutron) transfer or knockout reactions. The combination of this extraordinary effort leaves little probability for alternative interpretations: the neutron shell closure fades progressively in the most neutron-rich isotones. In particular, ^{44}S has been associated with the onset of collectivity. Nuclear models appear in agreement with the prediction of this progressive deterioration of the $N = 28$ energy gap both in the framework of density functional theory and shell-model calculations.

While these considerations might indicate that the physics in this particular region is well understood, a surprising discrepancy between theoretical models and experimental data has been observed in ^{46}Ar. The availability of radioactive beams in state-of-the-art facilities opened the possibility to perform Coulomb excitation experiments on isotopes far from stability. The comparison of transition probabilities between the shell model with the SDPF-U interaction and intermediate energy Coulomb excitation experiments reveals a discrepancy of more than factor two, with theory largely over-predicting the experimental value. While the experimental data give a drop in transition probability as the $N = 28$ shell closure is reached in the argon isotopic chain, the shell model predicts a sharp increase. This aspect is even more surprising if one considers the good performance of the shell model in the prediction of transition probabilities of nearby isotopes, with one exception. A recent intermediate-energy Coulomb excitation experiment revealed the same discrepancy of a factor of approximately two for ^{44}S, located just below $(-2p)$ with respect to ^{46}Ar.

An insightful study performed with the LISE setup at GANIL allowed the extraction of proton and neutron matrix elements that concur to the total transition probability. The authors concluded that the main factor in the large discrepancy of the transition probability in ^{46}Ar was related to an overestimation of the proton matrix element. This clue is also backed by the evidence that neutron-dependent observables are well described by the theoretical model.

The experiment presented in this work aimed at directly probing the proton component of the wave function. A proton transfer direct reaction was performed in GANIL at the SPIRAL1 facility on ^{46}Ar. This reaction, ^{46}Ar(^{3}He,d)^{47}K, relied on the production of this radioactive isotope with a primary beam of ^{48}Ca and a post acceleration to 9.9 MeV/u. The beam impinged on a newly developed gaseous cryogenic ^{3}He target cooled at ≈ 7 K. The experimental setup allowed the full reconstruction of the two-body reaction, with the detection of the heavy ^{47}K ion in the magnetic spectrometer (VAMOS) and of the deuteron by a position-sensitive silicon detector (MUGAST). The high-purity germanium

tracking array (AGATA) allowed the measurement of γ-rays emitted after the population of the states of the potassium isotope.

The experimental outcome hints at a suppressed $L = 2$ transfer, indicative of a high degree of occupancy of the $d_{3/2}$ orbital in the ^{46}Ar ground state, inconsistent with the shell-model calculation that predicts a somewhat similar occupation for the $s_{1/2}$ and $d_{3/2}$ orbitals. This discrepancy further motivates the argument concerning the failure of the shell model in the description of the proton component of the wave function.

From a heuristic point of view, the small experimental $B(E2)$ can be justified, in a shell-model framework, with a restriction of the $s_{1/2}$ and $d_{3/2}$ proton space that the SDPF-U interaction predicts as fully open (almost degenerate shells). The result found in this work, i.e. a significant closure of the $\pi d_{3/2}$ shell in ^{46}Ar combined with an empty $s_{1/2}$, points exactly in that direction.

A brief discussion has also been introduced on the implication of the low occupancy of the $s_{1/2}$ orbit on the density profile in the framework of density functional theory calculations. In particular, some calculations are able to predict the inversion of the two orbitals, hinting at the presence of a central proton density depletion. The same effect is shown in the case of ^{44}S that, remarkably, reflects the same discrepancy in terms of transition probabilities.

Ab initio calculations also provide an independent picture and predict a low spectroscopic factor relative to the $3/2^+$ state, compatible with the experimental evidence. At the same time, also the spectroscopic factor of the $7/2^-$ state appears compatible with the data. The same central proton density depletion is observed in *ab initio* calculation.

8.5 Future Perspectives

This thesis presents a fundamental insight on the nuclear structure problem of ^{46}Ar, offering also a hint for further investigation for this isotope and analogous ones such as ^{44}S. This work has pointed out the failure of shell-model interactions in describing the proton wave function of ^{46}Ar, and it will hopefully spur further experimental and theoretical studies.

The use of direct reactions to study nuclear structure properties of these isotopes could be extended with the proton-removal reaction ^{47}K(^{3}H,^{4}He)^{46}Ar that would offer a complementary picture to the current work and exploit the higher intensity achievable with radioactive ^{47}K beams in ISOL facilities. At the same time, the proton removal from ^{46}Ar (^{46}Ar(d,^{3}He)^{45}Cl) could help to confirm the ground state structure of this argon isotope with the potential of measuring absolute spectroscopic factors thanks to the simpler CD_2 target.

A more direct investigation on the charge density of ^{46}Ar, with the specific aim of studying the central depletion (bubble structure), could be performed with electron scattering techniques. This study could also be extended to other isotopes which are expected to share this peculiar structure, such as ^{44}S and ^{42}Si. These experiments could be carried out in facilities such as Scrit Electron

Scattering Facility At Riken [15] or in the future at the planned Facility for a High-Power Energy Recovery Linac at Orsay, PERLE [3].

The development of state-of-the-art high purity germanium tracking arrays such as AGATA and GRETINA offers the unique possibility to also perform precise lifetime measurements in combination with the plunger setup and various ancillary detectors. The high efficiency and Doppler correction capabilities of these arrays could represent a decisive factor to improve upon previous measurements. In particular, a high-statistic measurement of the lifetime of the 2^+ state of ^{46}Ar could help to resolve the disagreement between the lifetime and relativistic Coulomb excitation experiments.

Bibliography

[1] Bai, C. L. et al. “Effect of the Tensor Force on the Charge Exchange Spin-Dipole Excitations of ^{208}Pb”. In: *Phys. Rev. Lett.* vol. 105 (7 Aug. 2010), p. 072501. DOI: 10.1103/PhysRevLett.105.072501. URL: https://link.aps.org/doi/10.1103/PhysRevLett.105.072501.

[2] Barbieri, C., Somà, V., and Brolli, S. Private communication. 2021.

[3] Bogacz, S. “PERLE-ERL Test Facility at Orsay”. In: *Proceedings for the XXVIII International Workshop*. 2021.

[4] Caurier, E. and Nowacki, F. “Present Status of Shell Model Techniques”. In: *Acta Phys. Pol. B* vol. 30 (1999), p. 705. URL: https://www.actaphys.uj.edu.pl/R/30/3/705/pdf.

[5] Caurier, E. et al. “The shell model as a unified view of nuclear structure”. In: *Rev. Mod. Phys.* vol. 77 (2 June 2005), pp. 427–488. DOI: 10.1103/RevModPhys.77.427. URL: https://link.aps.org/doi/10.1103/RevModPhys.77.427.

[6] Cipollone, A., Barbieri, C., and Navrátil, P. “Isotopic Chains Around Oxygen from Evolved Chiral Two- and Three-Nucleon Interactions”. In: *Physical Review Letters* vol. 111, no. 6 (Aug. 2013). DOI: 10.1103/physrevlett.111.062501. URL: https://doi.org/10.1103/physrevlett.111.062501.

[7] Colò, G. Private communication. 2021.

[8] Dickhoff, W. and Barbieri, C. “Self-consistent Green’s function method for nuclei and nuclear matter”. In: *Progress in Particle and Nuclear Physics* vol. 52, no. 2 (2004), pp. 377–496. DOI: https://doi.org/10.1016/j.ppnp.2004.02.038. URL: https://www.sciencedirect.com/science/article/pii/S0146641004000535.

[9] Ekström, A. et al. “Accurate nuclear radii and binding energies from a chiral interaction”. In: *Phys. Rev. C* vol. 91 (5 May 2015), p. 051301. DOI: 10.1103/PhysRevC.91.051301. URL: https://link.aps.org/doi/10.1103/PhysRevC.91.051301.

[10] Gade, A. et al. “Is the Structure of ^{42}Si Understood?” In: *Phys. Rev. Lett.* vol. 122 (22 June 2019), p. 222501. DOI: 10.1103/PhysRevLett.122.222501. URL: https://link.aps.org/doi/10.1103/PhysRevLett.122.222501.

[11] Gottardo, A. Private communication. 2020.

[12] Riley, L. A. et al. “Inverse-kinematics proton scattering from ^{42,44}S, ^{41,43}P, and the collapse of the $N = 28$ major shell closure”. In: *Phys. Rev. C* vol. 100 (4 Oct. 2019), p. 044312. DOI: 10.1103/PhysRevC.100.044312. URL: https://link.aps.org/doi/10.1103/PhysRevC.100.044312.

[13] Rios, A. *Green’s functions techniques for extended nuclear systems*. 2020. arXiv: 2006.10610 [nucl-th].

[14] Somà, V. et al. “Novel chiral Hamiltonian and observables in light and medium-mass nuclei”. In: *Phys. Rev. C* vol. 101 (1 Jan. 2020), p. 014318. DOI: 10.1103/PhysRevC.101.014318. URL: https://link.aps.org/doi/10.1103/PhysRevC.101.014318.

[15] Tsukada, K. et al. “First Elastic Electron Scattering from ^{132}Xe at the SCRIT Facility”. In: *Phys. Rev. Lett.* vol. 118 (26 June 2017), p. 262501. DOI: 10.1103/PhysRevLett.118.262501. URL: https://link.aps.org/doi/10.1103/PhysRevLett.118.262501.

[16] Wang, Y.-Z. et al. “Pairing Effects on Bubble Nuclei”. In: *Chinese Physics Letters* vol. 36, no. 3 (Mar. 2019), p. 032101. DOI: 10.1088/0256-307x/36/3/032101. URL: https://doi.org/10.1088/0256-307x/36/3/032101.

Appendices

Appendix A

^{3}He equation of state

A.1 Equation of state

The equation of state is a functional relationship between some parameter which describe the thermodynamical state of a substance. In particular, for the current work, it is essential to extract the density of the ^{3}He gas contained in the cryogenic target as a function of the measured pressure and temperature. The equation of state is constituted by an implicit function of some macroscopic variables. In the case of a gas these often consist in pressure p, volume V and temperature T:

$$f(p, V, T) = 0$$

The knowledge of the equation of state allows to derive all other macroscopic quantities of the system. And in the case of a ideal gas, it takes the common form of:

$$pV - Nk_BT = 0$$

Where k_B represents the Boltzmann constant. This equation often represents a starting point for a physical equation of states which is applicable to real-world data as it fails to include the effect of long range correlations to the macroscopic variables of the system. The impact of the interaction among the gas molecules is more important near the critical point of the gas, making the equation of ideal gasses not a precise approximation.

Various models can be employed, nevertheless a direct measurement of the system near its critical point is necessary for a precise assessment of the density as a function of pressure and temperature. In the case of ^{3}He, the measurement of pressure, density and temperature for a pure ^{3}He gas has been performed in reference [1]. The authors were able to measure the gaseous density as a function of the pressure at different temperatures and near the critical point (Figure A.1, top). The appearance of a critical point for temperatures around 3.3 K is evident, as a inflection point gradually appears lowering the temperature. Another density measurement was performed varying the temperature at different pressure values (Figure A.1, bottom).

The results of the tables included in the article are presented in Figure A.1 and have been used to interpolate the equation of state in the experimental temperature and pressure range in order to compute the density of the ^{3}He gas.

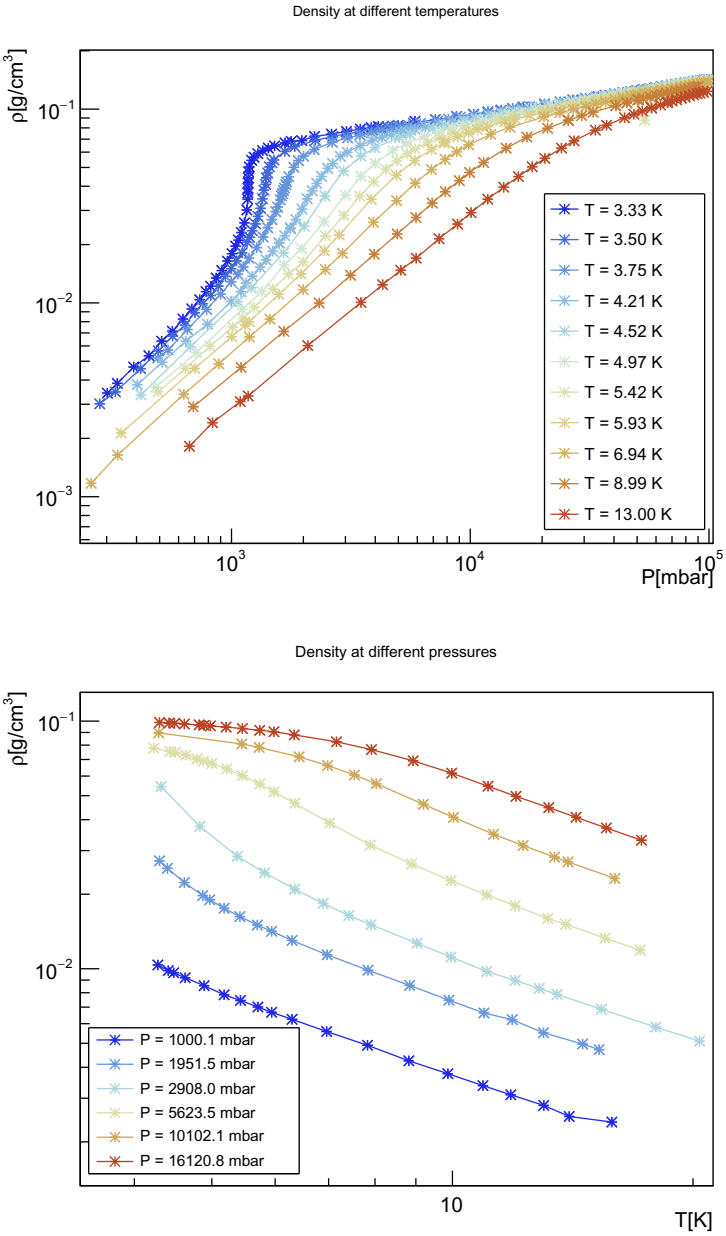

Figure A.1: Measurements of ^{3}He equation of state, data extracted from the table in reference [1]. (Top) Density as a function of the pressure at different temperatures. (Bottom) Density as a function of the temperature at different pressures.

Bibliography

[1] И. В. Богоявленский and Л. В. Карнацевич and В. Г. Конарева. Эксперимннмльнов изучение уравнения состояния ивотопов гвлия ($не^3$ и $не^4$) в твмпвратурном интервале от 3,3 к до 14 к. June 1978.

Appendix B

Resolution model

B.1 Resolution model

The to loss of charge collection is a common aspects of many kinds of detectors and is apparent in the response of the detector. In the particular case of this thesis, this aspect can be observed in the response of the γ-ray detector AGATA where the damage caused by neutrons on the crystalline structure of the high purity germanium detectors causes a loss of collected charge and as a consequence a left tail on each energy peak. The same behavior can be also observed on the silicon detectors, in this case on the energy spectra of Mugast.

It can be useful, in first approximation, to model the response due to a *lossy* detector as the convolution of the probability density functions (PDF), a general Gaussian distribution and a decaying exponential. The latter is introduced under the assumption that the amount of lost charge decays exponentially in probability.

The convolution of two PDF distributions can be computed with an integral as follows:

$$h(x;\mu,\sigma,\tau) = (f \circ g)(x;\mu,\sigma,\tau) = (g \circ f)(x;\mu,\sigma,\tau) = \int_{-\infty}^{\infty} f(x-t)\, g(t) dt$$

where in this case the two distributions are the common Gaussian distribution which simulates the intrinsic resolution:

$$g(x;\mu,\sigma) = \frac{1}{\sigma\sqrt{2\pi}} \left(e^{-\frac{1}{2}\left(\frac{x-\mu}{\sigma}\right)^2} \right)$$

And the exponential distribution limited on the negative values of x, accounting for the lossy behavior:

$$f(x;\tau) = \frac{1}{\tau} e^{\frac{(x-\mu)}{\tau}}\, \Theta(\mu - x)$$

It is possible to show that the analytical expression of the convolution has the form of the following equation [1]:

$$f(x;\mu,\sigma,\lambda) = \frac{1}{2\tau} e^{\frac{1}{2\tau}\left(\frac{\sigma^2}{\tau} - 2\mu + 2x\right)} \left(1 - \operatorname{erf}\left(\frac{\frac{\sigma^2}{\tau} - \mu + x}{\sqrt{2}\sigma} \right) \right)$$

Where $\operatorname{erf}(x)$ represents the error function, related to the cumulative distribution of the Gaussian PDF:

$$\operatorname{erf}(x) = \frac{2}{\sqrt{\pi}} \int_0^x e^{-t^2} dt$$

The mean of the distribution is given by $\mu - \tau$ and the variance by $\sigma^2 + \tau^2$. Figure B.1 shows an example of a convolution of the two distributions, in particular the parameters chosen correspond to those inferred from the fit in Figure 4.27 in subsection 4.6.2.

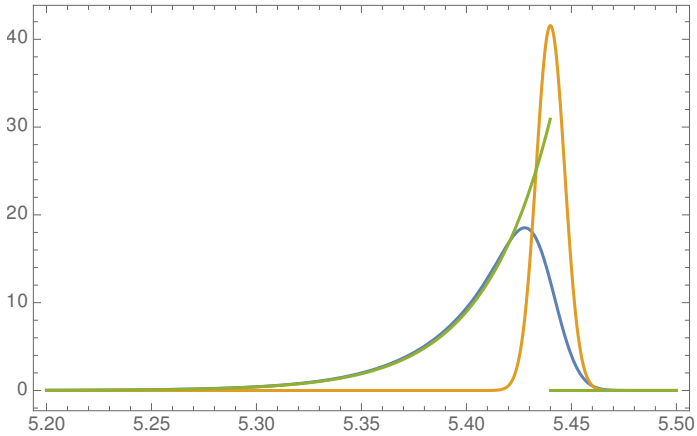

Figure B.1: Convoluted distribution (in blue) of a Gaussian distribution (in orange) and an exponential (in green) with $\mu = 5.44, \sigma = 0.0096, \tau = 0.032$. The FWHM can be computed numerically and corresponds to ≈ 0.044.

Bibliography

[1] Grushka, E. “Characterization of exponentially modified Gaussian peaks in chromatography”. In: *Analytical Chemistry* vol. 44, no. 11 (Sept. 1972), pp. 1733–1738. DOI: 10.1021/ac60319a011. URL: https://doi.org/10.1021/ac60319a011.

Appendix C

Electronics chain

C.1 Electronics chain

MUVI

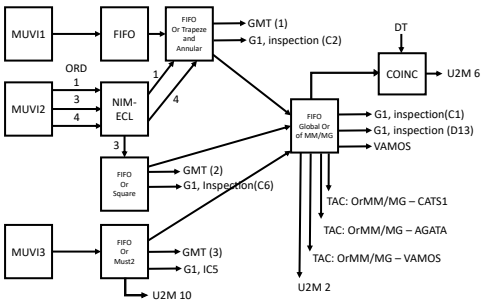

VAMOS trigger (MWPPAC)

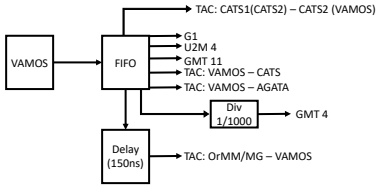

AGATA

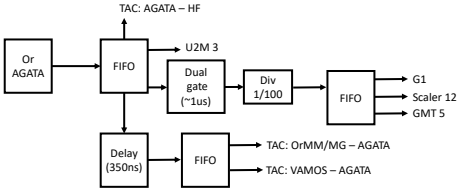

CATS2

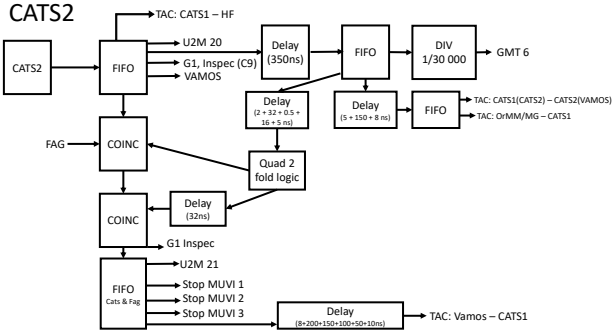

HF

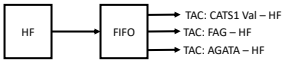

Dead Time

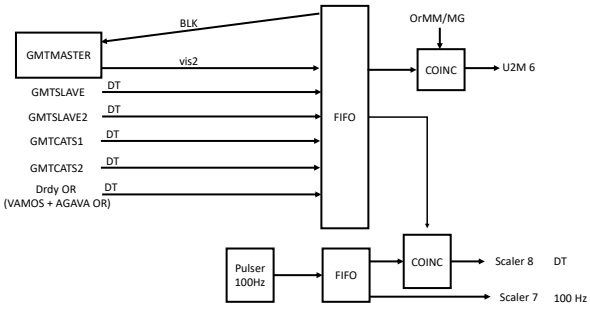

Ringraziamenti

A conclusione di questo elaborato desidero ringraziare tutte le persone senza le quali questo lavoro non esisterebbe.

In particolar modo al dott. Andrea Gottardo, che grazie al suo immancabile ottimismo mi ha spinto a cercare una soluzione ai vari grattacapi nel corso dell'analisi dati. Non credo potrò dimenticare tutte le discussioni sul ghiaccio del target, potenziali ottici, modello a shell, etc..

Un ringraziamento particolare anche al prof. Daniele Mengoni, per le utili discussioni nel corso dell'analisi dati e per la rilettura di questo elaborato che ora mi sembra non finire più.

Desidero ringraziare anche il dott. Jose Javier Valiente-Dobón, in particolar modo per avermi introdotto in questo ambiente di ricerca a partire dalla tesi magistrale e poi nel corso del dottorato.

Ovviamente non posso dimenticare di ringraziare il dott. Alain Goasduff, onnipresente risolutore di qualsiasi tipo di problema, sia esso di fisica, informatica, elettronica...

Non posso non essere riconoscente al dott. Simone Bottoni per l'aiuto con i calcoli di reazione, per tutte le proficue spiegazioni sulle reazioni dirette e la pazienza dimostrata nei miei confronti.

Infine vorrei ringraziare tutti i colleghi dei Laboratori Nazionali di Legnaro, dottorandi, postdoc e ricercatori che mi hanno accompagnato in questo percorso di dottorato.